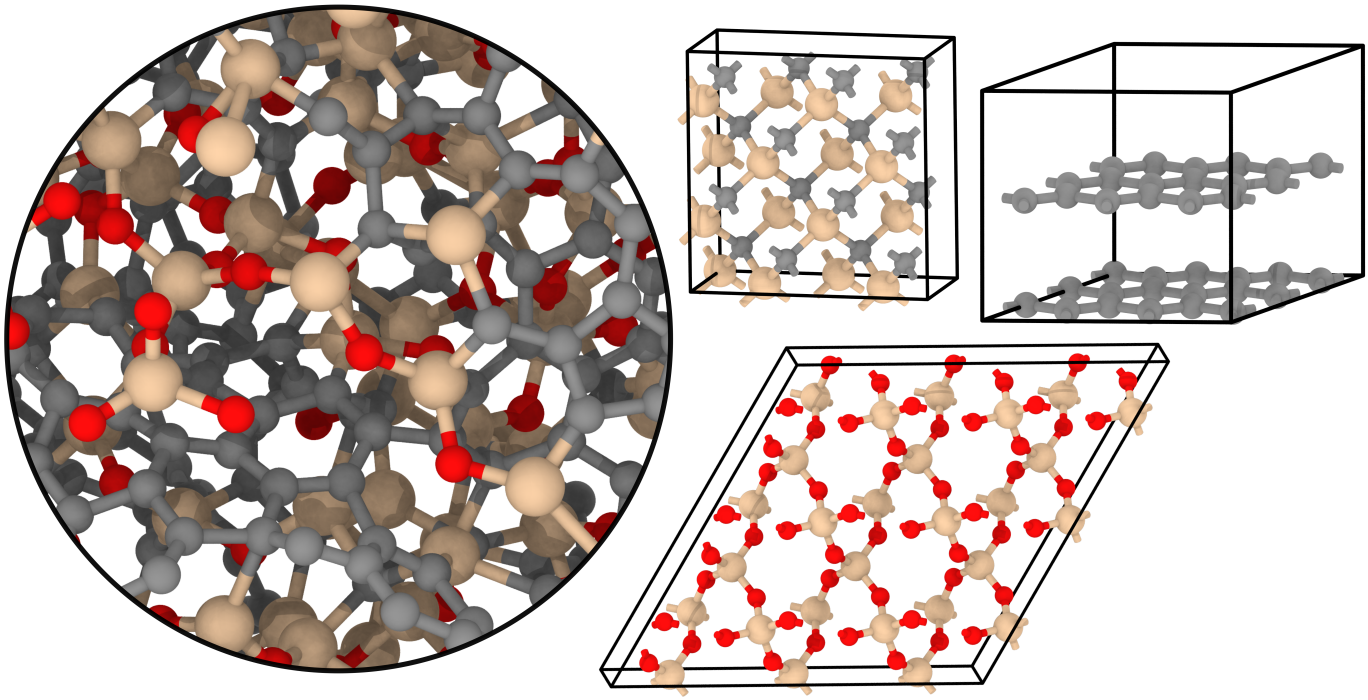

Atomistic modelling of crystalline and amorphous Cu-Zr and Si-O-C using machine learning interatomic potentials

Niklas Leimeroth

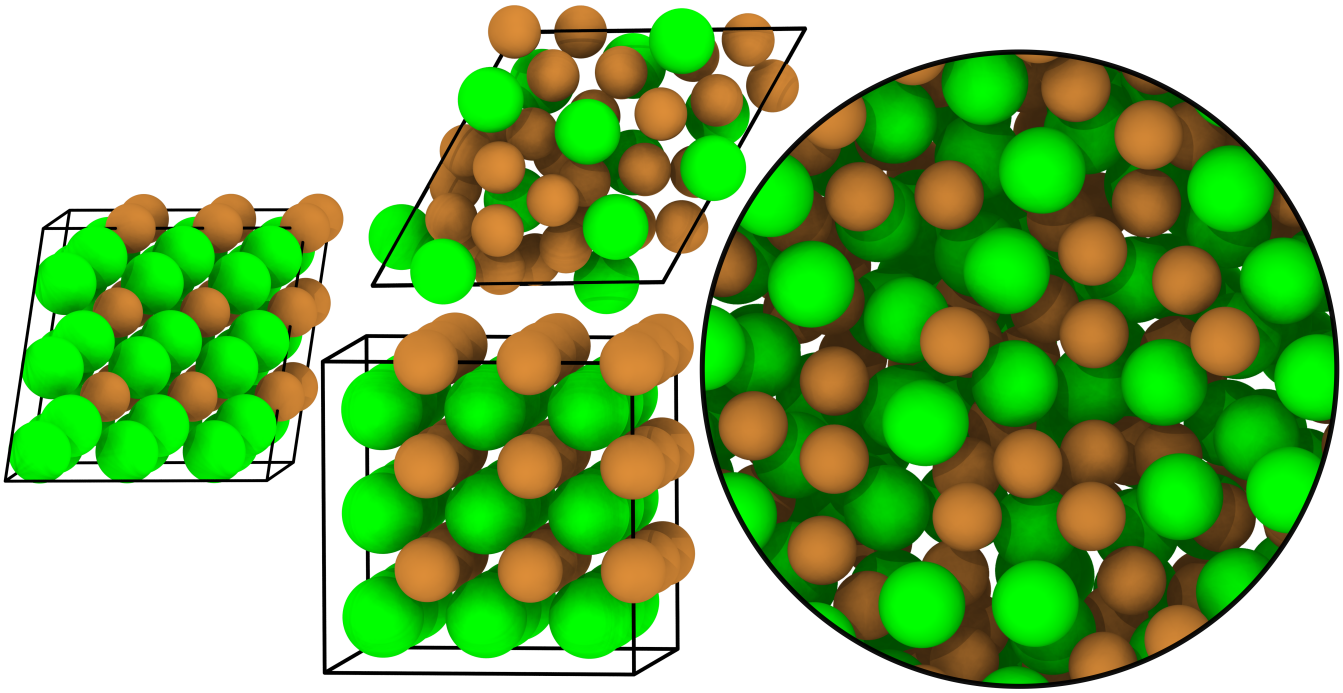

On the cover: Examples of amorphous and crystalline Si-O-C and Cu-Zr structures.

Atomistic modelling of crystalline and amorphous Cu-Zr and Si-O-C using machine learning interatomic potentials

Zur Erlangung des akademischen Grades Doktor der Naturwissenschaften (Dr. rer. nat.) genehmigte Dissertation vorgelegt von Niklas Leimeroth.

Fachgebiet:	Materialmodellierung
Fachbereich:	Material- und Geowissenschaften
	Technische Universität Darmstadt

Berichter:	Prof. Dr. Karsten Albe
	Technische Universität Darmstadt
Mitberichter:	Prof. Dr. Ralf Drautz
	Ruhr Universität Bochum
1. Prüfer:	Prof. Dr. Hongbin Zhang
	Technische Universität Darmstadt
2. Prüfer:	Prof. Dr. Magdalena Graczyk-Zajac
	Technische Universität Darmstadt

Tag der Einreichung:	27.05.2024
Tag der Prüfung:	02.10.2024
Jahr der Veröffentlichung:	2024

Darmstadt 2024

Please cite this document as:
URN: urn:nbn:de:tuda-tuprints-283064
URL: https://tuprints.ulb.tu-darmstadt.de/id/eprint/28306

Niklas Leimeroth: Atomistic modelling of crystalline and amorphous Cu-Zr and Si-O-C using machine learning interatomic potentials
Dieses Dokument wurde erstellt mit KOMA-Script und LaTeX.
Jahr der Veröffentlichung auf TUPrints: 2024
URN: urn:nbn:de:tuda-tuprints-283064
URL: https://tuprints.ulb.tu-darmstadt.de/id/eprint/28306
Tag der mündlichen Prüfung: 02.10.2024
Dieses Dokument wird bereitgestellt von TUPrints, E-Publishing-Service der TU Darmstadt
http://tuprints.ulb.tu-darmstadt.de
tuprints@ulb.tu-darmstadt.de

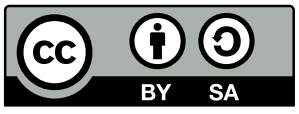

Erklärungen laut Promotionsordnung

§8 Abs. 1 lit. c PromO

Ich versichere hiermit, dass die elektronische Version meiner Dissertation mit der schriftlichen Version übereinstimmt.

§Abs. 1 lit. d PromO

Ich versichere hiermit, dass zu einem vorherigen Zeitpunkt noch keine Promotion versucht wurde. In diesem Fall sind nähere Angaben über Zeitpunkt, Hochschule, Dissertationsthema und Ergebnis dieses Versuchs mitzuteilen.

§9 Abs. 1 PromO

Ich versichere hiermit, dass die vorliegende Dissertation – abgesehen von den in ihr ausdrücklich genannten Hilfen – selbstständig verfasst wurde und dass die „Grundsätze zur Sicherung guter wissenschaftlicher Praxis an der Technischen Universität Darmstadt“ und die „Leitlinien zum Umgang mit digitalen Forschungsdaten an der TU Darmstadt“ in den jeweils aktuellen Versionen bei der Verfassung der Dissertation beachtet wurden.

§9 Abs. 2 PromO

Die Arbeit hat bisher noch nicht zu Prüfungszwecken gedient.

Darmstadt, 18. Oktober 2024

Niklas Leimeroth

Abstract

Modelling and simulation on the atomic scale play a pivotal role for the understanding of complex materials. In this field, machine learning interatomic potentials (MLIPs) are rapidly evolving tools, which allow the description of interatomic interactions with an accuracy approaching that of quantum mechanical methods. At the same time, they are computationally much more efficient, opening the possibility for large-scale molecular dynamics (MD) simulations with unprecedented fidelity. However, current research in the field is often focused on methodical advancements and uses simple single element test cases for this purpose. This thesis treats the development and application of MLIPs, more specifically highly efficient Atomic Cluster Expansion potentials (ACEPs), for structurally and chemically complex systems, namely Cu-Zr and silicon oxycarbide (Si-O-C). Both are representatives of important material classes, metals and glass-ceramics.

Cu-Zr has a plethora of intermetallic phases and is a well known metallic glass (MG) former. The performance of the developed potential is compared to previously published classical potentials and experimental data. Using the new MLIP, the concentration-temperature phase diagram of the material is calculated and found to be in good agreement with experiments. Furthermore, the MG structure is investigated, revealing a massively different short-range order compared to classical interatomic potentials (IPs), and tensile tests of a glass-crystal matrix sample show the occurrence of martensitic phase transitions in B2-CuZr.

Si-O-C has a highly tunable composition and microstructure. Consequently, training data for this material needs to cover a wide configuration space, which is achieved with an active learning strategy based on structural units present in the bulk material. The developed ACEP is the first publicly available IP for the system and employed to investigate the atomistic structure and its relation to the elastic properties. Contrary to common assumptions, graphite agglomerates in the system are of low importance for the Young's modulus. Instead, strong correlation to SiO_4 tetrahedra and SiC bonds are found.

Finally, different types of MLIPs are evaluated. During the work on Cu-Zr and Si-O-C equivariant structure descriptions and message-passing graph neural networks emerged as promising methods to reach ever improving accuracies. Novel NequIP, Allegro and MACE MLIPs implementing them are compared to the well established High-Dimensional Neural Network Potentials (HDNNPs), Gaussian Approximation Potentials (GAPs), Moment Tensor Potentials (MTPs) and ACEPs. The tests reveal the large data requirements for HDNNPs and emphasize the trade-off between achievable accuracies and computational cost. ACEPs still represent a good compromise in this regard.

Zusammenfassung

Modellierung und Simulation auf atomistischer Skala sind essenziell für das Verständnis komplexer Materialien. In diesem Bereich sind Machine-Learning Interatomare Potenziale (engl. machine learning interatomic potentials (MLIPs)) sich schnell entwickelnde Werkzeuge, die Beschreibung interatomarer Wechselwirkungen mit einer Genauigkeit nahe der von quantenmechanischen Methoden erlauben. Gleichzeitig sind sie deutlich effizienter zu berechnen. Dies ermöglicht große Molekulardynamik (engl. molecular dynamics (MD)) Simulationen mit nie dagewesener Detailtreue. Aktuelle Forschung in diesem Bereich ist häufig auf die Methodenentwicklung fokussiert und verwendet für den 'proof of concept' meistens elementare Systeme. Im Gegensatz dazu, befasst sich diese Dissertation mit der Entwicklung und Anwendung von MLIPs, insbesondere hocheffizienten Atomare Cluster Expansion Potenzialen (engl. Atomic Cluster Expansion potential (ACEP)), für die strukturell und chemisch komplexen Systeme Cu-Zr und Si-O-C. Beide sind exemplarisch für wichtige Materialklassen, Metalle und Glaskeramiken.

Cu-Zr weist eine Vielzahl intermetallischer Phasen auf und ist ein bekannter Glasbildner. Die Leistung des entwickelten Potenzials wird mit verfügbaren klassischen Potenzialen und experimentellen Daten verglichen. Das mit dem Potenzial berechnete Konzentrations-Temperatur Phasendiagramm stimmt weitgehend mit dem Experimentell überein. Darüber hinaus wird die Glasstruktur untersucht, wobei eine im Vergleich zu klassischen Potenzialen unterschiedliche Nahordnung der Atome festgestellt wird. Zugversuche an Glas-Kristall Proben zeigen das Auftreten martensitischer Phasenumwandlungen in B2-CuZr.

Silizium Oxycarbid hat eine weitgehend einstellbare Zusammensetzung und Mikrostruktur. Folglich müssen die Trainingsdaten für das Material einen breiten Konfigurationsraum abdecken, was durch eine Active-Learning Strategie auf Basis von im Material vorhandenen Struktureinheiten erreicht wird. Das entwickelte ACEP ist das erste öffentlich verfügbare Potenzial für dieses System. In dieser Arbeit wird es verwendet, um die atomare Struktur und ihren Zusammenhang mit elastischen Eigenschaften zu untersuchen. Entgegen allgemeinen Annahmen spielen graphitische Agglomerate im System für das Elastizitätsmodul eine untergeordnete Rolle. Stattdessen wird eine starke Korrelation zu SiO_4 Tetraedern und SiC-Bindungen festgestellt.

Das letzte Thema dieser Dissertation ist die Evaluierung verschiedener Arten von MLIPs. Während der Arbeiten an Cu-Zr und Si-O-C haben sich äquivariante Strukturbeschreibungen und Message-Passing Graph Neural Networks als vielversprechende Methoden zur Erzielung immer höherer Genauigkeiten herauskristallisiert. Neuartige NequIP, Allegro und MACE MLIPs, die diese Methoden imple-

mentieren, werden mit etablierten MLIPs verglichen. Die Tests zeigen den großen Datenbedarf von Hochdimensionalen Neuronalen Netzwerk Potenzialen auf und unterstreichen den Zusammenhang zwischen erreichbarer Genauigkeit und erhöhtem Rechenaufwand. ACEPs stellen hierbei weiterhin einen guten Kompromiss dar.

Acknowledgements - Danksagung

An dieser Stelle möchte ich mich bei all denjenigen Personen bedanken, die mich während meiner Promotion unterstützt haben. Ohne euch wäre die Arbeit der letzten Jahre deutlich trister und weniger erfolgreich verlaufen.

Zunächst danke ich meinem Doktorvater Prof. Dr. Karsten Albe für die Möglichkeit in seiner Arbeitsgruppe zu promovieren und die Unterstützung meiner wissenschaftlichen Arbeit, sowie sehr unterhaltsame Wanderungen stets eine guten halbe Stunde vom Ziel entfernt. Besonders danken möchte ich auch Ph.D. Jochen Rohrer, der mir mit vielen hilfreichen Ratschlägen zu wissenschaftlichen Problemen und durch zuverlässiges gegenlesen meiner Texte zur Seite stand. Hervorheben möchte ich auch Gabriele Rühl für ihre Anleitung auf dem Weg durch den Verwaltungsdschungel der Universität. Mein Dank gilt auch Prof. Dr. Ralf Drautz, Prof. Dr. Hongbin Zhang und Prof. Dr. Magdalena Graczyk-Zajac, die diese Dissertation als Mitberichter und Prüfer unterstützen.

Darüber hinaus dürfen natürlich auch meine Kollegen aus der Materialmodellierung nicht unerwähnt bleiben, die stets hilfsbereit waren und mit denen ich bei unseren Gruppenevents viel Freude hatte. Hier möchte ich zunächst meinen Büronachbarn Linus Erhard hervorheben; unsere Diskussionen über MLIPs waren von unschätzbarem Wert für meine Publikationen und diese Dissertation und auch einige Konferenzen wären ohne dich eher langweilig geworden. Einen besonderen Dank redlich verdient haben sich auch Marcel Sadowski und Daniel Utt, die als MM Admins unsere Bürorechner und Server am Laufen gehalten, mir bei wissenschaftlichen und technischen Problemen aller Art geholfen, Teamevents organisiert und hervorragende Reisetipps gegeben haben. Meinem ehemaligen Bürokollegen Lorenzo Villa möchte ich für eine Menge höchst unterhaltsamer Fluchtiraden und die Organsiation des wohl, trotz viel Gemeckers, besten MM Sportturniers aller Zeiten danken. Dankbar bin ich auch Ali Malik, dessen enstpannte Art den Alltag im Büro bereichert, Marie Charrier mit der ich die TMS in San Diego besuchen durfte, Elaheh Ghorbani die mich während meines ARLs betreut hat, sowie Arne Klomp, der mir noch während meiner Masterarbeit die Vorteile von BASH Skripten näher gebracht hat. Einen großen Dank auch an alle anderen aktiven und ehemaligen MMs für das Bereichern meines Arbeitsalltags.

Ebenfalls bedanken möchte ich mich bei meinen Projektpartnern aus der POTENTIALS Kollaboration und dem `pyiron` Entwicklungsteam. Hier sind Yury Lysogorskiy und Anton Bochkarev zu nennen, die mir eine Einführung in die Funktionen von `PACEMAKER` gegeben haben, Prof. Dr. Jörg Behler, Marius Herbold und Alexander Knoll für hilfreiche Tipps rund um das fitten von HDNNPs, sowie Jan Janssen und Marvin Poul für die gute Zusammenarbeit und Hilfestellungen beim

beheben von Bugs und der Entwicklung neuer Funktionen in `pyiron`. Weiterhin möchte ich mich bei allen Projektpartnern für die Organisation und Durchführung der POTENTIALS workshop Reihe bedanken.

Schließlich möchte ich mich bei meiner Familie und meinen Freunden für ihre Unterstützung bedanken, ohne die ich nicht bis hier gekommen wäre.

Contents

Acronyms

ACE Atomic Cluster Expansion

ACEP Atomic Cluster Expansion potential

ACSF atom-centered symmetry function

ADP Angular Dependent Potential

AL active learning

Ats isolated atom

BF bulk fragment

BMG bulk metallic glass

DFT density-functional theory

EAM Embedded Atom Method

EMT Effective Medium Theory

FI full icosahedron

GAP Gaussian Approximation Potential

GNN graph neural network

GrAts graphite flakes and isolated atoms

GSF generalized stacking fault

HDNNP High-Dimensional Neural Network Potential

IP interatomic potential

LRO long-range order

MAE mean absolute error

MB moving boundary

MD molecular dynamics

MEAM Modified Embedded Atom Method

MG metallic glass

MLIP machine learning interatomic potential

MS molecular statics

MTP Moment Tensor Potential

NequIP Neural equivariant Interatomic Potential

NMR nuclear magnetic resonance

NNP Neural Network Potential

PB polymer backbone

PBE Perdew-Burke-Ernzerhof

PES potential energy surface

PMSQ Polymethylsilsesquioxane

QM quantum mechanical

ReaxFF reactive force field

RMC reverse Monte-Carlo

RMSE root mean square error

SB shear band

Si-O-C silicon oxycarbide

SNAP Spectral Neighbor Analysis Potential

SOAP Smooth Overlap of Atomic Positions

SRO short-range order

STZ shear transition zone

TSF total structure factor

XC exchange-correlation

1 Introduction

Atomistic simulations play an increasingly important role in the understanding of materials due to the improvements of underlying theories and increased availability of computing resources as can be seen by increasing numbers of publications on the topic 'Atomistic simulation', shown in Fig. 1.1a. The commonly employed methodologies here are variants of molecular statics (MS) and molecular dynamics (MD). In MS calculations the energy E of a system of interacting particles (in this case an atomic structure) is minimized with respect to the particle positions and simulation cell. MD simulations evolve the system in time based on Newtons equations of motion. Both require a description of the potential energy surface (PES) and corresponding forces between atoms, i.e. the energy E as function of the particle coordinates $\boldsymbol{r}$. The accuracy, speed and achievable amount of particles in MS and MD mostly depend on the way the PES is determined.

In this thesis machine learning interatomic potentials (MLIPs), which are a rapidly evolving field (cf. Fig. 1.1b), are employed for this purpose. They are developed and evaluated as a tool for the description of structurally and chemically complex materials. The treated systems are Cu-Zr (chapter 2) and silicon oxycarbide (Si-O-C) (chapter 3), which can be seen as representatives of two different material classes. In the former, chemical interactions between atoms are mostly metallic, while they are covalent-ionic in the latter. Nonetheless, both systems are described with Atomic Cluster Expansion potentials (ACEPs), which is a posteriori justified in chapter 4, where different types of MLIPs are compared.

The remainder of this chapter is organized as follows. First an overview of different methods to calculate the PES is given, starting with a general introduction and an overview of classical interatomic potentials (IPs), before introducing the MLIPs employed in this work. Then relevant literature about the treated material systems is reviewed the research questions tried to answer in this work are raised. Finally, the employed computational and analysis methods are summarized.

1.1 PES of atomic systems

The energy of an atomic system depends on the coordinates of nuclei $\boldsymbol{R} = \{\boldsymbol{R}_i\}$ and electrons $\boldsymbol{r} = \{\boldsymbol{r}_i\}$ as schematically depicted in Fig. 1.2. In principle, it can be determined by solving the (time independent) Schrödinger equation

$$\hat{H}\Psi(\boldsymbol{R}, \boldsymbol{r}) = E\Psi(\boldsymbol{R}, \boldsymbol{r}). \tag{1.1}$$

Here, Ψ is the wavefunction of the system and $\hat{H}$ is the Hamiltonian operator. In the Born-Oppenheimer or adiabatic approximation it is assumed that lightweight

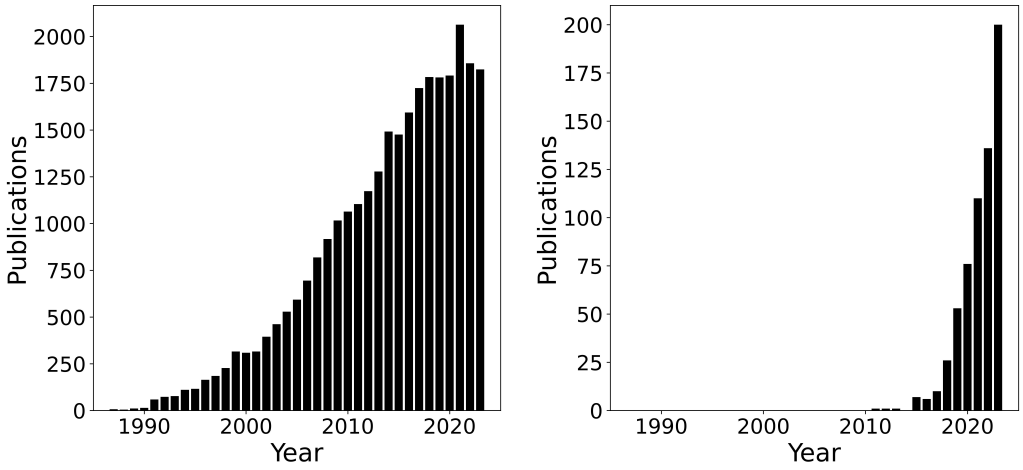

a **b**

Figure 1.1: Number of papers published per year on topics 'Atomistic simulation' (**a**) and 'Machine learning interatomic potentials' (**b**) according to Clarivate Web of Science™. Atomistic simulations and MLIPs are rapidly evolving fields with strongly increasing numbers of publications.

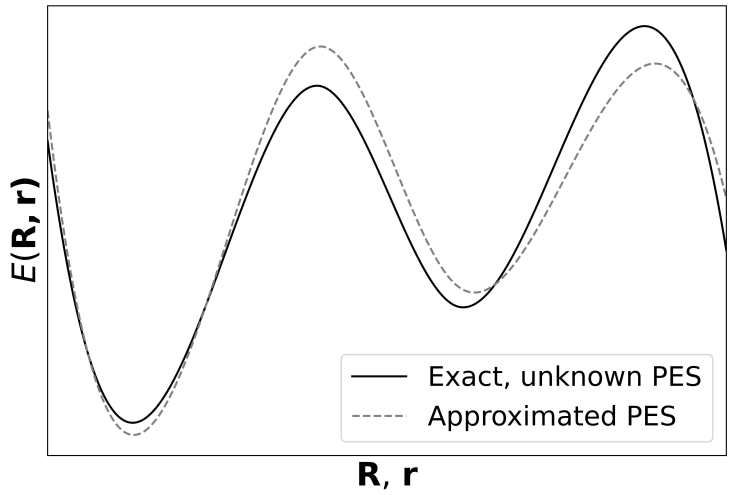

Figure 1.2: Schematic PES of an atomic system. The energy E depends on coordinates of nuclei $\boldsymbol{R}$ and electrons $\boldsymbol{r}$ and can in principle be obtained by solving the Schrödinger equation. However, exact solutions only exist for very simple systems, so approximate solutions are necessary.

electrons move much faster than heavy nuclei, allowing to separate their wavefunctions.[1] Using this assumption, $\hat{H}$ for a given set of nuclei positions $\boldsymbol{R}$ is

$$\hat{H} = \sum_i \frac{\hbar}{2m_e}\nabla^2 + \sum_{i<j} \frac{q_e^2}{|\boldsymbol{r}_i - \boldsymbol{r}_j|} + \sum_{ik} \frac{Q_k q_e}{|\boldsymbol{r}_i - \{\boldsymbol{R}_k\}|}. \tag{1.2}$$

The terms correspond to the kinetic energy with the reduced Planck constant $\hbar$ and electron mass m_e, Coulomb interactions between electrons with electron charge q_e and Coulomb interactions with the quasi-stationary nuclei with charges Q. However, despite the Born-Oppenheimer approximation, this multibody problem is impossible to solve exactly for all but simple molecular systems.[2,3] Consequently, alternative methods are required to estimate the PES. These methods can be split into two categories: approximate quantum mechanical (QM) methods, such as density-functional theory (DFT) (cf. section 1.4.1), and IPs. QM methods are highly accurate, but computationally expansive. They typically do not scale beyond few hundreds or thousands of atoms and tens to hundreds of picoseconds simulatable time. No knowledge about a system besides chemical elements and atomic positions is required for such simulations. IPs, on the other hand, approximate the PES of an atomic system based on an analytic function of the atomic coordinates, where atoms are assumed to be point masses, and require fitting of adjustable parameters for each kind of interatomic interaction that shall be described. They scale to billions of atoms and microseconds of simulatable time, but are less accurate than QM methods. Different schemes for their classification exist (see for example a recent review on IPs by Müser et al.[4]), but for this thesis they will be foremost considered as either empirical IP or MLIP. Empirical (or classical, both terms are used interchangeably[5–7]) IPs use physically motivated functional forms to describe chemical interactions between atoms. Typically, they have a few to a few tens of adjustable parameters, which often can be deduced from experimental data or a mixture from experiments and QM calculations. As stated for example by Behler[7] the term MLIP is not well-defined. In the following it is used for IPs with, a (sometimes learnable) complex descriptor that is combined with a regression technique to 'learn' atomic environments and associated energies and interatomic forces. This is achieved by adjusting hundreds or thousands of parameters to reproduce energies and forces obtained via QM calculations, mostly DFT, without the a priori assumptions inherent to a physically motivated functional form. MLIPs are a rapidly evolving field (cf. Fig. 1.1b), which can bridge the accuracy-scalability gap between QM methods and classical IPs,[8] as schematically depicted in Fig. 1.3.

1.1.1 The evolution of IPs

The MLIPs fitted in this work are compared to existing IPs at different points of this work. Consequently, some important types of classical IPs, as well as problems and ideas that lead to their development are quickly reviewed here. For a more comprehensive introduction to IPs the reader is referred to a book by Frenkel and Smit[9] or the recent review by Müser et al.[4]

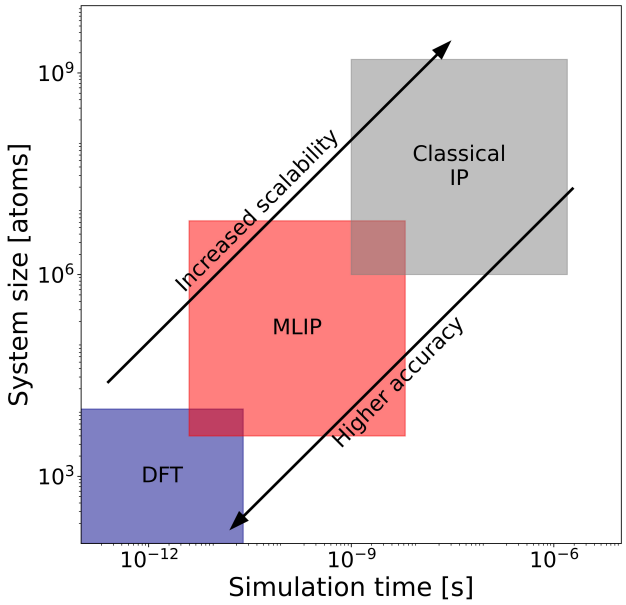

Figure 1.3: Schematic of reachable systems sizes and simulation time scales in atomistic MD simulations depending on the method employed to calculate interatomic interactions. QM methods, such as DFT have limited scalability, but high accuracy. Classical IPs are less accurate, but usable for much larger systems. MLIPs can be employed to bridge the accuracy-scalability gap between them.

The first IPs were pair potentials, which use only the scalar distance between pairs of atoms r_{ij} to describe atomic energies E_i via the summation of pair interactions $V(r_{ij})$

$$E_i = \frac{1}{2} \sum_{j \neq i} V(r_{ij}), \tag{1.3}$$

where j are indices of neighboring atoms. Here, the factor $\frac{1}{2}$ is introduced to split the energy gained by two atoms upon bonding between the two. Then, the energy E of the whole system is the sum of atomic energies E_i

$$E = \sum_{i}^{N} E_i, \tag{1.4}$$

where N is the total number of atoms in the system. Examples for these are Lennard-Jones[10,11] or Morse potentials.[12] However, such simplified models lead to severe problems in the description of all but the most simple-systems simple systems, such as ideal gases or diatomic molecules, for which they were made originally.[11–13] An example of this is the inability of pair potentials to give the correct number of independent elastic constants.[4]

For metallic systems the Embedded Atom Method (EAM) approach, developed by Daw and Baskes,[14,15] which is formally equivalent to Finnis-Sinclair[16] and Effective Medium Theory (EMT) IPs[17] proved very successful. It can be classified as

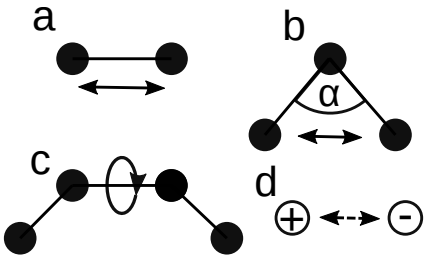

Figure 1.4: Schematic representation of exemplary physically motivated interatomic interaction terms. The simplest terms are pair interactions which just depend on the distance between pairs of atoms (a). Multibody terms can depend f.e. on angles (b) or describe rotations (c). The description of ionic systems benefits from the integration of long-range Coulomb interactions between charges (d).

pair functional, in which E_i are described by a sum of pair interactions V_{ij} and an embedding term F, which in turn is a functional of the 'electron density' pair term ρ_{ij}

$$E_i = \frac{1}{2}\sum_j V(r_{ij}) + F\left(\sum_{j\neq i}\rho(r_{ij})\right). \tag{1.5}$$

This approach is inspired by the idea that atoms are embedded in a cloud of delocalized electrons of a metallic matrix. In consequence, the amount of energy per bond gained by an atom is not linearly depending on the amount of bonds anymore. Instead, it often has some square root form inspired by tight-binding theory.[16,18] Modified Embedded Atom Method (MEAM)[19] and Angular Dependent Potentials (ADPs)[20] further extend the EAM formalism with angular dependent terms. The availability of multiple EAM IPs since the late 2000s[21–24] lead to a rapid increase in published MD based studies on Cu-Zr, as shown in Fig. 1.5a, despite several issues in the quantitative description of the system shown later on (cf. section 1.2.3.2). The new MLIPs for the system, which achieves unprecedented accuracy in the description of structural and thermodynamic properties is presented in chapter 2.

Covalent systems typically have a lower packing density than metals (for example diamond instead of FCC structure) and strongly directional interatomic bonds. Their description benefitted from the introduction of various flavors of bond-order potentials,[25–27] which include angular and bond counting terms to describe the atomic energy. Such potentials were, for example, successful in the description of some Si,[28,29] SiO_2[30] and SiC[31,32] phases.

For ionic systems improvements have been achieved by the incorporation of electrostatic Coulomb interactions. These can either rely on fixed charges or apply some global charge equilibration mechanism to keep the overall system charge neutral.[4] Fig. 1.4 shows schematic representations of some exemplary physically motivated interaction terms.

In computational chemistry the reactive force field (ReaxFF) formalism[33] has

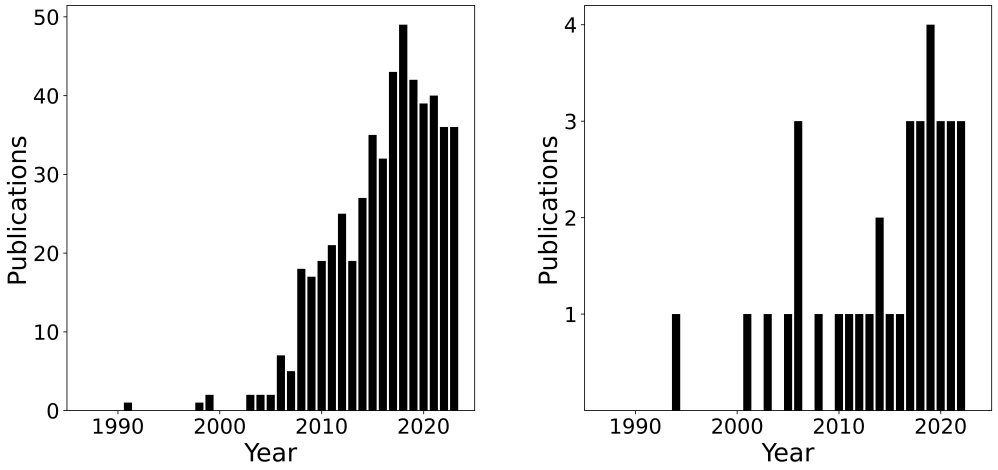

a **b**

Figure 1.5: Number of papers published per year on topics 'Cu Zr Molecular Dynamics' (**a**) and 'Silicon oxycarbide simulation' (**b**) according to Clarivate Web of Science™. MD based studies of Cu-Zr increased after several classical IPs for the system were published in the late 2000s, showing that the availability of suitable IPs can significantly help to advance research of a material. The few available potentials for Si-O-C have rather limited scopes and did not result in a publication spike for Si-O-C glass-ceramics, as observed for Cu-Zr simulations.

seen much success.[34] It combines many previous ideas to describe a wide variety of chemical interactions, incorporating expressions to describe angular dependent, bond order, Coulomb and Van der Waals interactions between atoms. Additionally, it uses under- and over-coordination terms. Considering the amount of fittable parameters resulting from the plethora of interaction terms, ReaxFF can be seen as an intermediate step between classical IPs and MLIPs, even though all terms are still physically motivated. ReaxFF are the only classical IPs which have been successfully used to model the formation of Si-O-C.[35–37] However, these ReaxFFs have rather specialized purposes (cf. section 1.2.4.2) and have not seen a wide adaption shown by the low number of simulation based Si-O-C studies in Fig. 1.5b.

Despite the incorporation of more and more chemical interactions in classical IPs their accuracy seems to be limited due to their fixed functional forms.[6,7] Exemplarily MLIPs recently developed for the Si-O-C subsystems C,[38–45] Si,[46–51] SiO_2[52,53] and SiC[54,55] have considerable improved accuracies compared to classical IPs, showing the possible benefits of employing them in the description of complex systems as done in this work.

1.1.2 Machine learning interatomic potentials

The field of MLIPs is rather new and a lot of progress has been achieved within the last two decades and especially the last few years. First machine learning based at-

tempts to describe the potential energy surface of atomic configurations employed neural networks for a global description of the system around 30 years ago.[56,57] Their application was limited to the system they were trained to, with only few degrees of freedom allowed to vary. In 2007, Behler and Parrinello[58] published a High-Dimensional Neural Network Potential (HDNNP) using short-ranged symmetry functions as descriptor and constructed the total energy of the system as sum of atomic energies. Consequently, their potential could be applied to systems of arbitrary size and orientation, significantly increasing its usefulness. Later on, a plethora of MLIPs was developed. Among them are the Gaussian Approximation Potential (GAP),[59] Moment Tensor Potential (MTP),[60] Atomic Cluster Expansion (ACE),[61] Neural equivariant Interatomic Potential (NequIP),[62] Allegro[63] and MACE,[64] which are compared with regard to their computational cost and accuracy as part of this thesis (cf. chapter 4). Some other recently developed MLIPs like Spectral Neighbor Analysis Potential (SNAP)[65] are not considered further in this work, because they are very similar to one of the treated potentials or can be indirectly evaluated using data from previous publications comparing MLIP.[51,66]

As stated previously, the term MLIP is not well-defined.[7] Some of them do not employ classic machine learning techniques, but they have in common a large amount of parameters, normally thousands and highly flexible functional forms. This allows them to accurately reproduce the PES of a material when fitted to energies and forces of training structures covering a suitable configuration space. In consequence, they have a high upfront computational cost for the generation of training data via large amounts of DFT calculations.

Typically, MLIPs can be divided into a descriptor and a subsequent method that calculates energies and forces based on that descriptor. MLIPs treated in this thesis are invariant against translation, rotation and permutations of the system, making them applicable for arbitrary system sizes and different ways the simulation box can be set up. Their complexity, i.e. the large amount of fitting parameters can be part of the descriptor or the subsequent method. Complex machine-learning methods such as neural networks are often combined with rather simple descriptors, while complex descriptors are usually employed in conjunction with simple models for the energy. An overview of various descriptors for atomic environments can for example be found in a review by Langer et al.[67] The following sections give an overview of the types of MLIPs employed in this thesis.

1.1.2.1 High-dimensional neural networks

Various flavors of neural network based MLIPs and corresponding fitting codes exist.[69–78] In this thesis, the HDNNPs originally developed by Behler and Parrinello[58] are employed. They are fitted using the program `n2p2`[74,79] and usable in the MD code `LAMMPS` via the `n2p2 LAMMPS` interface[80] (cf. section 1.4.2 for information on MD and `LAMMPS`).

The basic functionality of Behler-Parrinello HDNNPs is schematically shown in Fig. 1.6. The Cartesian coordinates of atoms $\boldsymbol{r}_i$ are used to calculate atom-centered

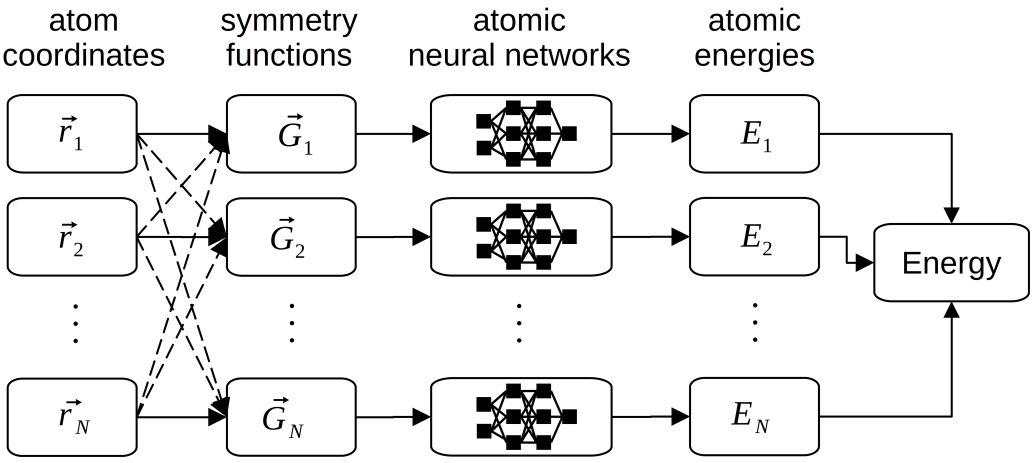

Figure 1.6: Schematic of a Behler-Parrinello HDNNP.[58] Symmetry function vectors G_i are calculated based on Cartesian coordinates r_i of all atoms within the cutoff radius and used as input vectors for atomic neural networks. The total energy of the system is the sum of atomic energies E_i. Drawing adapted from Ref. 68.

symmetry function (ACSF)[81] vectors $\boldsymbol{G}_i = \{G_i\}$. Each vector is used as input layer for an atomic neural network, which in turn gives an atomic energy E_i. The total energy of the system is than simply the sum of atomic energies.

ACSFs are radial and angular functions. They need to fulfill the requirements of rotational, translational and permutational invariance and are short-ranged, i.e. they are cut off after some distance assumed to capture the majority of chemical interactions between atoms. A comparison and detailed discussion of different ACSFs by Behler can be found in Ref. 81. In this thesis radial functions of the form

$$G_i = \sum_j \exp(-\eta(r_{ij} - R_s))^2 \cdot f_c(r_{ij}) \tag{1.6}$$

are used. Here η and R_s are parameters, $f_c(r_{ij})$ is a cutoff function and r_{ij} is the distance between atoms i and j. The employed angular functions have the form

$$G_i = 2^{1-\zeta} \sum_j \sum_k \left[(1 + \lambda \cos\theta_{ijk})^\zeta \exp(-\eta(r_{ij}^2 + r_{ik}^2 + r_{jk}^2)) f_c(r_{ij}) f_c(r_{ik}) f_c(r_{jk}))\right] \tag{1.7}$$

with parameters ζ and λ, where λ can only be 1 or -1.

Neural Network Potentials (NNPs) are under active development with the goal to achieve ever higher accuracies by including for example electrostatic interactions.[82] They can be categorized into four generations. First generation NNPs are simple networks that take Cartesian coordinates as input and directly calculate the energy of the complete system. The second generation are HDNNPs as employed in this thesis. Third generation HDNNPs include an additional set ACSF and atomic neural networks to calculate the charge state of atoms and the corresponding long-range Coulomb interactions. Here, charge neutrality of periodic systems is ensured

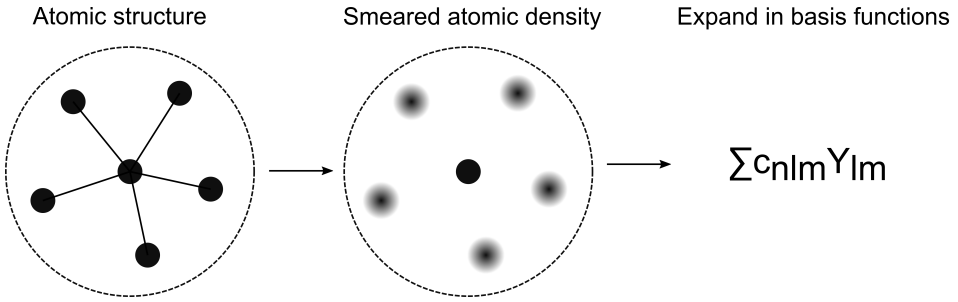

Figure 1.7: Schematic representation of the SOAP descriptor. Smeared out atomic densities are constructed using Gaussian functions and expanded in spherical harmonics for computational efficiency. Figure adapted from Ref. 87.

by rescaling the atomic charges or by adding a compensating background charge. In the fourth generation non-local charge transfers are included by charge equilibration techniques. Detailed information on each type of HDNNP can be found in a recent review by Behler.[7]

1.1.2.2 Gaussian approximation

GAPs have been developed by Bartók et al.[59] They are implemented in the `QUIP` code[83] and the corresponding python interface `quippy`.[84] GAPs determine the atomic energy using Gaussian process regression[85,86] on a descriptor of the atomic environment by interpolating between similar configuration from the training data. The atomic energy is given by

$$E_i = \alpha_n G(\boldsymbol{D}_i, \boldsymbol{D}_n) \tag{1.8}$$

where $\boldsymbol{D}$ are the descriptors of configuration i and the reference configurations n and G is a similarity kernel

$$G(\boldsymbol{D}, \boldsymbol{D}') = \exp\left(-\sum_j \frac{(D_j - D'_j)^2}{2\sigma_j}\right) \tag{1.9}$$

with hyperparameters σ. The interpolation coefficients α_n are calculated by

$$\{\alpha_n\} = \boldsymbol{\alpha} = \boldsymbol{C}^{-1}\boldsymbol{y} \tag{1.10}$$

with reference values $\boldsymbol{y} = \{y_n\}$ and

$$C_{nn'} = \delta^2 G(\boldsymbol{D}, \boldsymbol{D}') + \sigma^2 \boldsymbol{I}. \tag{1.11}$$

Here δ and σ are hyperparameters and $\boldsymbol{I}$ is the identity matrix.

The original formulation used the bispectrum obtained by projecting the local atomic density onto a 4D unit sphere and expanding it in 4D spherical harmonics as descriptor. In 2013 Bartók et al.[88] proposed the Smooth Overlap of Atomic

Positions (SOAP) kernel as an alternative. It is based on an atomic neighbor density with Gaussians at atom positions $\boldsymbol{r}_i$. The Gaussians are expanded in spherical harmonic functions for computational efficiency,

$$\rho(\boldsymbol{r}) = \sum_i \exp\left(-\frac{|\boldsymbol{r}-\boldsymbol{r}_i|^2}{\sigma}\right) = \sum_i \sum_{lm} 4\pi \exp\left(-\frac{(r^2+r_i^2)}{\sigma}\right) \eta_l(2arr_i) Y_{lm}^*(\hat{r}) Y_{lm}(\hat{r}), \quad (1.12)$$

where the width σ is a hyperparameter and η_l are modified spherical Bessel function of the first kind. This is schematically shown in Fig. 1.7 The similarity of two densities is given by

$$S(\rho, \rho') = \int \rho(\boldsymbol{r}\rho'\boldsymbol{r}) d\boldsymbol{r}. \quad (1.13)$$

Rotational invariance is achieved by integrating over all possible rotations $\hat{R}$

$$k(\rho, \rho') = \int |S(\rho, \hat{R}\rho')|^n d\hat{R}. \quad (1.14)$$

Based on the overlap between an atomic and a rotated environment with $n = 2$ one obtains

$$I_{mm'}^l = \sum_{i,i'} 4\pi \exp\left(-\frac{r_i^2 + r_{i'}^2}{2\sigma}\right) \eta_l(ar_i r_{i'}) Y_{lm}(\hat{r}_i) Y_{lm}^*(\hat{r}_{i'}). \quad (1.15)$$

This allows to simplify

$$k(\rho, \rho') = \sum_{l,m,m'} (I_{mm'}^l)^* I_{mm'}^l. \quad (1.16)$$

For the final SOAP kernel the rotationally invariant kernel is normalized

$$K(\rho, \rho') = \left(\frac{k(\rho, \rho')}{\sqrt{k(\rho, \rho), k(\rho', \rho')}}\right)^\zeta, \quad (1.17)$$

where ζ is a positive integer influencing the sensitivity of the kernel, typically set to 4.

1.1.2.3 Moment tensors

MTPs were developed by Alexander Shapeev.[60] They are fitted using the `MLIP` code developed by Novikov et al.[89] (Version 2) and Podryabinkin et al.[90] (Version 3). The subsequent description closely follows Ref. 90. The energy E of atom i in a MTP is given by

$$E_i(n_i) = \sum_{a=1} \xi_a B_a(n_i), \quad (1.18)$$

where n_i are atomic neighborhoods, ξ are parameters B are MTP basis functions. Atomic neighborhoods are given by a tuple of relative positions and atom types

$(\{\boldsymbol{r}_{i1}, z_i, z_1, \}, ..., \{\boldsymbol{r}_{ij}, z_i, z_j, \}, ..., \{\boldsymbol{r}_{iN}, z_i, z_N, \})$. The moment tensor descriptors are

$$M_{\mu,\nu}(n_i) = \sum_{j}^{N} f_\mu(r_{ij}, z_i, z_j)\boldsymbol{r}_{ij}^{\otimes\nu} = \sum_{j}^{N} \left[\sum_{\beta=1} c_{\mu,z_i,z_j}^{(\beta)} P^{(\beta)}(r_i j)(r_c - r_{ij})^2 \right] \boldsymbol{r}_{ij}^{\otimes\nu}, \tag{1.19}$$

with the radial part f_μ and angular part $\boldsymbol{r}_{ij}^{\otimes v}$. Here, $\otimes$ denotes the outer product and ν the order of the tensor product, $r_{ij} = |\boldsymbol{r}_{ij}|$, c are radial parameters, P are polynomial functions and r_c is a cutoff radius. The basis functions B are defined as contraction of one or more moment tensor descriptors yielding scalar values. The amount of basis functions and corresponding parameters of a MTP is given by its level. All basis functions with lev$B \leq$ levMTP are included. The level of basis functions is defined as

$$\text{lev}B = \prod_{p=1} \text{lev}M_{\mu_p,\nu_p} \tag{1.20}$$

with

$$\text{lev}M_{\mu,\nu} = 2 + 4\mu + \nu. \tag{1.21}$$

As stated by Novikov et al.[89] this definition of a level with coefficients 2, 4 and 1 is somewhat arbitrary. However, they empirically found it to be optimal for various tests and hard-coded these values in the `MLIP` package.

1.1.2.4 Atomic cluster expansion

The Atomic Cluster Expansion (ACE) descriptor for atomic environments was developed by Drautz.[61] Fitting of ACEP is implemented in `pacemaker`[51,91] and `ACEsuit`,[92] of which the former was employed for this thesis. Generally, the ACE descriptor χ can be employed to calculate a property of interest P of atomic systems using basically arbitrary functional forms F

$$P = F(\chi_1, .., \chi_a, ...\chi_N). \tag{1.22}$$

For ACEPs fitted in this thesis the energy of an atom is given by

$$E_i = \sum_a m_a \chi_{i,a}^{b_a}, \tag{1.23}$$

where m are prefactors and b some exponents. The descriptors are expanded as

$$\chi_i = \sum_{\nu}^{\nu_{max}} \sum_{\boldsymbol{w}} c_{\boldsymbol{w}} \sum \Phi_{\boldsymbol{w}}(\boldsymbol{r}_{ij_1}, ..., \boldsymbol{r}_{ij_\nu}) \tag{1.24}$$

with functions $\Phi_{\boldsymbol{w}}$ of body-order ν that depend on neighbors j and parameters $c_{\boldsymbol{w}}$. Here, $\boldsymbol{w}$ are the basis function indices. As is, this would scale as $\mathcal{O}(N^\nu)$. In ACE linear scaling with N is achieved. For this, the atomic density

$$\rho_i = \sum_{j \neq i} \delta(\boldsymbol{r} - \boldsymbol{r}_{ij}) \tag{1.25}$$

is projected onto atomic basis functions $\phi(\boldsymbol{r})$. This results in

$$A_{iw} = \sum_{i \neq j} \phi_w(\boldsymbol{r}_{ij}). \tag{1.26}$$

The atomic basis functions ϕ are a combination of radial functions $R_{z_i z_j nl}(r_{ji})$ and spherical harmonics $Y_{lm}(\hat{r}_{ij})$

$$\phi_{z_i z_j nlm}(\boldsymbol{r}) = R_{z_i z_j nl}(r_{ji}) Y_{lm}(\hat{r}_{ij}), \tag{1.27}$$

where z are indices for chemical elements. To obtain permutation-invariant basis functions the products

$$\tilde{A}_{z_i znlm} = \prod_{t=1}^{\nu} A_{z_i z_t n_t l_t m_t} \tag{1.28}$$

are calculated. Here ν is the maximum number of neighbors the terms depend on. Finally, one arrives at the expression,

$$\chi_i = \sum_{znlm} \tilde{c}_{z_i znlm} \tilde{A}_{z_i znlm} = \boldsymbol{cB}. \tag{1.29}$$

In the last step, rotational invariance is obtained by reducing the basis as $\boldsymbol{B} = \boldsymbol{CA}$ using generalized Glebsch-Gordan coefficients $\boldsymbol{C}$. Accordingly, the final fitting coefficients are obtained as $\tilde{\boldsymbol{c}} = \boldsymbol{C}^T \boldsymbol{c}$.

Further details of the ACE formalism and the relation to other models can be found in Refs. 61, 92.

1.1.3 Graph neural networks, equivariant descriptors and message-passing

A recent development in the field of MLIPs is the representation of atomic environments as graphs and the corresponding use of graph neural network (GNN).[93–96] General information about GNNs can be found for example in Refs. 97, 98. For the description of atomic systems with GNNs, atoms are considered as nodes, which are connected with all other atoms within some cutoff radius via edges. Each atom or node has some state vector which depends on its neighbors. In message-passing GNNs this state vector is sent to neighboring nodes as a message, which influences the state of all nodes it is sent to. This is done iteratively, effectively increasing the maximum possible interaction range to $N * r_c$, where N is the number of iterations and r_c the cutoff radius. The message-passing process is schematically depicted in Fig. 1.8.

In the former MLIPs invariance against rotation, translation and permutations of atoms of the same species was ensured by using descriptors with the corresponding invariances. However, vector quantities (f.e. forces) are equivariant under rotation, and transform together with the atomic environment. When using only equivariant operations on the input equivariant descriptors can be employed, increasing the contained amount of information and possibly the achievable accuracy.[99]

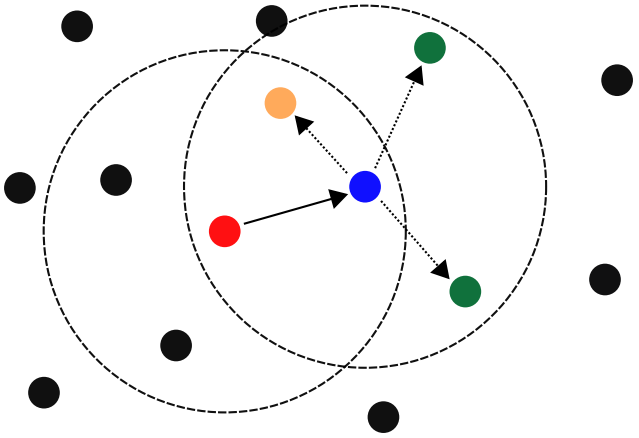

Figure 1.8: Schematic representation of the message-passing mechanism employed in NequIP and MACE. Within a GNN the red atom is a node connected to all atoms within its cutoff radius (indicated as dashed line) via edges (not shown). In the first iteration it sends its feature vector (message) to all connected nodes, as exemplarily shown by the arrow to the blue atom. In the second iteration the feature vector of the blue atom is influenced by the features of the red atom and sends it to all atoms it is connected to. This way, the green atoms obtain information from the left red atom which is outside their cutoff, leading to a larger effective interaction range. The orange atom is directly and indirectly influenced by the red atom.

1.1.3.1 Neural equivariant graph neural networks

Neural equivariant Interatomic Potentials (NequIPs) developed by Batzner et al.[62] employ E(3)-equivariant graph neural networks to reproduce the PES of atomic systems with the aim to require less training data than comparable MLIPs. They are implemented in the `NequIP` code, which is based on the `e3nn` framework.[100,101] In the network each node has associated feature tensors of different orders V_{icmlp}, where i, c and m are the atom index, elements of V and representation index, while l is the rotation order and p the parity. The employed convolution filters are radial functions and spherical harmonics

$$S_{ml}(\boldsymbol{r}_{ij}) = R(r_{ij}) + Y_{lm}(\hat{r}_{ij}), \tag{1.30}$$

ensuring rotation equivariance, with all learnable weights being a part of the radial function R. For the convolution feature vectors and filters are combined using geometric tensor products, again yielding rotationally equivariant features. Here, tensor products that would exceed some rotational order $l_{\max}$ are omitted. Parity equivariance requires that

$$p_O = p_I p_f, \tag{1.31}$$

where indices O, I and F denote output, input and filter, respectively. The final convolutional layer can be written as

$$L_{l_O p_O l_F p_F l_I p_I i c m_O}(\boldsymbol{r}_i, V_{l_I p_I i c m_I}) = \sum_{m_F, m_I} C_{l_O m_O l_I m_I l_F m_F} \sum_j R(r_{ij})_{c l_O p_O l_F p_F l_I p_I} Y_{l_F m_F}(\hat{r}_i j) V_{l_I p_I j c m_I}, \quad (1.32)$$

where C are the Glebsch-Gordan coefficients used to compute the tensor product and neighbor atoms are denoted with index j. Overall, NequIPs does the following in its network:

- An initial set of features is generated based on the atomic numbers.
- Higher order feature tensors are created in interaction blocks, where convolution operations, self-interaction and concatenation of tensors takes place.
- Final features with rotational order $l = 0$ are processed in two output layers, giving the atomic energy.

As stated in the original publication Ref. 62, NequIP combines ideas of a variety of previous neural networks. The initial generation of features follows SchNet.[94] Interaction blocks are updated similar to ResNet.[102]

1.1.3.2 Allegro

Allegro is a local equivariant neural network potential developed in the same group as NequIP[99] and the corresponding `Allegro` code builds on top of the `NequIP` code. The capturing of non-local effects via message passing appearing due to usage of a graph network, as done within NequIP, can improve the accuracy of potentials. However, it also reduces their computational efficiency and parallelizability. The aim of Allegro is a higher accuracy due to the usage of equivariant features combined with the efficiency of strictly local potentials. This is realized by employing similar ideas as in NequIP for equivariant features, but a deep neural network instead of a graph network for their evaluation. The original publication Ref. 99 shows similar errors compared to NequIP for the description of a wide range of molecules and demonstrates strong scaling for a system with over 400000 atoms.

1.1.3.3 MACE

MACE is a message passing neural network architecture with equivariant messages of a high body order developed and implemented in the same name code `MACE` by Batatia et al.[64,103] The high body order supposedly leads to accurate results within 1 to 2 message layers, so the number of atoms within the effective cutoff range is still small enough for efficient parallel computation.

In the MACE network nodes are assigned a state tuple

$$\sigma_{it} = (\boldsymbol{r_i}, z_i, \boldsymbol{h}_{it}), \quad (1.33)$$

containing the position $\boldsymbol{r_i}$, chemical element z_i and learnable features $\boldsymbol{h}_{it}$. Indices i and t denote the atom and layer within the network, respectively. Messages $\boldsymbol{m}$ are constructed for each node using a learnable pooling operation $\oplus$ over neighbors j and an also learnable message function M

$$\boldsymbol{m}_{it} = \oplus_j M_t(\sigma_{it}, \sigma_{jt}). \tag{1.34}$$

The features of nodes are updated using messages evaluated via a learnable update function U

$$\boldsymbol{h}_{i,t+1} = U_t(\sigma_{it}, \boldsymbol{m}_{it}). \tag{1.35}$$

The network's forward pass involves T iterative message construction and update processes. Finally, learnable readout functions $\mathcal{R}_t$ determine the atomic energy

$$E_i = \sum_t^T \mathcal{R}_t(\sigma_{it}). \tag{1.36}$$

As stated by the original authors,[64] the key innovation of MACE is that messages are expanded in a hierarchical body order

$$\boldsymbol{m}_{it} = \sum j \boldsymbol{u}_1(\sigma_{it}, \sigma_{jt}) + \sum_{j_1,j_2} \boldsymbol{u}_2(\sigma_{it}, \sigma_{j_1 t}, \sigma_{j_2} t) + ... + \sum_{j_1,...,j_\nu} \boldsymbol{u}_3(\sigma_{it}, \sigma_{j_1 t}, ..., \sigma_{j_\nu t}) \tag{1.37}$$

with learnable functions $\boldsymbol{u}$ and hyperparameter ν. Messages are constructed using the previous features and a combination learnable radial basis functions and spherical harmonics to embed edges of the graph network, similar to the description of atomic environments in ACE. Further details on the employed network can be found in the original publication Ref. 64.

1.1.4 Active learning

MLIPs can reproduce the PES of an atomic system with a much higher accuracy than empirical IPs. To do so, however, they require a large amount of training data. Configurations such as simple crystalline structures can be created using the `ase` python package[104] or similar tools. Additional structures with low formation energies can be found in public databases such as Materials Project,[105] Crystallography Open Database or Open Quantum Materials Database.[106,107] Specific defects within the structures or randomized deformations and atomic displacements can be created using tools such as `ase` or `pymatgen`.[108] However, this typically requires a significant amount of human intervention and different regions of configuration space are most likely sampled very unevenly. Alternatively, structures can also be extracted from MD simulations, employing classical potentials or DFT. The big drawback of this are long simulation times required to escape local minima and the consequent dependence on initial structures, again leading to an uneven and lacking sampling of phase space.

Over the last few years active learning (AL) has been established as an alternative way to create training data in a more efficient manner, both in regard to

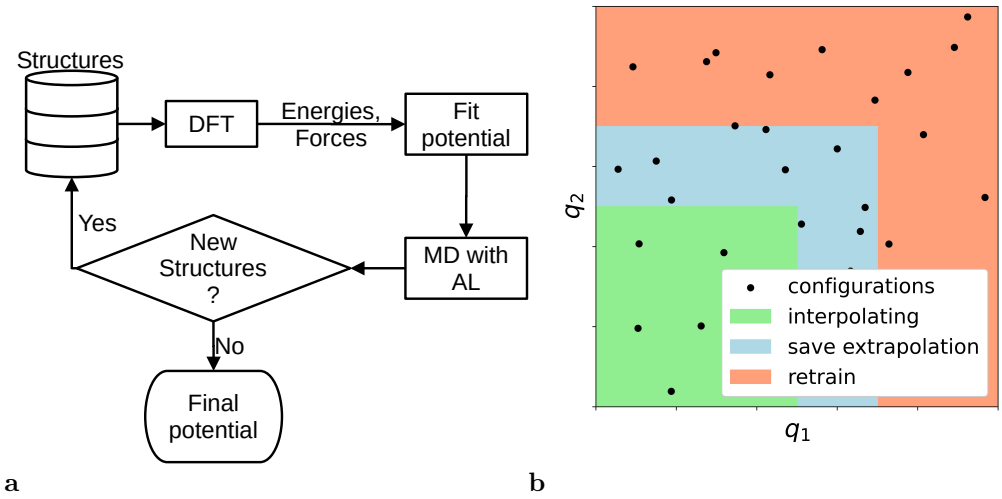

Figure 1.9: Initial MLIPs can be fitted to a few training structures and iteratively improved using AL as schematically shown in (**a**). Typically, some degree of uncertainty is considered as 'save' extrapolation and only structures that are further away from the training data are used to retrain the potential, as schematically depicted for two degrees of freedom in (**b**).

human and computational time. The basic idea of AL is to measure the uncertainty or extrapolation grade in the description of atomic environments, which can then be added to the training data to fit an improved potential. This can be incorporated into an iterative scheme as shown in Fig. 1.9a to quickly generate training data for MLIPs. An initial potential is fitted to a small amount of training data. Consequently, this potential is employed in MD simulations, where the uncertainty is constantly measured. Structures with a high uncertainty are extracted from the trajectory, calculated using DFT and added to the training data. This process is repeated until no structures with high extrapolation grade are found anymore. At this point the training data can be considered as converged regarding some configurational space covered by the MD trajectories. Depending on the initial structures put into the simulation and settings such as temperature and pressure this can cover wide or only narrow regions of configuration space. The former is required when the MLIP should be applicable to a wide range of problems, while the latter may be sufficient for specific simulations.

The uncertainty of a structure description can be defined in various ways. Different methods are implemented in the codes employed for this thesis depending on the descriptor. However, their output is always some per atom quantification of the extrapolation grade as depicted in Fig. 1.10. A generally applicable and conceptually simple variant is to fit multiple IPs to the same set of training data and compare the forces they predict for a given atom.[109] Assuming that the MLIPs

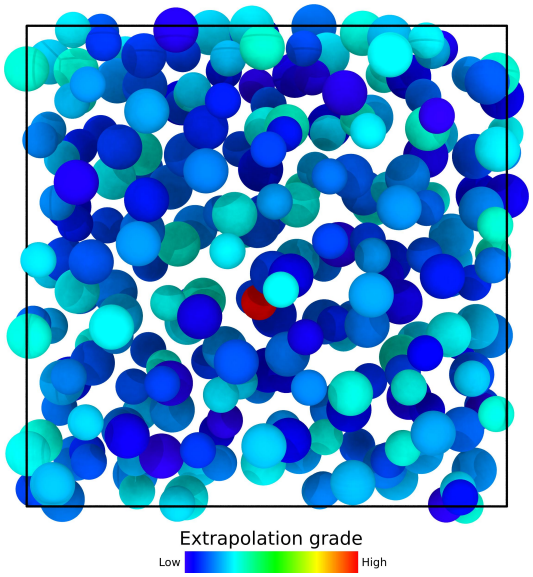

Figure 1.10: The degree of extrapolation in the description of atomic environments can be 'measured' with different techniques. They depend on the employed descriptor and result in a per atom extrapolation grade.

are in principle able to accurately reproduce the PES of the material, a large difference between the two potentials naturally means an insufficient sampling of the atoms' environment, i.e. a high extrapolation grade. This method is called query by committee and has for example been employed for HDNNPs in.[110,111] The SOAP descriptor directly measures the similarity between two structures. Consequently, a low similarity with all training structures can be interpreted directly as high extrapolation grade.[46,112] MTPs and ACEPs implement an extrapolation measure based on D-optimality,[89,90,113–115] which can be interpreted as maximizing the volume of configuration space spanned by a training dataset.[114]

Besides an efficient generation of training data the extrapolation grade can also be used in on the fly learning for coupled ab initio/classical MD simulations[112,116,117] or to judge the reliability of a MLIP in large scale simulations. For example some grain boundary or interface structures may be described in terms of local environments of atoms that do not naturally occur in small-scale MD simulations, as typically employed in AL MD. If one measures a high extrapolation grade for an atom within such large scale simulations the question arises how the local environment of that atom can be included in the training data. The naive approach, which was also employed for the Si-O-C training data in this thesis, is to cut out a box with side lengths greater than $2 * r_c$ around the atom. Here r_c is the cutoff distance of the potential. While this captures the environment, the artificial boundaries created this way may lead to broken bonds and the resulting structures are inefficient to calculate with DFT. A possible alternative is to cut out a box with side lengths $2r_c + 2r_b$, where r_b results in a buffer region that can be modified to obtain more

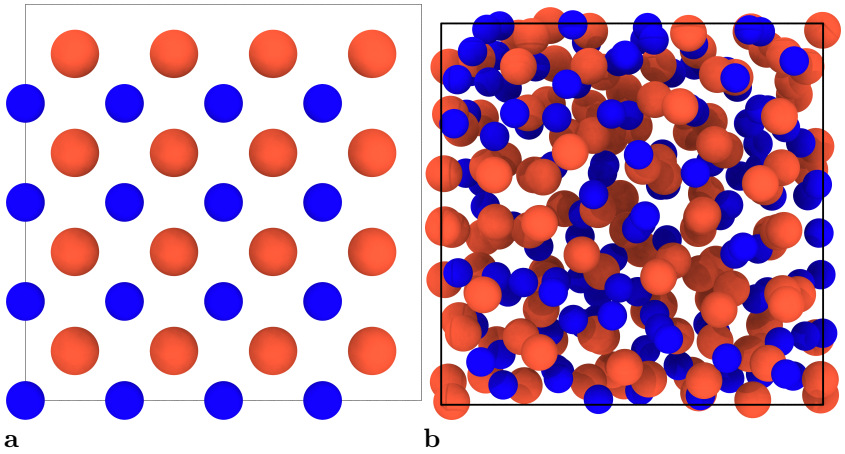

Figure 1.11: Examples for a perfectly crystalline (**a**) and an amorphous (**b**) atomic arrangement.

realistic boundaries, without interfering with the atoms in r_c directly. For example, the buffer region can be selectively heated and quenched to embed the sphere around r_c in an amorphous matrix[53] or minimized in regard to their extrapolation grade.[115,118]

1.2 Materials

This section is organized as follows. First a general introduction into amorphous structures, which play an important role in both Cu-Zr and Si-O-C, is provided. Then metallic glasses (MGs) are treated, because Cu-Zr is a prototypical MG former. Finally, specific aspects of Cu-Zr and Si-O-C themselves are reviewed.

1.2.1 Amorphous materials

> "Liquids and glasses have been well known to human kind for millennia. And yet major mysteries remain in the behavior of glasses and liquids at the atomic level, and identifying the microscopic mechanisms that control the properties of glasses is one of the most challenging unsolved problems in physical sciences"
>
> – *T. Egami*[119]

The structural and functional properties of materials depend on their composition and atomic arrangement. In many materials of everyday life, such as metals the most common atomic arrangements are periodic, i.e. crystalline. In contrast, ideal amorphous materials have a random atomic arrangement. Real amorphous materials typically have some degree of short-range order (SRO) in the form of favorable local environments that lead to recurring structural motifs, but do not exhibit long-range order (LRO).[120] Examples for a crystalline and an amorphous structure are shown in Fig. 1.11. As consequence of their structural randomness,

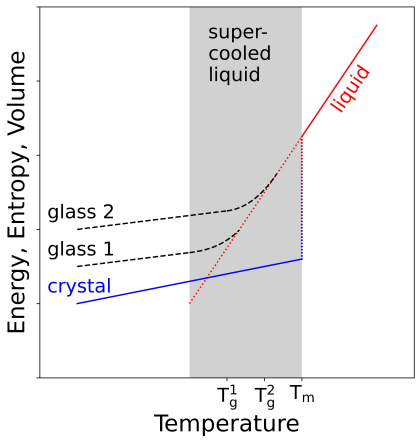

Figure 1.12: Glasses can be produced by fast quenching a melt. Glass transition temperature, as well as structure and properties of the final glass depend strongly on the cooling rate. Here glass 1 is cooled slower than glass 2, leading to a lower volume, energy and entropy.

amorphous phases can have vastly different characteristics than their crystalline counterparts made of the same elements. For example, MGs have a high elastic limit and tensile strength, which makes them interesting for a variety of structural applications.[121–123]

Strictly speaking, glasses are a subgroup of inorganic amorphous materials that undergo a glass transition upon rapid quenching from the melt, as shown in Fig 1.12, but broader definitions that include organic materials and matter that undergoes a glass transition upon heating are also common.[124–126] The quenching process 'freezes' the movement of atoms, preventing the formation of an ordered crystal structure. The liquid-crystal transition is a first order phase transition. It requires latent heat and the transition temperature T_m is a well-defined quantity. Contrary to that, the glass transition temperature T_g strongly depends on the applied cooling rate $\dot{T}$, along with the structure, energy, entropy and volume of the final glass. Lower $\dot{T}$, i.e. slower cooling leads to a lower T_g, energy, entropy and volume. The most widespread glasses are based on silicates. They have been used by humankind since thousands of years[127] because the required cooling rate of below $1\,\mathrm{K/s}$[128] could be achieved easily. Technical improvements dramatically increased the achievable quench rates, nowadays allowing the formation of amorphous phases in materials with a high tendency for crystallization such as metallic alloys (cf. 1.2.2).[121,129,130]

Large scale amorphous phases are energetically unfavorable compared to their crystalline counterparts, so their production requires a kinetically driven transition. Besides melt quenching, these can for example be the deposition of thin films[131,132] or the pyrolysis of polymers as typically done for Si-O-Cs.[133,134] Other possible production routes of amorphous phases include ion irradiation,[135,136] or severe mechanical deformation,[137] although it is unclear whether the resulting structures

should be described as amorphous or strongly disordered crystals.[120]

1.2.2 Metallic glasses

In 1960 Klement et al.[129] produced the first MG, an amorphous $SiAu_3$ flake of approximately 10 µm thickness that started to decompose within a few hours at room temperature. 14 years later Chen[130] found that alloys of elements with different atomic sizes and strong interactions have a higher glass forming ability and produced cylindrical samples with diameters of a few mm. Subsequent studies showed that MGs could be produced from a wide variety of alloys,.[138–146] When exceeding casting thicknesses around 1 mm to 10 mm in the smallest dimension, which is a necessity for many possible applications, they are typically called bulk metallic glasses (BMGs).[121,147]

A common characteristic of MGs is a higher yield strength, elastic limit and corrosion resistance compared to their crystalline counterparts, which makes them interesting for high-tech structural applications such as sports equipment or medical instruments.[121,147–149] Currently, they are employed in golf clubs heads[150,151] and luxury watches,[152] while patents for application in mobile phone cases have been filed.[153,154] Furthermore, Fe based metallic glasses with nanocrystalline inclusions are employed as soft magnets in transformers.[155–159] However, MGs are brittle and tend to fail in catastrophic manner, preventing their usage in many fields.[147,149,160] This brittleness results from shear localization within shear bands (SBs). The free volume and shear transition zone (STZ) models for this deformation mode are discussed in section 1.2.2.1. The ductility of MGs can be improved by the inclusion of a secondary phase into the amorphous matrix,[123,147] that can be introduced as particles or precipitate within the amorphous phase by annealing.[161,162] A special kind of inclusions are B2 crystallites that undergo a martensitic phase transformation to the B19 or B33 structure, extending the concept of transformation induced plasticity from steels into the field of MGs.[163–169] This transformation within a Cu-Zr glass crystal composite is investigated in section 2.4.2. Corresponding experimental and simulational findings are discussed in more detail in section 1.2.3.3.

1.2.2.1 Deformation of MGs in the free volume and STZ models

Macroscopically, MGs can deform in a homogeneous or inhomogeneous manner, depending on temperature, deformation rate and sample size.[122,173] In the case of inhomogeneous deformation the MG quickly fails due to the localization of deformation within a SB. Consequently, understanding SB formation could help to develop glasses with improved ductility.

In an early model developed by Spaepen[170] based on the free volume theory of Cohen and Turnbull[174–176] an applied stress creates structural disorder, which is than resolved by diffusion processes. However, as already discussed by Cohen and Turnbull in their original work[174] and also in a review by Egami[119] with support of more recent data, the free volume theory itself fails to describe the volume

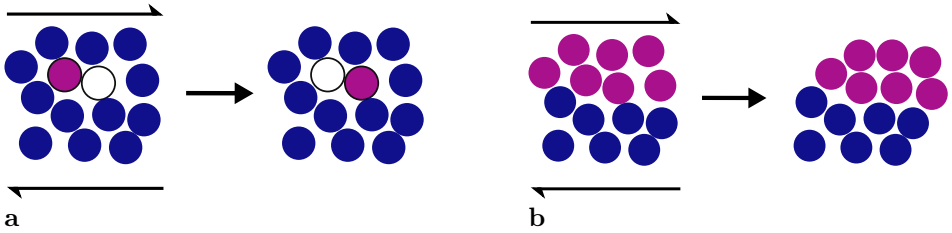

Figure 1.13: Deformation models for MGs. In the model of Spaepen diffusive jumps resolve the macroscopic deformation (**a**).[170] According to the STZ model deformations are localized in within groups of atoms, the STZs (**b**).[171,172]

change upon melting and the pressure sensitivity of diffusion in metals, which are important measures for their underlying assumptions. Furthermore, simulations have shown collective atomic motion instead of diffusive jumps,[177–180] so neither Spaepen's model nor the free volume theory will be considered further in this thesis.

In an alternative model originally developed by Argon,[171,172] which was extended several times[178,181–185] and reviewed by Falk and Langer[186] deformations are localized in STZs. STZs are formed by groups of atoms that are sheared under applied stress. Due to the inherent inhomogeneity of glassy structures STZs have different activation barriers. At high temperatures and strain rates, STZs can be activated in the whole system, leading to macroscopically homogeneous deformation. At lower temperatures and shear rates, STZs lower the activation barrier for nearby STZ formation, so they start to percolate and form a shear band. The model of Spaepen and Argon are schematically depicted in Fig. 1.13.

1.2.3 Cu-Zr(-Al)

Cu-Zr and derived alloys are prototypic MG forming systems. They can be used to investigate fundamental aspects of MGs and belong to the most studied representatives of this material class, both experimentally[143,187–195] and based on atomistic simulations.[196–203] The former is a result of the relatively high glass forming ability in a wide compositional range,[143,188] which can be further improved by the addition of elements such as Al[204] or Ti.[205] The latter probably stems from the availability of a plethora of empirical IPs.[21–24,206–208] In the following sections the phase diagram, published empirical IPs and literature relevant to this thesis regarding Cu-Zr and, to a lesser extent, Cu-Zr-Al, which is employed in the comparison of MLIPs in chapter 4, is reviewed.

1.2.3.1 Thermodynamics and structure

Crystalline phases

Cu-Zr is not only a formidable glass former,[143,188,216,217] it also has a rich phase diagram with multiple stable intermetallic phases. The exact composition, crystal

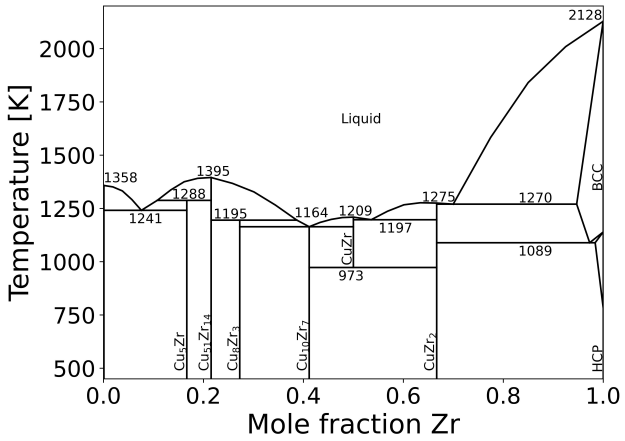

Figure 1.14: Reproduction of the Cu-Zr phase diagram suggested by He et al.[209] Temperature stability, composition, crystal structure and even existence of many intermetallic Cu-Zr phases is controversially discussed.[209–215] This phase diagram version includes all intermetallics, about whose existence a consensus exists. More details about the differences between published phase diagrams are given in the main text.

structure, temperature stability range and even existence of many intermetallics is controversially discussed in literature, as can be seen by a variety of differences within published phase diagrams.[209–215] In section 2.2.2 a concentration-temperature phase diagram is calculated using the developed MLIP, so these differences are discussed in some detail in the following. Fig. 1.14 exemplarily shows the version suggested by He et al.[209] Starting from the Cu rich side, it contains the six intermetallic phases Cu_5Zr, $Cu_{51}Zr_{14}$, Cu_8Zr_3, $Cu_{10}Zr_7$, CuZr and $CuZr_2$ which are present in most published phase diagrams. Some authors include Cu_9Zr_2 instead of Cu_5Zr[211,212,214] and different combinations of the four Cu rich phases Cu_5Zr, $Cu_{51}Zr_{14}$, Cu_8Zr_3 are considered stable only at elevated temperatures.[210,212,214,215,218] Additionally, $Cu_{24}Zr_{13}$ and/or Cu_2Zr phases with small temperature stability ranges are included in,[210,212,214,215] however, their crystal structure remained unclear and others considered them as artifacts of the experimental procedure.[211,219] On the Zr rich side, the existence of a high temperature Cu_5Zr_7 or Cu_5Zr_8 phase is suggested in,[210,212,214,218] again with an unclear crystal structure. Moreover, they did not occur in annealing experiments by Zhou et al.[220] The $CuZr_2$ phase is sometimes split into a low and high temperature phase.[210,212]

Technologically, the CuZr phase, which forms a B2 structure, is the most relevant. Upon fast quenching or mechanical deformation, it can undergo a martensitic phase transition to the B19' or B33 structure leading to a shape memory effect.[221] In sections 2.2.2 and 2.2.3 the predicted thermodynamical and mechanical stability of the phase are investigated. Furthermore, B2 crystallites can be grown in Cu-Zr-(Al, Ti) BMGs,[163,164] improving their ductility, via martensitic phase transformation (cf. section 1.2.3.3).

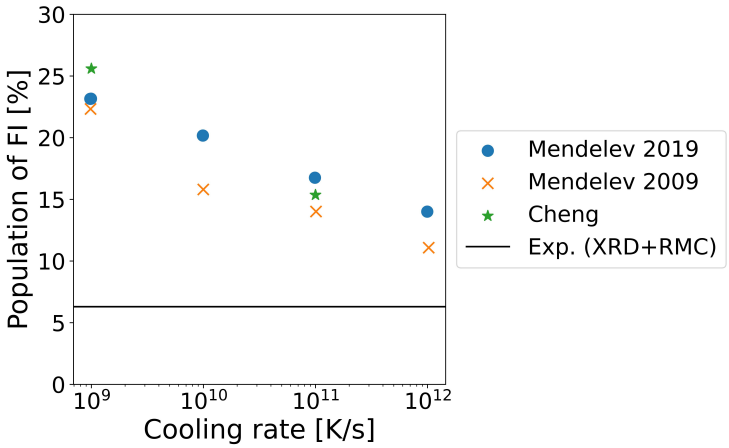

Figure 1.15: The FI population as predicted by the Mendelev 2009, Mendelev 2019 and Cheng IPs (cf. section 1.2.3.2) compared to the amount found by Mattern et al.[223] via diffraction experiments and RMC modelling. Samples produced via cook and quench simulations show a far higher amount of FI for lower cooling rates. These cooling rates, however, are still a few orders of magnitude higher than typical experimental cooling rates, so the difference between experimental and simulational results is probably underestimated. The data for the Mendelev IPs is taken from Ref. 206, the data for the Cheng IP from Refs. 228 and 199.

Glass structure

The structure of Cu-Zr based MGs has been the topic of multiple studies and is investigated using the new potential in section 2.3. Experimentally, the atomic structure is accessible in the form of aggregated diffraction data (see section 1.4.3.1). In a series of studies by Mattern et al.[222–224] this was combined with reverse Monte-Carlo (RMC) modelling to investigate structural motifs of Cu-Zr glasses with different composition and under mechanical load. They found structural features, density and thermal stability to change monotonically with compositional changes without outstanding properties at certain compositions, nor any tendency for phase separation,[222] which is contrasting some older works.[225,226] Furthermore, they used Voronoi tessellation (cf. section 1.4.3.2) to classify SRO as polyhedral atomic arrangements. Cu is often found with 12-fold coordination, but no dominating motif or preferred chemical SRO was identified.[223] These findings disagree with simulational studies using different classical IPs, where the Cu-centered full icosahedron (FI) motif was found in large amounts,[24,198,199,227–231] as shown in Fig. 1.15

Furthermore, many studies find relations between the plastic behavior of the MG and the amount of FI.[199,227,232,233] In section 2.4.1 we show that MG samples produced using the new MLIPs show similar shear banding behavior despite predicting a far lower amount of FI in good agreement with the results from Mattern et al. (cf. section 2.3.2).

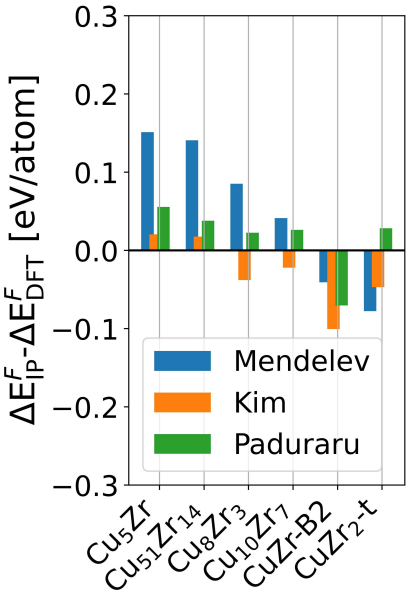

Figure 1.16: Error in formation energy ΔE^F with respect to DFT data as calculated for the IP from Mendelev et al.,[206] Kim et al.[207] and Paduraru et al.[21]

1.2.3.2 Review of available interatomic potentials

A plethora of classic IP of EAM and MEAM type,[21–24,206–208] as well as a recently published deep learning MLIP[234] have been developed for the Cu-Zr system, mostly with the aim of investigating the glassy phase. Naturally, the deep learning MLIP would be an interesting candidate for the comparison with our newly developed ACEP. However, it is not publicly available and therefore is not considered further. In the following some known problems of the classical IPs are presented to motivate the development of a new MLIP.

A common problem of the classical IPs is their limited high accuracy regime due to the fixed functional form. While they can accurately reproduce specific properties of certain phases, they can not fully describe complex systems. An example for this are formation energies of multiple crystalline phases. Fig. 1.16 shows the error compared to the values predicted by PBE-DFT for the Paduraru,[21] Mendelev[206] and Kim[207] IPs. The error is shown for all phases in the Cu-Zr phase diagram by He et al.[209] (cf. Fig. 1.14). The potentials are named according to the first authors of the corresponding publications. Mendelev et al. published three versions of their EAM potential in 2007,[197] 2009[23] and 2019.[206] If not otherwise noted, Mendelev potential refers to the latest version throughout this work. It can be seen that the maximum error for at least one of the crystal structures is on the order of roughly 100 meV/atom for all three IPs. Small deviations are to be expected when using different exchange-correlation functional for the calculation of formation energies. Here, the errors are the difference to the DFT formation energies, which in principle

depend on the employed exchange-correlation functional. In this case, however, the Mendelev and Paduraru potentials employed DFT data calculated with the Perdew-Wang exchange-correlation functional,[235] which should give similar results to Perdew-Burke-Ernzerhof (PBE). Kim et al. used experimentally determined formation energies of the liquid phase and B2-CuZr in the fitting procedure. The errors are shown for all structures included in the phase diagram. Despite this rather general problem, some more specific issues of potentials are discussed next.

The Mendelev IPs[23,197,206] are probably most common in the simulation of Cu-Zr MGs. Among other properties, they are fitted to XRD data of the liquid phase (the composition varies between the versions) and use rather complex truncated polynomials for the pair, electron-density and embedding term. However, as shown by Brink et al.[200] they are not suitable to simulate the boundary phases Cu and Zr. For example, the stacking fault energy of Cu is severely overestimated. The same principle shortcoming, even though to a lesser extent, was identified for the Cheng IP.[24,173] They identified the Ward IP[208] as more suitable in this regard, which, however, severely overestimates the stiffness of the amorphous phase and shows a nonlinear elastic behavior for Cu at very low strains. All of these potentials (including all three versions of the Mendelev IP) seem to be unable to describe the SRO of the glass phase, in the sense that they severely overestimate the amount of FI, when comparing to the experimental data from Mattern et al.[223] (cf. section 1.2.3.1) and to the results obtained with the new ACEP later on (cf. section 2.3). A direct comparison of the total structure factor (TSF) of glassy samples obtained with the newest Mendelev IP with experimental data shown in Fig. 1.17 additionally supports this claim. Details on this are described later on, where the same simulations are repeated for the new ACEP (cf. section 2.3).

Another important aspect of the Mendelev IP from 2009[23] is the overstabilization of Cu_2Zr Laves phases. Their stability at elevated temperatures is controversially discussed (cf. section 1.2.3.1), but the IP massively underestimates their formation energy and, more importantly for the formation of the amorphous phase, their nucleation barrier.[206,236,237] A similar, but less pronounced, crystallization tendency was found for the Cheng IP and seems to be related to the overestimation of FI.[238] This leads to the formation of crystalline precipitates on timescales accessible in MD simulations, i.e. multiple orders of magnitude faster than experimentally achievable values. While naturally being a problem, Brink and Albe[239] made a virtue of necessity and used the IP to grow nanocrystallites in a glassy $Cu_{64}Zr_{36}$ matrix to investigate the deformation behavior of nanocrystals and glasses. This has the advantage, that no artificial phase boundaries are introduced into the system. Nonetheless, Mendelev et al.[206] specifically aimed to reduce the crystallization tendency in the 2019 version of their IP.

1.2.3.3 Experiments and simulations

In section 2.4 tensile tests are conducted on Cu-Zr glasses and glassy-crystal composites. To put these simulations into perspective and show possible applications

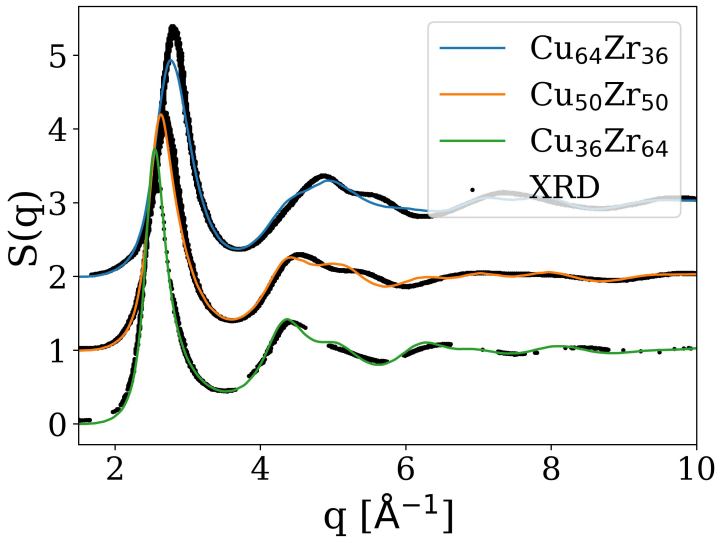

Figure 1.17: TSF of Cu-Zr glasses with three different compositions produced using the Mendelev IP,[206] and experimental data from Mattern et al.[223] for reference.

of the newly developed ACEP, this section on Cu-Zr is concluded with a short overview of related experimental and simulational studies. For comprehensive reviews of metallic glasses and their deformation the reader is referred to Refs. 160, 186, 240, 241.

Experimentally, pure Cu-Zr MG samples can be produced with comparatively high casting thickness over a wide compositional range,[188] but are not outstanding otherwise. Addition of Al and Ti can further improve the glass forming ability.[242–244] Pauly et al.[163,164,245] investigated improved ductility and work-hardening for Cu-Zr-Al and Cu-Zr-Ti glasses. This effect is due to the precipitation of nanocrystalline B2 inclusions, which can undergo twinning and a deformation induced martensitic phase transformation to the B19' phase to accommodate plastic strains. The effect of Al contents on the volume fraction and distribution of the B2 phase was further investigated by Wu et al.[166] They found that the B2 crystallites form in a narrow range of 3 % to 8 % Al content and achieved a tensile ductility >2 % for a sample with 15 % homogeneously distributed B2 crystals.

On the simulational side, the deformation of Cu-Zr MGs and glass-crystal composites has been studied extensively. Ritter and Albe[180,198] investigated shear bands in the MG, finding a lower degree of topological order compared to the surrounding matrix. By investigating both, $Cu_{64}Zr_{36}$ and $Cu_{36}Zr_{64}$ samples, they could show that the formation of SBs does not depend on the existence of a structural backbone sometimes claimed in literature.[229,246–249] Their observations are consistent with the results shown in section 2.4.1, which suggest that the new ACEP leads to qualitatively similar shear band formation, despite predicting far less FI. Brink et al.[200] simulated a $Cu_{64}Zr_{36}$ glass matrix with different spherical inclusions of varying size

to derive a qualitative map of SB-precipitate interaction mechanisms depending on the critical stress for nucleation of dislocations in the precipitate and its size. Small precipitates can be dissolved when a SB hits them during their propagation through the glassy matrix. Different shapes of crystalline inclusions were studies by Şopu et al.[250,251] They observed the martensitic transformation of B2-CuZr similar to the results in section 2.4.2 in nanowires and glass-crystal laminates. Kalcher et al.[252,253] investigated how creep in Cu-Zr glasses is influenced by different B2-CuZr inclusions. Finally, it should be noted that this overview can by no means be an exhaustive list, considering the huge amounts of publications shown in Fig. 1.5a.

1.2.4 Silicon oxycarbide

Silicon oxycarbides (Si-O-Cs) are polymer derived glass-ceramics with remarkable versatility due to a highly tunable composition and microstructure. They combine outstanding structural and functional properties such as high temperature resistance and mechanical strength,[254,255] a great creep- and corrosion resistance,[256,257] piezoresistivity[258–260] and high storage capacity for Li^+, Na^+ and K^+.[261–268] Consequently, Si-O-C has possible applications among diverse fields ranging from protective coatings[269] over gas and pressure sensing devices[270,271] to energy storage[272] and biomedicine.[273] While the research on carbon containing silica glasses dates back over 70 years,[274] structural details on the atomistic scale and their relation to properties in Si-O-C often remain elusive and are investigated as part of this thesis. The following sections give a short overview of current literature on the system that is of relevance for this thesis, not limited to, but focusing on a modelling and simulation viewpoint.

1.2.4.1 Thermodynamics and structure

Besides some hypothetical crystal structures, whose existence has not been experimentally confirmed Si-O-C has a glass-ceramic structure, i.e. an amorphous phase and ceramic precipitates. These precipitates, however, do not contain all three elements, but are SiC or graphite resulting from phase separation. As evidenced by nuclear magnetic resonance (NMR) and UV Raman spectroscopy, Si-O-C consist of corner shared $SiO_{4-x}C_x$ tetrahedra with sp^3-hybridized C and a segregated sp^2-hybridized turbostratic C phase.[278,279] Different models for the nature of the segregated carbon and the distribution of the two phases exist, which are both consistent with NMR and small angle X-ray scattering data. According to one, called model 'a', the 'free' carbon phase exists as graphene like layers that form an interpenetrating network with domains of $SiO_{4-x}C_x$ tetrahedra. In the other, called model 'b', graphitic agglomerates are embedded within a matrix of $SiO_{4-x}C_x$ tetrahedra. Scarmi et al.[275] and Saha et al.[276] argued that the viscoelastic behavior and creep resistance of Si-O-C could only be explained by model 'a', which was further supported by etching experiments.[280] On the other hand, Widgeon et al.[277] obtained mass fractal dimensions from NMR spin-lattice relaxation measurements

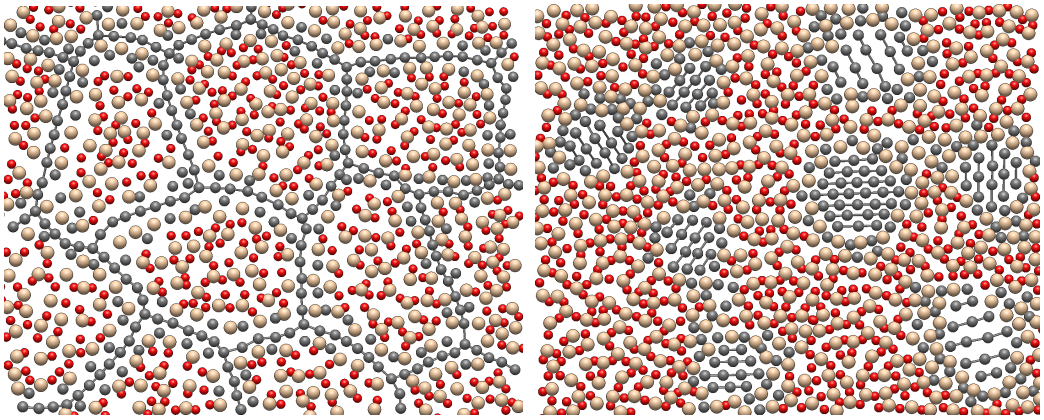

a **b**

Figure 1.18: Schematic 2D representations of the Si-O-C structure models as argued for by Scarmi et al.[275] and Saha et al.[276] (**a**) and by Widgeon et al.[277] (**b**). In (**a**) the sp^2-C phase is consists of graphene like layers forming an interpenetrating network with the $SiO_{4-x}C_x$ tetrahedra. In (**b**) the 'free' carbon agglomerates to graphite like inclusions within a $SiO_{4-x}C_x$ matrix. Both figures show C in gray, O in red and Si in beige.

and Roth et al.[279] measured turbostratic carbon with small spatial extensions via UV Raman spectroscopy, both supporting model 'b'. Schematics of both models are shown in Fig. 1.18.

The amount of free carbon phase in Si-O-Cs depends on their processing and composition. In 'stoichiometric' Si-O-C, i.e. a $SiO_{2(1-x)}C_x$ composition that can be split into SiO_2 and SiC without excess carbon, no thermodynamic driving force for the creation of a free carbon phase exists. Below 1000 °C to 1100 °C excess C remains in the structure in a strongly disordered state with small spatial extents and some degree of H-termination.[259,279] Higher processing temperature lead to an increased ordering and growth of the free carbon phase, supported by dehydrogenation. Finally, carbothermal reduction consuming the free carbon phase sets in around 1500 °C.[281]

1.2.4.2 Review of available interatomic potentials

As mentioned before, the amount of published IP for the Si-O-C system is much smaller than for Cu-Zr (cf. section 1.1.1). If only those publicly available and fitted to the glass-ceramic are considered there are none, so no further tests with the existing ReaxFFs could be conducted. Consequently, only information available in the publications of the IP developers themselves is used here.

Newsome et al.[35] developed a ReaxFF for the oxidation of SiC by O_2 and H_2O. This IP was employed by Gao et al.[36] to simulate the pyrolysis of polymeric precursors to amorphous Si-O-C structures. However, Ponomarev et al.[37] have shown later, that the ReaxFF developed by Newsome et al.[35] can not describe mixed

$SiO_{4-x}C_x$ tetrahedra, as well as the energetics and thermal stability stoichiometric Si-O-C glasses accurately. They also state the inability to describe $SiO_{4-x}C_x$ tetrahedra for ReaxFF from Soria et al.[282] The published version of the ReaxFF from Soria et al.,[282] however, does not contain an O parameterization at all. Consequently, we assume that the IP was developed further or combined with another ReaxFF in some unpublished version, which they employed for their tests, but is not available for this work. After identifying shortcomings of the other IPs, Ponomarev et al.[3735] reparametrized the ReaxFF of Newsome et al. for the pyrolysis of Si-O-C glass-ceramics, but did not publish their version of the ReaxFF.

Besides IP fitted for the Si-O-C system, it is also possible to combine IPs fitted to the subsystems. However, this way cross-terms are lacking, i.e. if IPs for SiO_2 and SiC are combined, as done for example in,[283–285] the C-O interaction has to be defined somehow. Typically, a purely repulsive IP is used.[285] Furthermore, some interatomic interactions, in this case Si-Si, are defined in both IPs. This can be treated by either disabling one of them or mixing them. Overall, many approximations are added on top of the approximation that an IP is by nature, further reducing the ability to accurately reproduce physical properties of a material.

1.2.4.3 Experiments and simulation

Synthesis and simulational samples

An important aspect of Si-O-C is the flexible and complex synthesis process. The most common route to produce Si-O-C glass-ceramics is the crosslinking of polymeric precursors, typically alkoxysilanes and polyorganosiloxanes, and subsequent pyrolysis.[281,286,287] This can be combined with stereolithography and other additive manufacturing techniques to obtain complex shaped parts.[254,288–290] For pyrolysis temperatures below around 1200 °C the resulting samples are completely amorphous. Above, increasing degrees of phase separation and crystallization can be observed, but even at 1500 °C a large amorphous faction remains.[291] Furthermore, the composition of the samples changes depending on the pyrolysis conditions due to the release of gaseous products. A detailed explanation of the chemical reactions that take place during processing is for example given in a review by Stabler et al.[281]

The complex processing route and amorphous structure with different phases raise the question of how atomistic Si-O-C models for simulations can be created. The melt and quench technique applied to produce metallic glasses in experiments can be naively reproduced using MD simulations. Simulation times achievable when employing IPs are limited to nano- or microseconds. This leads to extremely high quench rates, typically in the range of 1×10^9 K/s to 1×10^{12} K/s, but otherwise the process can be accurately described. The pyrolysis of Si-O-C, however, involves more complex chemical reactions and the covalent interatomic bonds require advanced potentials for an accurate description. Nonetheless, examples for both simple melt quenching and attempts to accurately simulate the pyrolysis process

can be found.[36,285,292] Due to the time limitations of MD simulations temperatures of >2500 K, instead of 1200 K to 1500 K used in experimental setups are typically employed in simulated pyrolysis processes to obtain faster kinetics.[36,37]

An alternative way to generate networks of $SiO_{4-x}C_x$ tetrahedra are bond-switching algorithms, which are computationally cheaper than MD simulations. They can be combined with geometrical optimization methods as implemented by Wooten et al.[293] Extended versions of this method were for example employed by Kroll[294–296] in a series of DFT based studies investigating the structure of Si-O-C. Melt-quenching with very high quench rates that can be simulated using DFT leads to high amounts of defects such as under- or overcoordination of atoms. These defects are rarely observed in experiments. A detailed description of the algorithm is given by Kroll in.[297]

Elastic properties

In section 3.3.2 the Young's modulus of simulated Si-O-C samples is related to the structural motifs of the glass-ceramics. Related experimental and simulational publications are quickly reviewed here. Sorarù et al.[298] investigated the Vickers hardness and Young's modulus of multiple Si-O-C samples with varying compositions. They found both to increase with the amount of C in $SiO_{4-x}C_x$ tetrahedra, which fits well to our observations in section 3.3.2. In a more recent work, Stabler et al.[299] included experimental data from multiple sources[133,256,298,300–302] and conducted own measurements to relate the Young's modulus to the volume fractions of 'free' carbon and SiC in the structure. They found a decrease with the former and increase with the latter. Haseen and Kroll[285] used a combination of IPs by Tersoff[31,303,304] and Munetoh et al.[30] to simulate Si-O-C and investigate its Young's modulus. They found relations to composition, density and morphology of the 'free' carbon phase. Their results suggest, that an increased density and carbon content within the glassy $SiO_{4-x}C_x$ phase lead to higher stiffness. Furthermore, the density of their samples decreases with increasing 'free' C content, leading to an indirect effect on the Young's modulus, which is not considered in the experimental results. For samples with equal density they find a slight increase of the Young's modulus with increasing amounts of 'free' C, which is consistent with our results in section 3.3.2.

1.3 Research questions

To conclude the introduction into MLIPs and treated material systems the following research questions are raised. They summarize the motivation for this thesis, before continuing with the methods employed to answer them.

Chapter 2: Thermodynamics and glassy structure in the Cu-Zr system

- How well can MLIPs describe structurally and chemically complex systems, compared to experimental and ab initio computational data?

- Are mechanical and thermodynamic properties well reproduced and to which extent does the error inherent to DFT training data influence results?
- What is the topology of Cu-Zr glasses and how important are specific structural motifs?
- How do glass and glass-crystal samples behave under tensile load?

Chapter 3: Structure and properties of silicon oxycarbides

- How can a training data set for the Si-O-C system be produced and what does it look like?
- What is the microstructure of Si-O-C, how does it form?
- How does this microstructure relate to existing models and the discrepancies between them?
- Which structural features are good descriptors for mechanical properties of the system?

Chapter 4: Comparison of machine learning interatomic potentials

- How do different MLIPs compare, what are their advantages, disadvantages and limits?
- What is the effect of different error measures and which error measure is suitable for which purpose?
- Which amount of training data is required for which potential?
- How much computational time is required by MLIPs, and what are the accuracy-cost trade-offs?

1.4 Methodology

In this thesis materials are investigated by simulation of their atomic structure using molecular dynamics (MD) employing machine learning interatomic potentials (MLIPs) fitted to large amounts of DFT data. Subsequently, their structural features and properties are analyzed. This workflow is schematically depicted in Fig. 1.19. The following sections give an overview of DFT and MD followed by a description of analysis methods employed in this work.

1.4.1 Density-functional theory

As noted in section 1.1, atomic systems can in principle be described by the Schrödinger equation (eq. 1.1), which, however, is not solvable for a manybody system. DFT offers an alternative way to obtain information such as energy and

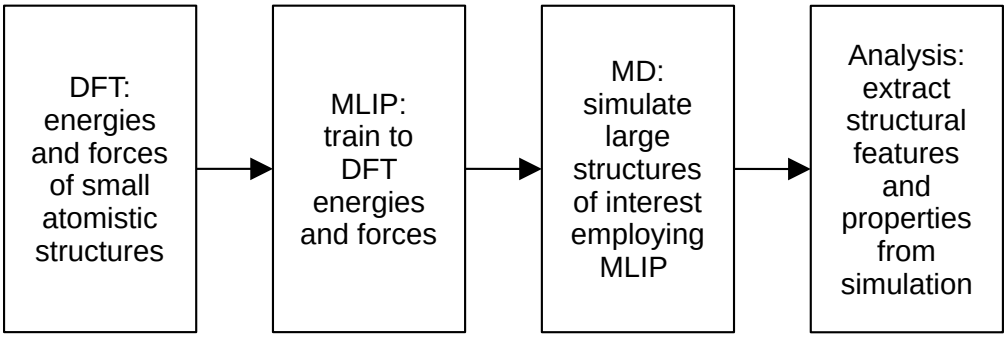

Figure 1.19: Overview of workflow employed to investigate materials in this thesis.

interatomic forces within a system without a priori knowledge besides chemical species and atomic coordinates. The basis for this are the theorems of Hohenberg and Kohn,[305] which prove that all properties for a system in ground state, i.e. at 0 K, are unique functionals of the electron density $n(\boldsymbol{r})$. Kohn and Sham[306] then showed that the multi body problem can be mapped to a solvable independent-particle problem of the form

$$H_{\mathrm{KS}}\Psi_i(\boldsymbol{r}) = \left[-\frac{\hbar^2}{2m}\nabla^2 + V_{\mathrm{eff}}\right]\Psi_i(\boldsymbol{r}) = \epsilon_i\Psi_i(\boldsymbol{r}), \tag{1.38}$$

where H_{KS} is the Kohn-Sham Hamiltonian, m the mass, and V_{eff} the effective potential. Within V_{eff} many-body effects are considered via an exchange-correlation (XC) functional of the density. In principle, the accuracy of DFT calculations is only limited by this functional, but only approximate forms of it exist, and their development is an ongoing field of research.[307] A sophisticated description of the Kohn-Sham method and various XC functionals is out of the scope of this thesis; it can be found for example in ref.[308] Computationally, the Kohn-Sham ansatz requires to obtain a ground-state $n(\boldsymbol{r})$ that is self-consistent with V_{eff}, depicted schematically in Fig. 1.20.

While DFT allows to accurately calculate many properties for atomic system of interest, it scales as $\mathcal{O}(n^3)$, where n is the number of electrons explicitly considered

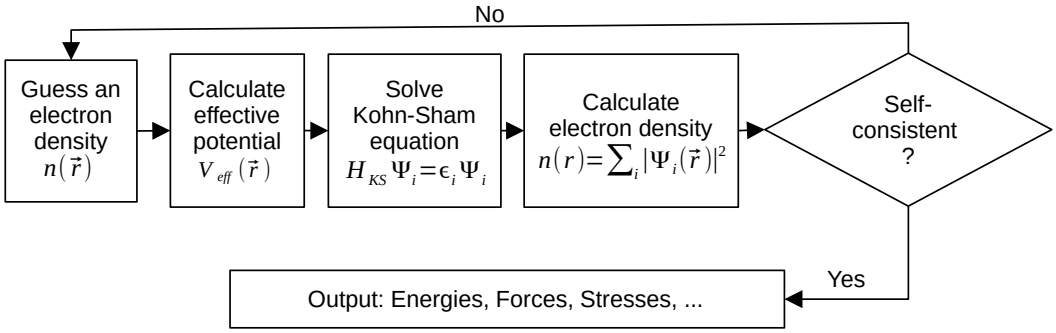

Figure 1.20: Schematic of computational steps in a DFT calculation.

	(Al)-Cu-Zr	Si-O-C
plane wave cutoff [eV]	350	900
k-point spacing [2πÅ^{-1}]	0.1 (crystalline) 2/13 (amorphous)	0.23

Table 1.1: Plane wave cutoff and k-point spacing employed for DFT calculations in this thesis. Si-O-C settings were kept consistent with the Si-O data set from.[52,53]

in the calculations. Therefore, it is not suitable to describe systems containing more than a few thousand electrons, which corresponds to a few hundred atoms.

Within this thesis DFT calculations were employed foremost to generate training and testing data for MLIPs. The calculations were carried out using the VASP code[309–311] with projector augmented-wave pseudopotentials.[312] For the (Al)-Cu-Zr system the Perdew-Burke-Ernzerhof[313] and for the Si-O-C system the SCAN[314] XC functionals were employed. The employed plane wave cutoff and k-point spacings are listed in Tab. 1.1.

1.4.2 Molecular Dynamics

> "We may regard the present state of the universe as the effect of its past and the cause of its future. An intellect which at a certain moment would know all forces that set nature in motion, and all positions of all items of which nature is composed, if this intellect were also vast enough to submit these data to analysis, it would embrace in a single formula the movements of the greatest bodies of the universe and those of the tiniest atom; for such an intellect nothing would be uncertain and the future just like the past could be present before its eyes."
>
> *– Pierre Simon Laplace, A philosophical essay on probabilities*

MD simulations evolve a system of interacting particles, for example a system of atoms treated as mathematical mass points, in time by integrating Newtonian equations of motion. When considering atoms as particles of interest some assumptions have to be made. Typically, the Born-Oppenheimer approximation is applied, because the interatomic forces depend on the electronic interactions, while atoms considered as point masses are moved. Therefore, it is assumed that the electron system and corresponding forces instantaneously react to the movement of the nuclei. Furthermore, atoms are considered heavy and slow enough to be treatable within classical mechanics. Then the equation of motion for an atom i in an N atom system is given by

$$m_i \frac{d^2 \boldsymbol{r}_i}{dt^2} = \boldsymbol{F}_i(r_1, ..., r_N) + \boldsymbol{F}_{i,\text{ext}}, \tag{1.39}$$

where m is its mass, $\boldsymbol{r}_i$ the position, $\boldsymbol{F}_i$ the force acting on the atom due to other atoms and $\boldsymbol{F}_{\text{ext}}$ an applied external force. Forces on an atom i can be obtained

using ab initio methods such as DFT or from an IP V according to

$$\boldsymbol{F}_i = -\nabla_i V. \tag{1.40}$$

The former comes with the previously discussed scaling problems for larger systems, while the latter scales as $\mathcal{O}(N)$ when the IPs are limited to short-range interactions, i.e. some interaction cutoff is applied.

In MD simulations equation 1.39 is numerically integrated for all atoms at each discrete timestep. The Large-scale Atomic/Molecular Massively Parallel Simulator (`LAMMPS`) code[315,316] is used for MD simulations in this work. It implements equations of motion as proposed by Shinoda et al.[317] They allow simultaneous and independent control over T and P. The time integrator follows the scheme proposed by Tuckerman et al.[318] To speed up simulations `LAMMPS`' `KOKKOS` package was employed, which ports performance critical parts of the code to GPU accelerators.

Without further measures the number of particles N, the volume V and the energy E of the system stay constant during the MD simulation, i.e. the microcanonical NVE ensemble is sampled. To control the temperature T and pressure P thermo- and barostats are necessary. The temperature of the system is determined by the kinetic energy of the particles, so thermostats work by influencing the momenta of atoms. A common choice also used in this thesis is the Nosé-Hoover thermostat,[319,320] which couples a virtual heat bath to the system via an additional "frictional" force. This force accelerates atoms when T is below the desired value and decelerates them when it is above. The pressure P in the system is determined by the shape and volume of the simulation cell. In analogy to the thermostat a Nosé-Hoover or Parrinello-Rahman barostat[321] modifies the equations of motion to create a desired stress state in the system. In depth explanations of MD and related techniques can be found for example in the books from Frenkel and Smit[9] or Tadmor and Miller.[322]

1.4.3 Structure analysis

Experimentally, diffraction techniques play an important role in understanding atomistic structures. They average information over their characteristic length scales. This works very well in the case of crystalline matter, because its periodicity allows a direct interpretation based on comparatively simple structure models. For amorphous structures, however, a detailed atomistic picture can not be obtained from diffraction experiments alone due to their inherent randomness. Consequently, modelling techniques in conjunction with experiments and MD simulations play an important role in the understanding of amorphous phases. The following section treats the calculation of diffraction data from atomistic structure models, enabling a direct comparison with experimental data as done for Cu-Zr glasses in section 2.3.1. Furthermore, Voronoi tessellation is explained, which is commonly used to classify local structural motifs within MGs and used in section 2.3.2 to compare results between the ACEP and other IPs, as well as RMC results.

1.4.3.1 Total structure factor

The TSF (q) is the normalized intensity measured in a scattering experiment and can be calculated. For isotropic matter, such as amorphous materials q is the absolute value of the scattering vector $q = 4\pi \sin(\Theta)/\lambda$ with incident angle Θ and wavelength λ.[223] It is related to the pair distribution function $g(r)$

$$4\pi r\rho_0(g(r) - 1) = \frac{2}{\pi}\int_0^\infty q(S(q) - 1)\sin(qr)dq, \tag{1.41}$$

where ρ_0 is the average number density of atoms.[323] The radial distribution $R(r)$ function can be obtained from $g(r)$

$$R(r) = 4\pi r^2\rho_0 g(r). \tag{1.42}$$

While experimentally the TSF is directly measurable, atomistic structure data can be used to directly calculate $R(r)$. To compare simulational and experimental data of multicomponent system the atomic form factors $f(q)$, which determine the scattering amplitude have to be considered. Then, the TSF can be calculated as a weighted sum of partial structure factors

$$S(q) = \sum_{i\leq j} w_{ij}(q)S_{ij}(q), \tag{1.43}$$

where weights can for example be obtained from the Faber-Ziman formalism[223,324] as

$$w_{ij}(q) = (2 - \delta_{ij})c_i c_j \frac{f_i(q)f_j(q)}{\langle f(q)\rangle^2}, \tag{1.44}$$

which is also employed to calculate the TSF of MG samples (cf. section 2.3.1)

1.4.3.2 Voronoi tessellation

In Voronoi tessellation an n-dimensional space is partitioned by assigning the region around some point $\boldsymbol{p}_i$ that is closer to any other point $\boldsymbol{p}_j$ in space to $\boldsymbol{p}_i$.[325,326] The corresponding region is the Voronoi area or volume of the point. Examples for two- and three-dimensional Voronoi tessellation are shown in Fig. 1.21. In the case of atomic systems, radical or polydisperse Voronoi tessellation is commonly employed. For this, spheres with a spatial extent, typically atomic radii, instead of points are considered when calculating the boundaries between particles.[199,327]

Local structure motifs in MGs are classified using Voronoi tessellation by analyzing the faces of the resulting Voronoi polyhedra. The number n of faces with i edges n_i is counted and denoted in the Voronoi index $\langle n_3, n_4, n_5, n_6, ...\rangle$. The Voronoi tessellation can also be used to calculate a well-defined coordination number despite varying bond lengths in the amorphous phases by counting all faces. A common motif in metallic glasses is the $\langle 0, 0, 12, 0\rangle$ Voronoi polyhedron, which is also named FI, after the atomic arrangement resulting in it. The FIs and distorted variants

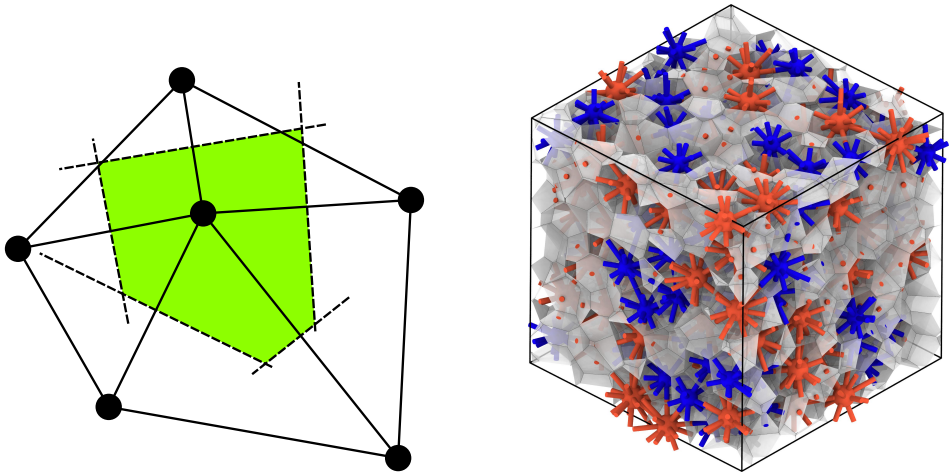

a **b**

Figure 1.21: Voronoi construction in 2D, where atoms are shown as black dots and the Voronoi area of the center atom is shaded green (**a**) and 3D Voronoi construction for an exemplary atomistic structure with atoms shown in blue and red, while gray areas indicate Voronoi faces (**b**).

with Voronoi indices such as $\langle 0, 2, 8, 2\rangle$ are considered the dominant structural and motifs in Cu-Zr based glasses and supposedly play an important role in the structural stability and formation of shear bands,[24,199,228,229,231] which is discussed in more detail in the results on Cu-Zr. Examples for $\langle 0, 0, 12, 0\rangle$ and $\langle 0, 2, 8, 2\rangle$ motifs are shown in Fig. 1.22.

The Voronoi analysis of MG structures in this thesis was done with the `OVITO` software for visualization and analysis of atomistic simulations.[328]

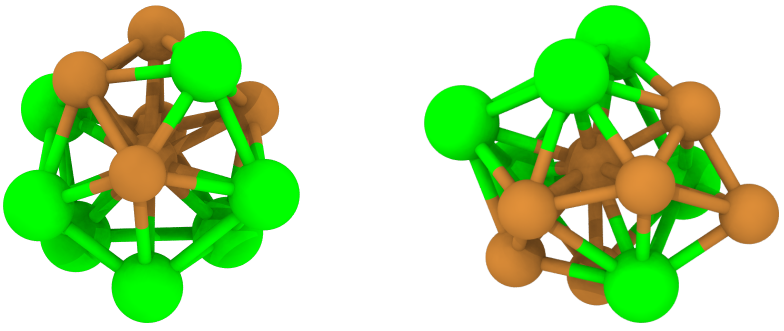

a **b**

Figure 1.22: Examples for atomic arrangements forming $\langle 0, 0, 12, 0\rangle$ (**a**) and $\langle 0, 2, 8, 2\rangle$ (**b**) polyhedra in Cu-Zr. Cu is shown in brown and Zr in green.

1.4.4 Thermodynamic properties

DFT allows calculating formation energies with a high accuracy, but besides some examples of small and simple systems it is limited to ground state, i.e. 0 K descriptions and associated with a high computational cost.[329–335] Through the combination of MLIP with thermodynamic integration techniques finite temperature properties of much larger and more complex systems can be calculated with near DFT accuracy. In this thesis they are employed to construct a composition-temperature phase diagram of the Cu-Zr system in section 2.2.2.

1.4.4.1 Calculation of free energies

Finite temperature Helmholtz and Gibbs free energies can be calculated using thermodynamic integration by continuously switching from a reference system with analytically known free energy to a system of interest. The work required to switch from an initial system i to a final system f is given by

$$W_{i\to f} = \int_{t_i}^{t_f} \frac{d\lambda(t)}{dt} \frac{\partial H(\lambda)}{\partial \lambda} dt \tag{1.45}$$

where H is the Hamiltonian, t is time and λ is a parameter continuously switching from H_i to H_f. The free energy difference between i and f is $\Delta F = W - E_d$, where E_d is the dissipated energy. If the switching process is sufficiently slow $E_{d,i\to f}$ and $E_{d,f\to i}$ become equal,[336] so that

$$\Delta F = \frac{1}{2}\left((W_{i\to f} - E_{d,i\to f}) - (W_{f\to i} - E_{d,f\to i})\right) = \frac{1}{2}\left(W_{i\to f} - W_{f\to i}\right). \tag{1.46}$$

For solids the reference system is typically the Einstein crystal.[337] Different systems can be chosen for liquids. For this thesis, the `calphy`[338] code is employed, which uses the Uhlenbeck-Ford model.[339] Furthermore, `calphy` uses reversible scaling[340] and nonequilibrium calculations[341] for computational efficiency.

1.4.4.2 Construction of phase diagram

The output of `calphy` are tables containing the Helmholtz or Gibbs energy as function of temperature. To compute the composition-temperature phase diagram the phase or phase mixture with the lowest free energy has to be found for each composition and temperature. In the case of the Cu-Zr phase diagram the Gibbs energy at zero pressure was calculated for FCC Cu, BCC and HCP Zr and each of the intermetallic phases shown in the Cu-Zr phase diagram suggested by He et al.,[209] which was also shown in Fig. 1.14. G of the liquid phases was calculated explicitly for the pure elements and the compositions given by the intermetallic phases. The phase with minimum G was calculated on a grid with 1% composition and 1 K temperature steps, where the composition dimension was supplemented with the compositions of intermetallic phases. All possible solid-solid and solid-liquid

mixtures at some concentration were considered by linear combinations of G of the boundary phases according to the lever rule. G_{liquid} at arbitrary concentrations was obtained by interpolation between the explicitly calculated values using the `SciPy` Clough-Tocher 2D interpolator.[342] All phases were treated as stoichiometric compounds, neglecting solubility. Considering that published phase diagrams for the Cu-Zr system do not show a significant solubility for any phase besides pure Zr, we do not expect that this causes major differences and avoid additional complexity. A proper treatment of solubility would require to take the configurational entropy into account, but thermodynamic integration via `calphy` only calculates the vibrational entropy. Under the assumption of a dilute solution and randomly distributed solvents, it could be calculated using the Boltzmann entropy. However, it seems unlikely that these assumptions are valid, as the interactions in the Cu-Zr system prevent random distribution of solvents, so the Boltzmann entropy can only be considered as upper limit. For better results, a computationally expansive method like Monte-Carlo sampling would be required. Finally, the phase with minimum G at each grid point was found using the `xarray` python package.[343]

1.4.5 Mechanical properties

The mechanical properties of materials are relevant for their application both as structural and functional components. Furthermore, many of them can be measured in experiments and calculated using DFT and IP levels of accuracy, so they offer an opportunity to judge on the quality of the employed simulation methods. As part of this thesis the elastic constants of Cu-Zr alloys and Si-O-C are calculated as described in the next section. In the case of Cu-Zr glasses also plastic deformation is investigated. Thereby the formation of shear bands is important, which require a measure for localized deformation as discussed in the very next section.

1.4.5.1 Elastic constants

The elastic tensor $\boldsymbol{C}$ relates the stress $\boldsymbol{\sigma}$ and strain $\boldsymbol{\epsilon}$ states of a material in the linear elastic regime

$$\boldsymbol{\sigma} = \boldsymbol{C}\boldsymbol{\epsilon}. \tag{1.47}$$

Formally, $\boldsymbol{C}$ is a fourth-order tensor containing 81 components, which are reduced to a maximum of 21 independent ones due to symmetry in materials with triclinic structure. In isotropic materials, such as amorphous phases only 2 components are independent. $\boldsymbol{C}$ can be calculated from the stress-strain or energy-strain relation by applying deformations to a system, calculating the resulting stresses and solving the corresponding linear equations. This is implemented in a widely automated way in different codes. For this work `pymatgen`[108] was employed.

Lamé constants μ and λ as well as Young's modulus E, shear modulus G and bulk modulus B can be measured explicitly or derived from the elastic tensor. For example the elastic tensor and Lamé constants are related via $\lambda = C_{12}$ and $\mu = C_{44}$, where the indices of $\boldsymbol{C}$ are given in Voigt notation. In the case of polycrystalline

materials, which are isotropic but consist of anisotropic crystallites, lower and upper limits can be estimated using the Reuss[344] and Voigt[345] approximation, respectively.

1.4.5.2 Atomic level deformation

To identify shear bands within a deformed glass sample a local measure of strain has to be considered. This is done in section 2.4 Here, the approach by Shimizu et al.[346] is followed. The corresponding algorithm is implemented in `OVITO`.[328] Within the algorithm, the local deformation gradient tensor $\boldsymbol{J}$ for an atom i is calculated from relative displacements of neighbors compared to some reference state. Then the Green-Lagrangian strain tensor

$$\nu_i = \frac{1}{2}\left(\boldsymbol{J}_i \boldsymbol{J}_i^T - \boldsymbol{I}\right) \tag{1.48}$$

is determined. Here $\boldsymbol{I}$ is the identity matrix. Based on this a von Mises local shear invariant, also called atomic shear strain, is defined as

$$\nu_{i,\mathrm{Mises}} = \sqrt{\nu_{yz}^2 + \nu_{xz}^2 + \nu_{xy}^2 + \frac{(\nu_{yy} - \nu_{zz})^2 + (\nu_{xx} - \nu_{zz})^2 + (\nu_{xx} - \nu_{yy})^2}{6}}. \tag{1.49}$$

In shear bands the atomic shear strain is considerably higher than in other parts of MG samples.

2 Thermodynamics and glassy structure in the Cu-Zr system

The results presented in this chapter are published in:

Niklas Leimeroth, Jochen Rohrer, and Karsten Albe. "General Purpose Potential for Glassy and Crystalline Phases of Cu-Zr Alloys Based on the ACE Formalism." In: *Physical Review Materials* 8.4 (2024), p. 043602. DOI: 10.1103/PhysRevMaterials.8.043602

and the corresponding supplemental material. Some sections closely follow the structure and formulations of the original publication. The training dataset and fitted potential are publicly available on `zenodo`.[348]

2.1 Fitting and validation of ACE potential for Cu-Zr

Cu-Zr is a prototypical MG forming system, for which a plethora of classical IP exist (cf. section 1.2.3.2). However, these classical potentials have a limited fidelity, especially in complex scenarios with different involved phases. The following sections treat the development and validation of an ACEP that offers superior accuracy for a wide range of possible problem settings.

2.1.1 Training data and fitting

The aim for the ACEP is applicability to crystalline and amorphous phases, both in pristine and defective state, over the whole compositional range, to allow simulations of complex scenarios like glass-crystal composites under deformation. Thus, the training data is required to cover the configuration space of local environments present in such structures. For a newly fitted potential, this could have been achieved by applying the active learning strategy outlined in section 1.1.4. However, at the time AL techniques were not implemented for ACEPs, so the training data was generated without them. This 'manual' structure generation generally consisted of two steps. First, a variety of structures was obtained and relaxed within DFT. Second, those structures were modified in different ways to cover a larger configurational space. In the case of pure Cu and Zr the relaxed structures were simple lattices (FCC, BCC, HCP, SC, diamond). The intermetallic phases present in the phase diagram were obtained from Materials Project.[105] Their names used in this thesis and the corresponding IDs are listed in the appendix Tab. A.1. Additional, typically high energy, configurations such as zinc blende and wurtzite were

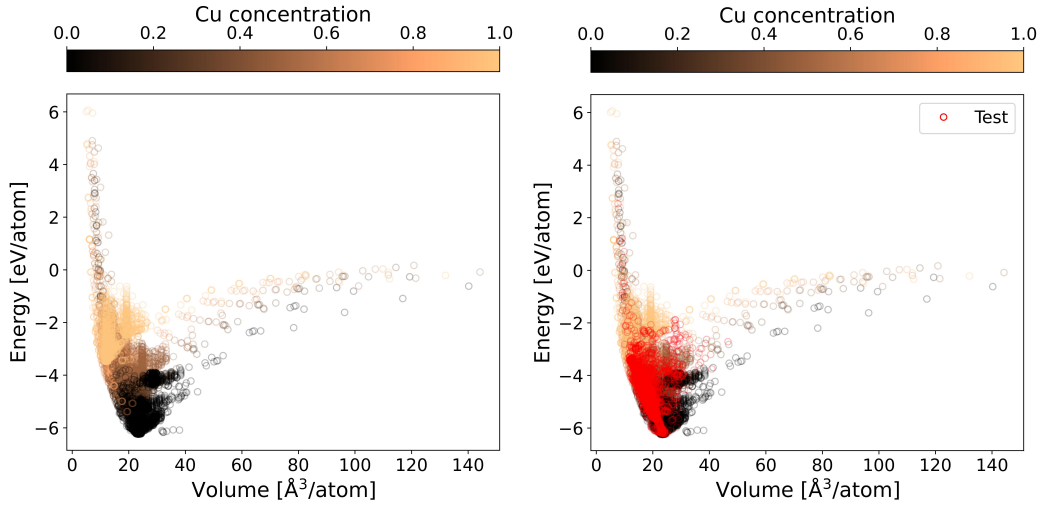

Figure 2.1: Energy-volume relation of the Cu-Zr training dataset without (**a**) and with overlapping testing data (**b**). A wide range of energies and volumes is covered over the whole compositional range, which is considered a necessity to fit a widely applicable MLIP.

generated using `ase`.[104] Amorphous structures were produced by cook and quench simulations with the Mendelev potential,[23] as schematically depicted in Fig. 2.2. They contain 128 atoms and their composition was varied from 20 to 80% Zr in one atom steps. The applied structural modifications are isotropic scaling, deformations for elastic constants, grain boundaries, vacancies, interstitials, surfaces, as well as random atom displacements and cell distortions. Fig. 2.1 shows that a wide range of atomic energies and volumes is covered by the resulting training data.

A separate testing data set was used to prevent overfitting. It contains structures with interfaces as well as random atom displacements and cell deformations. The interfaces are made from pure Cu and Zr crystals with mixed amorphous structures of varying compositions.

Both data sets are filtered to prevent the occurrence of structures that can't be described by the potential due to the locality of the descriptor, lie very far from other structures or could cause numerical problems in the fitting process. All structures with one or more of the following were removed:

- An absolute force greater than 50 eV/Å on any atom
- Formation energy greater than 10 eV/atom above the convex hull
- Minimal distance between atoms smaller than 1.4 Å
- A volume per atom greater than 150 $Å^3$ (Surface structures were excluded from this criterion)

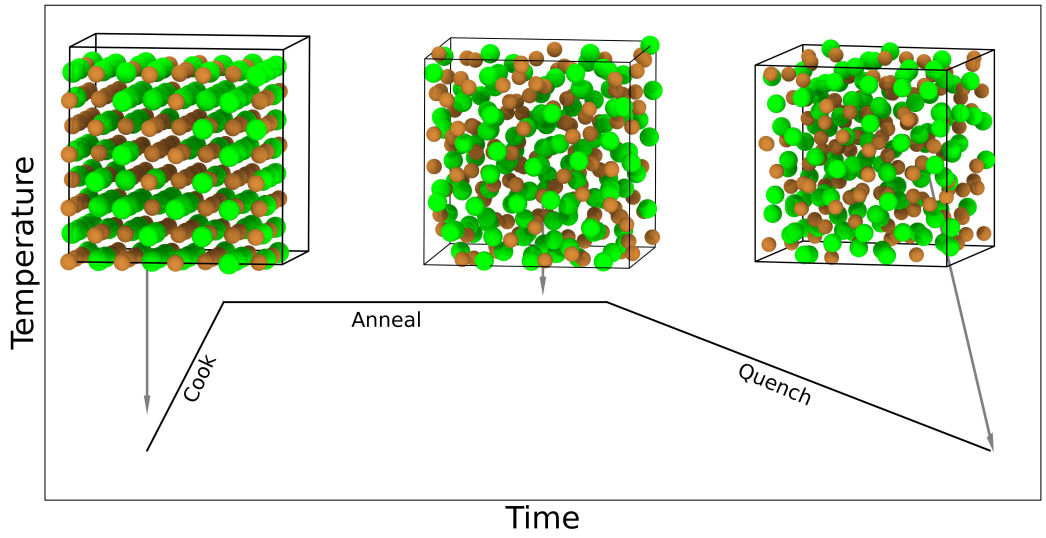

Figure 2.2: Schematic of the cook and quench process employed to produce glassy Cu-Zr samples. Crystalline structures with randomized distribution of Cu and Zr on lattice sites were heated to the liquid phase, equilibrated and rapidly cooled to obtain amorphous structures.

- Atoms with no other atom closer than 5 Å

After filtering the whole training dataset contains 24,232 structures with 2,168,544 atoms. The testing set consists of 4242 structures with an average size of roughly 118 atoms.

To ensure an appropriate coverage of configuration space the robustness of the training data is probed with the AL capabilities of the `MLIP`code.[60,89,114] An additional MTP of level 22 was fitted to the training data. Then it was employed in cook and quench simulations with around 500 structures and temperatures up to 3000 K. Here, the structures were made by randomly placing Cu and Zr atoms on an FCC lattice with 108 atoms. During the simulations no configurations with high extrapolation grade appeared, showing that the training data sufficiently covers regions with high temperatures and high mobility including the liquid regime. For the fit the DFT energies are shifted to reproduce the cohesive energies of pure FCC Cu and HCP Zr from the NIST-JANAF thermochemical tables.[349]

Finally, four distinct ACEPs with 514, 1352, 2838 and 6084 basis functions and

$$E_i = \chi_{i,1} + \sqrt{\chi_{i,2}} \tag{2.1}$$

embedding were fitted. Their cutoff was set to 7.6 Å, which corresponds to the value used in several Cu-Zr EAM potentials by Mendelev et al.[23,197,206] More basis functions correspond to more fittable parameters and lead to a higher accuracy for the training data set, at the cost of slower evaluation. In this case the description of the test data set got worse with increasing number of functions, indicating overfitting

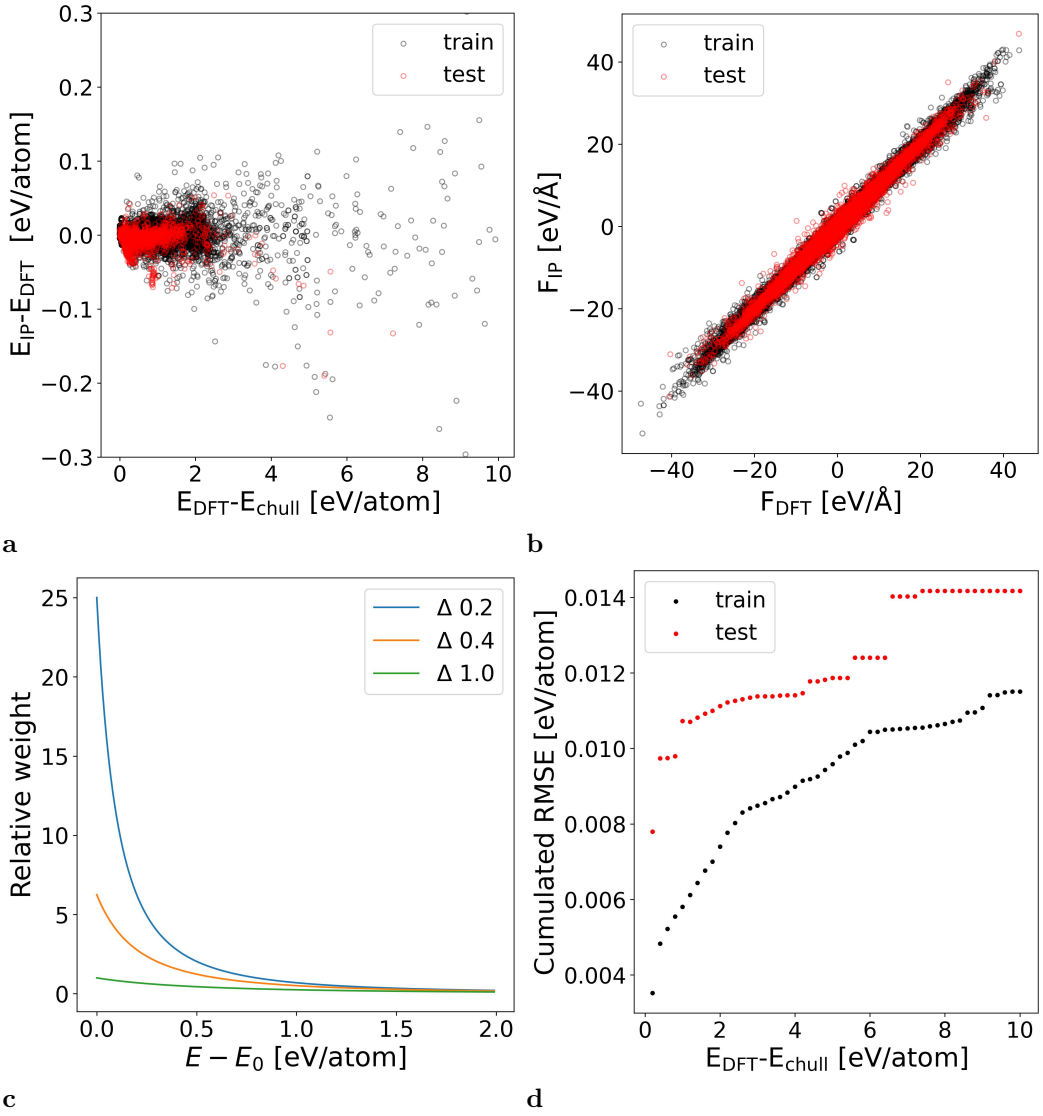

Figure 2.3: Energies (**a**) and forces (**b**) calculated with the ACEP and DFT agree well for both, the training and testing datasets. They are weighted relative to their deviation from thermodynamic equilibrium with hyperparameter Δ (**c**). Consequently, the error is significantly lower for structures that are closer to the convex hull of formation energies (**d**).

and lower transferability to other problem settings. Consequently, the potential with 514 basis functions was chosen. For the training data it has an energy and force root mean square error (RMSE) of 11.5 meV/atom and 168 meV/Å. For the testing set they are 14.2 meV/atom and 188 meV/Å, respectively. Fig. 2.3 shows scatter plots of the energy error as function of the distance from the convex and the calculated forces.

Structures closer to thermodynamic equilibrium, i.e. with low formation energies and forces were assigned a higher relative weight as described in Ref. 91. The weight of structures (and energies) w_S is given by

$$w_S = \frac{1}{(E_S - E_h + \Delta_E)^2}, \tag{2.2}$$

where the Δ_E is an adjustable hyperparameter, E_S is energy of the structure and E_h is the energy of the convex hull, i.e. the structure with the lowest energy at the corresponding composition. Forces F are weighted based on their absolute value F as

$$w_F = \frac{w_S}{F^2 + \Delta_F}, \tag{2.3}$$

where Δ_F is another hyperparameter. For the potential Δ_E was set to 0.4 eV and Δ_F to 1 eV/Å and the relative weight of energies and forces to 0.99:0.01. The relative weights for different Δ_E values and the cumulated energy RMSE as function of the distance from the convex hull are visualized in Fig. 2.3c and **d**.

2.1.2 Validation against DFT and experiment

To further validate the potential beyond a simple comparison of energies and forces a series of properties was calculated and compared to DFT or experimental results. Fig. 2.4 and 2.5 show energy-volume curves of pure and intermetallic phases, respectively. The volumes were scaled isotropically up to ±30 %. The energies are calculated using the ACEP and DFT. While simple to calculate, the energy-volume relations already show several properties of interest. The minimum in the energy curve determines equilibrium lattice constants, the curvature gives bulk moduli and different energy levels determine the relative stability of multiple phases of the same composition.

For pure Cu a very good agreement between ACEP and DFT data can be observed. In the case of Zr it is worse, but mostly for high energy structures. The BCC and HCP lattices, which are the stable polymorphs at low and high temperature, are still described very well around the equilibrium lattice constant. A similar behavior can be seen for the intermetallic phases.

Tab. 2.1 summarizes lattice constants, bulk moduli, vacancy formation energies, and melting temperature of elemental Cu and Zr and the intermetallic B2 CuZr phase. In the following each of them will be shortly discussed.

Lattice constants [Å]	Exp.	DFT (0 K)	ACE (0 K)		
Cu_{FCC}	3.602 (0 K)[350]	3.634	3.634		
Zr_{HCP}-a	3.229 (4.2 K)[351]	3.235	3.228		
Zr_{HCP}-c	5.141 (4.2 K)[351]	5.172	5.189		
Z_{BCC}	3.579 (0 K)[352]	3.574	3.576		
CuZr	3.246 (0 K)[353]	3.273	3.272		
E^f_{vac} [eV]	Exp.	Clamped		Relaxed	
		DFT	ACE	DFT	ACE
Cu_{FCC}	1.27-1.29[354,355]	1.11	0.96	1.08	0.92
Zr_{HCP}	>1.5[356]	2.06	1.92	1.94	1.88
Zr_{BCC}		2.18	1.82	-0.79	-0.97
B [GPa]	Exp.	DFT	ACE		
Cu_{FCC}	142[357]	139	149		
Zr_{HCP}	95[358]	98	115		
Zr_{BCC}		90	116		
CuZr		121	134		
C_{11}	Exp.	DFT	ACE		
Cu_{FCC}	177[357]	180	202		
Zr_{HCP}	155[359]	173	206		
Zr_{BCC}		71	101		
CuZr		143	168		
C_{12}	Exp.	DFT	ACE		
Cu_{FCC}	125[357]	117	121		
Zr_{HCP}	67[359]	42	81		
Zr_{BCC}		97	136		
CuZr		110	127		
C_{44}	Exp.	DFT	ACE		
Cu_{FCC}	81[357]	85	95		
Zr_{HCP}	36[359]	31	45		
Zr_{BCC}		24	7		
CuZr		44	45		
$T_{transition}$ [K]	Exp.	DFT	ACE (MB)	ACE (`Calphy`)	
$Cu_{FCC\leftrightarrow Melt}$	1358[211]	1251±15[335]	1225	1223	
$Zr_{HCP\leftrightarrow BCC}$	1136[211]	976±6[360]		938	
$Zr_{BCC\leftrightarrow Melt}$	2128[361]		1693	1699	
$CuZr_{B2\leftrightarrow Melt}$	1208-1233[211,212,362]		870±50	865	
Cu GSF energy [mJ/m^2]	DFT	ACE			
stable	41	31			
unstable	171	167			

Table 2.1: Comparison of several important properties of pure Cu, Zr and the intermetallic CuZr-B2 phase as calculated with the ACEP and DFT, as well as experimental data. The table lists lattice constants, bulk moduli, vacancy formation energies, melting temperatures and Cu GSF.

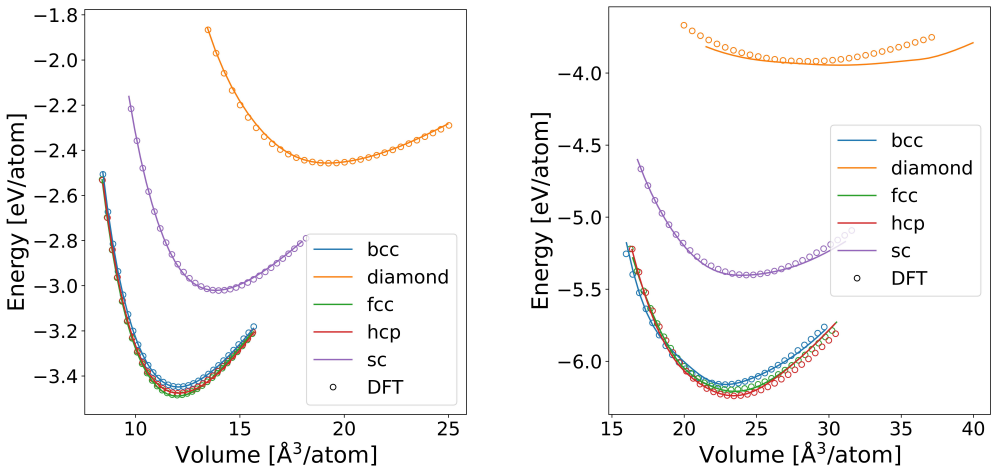

Figure 2.4: Energy-volume curves for pure Cu (**a**) and Zr (**b**) structures with isotropically scaled volume. In the case of Cu, the ACEP agrees very well with the DFT data across different structures and volume ranges. For Zr the high energy structures show higher deviations, but the more important HCP and BCC phase are well reproduced.

2.1.2.1 Cu

Cu remains in the FCC structure up to the melting point. The potential slightly overestimates its lattice constant compared to the experimental value, but agrees very well with the underlying reference DFT data.

The vacancy formation energy E^f_{vac} calculated using DFT lies roughly 0.2 eV below the experimental values. However, Glensk et al.[363] argue that experimental values should be revised. According to them, the applied extrapolation from high temperature measurements to formation energies at 0 K is not taking all anharmonic effects into account. By applying their corrections a vacancy formation energy of 1.06 eV is obtained for FCC Cu, which fits very well to the results from DFT. The ACEP underestimates both, clamped and relaxed E^f_{vac} by around 0.15 eV. As this error is quite large, it was employed to test the performance of the ACEP compared to a potential fitted in the same way, but only to the pure Cu training data subset. For this potential $E^{f,\text{clamped}}_{\text{vac}} = 1.12\,\text{eV}$ and $E^f_{\text{vac}} = 1.09\,\text{eV}$ were calculated. These much lower errors for the Cu only potential show that a limitation of the training data can be beneficial when fitting potentials for more specialized purposes.

The elastic tensor and bulk modulus show good agreement between ACEP, DFT and experimental data. The melting temperature was calculated using the moving boundary (MB) method[364,365] and thermodynamic integration as implemented in `calphy`.[338] Both values are similar, but about 135 K off from the experimental value. Similar to the lattice constant, however, the potential can not be better than the data it is trained too and an underestimation of the melting point can be

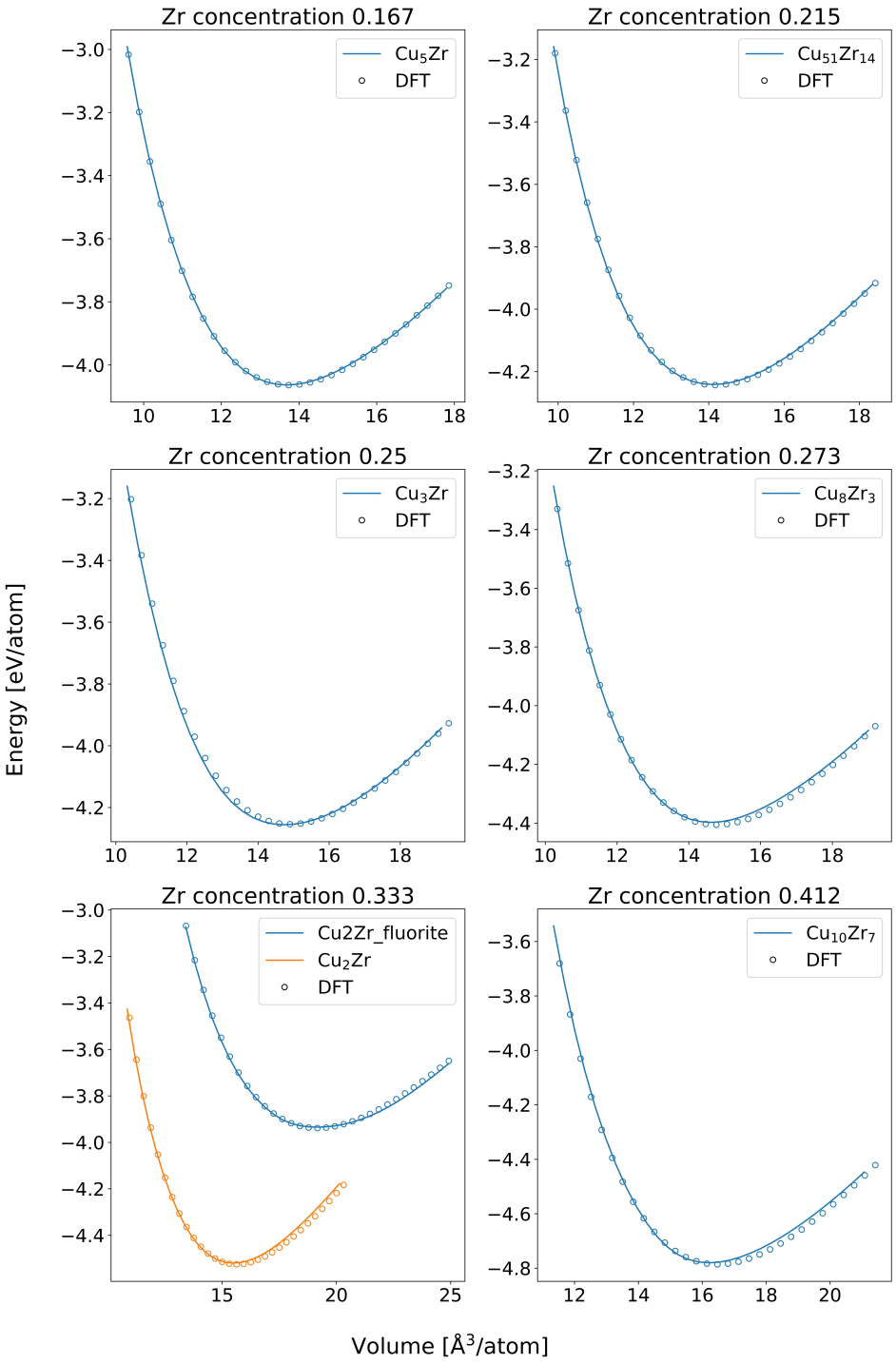

Figure 2.5: Energy-volume curves for intermetallic Cu-Zr compounds, grouped by their composition. Continued in Fig. 2.6

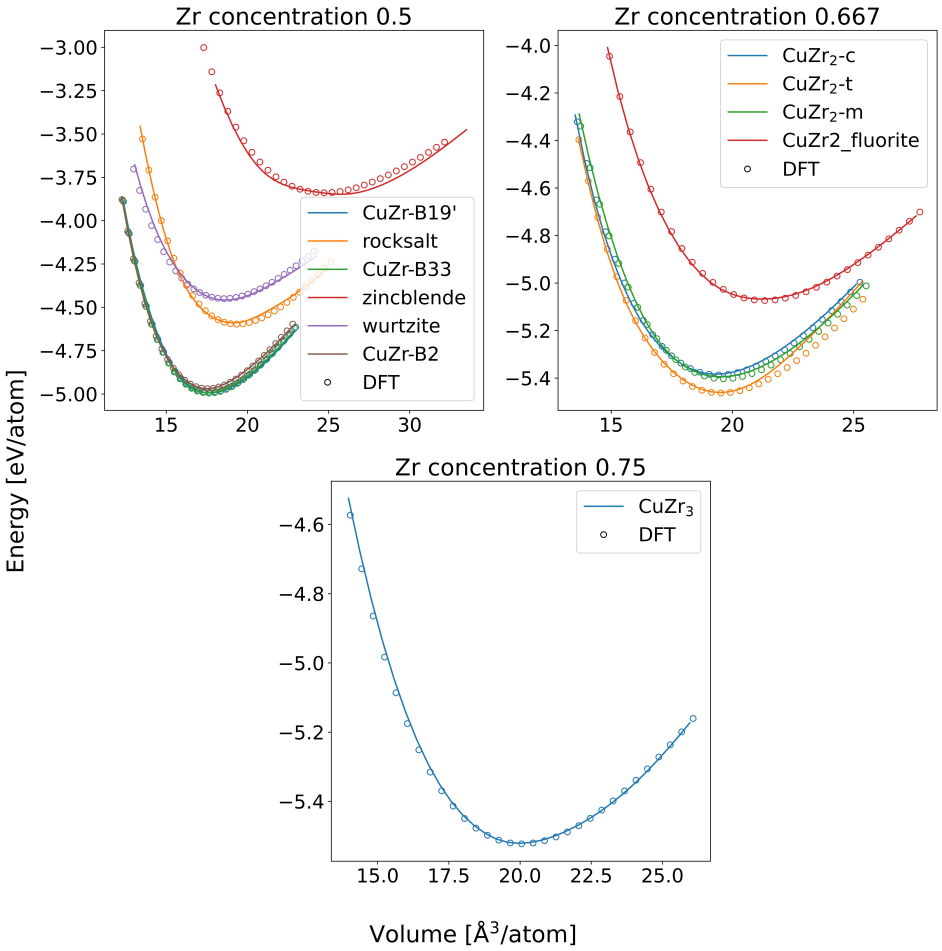

Figure 2.6: Energy-volume curves for intermetallic Cu-Zr compounds, grouped by their composition. The volume is scaled isotropically. The good agreement of the developed ACEP with DFT data across compositions already suggests a reasonable description of several related properties, such as relative formation energies, lattice constants and bulk moduli. Continued from Fig. 2.5

expected for PBE-DFT data, due to the tendency to underbind atoms. Indeed, a good agreement with the value reported by Zhu et al.,[335] who developed the TORTILD approach to calculate the melting temperature directly from ab-initio MD simulations, is achieved.

Stacking faults occurring on {111} planes are relevant for the formation of partial dislocations, twin boundaries and cross slip in FCC metal. Borovikov et al.[366] fitted a series of EAM potentials with widely different stacking fault energies but otherwise similar properties. Consequently, the stable and unstable stacking fault energy are calculated explicitly and also reported in Tab. 2.1. The values are obtained from generalized stacking fault (GSF) calculations along the ⟨112⟩ direction. They are well reproduced, with respective errors of $10\,\mathrm{mJ/m^2}$ and $4\,\mathrm{mJ/m^2}$ compared to

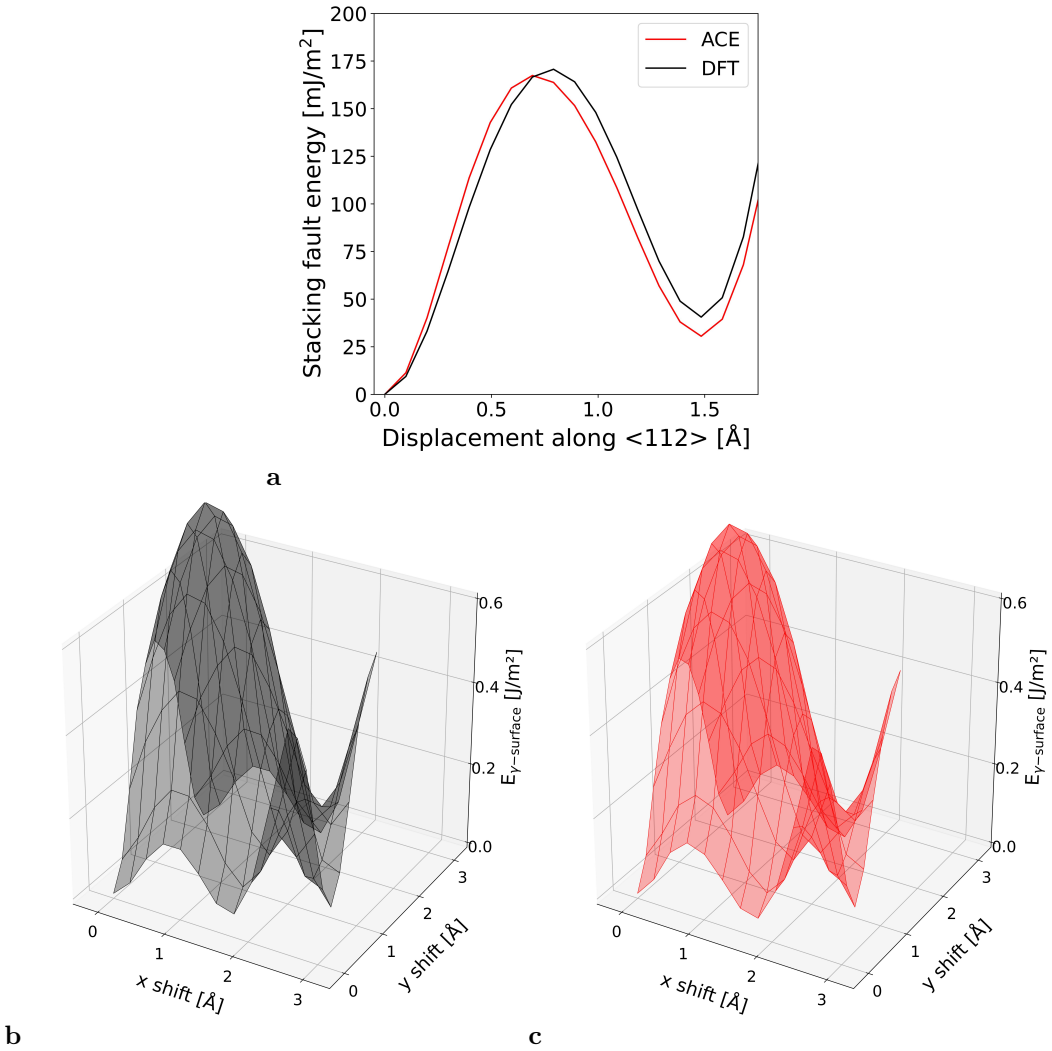

Figure 2.7: Comparison of Cu generalized stacking fault (GSF) energy along $\langle 112 \rangle$ on a $\{111\}$ plane (**a**). Additionally, the γ surface excess energy was calculated for 11x11 grid on $\{111\}$ planes with DFT (**b**) and ACE (**c**), showing good agreement between the two.

DFT. Furthermore, the γ-surface energy was calculated on a 11x11 grid with both DFT and the ACEP, where atoms were allowed to relax in the direction of the surface normal. The GSF and γ-surface are shown in Fig. 2.7.

2.1.2.2 Zr

Zr has a HCP structure at room temperature and transitions to the BCC lattice before melting. The transition temperatures were calculated using `calphy`[338] and lie below the experimental values. As already discussed for Cu this is consistent with the expectations for PBE-DFT data. However, in this case no explicit simulations for comparison are available. Both, HCP and BCC, lattice constants deviate by less than 1% compared to experiment and DFT. Calculated clamped and relaxed E^f_{vac} agree well with DFT data, but no accurate measurements are available. For the BCC structure a negative $E^{\text{relaxed}}_{\text{vac}}$ was found. This is caused by a structural collapse to energetically favorable HCP like coordination around the vacancy. The elastic constants deviate much stronger from the DFT data than in the case of Cu, pointing towards the more complex nature of Zr-Zr bonds. To estimate the achievable accuracy within the employed settings for the ACEP an additional pure Zr potential was fitted similar to the pure Cu potential. The resulting energy RMSE is 14.7 meV/atom compared to 3.1 meV/atom for pure Cu. In most cases such a direct comparison of RMSEs is not useful because it strongly depends on the complexity of the underlying training data. Here, however, both training data sets were produced similarly, so the larger error can be seen as a measure for the higher complexity of chemical interactions in Zr compared to Cu.

2.1.2.3 CuZr-B2

CuZr-B2 phase becomes stable at elevated temperatures and is of technological interest because it can undergo a martensitic phase transformation to the B19' or B33 structure and consequently shows a shape memory effect and is of interest as crystalline precipitate in strain hardening MGs (cf. section 1.2.3.1). The B2 structure is a simple cubic lattice with a two atomic basis at (0,0,0) and (1/2,1/2,1/2). The potential reproduces its DFT lattice constant almost perfectly, while elastic constants are described with an accuracy in between that of pure Cu and pure Zr. Similar to the pure phases, the melting point is severely underestimated. Here, the MB method comes with a much higher uncertainty than for elemental phases. This is caused by the increased complexity due to the compositional degree of freedom, leading to a situation in which chemical segregation instead of simple melting or crystallization could lead to energetically favorable states and slows down kinetics. Consequently, the value calculated using thermodynamic integration should be considered as the melting point predicted by the ACEP.

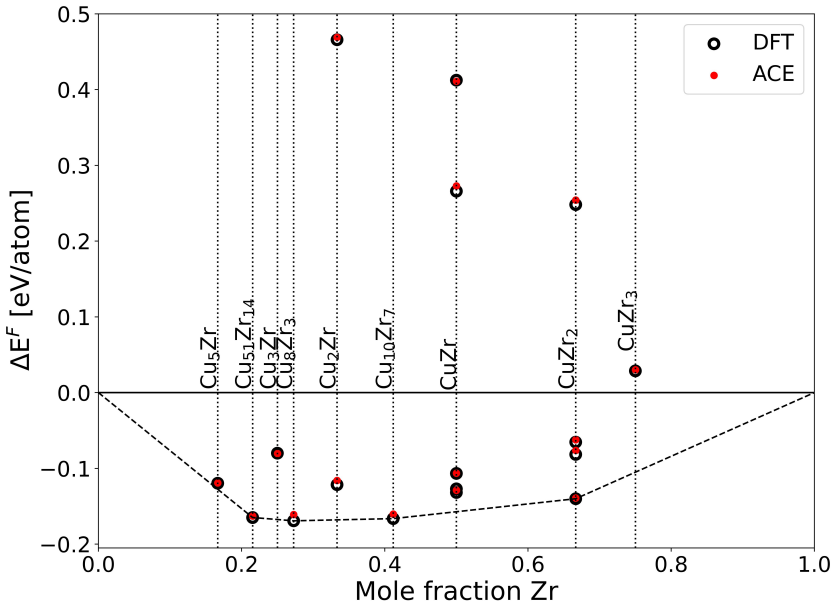

Figure 2.8: Formation energies calculated with the ACEP (red) and DFT (black). The DFT convex hull is shown as dashed line.

2.2 Thermodynamics and mechanical stability of intermetallic phases

The Cu-Zr system features a plethora of intermetallic phases. In this section, the ACEP is employed to calculate a Cu-Zr phases diagram. In an intermediate step the formation energies of the intermetallics are determined and compared to other potentials. Furthermore, their phonon dispersions are calculated to judge their mechanical stability.

2.2.1 Formation energy

All formation energies ΔE^f are calculated with FCC Cu and HCP Zr as reference states α according to

$$\Delta E^f = E_{\text{compound}} - \sum_\alpha x_\alpha E_\alpha, \tag{2.4}$$

where E are energies per atom and x_α are the corresponding mole fractions. Fig. 2.8 shows the formation energies calculated with the ACEP and DFT for all intermetallic phases used in the training data. This includes the low energy structures present in the phase diagram and found on materials projects, but also highly unstable structures created using `ASE`. Over the whole range of compositions and energies the potential and DFT match well.

A high ground state accuracy is prerequisite for an accurate description of finite temperature thermodynamics. Fig. 2.9 shows the formation energy errors for em-

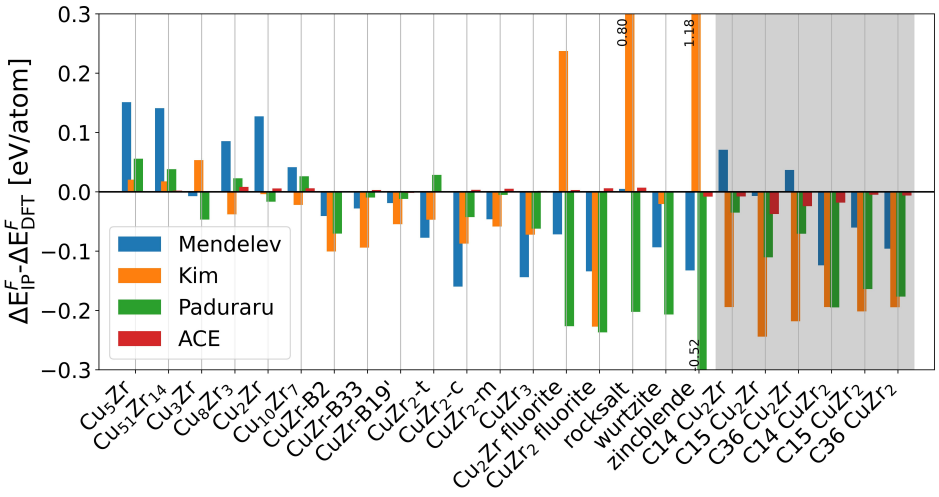

Figure 2.9: Formation energy errors compared to DFT data for the ACEP and potentials by Mendelev et al.,[206] Kim et al.[207] and Paduraru et al.[21] The error is shown with a white background for structures included in the training data and a gray background for the extrapolating regime. Here, Laves phases were employed to test the extrapolation capabilities.

pirical potentials and the ACEP, similar to the error of classical IPs in Fig. 1.16. The values shown are the difference to the DFT formation energies. As discussed in section 1.2.3.2, a part of the error could be explained by the use of different fitting data. However, Paduraru and Mendelev employed the Perdew-Wang[235] exchange-correlation functional to calculate formation energies, which should give similar results to PBE, while Kim used experimental values. The errors are shown for all structures included in the training data* and for Cu_2Zr and $CuZr_2$ Laves phases with C14, C15 and C36 structure, which were not included in the training data, i.e. where the ACEP extrapolates.

Laves phases were chosen for the extrapolation test due to their relevance in the Cu-Zr system. Some ternary Cu-Zr containing compounds and other systems with similar ratios of ionic radii show stable C14 or C15 phases.[205,367] Furthermore, the Mendelev 2009 potential[23] overstabilizes the C14 Cu_2Zr phase. Combined with a low kinetic barrier, this leads to crystal nucleation on MD simulation timescales.[231]

Compared to the empirical potentials the ACEP is always considerably more accurate for the training data. Even in the extrapolating area it consistently performs better for all structures. The only exception is the C15 Cu_2Zr phase, which is more accurately described by the Mendelev 2019 potential.[206] This Mendelev potential specifically addresses the shortcomings of the previous 2009 version regarding the overstabilization of Laves phases by explicitly including them in the fit.

*Unique compositions are named accordingly. $CuZr_2$ structures are named t, c, and m corresponding to tetragonal, cubic and monoclinic structures from materials project. The CuZr phases are high temperature B2 and metastable B19' and B33.

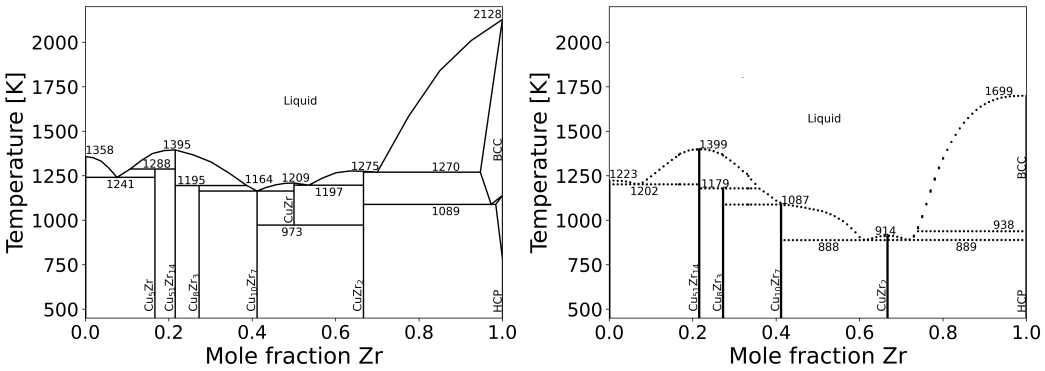

a **b**

Figure 2.10: Phase diagrams based on the work of He et al.[209] (**a**) and calculated with the ACEP (**b**).

2.2.2 Phase diagram

Fig. 2.10 shows the calculated Cu-Zr phase diagram and the version proposed by He et al.[209] for comparison. The significant differences between published Cu-Zr phase diagrams have already been discussed in the introduction and will not be repeated. The version by He phases diagram is mostly consistent with the convex hull obtained using PBE. According to the DFT data Cu_5Zr lies above the convex hull, in the work of He it is stable at low temperatures.

For the calculated phase diagram shown in 2.10b the Gibbs energies calculated using `calphy` have been shifted to match the ground state values obtained from DFT. This is a necessity to stabilize the Cu_8Zr_3 phase. A version without this correction can be found in Fig. A.1.

Due to the usage of PBE reference data the melting points are considerably underestimated, as already discussed in the previous chapter. Besides this, two main differences between the phase diagrams can be found. The Cu_5Zr and the CuZr phase are not present in the calculated version. Fig. 2.11 shows the Gibbs energy of both phases relative to the actual equilibrium structures. In the case of Cu_5Zr the relative stability decreases with increasing temperatures and its absence can be attributed directly to the DFT data, which places it around 8 meV/atom above the convex hull. For CuZr the situation is more complex, because it is supposed to be stable only at elevated temperatures. Qualitatively, this behavior is correctly reproduced. However, due to a combination of underestimated melting point and overestimated formation energy it would be stable only above roughly 1350 K. This also illustrates the strong sensitivity to small energetic differences. A lowering of the formation energy by 5 meV would suffice to bring the stability range close to the experimental value of approximately 1000 K.

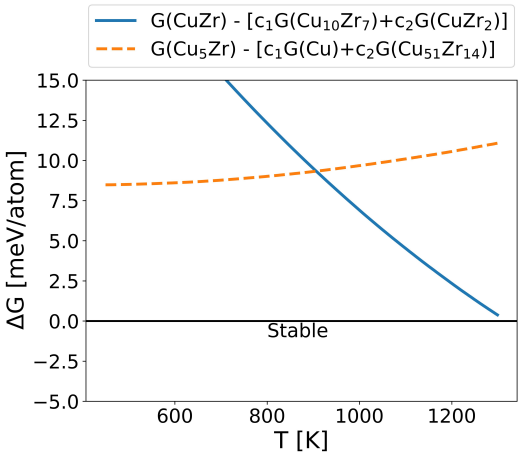

Figure 2.11: Gibbs energy difference of Cu_5Zr and CuZr compared to the actually stable phase mixtures. A few meV/atom would be enough to stabilize both phases showing the high sensitivity to small energetic differences. The CuZr shows qualitatively correct behavior and would become stable at elevated temperatures. However, due to the underestimated melting points and a slightly overestimated formation energy the system will melt before.

2.2.3 Dynamic stability

Besides their thermodynamic stability, it is also of interest whether the potential predicts the intermetallic phases to be dynamically stable. This is especially true for the important B2 phase, since the potential predicts it to be thermodynamically unstable. Structures that would undergo a spontaneous lattice change have a soft or imaginary phonon mode. Consequently, the phonon dispersion was calculated for the intermetallic phases. To this end, the harmonic approximation as implemented in `phonopy`[368,369] was employed. The results are shown in Fig. 2.12. Phases that should be stable at low temperatures, i.e. all except B2, do not show soft phonons.

The B2 phase is unstable in the harmonic approximation, which matches the observation of a martensitic phase transition upon cooling. To further investigate the phase transition MD simulations of small B2 particles were conducted. However, no spontaneous phase change was observed. Consequently, the stability was further investigated using the self-consistent phonon method as implemented in `ALAMODE`[370,371] to obtain finite-temperature phonon dispersions. The result with anharmonic effects up to the fourth order is shown in Fig. 2.13a. Here, no soft phonon modes are present, so no spontaneous phase change should be expected in MD simulations.

A similar B2-B19' martensitic phase transformation is observed in the common shape memory alloy NiTi. Hatcher et al.[372,373] found a barrier free two-step phase transition path in this material. First two center layers of a six layer $\{011\}$ B2 structure are displaced by $a_0/2$ along the $\langle 100 \rangle$ direction, where a_0 is the lattice constant. Second the monoclinic angle changes to the equilibrium one during re-

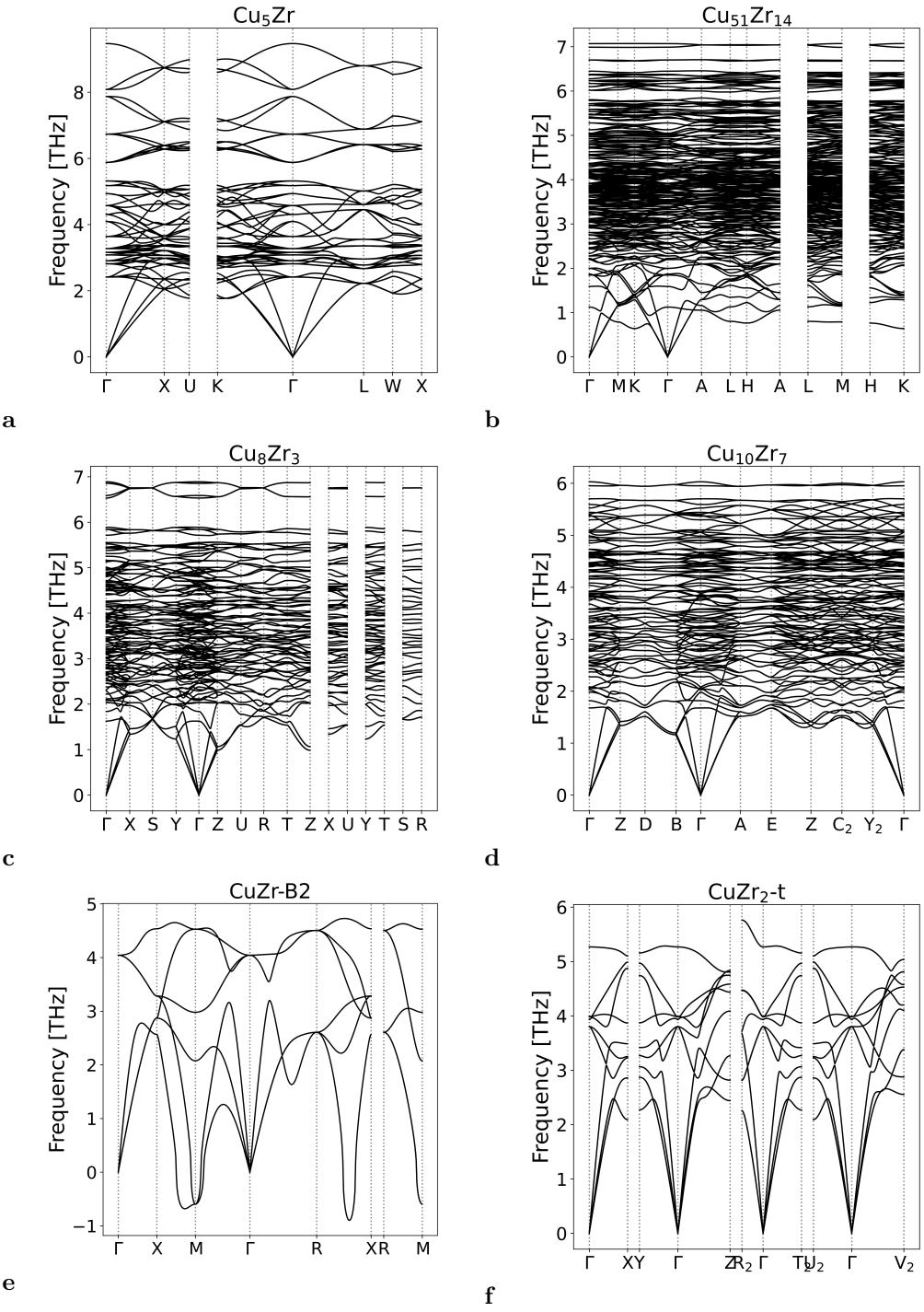

Figure 2.12: Phonon dispersion of intermetallic Cu-Zr structures using the ACEP and the `phonopy` code. All structures but CuZr-B2, which shows soft phonon modes, are predicted to be stable within harmonic approximation.

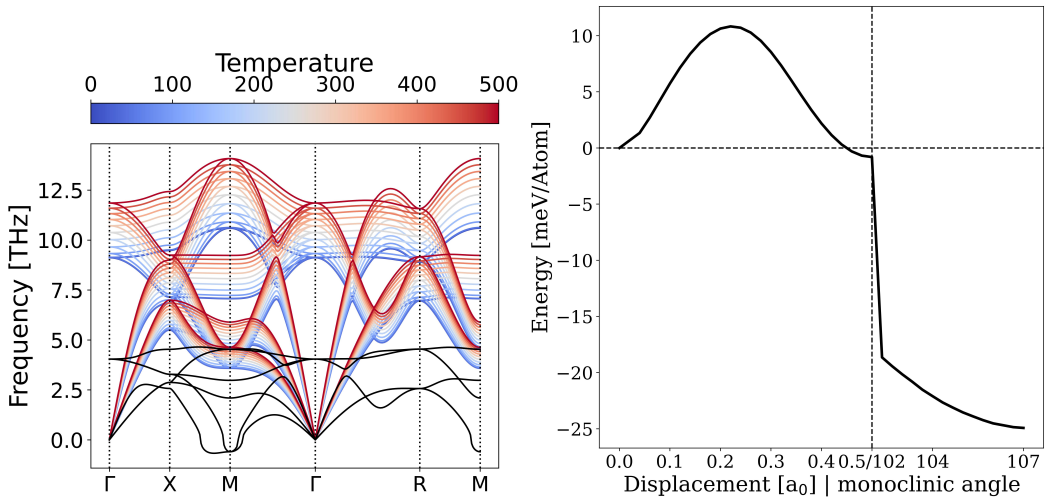

Figure 2.13: Anharmonic, finite temperature phonon dispersion of B2 CuZr calculated with the ACEP using the self-consistent phonon method implemented in ALAMODE[370,371] (**a**). Anharmonic effects up to fourth order are considered. For reference, the harmonic approximation results are shown as black line. In (**b**) the energy along the B2-B19' transformation path suggested by Hatcher et al.[372,373] for NiTi is shown. They found the path to be barrier free. Contrary to their findings for NiTi, the ACEP predicts a barrier of around $10\,\mathrm{meV/atom}$ in CuZr.

laxation. Fig. 2.13b shows the energy along this path as calculated for CuZr with the ACEP. In line with the anharmonic phonon dispersion a small energy barrier is found for the phase transition, so again no spontaneous phase change should be expected.

2.3 Structure of Cu-Zr glasses

The atomic structure of MGs is an ongoing topic of research (cf. section 1.2.3.1). In this chapter the new ACEP is employed to produce glass samples in MD via cook and quench simulations. Consequently, the structure of the samples is compared to experimental data showing excellent agreement and a detailed analysis of local motifs is carried out. Finally, the results are verified by DFT calculations.

2.3.1 Comparison to XRD data

To be able to compare simulated and experimental amorphous structures the TSF is calculated for simulated samples. Fig. 2.14 shows the TSF of ACEP (**a**) and Mendelev 2019 (**b**) samples compared to experimental data from Mattern et al.[223] The MG samples contain 256,000 atoms and were produced by quenching a melt with a rate of $1 \times 10^{11}\,\mathrm{K/s}$. To calculate the TSF the radial distribution function

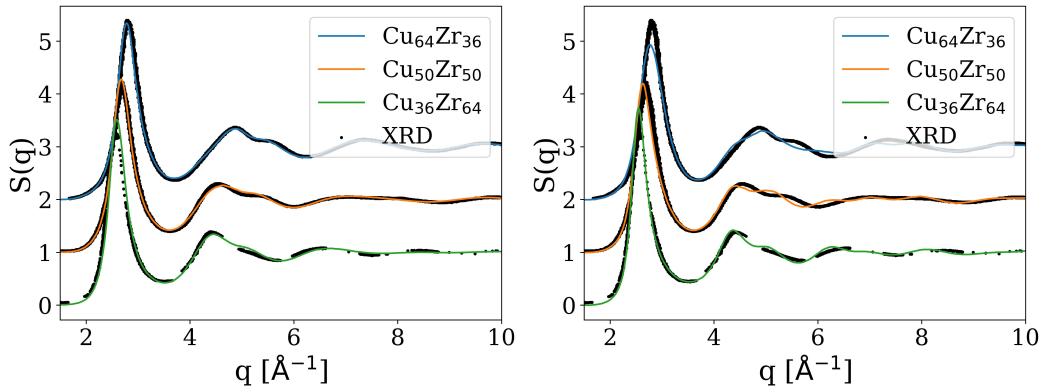

Figure 2.14: Comparison of experimental and simulated amorphous Cu-Zr structures via their TSF. In (**a**) ACEP the samples were produced using the ACEP, in (**b**) the Mendelev potential was employed. Experimental data is taken from Mattern et al.[223] and the same in both plots. The composition of experimental samples is $Cu_{65}Zr_{35}$ and $Cu_{35}Zr_{65}$ instead of $Cu_{64}Zr_{36}$ and $Cu_{36}Zr_{64}$, respectively. For improved visibility the S(q) values are shifted by +2 and +1 for $Cu_{64}Zr_{36}$ and $Cu_{50}Zr_{50}$. The Mendelev MG samples do not show an accurate splitting of the second peak. Additionally, the height of the first peak agrees better for the ACEP.

was averaged over 40 snapshots taken over 1 ns in NPT MD simulations at 300 K. As can be seen, ACEP samples agree very well with the experimental data. The Mendelev potential can excellently reproduce the TSF of the melt.[206] Despite this, it fails to describe the height of the first and splitting of the second peak in the glassy samples.

2.3.2 Topology

To investigate the atomistic details of the samples the structural motifs were classified using polydisperse Voronoi tessellation with radii set to 1.35 Å and 1.55 Å for Cu and Zr, respectively.* Fig. 2.15 shows the population of all motifs that occurred with a frequency of at least 1% in one of the compositions.

No dominant motif can be identified. This differs from other MD based studies, where Cu-centered FIs with the Voronoi index $\langle 0, 0, 12, 0\rangle$ were found to be the primary structural motif in amorphous Cu-Zr.[199,227,228,231] For instance, Ding et al.[199] investigated $Cu_{64}Zr_{36}$ glasses using the Cheng[24] and Mendelev[23] (2009) potentials. For these potentials they respectively found up to 25.6 % and 22.4 %† of all atoms

*This is similar to other works, but exact employed radii are seldomly given. The sensitivity to this parameter was analyzed and no effects influencing the conclusions drawn in this chapter were found. This is shown in the appendix Fig. A.2.

†Ding et al. reported 40 % and 35 % of all Cu atoms to be in the center of FI. To compare the numbers with those of Mattern et al. they are given as fraction of all atoms here. They are calculated

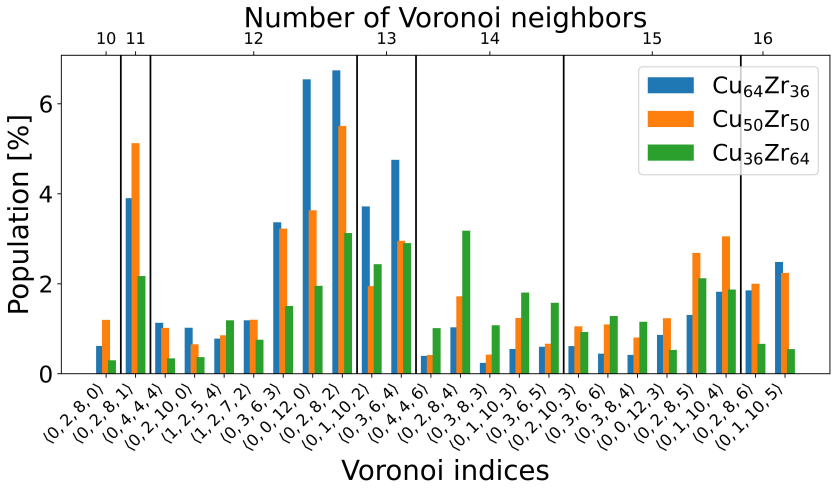

Figure 2.15: Population of Voronoi polyhedra in the ACEP Cu-Zr samples also employed for the TSF calculation.

being in the center of a FI.

Voronoi polyhedra can not be quantified directly in experiments. However, by combination multiple diffraction measurements and RMC simulations Mattern et al.[223] found a FIs population 6.3%, 4.5% and 3.5% for $Cu_{65}Zr_{35}$, $Cu_{50}Zr_{50}$ and $Cu_{35}Zr_{65}$, respectively. Furthermore, they report a plethora of different structural motifs. This matches well with the population within the ACEP samples.

Previous simulation studies found a drastic increase of FI population with decreasing quench rates.[199,206] To exclude the quench rate as a decisive factor samples quenched with 1×10^{14} K/s to 1×10^{11} K/s were produced and analyzed. The result is shown in Fig. 2.16. A dependence on the quench rate is observed, but it is already rather small for the applied quench rate of 1e11K/s. Overall far less FI than for example in[206,228] are found across all quench rates. In combination with the excellent agreement of ACEP and experimental TSF no major changes are expected to occur at lower quench rates.

As shown in section 2.2.3, the structural differences do not lead to qualitatively different behavior of the MGs. However, before continuing with the mechanical properties, we show that the ACEP can also reproduce the energetics of the MGs, and that less FI are consistent with DFT results.

2.3.3 Energetics

Finally, the formation energy of different glass samples produced using the ACE and Mendelev potentials were evaluated. Three samples with 256 atoms each were

as $P_{\text{all}} = P_{\text{Cu}} \cdot c_{\text{Cu}}$, where P denotes the population of FI clusters as fraction of all and only Cu atoms and c the concentration. This expression is valid under the assumption that the fraction of Zr atoms in the center of FI is negligible.

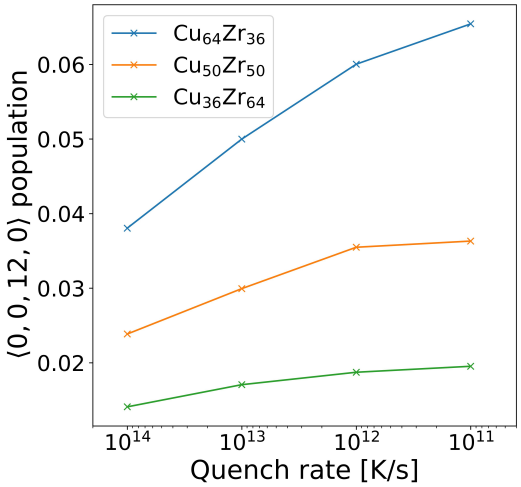

Figure 2.16: Frequency of the FI motif in MG samples for different quench rates. Their amount only increases very slightly between 1×10^{12} K/s to 1×10^{11} K/s already.

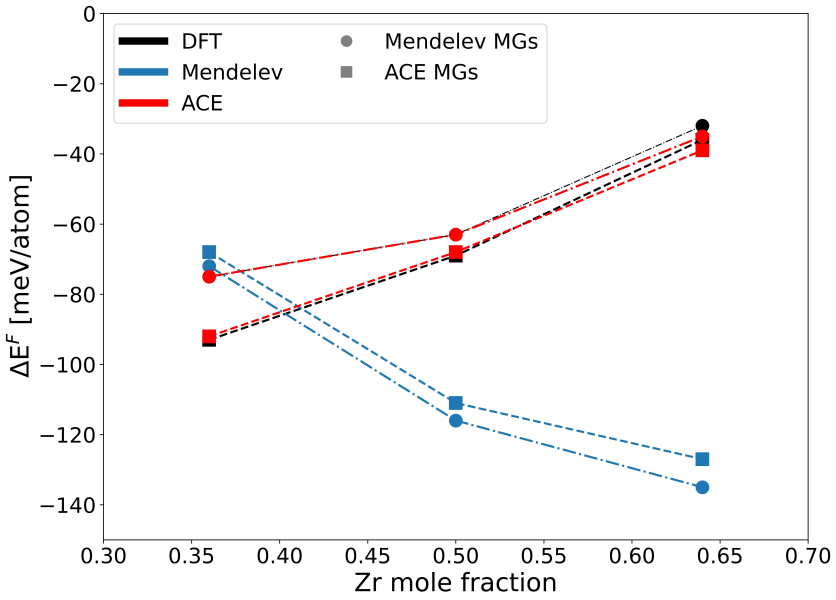

Figure 2.17: Formation energy of MG samples with 256 atoms calculated with DFT, ACE and Mendelev potentials. Cu_{FCC} and Zr_{HCP} were used as reference states. Samples were produced using the ACE and Mendelev potentials, respectively. The ACEP accurately reproduces the values predicted by DFT and correctly estimates Zr rich structures to be less stable than Cu rich ones.

produced for each composition and potential by quenching a melt with 1×10^{10} K/s. Their formation energies were calculated using the IPs and DFT, after relaxing volume and atomic positions with the respective method. Fig. 2.17 depicts the results. Here, the formation energy is averaged over the three samples. The ACEP and DFT formation energies agree well. According to them, the ACEP structures with a lower amount of FI are favorable. The Mendelev potential favors its own glasses, showing that the different structures are not a result of different kinetics. Furthermore, ACEP and DFT predict Cu rich glasses to be energetically favorable compared to Zr rich glasses, while the opposite trend is observed for the Mendelev potential.

The DFT relaxations also pointed towards and overestimation of FI population in empirical potentials. A Voronoi tessellation of the Mendelev samples before and after relaxation revealed that out of the 768 atoms for each composition the number of FI coordinated ones reduced from 112 to 108, 41 to 34 and 17 to 14 for $Cu_{64}Zr_{36}$, $Cu_{50}Zr_{50}$ and $Cu_{36}Zr_{64}$, respectively.

2.4 Tensile testing

This section presents tensile test simulations on pristine Cu-Zr glasses and a glass-crystal composite structure. The former is of interest because the impact of the different short-range order (SRO), and especially the lack of FIs is unclear. The latter is a showcase for the capability of the potential to accurately describe complex scenarios and helps to understand the occurrence of the martensitic phase transition within B2 CuZr inclusions.

2.4.1 Glasses

According to several studies employing classical potentials the FI motif leads to an increased shear localization and significantly influences the mechanical behavior of Cu-Zr MGs.[228,229,231,375] Ding et al. even found a massively increased shear modulus upon reaching the percolation threshold for FIs.[199]

Considering the much lower number of FI found for the ACEP, the question arises whether a qualitatively similar behavior should still be expected under mechanical load. To test this $Cu_{36}Zr_{64}$, $Cu_{50}Zr_{50}$ and $Cu_{64}Zr_{36}$ samples were subjected to tensile tests at 50 and 300 K. A strain rate of 4×10^7 1/s and periodic boundary conditions in all dimension were applied. The samples were generated by a $6 \times 2 \times 6$ replication of smaller cubic samples, which contain 10976 atoms and were quenched with 5×10^{10} K/s. The artificial periodicity introduced by this procedure was reduced by annealing at 450 K for 0.5 ns.

At 50 K the localization of strain within SBs can be observed for all compositions. At 300 K STZs are activated across the complete samples, leading to a homogeneous deformation mode. Despite the different employed potentials these results are similar to previous works,[374] i.e. no qualitatively different deformation mode is observed.

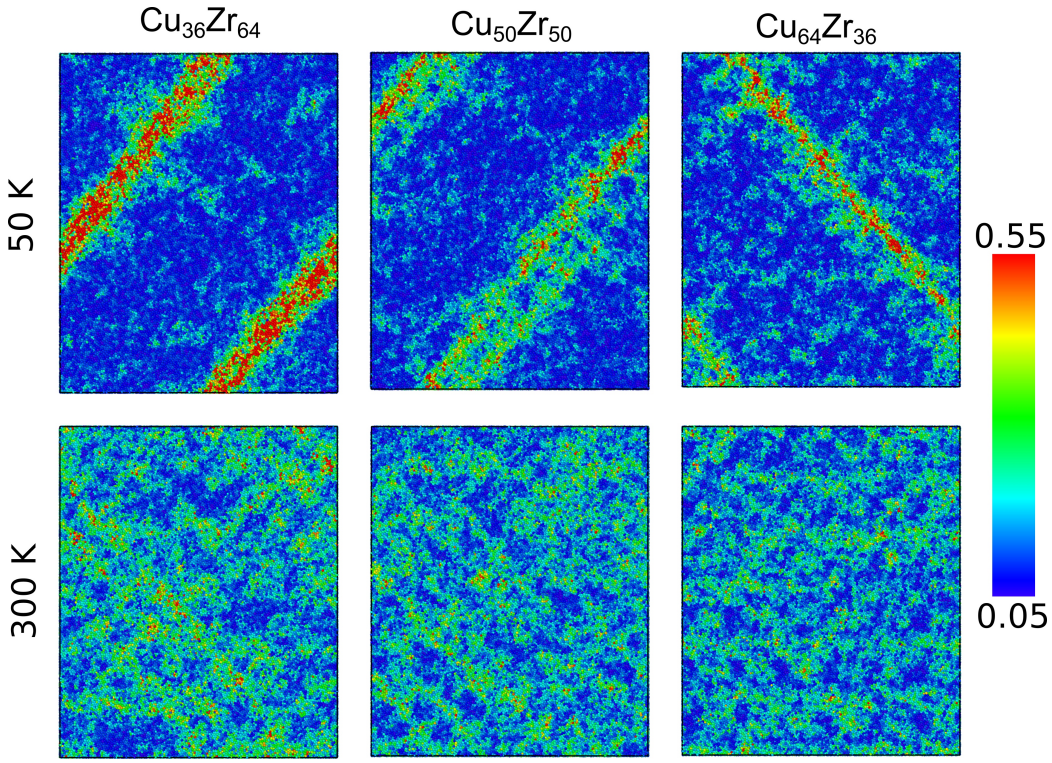

Figure 2.18: Atomic shear strain in $Cu_{36}Zr_{64}$, $Cu_{50}Zr_{50}$ and $Cu_{64}Zr_{36}$ samples under tensile load at 12 % strain. The tests were conducted at 50 K and 300 K with a strain 4×10^7 1/s. In the cryogenic temperature regime, strain is strongly localized within SBs. At room temperature multiple STZs are activated, leading to a more homogeneous deformation mode. These results are in line with observations made for classical IPs.[374]

2.4.2 Glass-Crystal composite

Finally, the deformation behavior of a glassy matrix with a crystalline B2 inclusion was investigated to better understand the occurrence of the martensitic phase transition on the atomic level. To generate the glass matrix the previously employed $Cu_{50}Zr_{50}$ sample was replicated again by $1 \times 2 \times 1$. The final sample has size of $34.5 \times 23 \times 34.5$ nm. A spherical B2 CuZr inclusion with 14 nm diameter was placed in the center of the cell. Then the sample was annealed at 450 K for 0.5 ns to equilibrate the glass-crystal interface. Then the sample was strained with a rate of 4×10^7 1/s at 50 K.

The structural evolution during the simulation was evaluated using the SOAP descriptor,[88] as implemented in the `dscribe` code.[376] The similarity to the reference configurations is defined as

$$\left(\frac{\boldsymbol{S}_1 \cdot \boldsymbol{S}_2}{\sqrt{|\boldsymbol{S}_1| \cdot |\boldsymbol{S}_2|}} \right)^4, \tag{2.5}$$

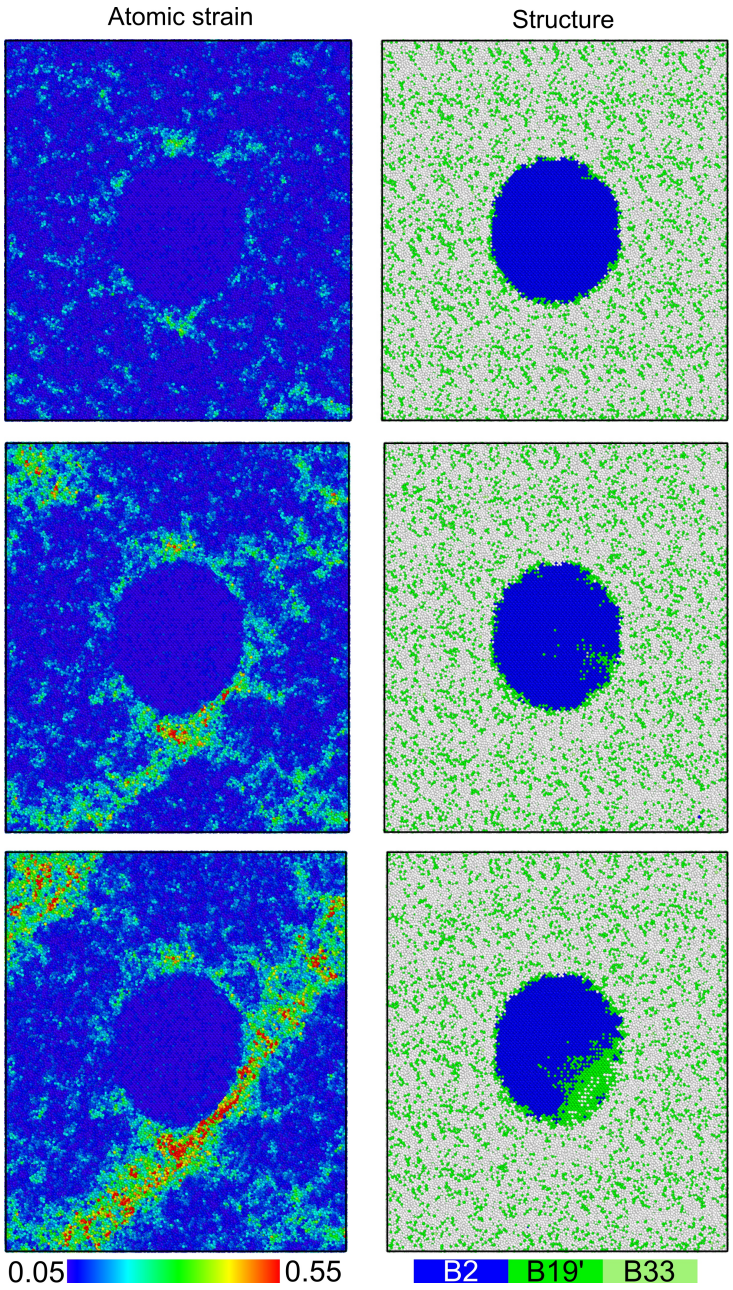

Figure 2.19: Formation of a SB in a $Cu_{50}Zr_{50}$ glass matrix with a crystalline B2 CuZr inclusion under tensile load. The inclusion has a spherical shape and [1,0,0] points along the strain direction. The strain localizes at the interface until a shear band is formed. Once this happens, the martensitic phase transition from the B2 to the B19' structure can be observed in the crystalline phase. It takes place within a band of similar width as the SB.

where $\boldsymbol{S}_1$ and $\boldsymbol{S}_2$ are the soap vectors of the two structures to compare (cf. section 1.1.2.2).

Fig. 2.19 shows snapshots of the atomic shear strain and structure analysis at different stages of the simulation. Initially, the interface serves as nucleation site for STZs and strain concentrates at the top and bottom of the inclusion. Starting from these strain concentrations, a SB begins to form within the MG matrix. It occurs at a 45° angle, corresponding to the direction with the highest Schmid factor. Lastly, a mature SB crossing the whole sample forms. Along its path, the crystalline inclusion undergoes a martensitic phase transition to the B19' phase to accommodate the strain.

2.5 Conclusion

A new ACEP for the Cu-Zr system was developed. It is fitted to PBE-DFT training data spanning the whole compositional range and a variety pristine and defective, crystalline and amorphous structures. Energies and forces of the training data and a separate testing set are reproduced with a high accuracy. Furthermore, the MLIP is validated by comparing to several properties of Cu, Zr and B2-CuZr. Here, the error for Cu rich structures is lower than for Zr rich structures and potentials fitted to limited subset of the data can describe the corresponding subsets with a higher accuracy.

The formation energy of intermetallic phases are described with a drastically improved accuracy compared to classical IPs, even for structures not included in the training data. Using Gibbs energies calculated with `calphy`, the concentration-temperature phase diagram of the potential is constructed. Melting points are underestimated due to the usage of PBE-DFT training data, but otherwise it matches well with experimentally determined phase diagrams. It is shown that errors in the range of few meV/atom can significantly influence the thermodynamic stability range of phases.

The TSF of MG samples produced with the ACEP via cook and quench simulation excellently agrees with XRD measurements. A subsequent Voronoi tessellation revealed that the SRO in the samples differs considerably from the SRO obtained with commonly employed EAM potentials. The FI unit is much rarer and a plethora of different motifs is found instead. These findings are in line with RMC models. Furthermore, ACEP glasses are more stable than samples produced using the Mendelev potential according to DFT.

Despite these structural differences, a similar qualitative behavior is observed in tensile tests. SBs form at low temperatures and homogeneous deformation takes place at room temperature. The simulation of a $Cu_{50}Zr_{50}$ glass matrix with a spherical B2-CuZr inclusion under tensile load showed that a martensitic phase transformation to the B19' phase takes place along the SB path, accommodating the strain.

3 Structure and properties of silicon oxycarbides

The results presented in this chapter are published in:

Niklas Leimeroth, Jochen Rohrer, and Karsten Albe. "Structure–Property Relations of Silicon Oxycarbides Studied Using a Machine Learning Interatomic Potential." In: *Journal of the American Ceramic Society* 107.10 (2024), pp. 6896–6910. ISSN: 1551-2916. DOI: 10.1111/jace.19932

Some sections closely follow the structure and formulations of the preprint and the corresponding supplemental material. The training dataset and fitted potential are publicly available on `zenodo`.[378]

3.1 ACE potential

Si-O-Cs have a highly complex structure with strong angular dependencies and no stable crystalline phase. The only classical IPs which have seen some success in describing the material are complex ReaxFF. However, they come at similar computational cost as fast MLIPs (cf. Fig. A.3) and require specialized parametrizations to achieve high accuracies for a given problem setting. The following chapter describes the development of an ACEP for the Si-O-C system.

3.1.1 Training data

The complexity of the amorphous structure combined with the lack of crystalline phases in the system make a 'manual' generation of Si-O-C training data basically impossible. Consequently, it was generated using an iterative AL process as depicted in Fig. 3.1a. For early iterations a MTP was employed because corresponding functionality was not implemented for ACEPs. After the process converged with the MTP, i.e. no new structures were found, an ACEP was employed instead.

The initial Si-O-C structures were generated to match chemical intuition, i.e. 4-fold coordination for Si and C and 2-fold for O atoms, using a bond switching algorithm as described in.[379,380] In order to create structures covering a wider phase space, including molecules and polymer-like structures, the `PACKMOL`[381] program was employed. `PACKMOL` implements an algorithm to densely pack structural units, while keeping adjustable minimal distances between the atoms they are made of.[382] The packed structures fed into the AL cycle are based on polymer backbone (PB), bulk

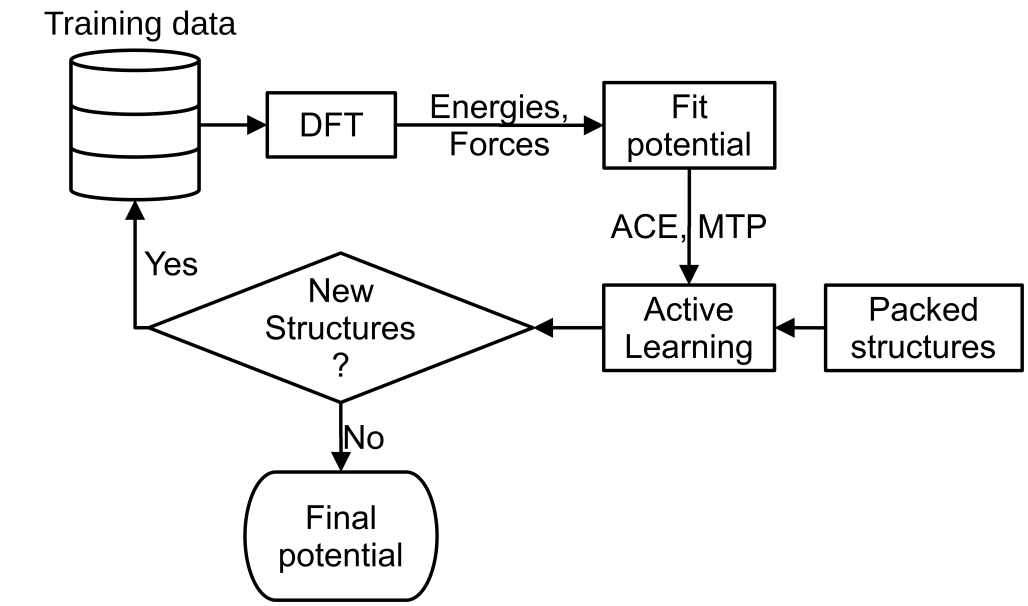

a

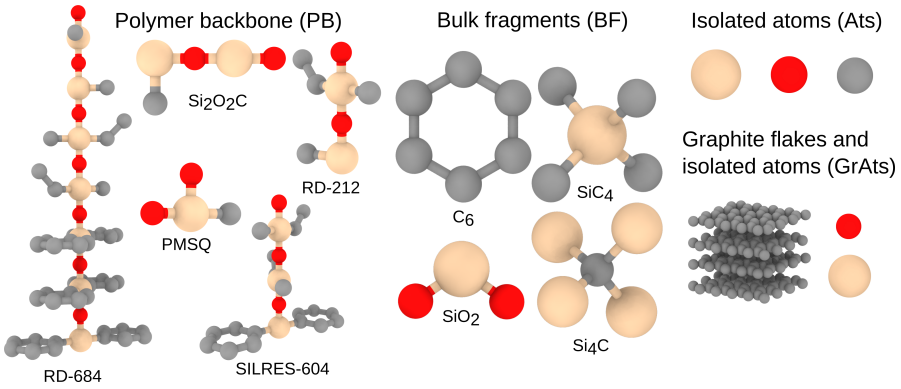

b

Figure 3.1: The Si-O-C training data was generated using the MTP and ACEP AL implementations in an iterative process (**a**). In addition to the AL process described in section 1.1.4, structures consisting of closely packed smaller building blocks created with `PACKMOL` were fed into the AL cycle to cover a wider phase space. These additional structures process were obtained packing the polymer backbone (PB), bulk fragment (BF) and isolated atom (Ats) structure fragments shown in (**b**) using the `PACKMOL` program. The graphite flakes and isolated atoms (GrAts) were used to produce large sample structures later on, but not in the AL process. polymer backbone (PB) structures are the backbones of polymers stripped of H atoms. Si is shown in beige, O in red and C in gray.

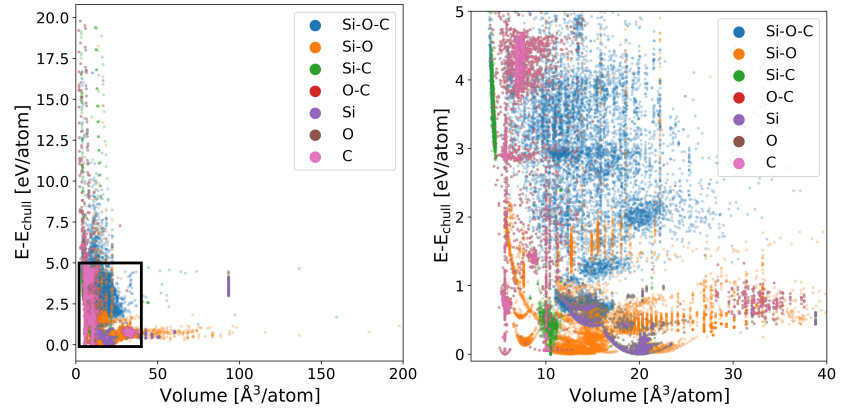

Figure 3.2: The AL generated training data covers a large range of energies and volumes (**a**). The area in the black box is magnified in (**b**).

fragment (BF) and isolated atom (Ats) units, as shown in 3.1b. graphite flakes and isolated atoms (GrAts) units, which are also shown, were used to produce large samples later on, but not directly for AL. PB structures are inspired by Polymethylsilsesquioxane (PMSQ), the polyorganosiloxanes RD-212, RD-684 and SILRES-604. Additionally, an artificial Si_2O_2C monomer was used.

The configuration space for quaternary systems is much larger than for ternary ones, so by stripping the H atoms from the PB structures a massive extension of the training data is avoided. In samples synthesized at 1273 K to 1523 K and higher the remaining amount of H is very small.[383–385] Thus, this is expected to have negligible influence on structures pyrolyzed at these and higher temperatures. Furthermore, the removal of H atoms leaves underbonded atoms with high reactivity, so it could speed up reactions at lower temperatures and lead to a quicker formation of the Si-O-C microstructure elements. However, we can not exclude that the relative speed with which they form is influenced. This could be the topic of further studies and is not investigated here. Regarding the results presented in this chapter, we expect that calculated formation energies (cf. section 3.2.2) would be lower if H was included, because some 'dangling' bonds could be saturated, but qualitative trends should not be influenced. For the calculated Young's moduli (cf. section 3.3.2), we expect no relevant influence.

For the complete training set, the Si-O-C data was supplemented with training data for the subsystems. Si, O and Si-O data was taken from a previous ACEP fit by Erhard et al.[53] C structures were generated with the `ASE` package[104] and Si-C structures were obtained from materials project.[105] The AL MD simulations were cook and quench processes with temperatures up to 3000 K and pressures up to 200 GPa. The process was considered converged, when now new structures with a maximum DFT force of less than 150 eV/Å were found.

Fig. 3.2 shows the distribution of training data in terms of atomic energy and

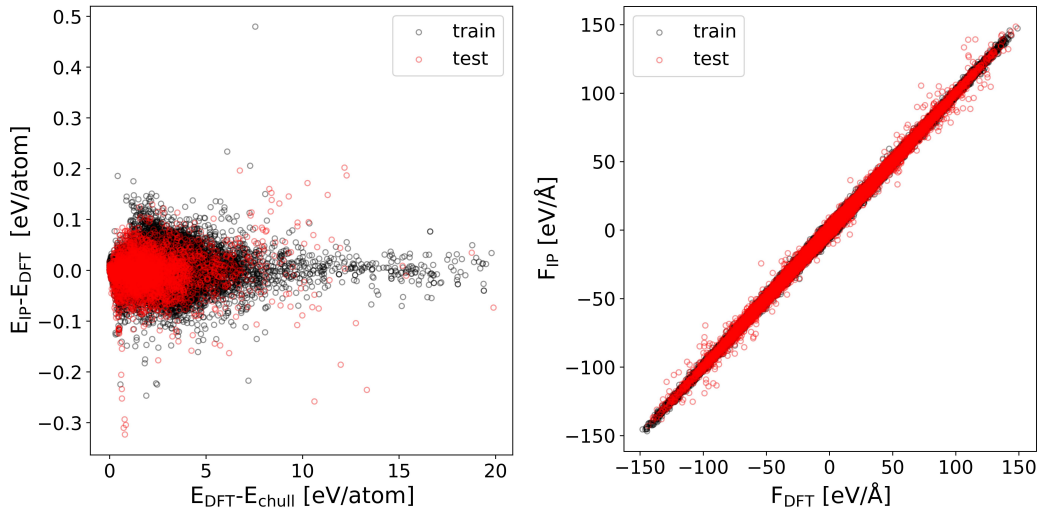

a **b**

Figure 3.3: Energy error as function of the distance to the convex hull (**a**) and correlation of ACEP and DFT forces (**b**).

volume. The Si-O-C data obtained by AL scatters widely across this 2D representation of configuration space. Pure elements and Si-C show a narrower distribution due to the reduced compositional degree of freedom and more manual data generation. An aggregate of Si-C structures with high energy and density can be observed. This data was added to prevent the occurrence of unphysically large forces when atoms came close in MD simulations.

For the testing data separately created Si-O-C structures and the testing data of the Si-O dataset[53] were combined. The Si-O-C test structures were created with varying densities and compositions using `PACKMOL`. After packing, the atoms in the structures were randomly displaced.

Training and testing datasets were filtered to fulfill the following criteria:

- No force larger than 150 eV/Å
- Minimal distances between two atoms ranging from 0.6 Å to 5 Å
- Formation energy distance from the convex hull below 20 eV/Atom

3.1.2 Fitting

A cutoff of 5 Å was employed for the MLIPs. Early AL was carried out with a level 26 MTP. Intermediate ACEPs employed in the AL process were fitted with a triple embedding

$$E_i = \chi^{0.5}_{i,1} + \chi^{1}_{i,2} + \chi^{2}_{i,3} \tag{3.1}$$

and 2325 basis functions. In most cases, the accuracy of ACEs is increased by increasing the number of basis functions. However, this considerably increases the

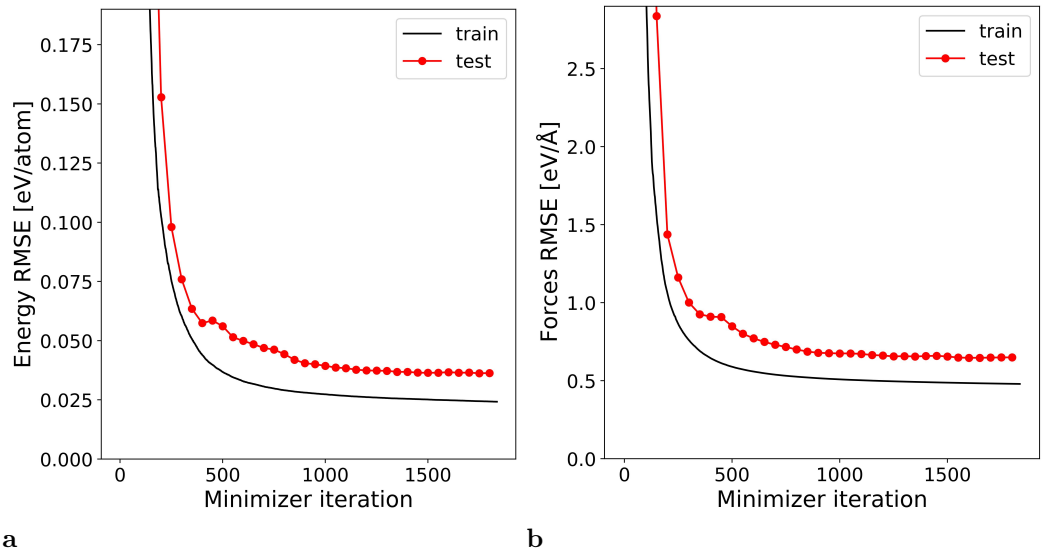

Figure 3.4: RMSEs of energies (**a**) and forces (**a**) during optimization of the potential.

computational cost.[91] Instead, different embeddings for the final potential were tested in a non-systematic manner. Here, a 10-fold embedding with exponents 0.125, 0.25, 0.375, 0.5, 0.75, 0.875, 1, 1.25, 1.5 and 2 gave the best results. The DFT single atom energies were subtracted from the fit values to improve numerical consistency in case of atomic distances close to the cutoff radius.

The final potential predicts energies and forces in good agreement with the DFT data, as shown in Fig. 3.3. Energy RMSEs of 24 and 36 meV/atom were obtained for training and testing data, respectively. The corresponding force RMSEs are 479 and 650 meV/Å. Here, higher errors for the testing set are a result of the different distribution of structures regarding compositions and energy. Fig. 3.4 shows a continuous decrease of training and testing errors, i.e. no overfitting.

3.2 Structure and energetics of amorphous Si-O-C

As discussed in the introduction, the microstructure of Si-O-C remains elusive (cf. section 1.2.4.1). In this section the generation of Si-O-C samples based on different precursors and their subsequent analysis is described.

3.2.1 Sample creation

The structure of Si-O-C glass-ceramics produced via pyrolysis depends strongly on the employed precursors and processing conditions, such as pyrolysis temperature.[281] However, experimental time and length scales are not accessible in MD simulations. To still be able to investigate a variety of microstructures a series of Si-O-C samples were produced. Here, two degrees of freedom, the precursor structure

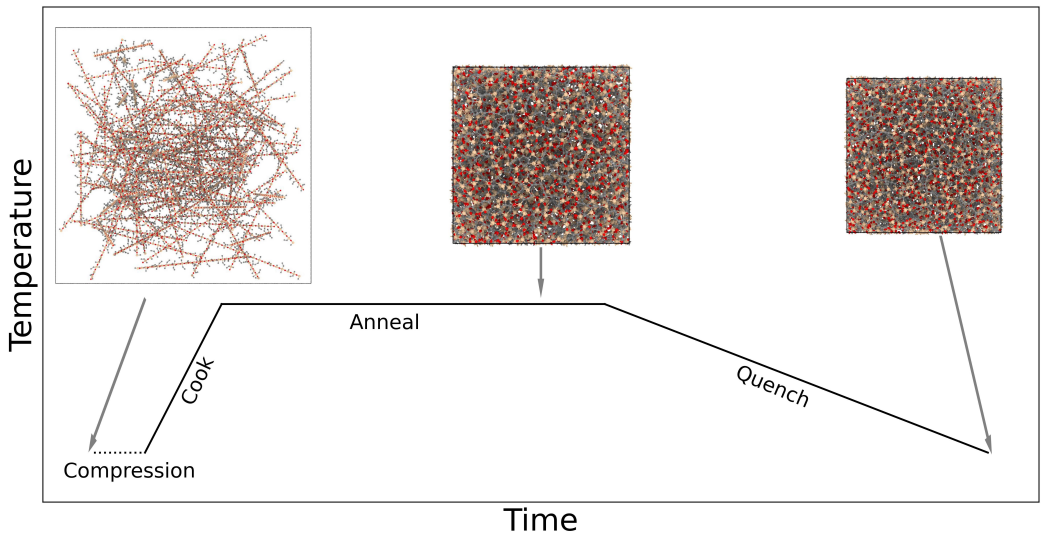

Figure 3.5: Cook and quench process used to generate Si-O-C samples. Depending on the precursor an additional compression step was necessary to obtain structures with reasonable densities.

and the composition, were varied. The compositions were chosen to match those of the five PB derived structures as given in Tab. 3.1. For each composition the four PB, BF, Ats or GrAts structural units, as shown in the previous chapter, were employed as precursors. They were packed to structures containing roughly 10,000 atoms using `PACKMOL`, resulting in a total of 20 initial structures. Consequently, these 20 structures were processed via cook and quench simulations as depicted in Fig. 3.5. Each structure was processed with an annealing temperature of 1000 K, 1500 K and 2000 K, leading to 60 samples in total. The annealing time was 1 ns and a quench rate of 1×10^{12} K/s was employed. For PB and GrAts structures an initial compression step was necessary to obtain reasonably dense structures. They were equilibrated for 10 ps at 500 K with an applied isotropic pressure of 10 GPa, before heating to the annealing temperature.

	X_{Si}	X_O	X_C
Si_2O_2C	0.4	0.4	0.2
PMSQ	0.25	0.5	0.25
RD-212	0.25	0.25	0.5
SILRES-604	0.125	0.125	0.75
RD-684	≈0.121	≈0.121	≈0.758

Table 3.1: Compositions of hydrogen stripped PB structures, sorted from low to high carbon content. Samples with these compositions were generated by packing PB, BF, Ats and GrAts units.

3.2.2 Structure analysis

To separate the influence of precursor and composition, $Si_{0.4}O_{0.4}C_{0.2}$ and $Si_{0.25}O_{0.5}C_{0.25}$ samples are analyzed individually, before the carbon rich $Si_{0.25}O_{0.25}C_{0.5}$, $Si_{0.125}O_{0.125}C_{0.75}$ and $Si_{0.121}O_{0.121}C_{0.758}$ are considered. The later are grouped, because their composition is similar in the sense that they would decompose into SiO_2, SiC and different amounts of C, while $Si_{0.4}O_{0.4}C_{0.2}$ and $Si_{0.25}O_{0.5}C_{0.25}$ should not form C and SiC, respectively.

3.2.2.1 $Si_{0.4}O_{0.4}C_{0.2}$

Fig. 3.6 shows $Si_{0.4}O_{0.4}C_{0.2}$ samples as packed and processed at 1500 K. No major differences between PB, BF and Ats structures are observable by visual inspection. Only the GrAts structures stick out because they still contain graphite agglomerates after annealing. The graphite flakes are thermodynamically unstable, because $Si_{0.4}O_{0.4}C_{0.2}$ should decompose into SiO_2 and SiC. However, they do not dissolve due to their apparently slow kinetics.

To reveal structural differences, a quantitative analysis of the Si-O-C samples was carried out. The Voronoi volume fractions all 3-fold coordinated C atoms, i.e. the free carbon phase, and the SiO_4 tetrahedra, i.e. the silica phase, were determined. Additionally, formation energies with respect to α-quartz, β-SiC and graphite were calculated. The result is shown in Fig. 3.7.

In the case of $Si_{0.4}O_{0.4}C_{0.2}$, only GrAts based structures contain free carbon in a relevant amount. Based on the expected decomposition products, there is no thermodynamic driving force for the formation of the phase. In the GrAts sample, its amount stays constant between 1000 K and 1500 K and even for 2000 K it is only reduced slightly. This shows a kinetic stabilization of the phase and suggests that it forms a deep local energetic minimum. The silica volume fraction increases with increasing temperatures, but the absolute values differ massively between samples. GrAts structures contain the highest fraction, Then BFs, Ats and PB follow. This observation can be rationalized considering the thermodynamics and kinetics of the system. In GrAts samples the carbon atoms are trapped in the graphite structure, while the previously isolated Si and O atoms can form silica. Without long-range diffusion, SiC can only form in interface regions. The BFs SiO_2, SiC_4 and Si_4C can form interconnected SiO_4 and SiC_4 clusters by small rotations and rearrangements. When starting from Ats basically all bonds that can form are local minima, favoring the formation of mixed tetrahedra and slowing down the evolution of the system. In the PB structure the situation is similar. All Si atoms are initially bonded to a C and a O atom, leading to an easy formation of mixed tetrahedra, which form local minima and thus a barrier to phase separation into SiC and SiO_2.

The formation energy does not show a strong dependence on the precursors compared to the other compositions. Especially the samples annealed at 2000 K are very similar, which is somewhat surprising, considering the high amount of (thermodynamically unfavorable) free carbon in the GrAts structure. However, the

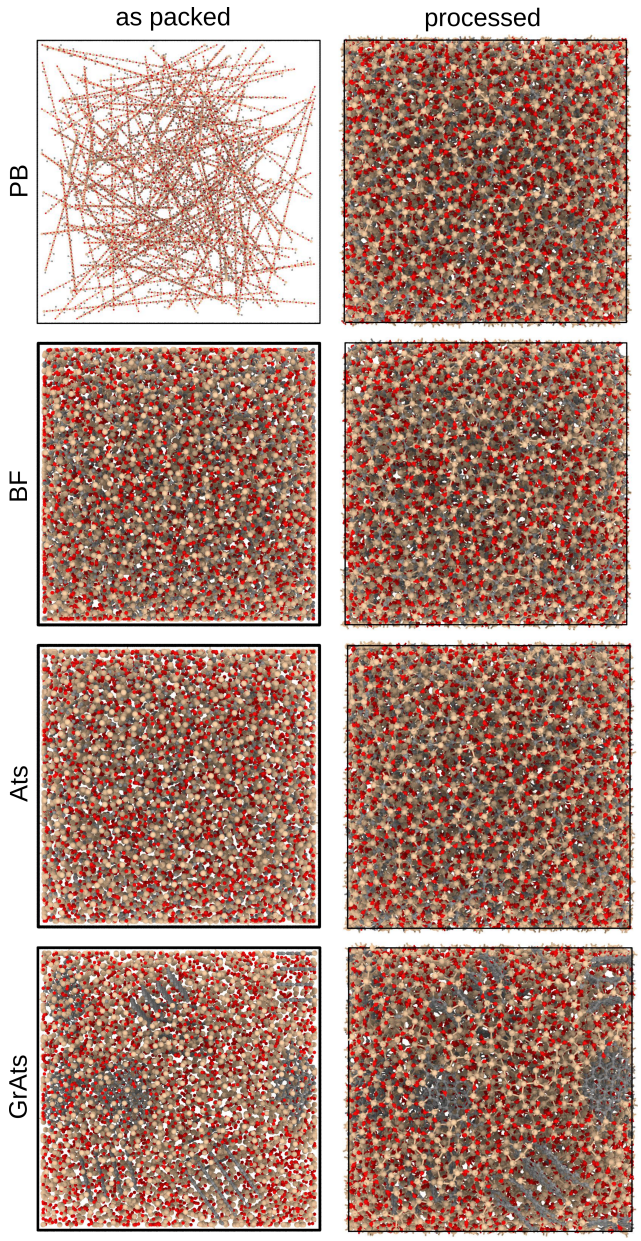

Figure 3.6: Packed $Si_{0.4}O_{0.4}C_{0.2}$ precursors (left) and corresponding structures obtained by cook and quench processing (right). Samples produced with an annealing temperature of $1500\,\mathrm{K}$ are shown. PB, BF and Ats structures look very similar. In GrAts based structures graphite like flakes are still present after processing. This shows their kinetic stabilization, as one would expect a decomposition into SiO_2 and SiC from a thermodynamic viewpoint.

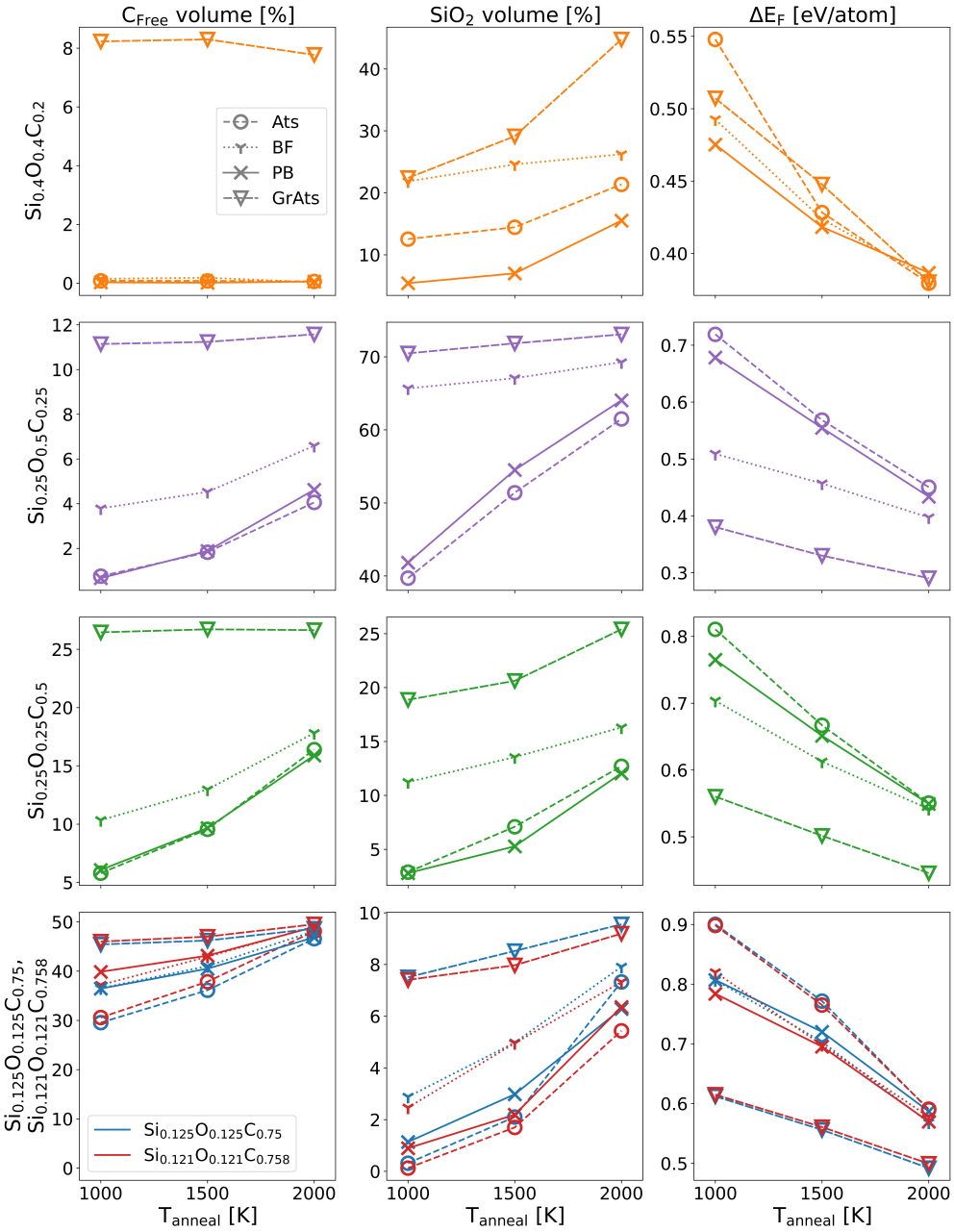

Figure 3.7: From left to right the columns show free carbon volume fraction, silica volume fraction and formation energy of Si-O-C samples. Rows correspond to compositions. The last row contains $Si_{0.125}O_{0.125}C_{0.75}$ and $Si_{0.121}O_{0.121}C_{0.758}$. Due to their compositional similarity a direct comparison of them is of interest. The symbol legend shown in the first plot is valid for the whole figure.

large amount of (thermodynamically favorable) silica apparently compensates for it.

3.2.2.2 $Si_{0.25}O_{0.5}C_{0.25}$

Due to the different Si:O ratio, $Si_{0.25}O_{0.5}C_{0.25}$ and $Si_{0.4}O_{0.4}C_{0.2}$ have different decomposition products despite the similar C content. $Si_{0.25}O_{0.5}C_{0.25}$ should form graphite and α-quartz in thermodynamic equilibrium. However, the same kinetic arguments regarding the formation of mixed tetrahedra and the barriers to phase separation as before apply. Consequently, similar trends can be observed for the silica volume fraction, while the amount of free carbon slightly increases with increasing temperatures across all precursors. As a result GrAts samples have the lowest formation energies, followed by BF structures, while PB and Ats are very similar.

3.2.2.3 $Si_{0.25}O_{0.25}C_{0.5}$, $Si_{0.125}O_{0.125}C_{0.75}$ and $Si_{0.121}O_{0.121}C_{0.758}$

$Si_{0.25}O_{0.25}C_{0.5}$, $Si_{0.125}O_{0.125}C_{0.75}$ and $Si_{0.121}O_{0.121}C_{0.758}$ have a 1:1 Si:O ratio and contain excess carbon. Consequently, their thermodynamic equilibrium would be a mixture of SiO_2, SiC and graphite. Due to their high C content, all three have a high free carbon volume fraction and low amount of silica. The observed qualitative temperature dependence of both phases and the formation are similar between the three and also $Si_{0.25}O_{0.5}C_{0.25}$.

$Si_{0.125}O_{0.125}C_{0.75}$ and $Si_{0.121}O_{0.121}C_{0.758}$ have a very similar composition, allowing to single out the influence of different PB precursors. As shown in Fig. 3.1b, $Si_{0.121}O_{0.121}C_{0.758}$ (RD684) contains closely stacked C_6 rings, while they are further apart in $Si_{0.125}O_{0.125}C_{0.75}$ (SILRES604). This could lead to the existence of a low barrier path for graphite formation. However, no significantly increased fee carbon volume fraction, which would be expected in this case, is observed.

3.2.3 Relation to model structures

Two models for the microstructure of Si-O-C exist (cf. section 1.2.4.1). In the first silica rich nanodomains and graphene like carbon layers form interpenetrating networks.[275,276] The second model suggests graphitic inclusions within a silica rich matrix.[277] Of all samples GrAts structures, corresponding to the second model, are closer to thermodynamic equilibrium whenever graphite is expected as decomposition product. However, no formation of graphitic carbon was observed in the other samples due to the slow kinetics within the system. Instead, small graphene like clusters were forming spread out across the system and started to interconnect, hinting to model one.

These observations lead to the conclusions depicted in Fig. 3.8. The models represent different stages in the formation of Si-O-C. Short pyrolysis times or low temperatures are not sufficient to overcome the kinetic barriers associated with the formation of graphitic inclusions leading to structures as suggested by model

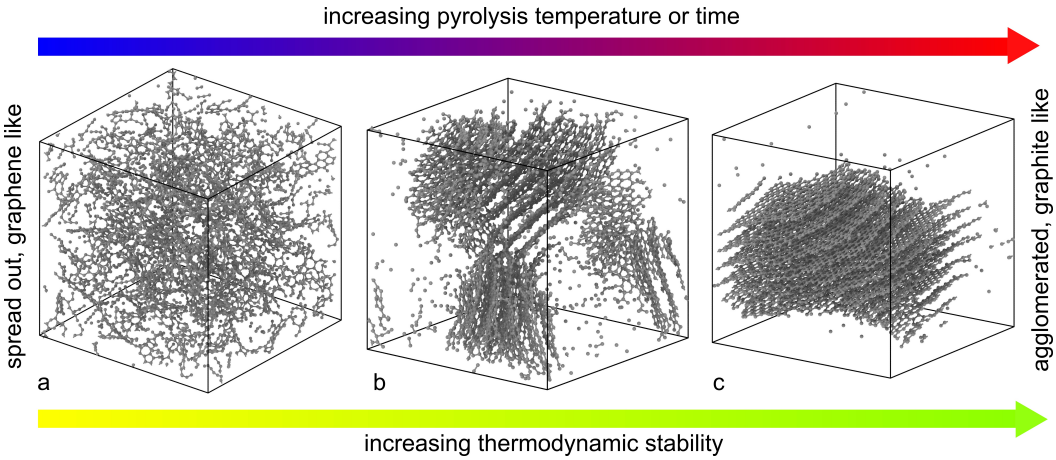

Figure 3.8: Formation of free carbon phase in Si-O-C. Low pyrolysis temperatures and short times lead to formation of graphene like carbon segregations as argued by Scarmi et al.[275] and Saha et al.[276] Higher C mobility resulting from higher temperatures allows the formation of graphite like agglomerates, which are consistent with the mass fractal dimension as found by Widgeon et al.[277] The figures show the free carbon phase in $Si_{0.25}O_{0.25}C_{0.5}$ PB samples annealed at $2000\,\mathrm{K}$ (a), $3000\,\mathrm{K}$ (b) and at $3500\,\mathrm{K}$ (c). The latter two were annealed and quenched with an isotropic pressure of $10\,\mathrm{GPa}$ to prevent the formation of pores. Following the thermodynamic driving force, the Si-O-C system evolves from spread out graphene like carbon to structures similar to the GrAts samples and finally nearly complete phase separation with a single graphite like carbon agglomerate. MD timescales, however, do not allow a direct observation of this evolution without very high temperatures.

one. Longer times and higher temperatures allow the system to evolve towards thermodynamic equilibrium by forming large graphitic agglomerates, corresponding to model two.

3.3 Elastic properties

The investigation of structure-property relations in Si-O-C glass ceramics is difficult due to the large amount of degrees of freedom within the structure. Here, the samples from the previous chapter are employed to establish relations between Young's modulus (E) and different structural features, after testing the performance of the potential in predicting elastic constants of exemplary crystalline structures.

3.3.1 Elastic tensor

Before calculating the elastic properties of Si-O-C samples, the ability of the fitted ACEP to predict elastic tensors compared to experimental data was evaluated for graphite, α-quartz and β-SiC. The results are shown in Tab. 3.2. In the case of α-quartz and β-SiC the potential and experimental data show excellent agreement.

		C_{11}	C_{12}	C_{13}	C_{14}	C_{33}	C_{44}	C_{66}
graphite	Exp.[386,387]	1060, 1109	180, 139	15, 0		36.5, 38.7	4, 5	440, 485
	ACE	1013	239	55		201	56	387
α-quartz	Exp.[388]	85-88	5-8	11-19	17-19	105-108	57-59	
	ACE	86.4	13.3	11.8	17.1	99.6	55.1	
β-SiC	Exp.[389]	360-393	142-154				149-256	
	ACE	384	136				226	

Table 3.2: This table lists independent elastic constants of graphite, α-quartz and β-SiC calculated with the ACEP and different experimentally determined values. Excellent agreement is observed for α-quartz and β-SiC. For graphite C_{11} is well reproduced, but directions depending on Van der Waals interactions between layers are strongly overestimated.

Graphite C_{11} also agrees very well with the experimental data. However, other directions, where Van der Waals interactions are relevant are overestimated. This shortcoming presumably stems from the inability of the underlying SCAN DFT to reproduce these interactions correctly. Due to the directional averaging effects and presence of other phases in larger Si-O-C samples only a small error is expected due to this difference.

3.3.2 Young's modulus of Si-O-C samples

For Si-O-C samples E was determined from the elastic tensor as

$$E = \mu(3\lambda + 2\mu)/(\lambda + \mu) \tag{3.2}$$

with the Lamè constants $\mu = C_{44}$ and $\lambda = C_{12}$. This expression is valid for isotropic materials. The isotropy of samples was verified by comparing C_{ij} which should be equivalent in symmetric materials. Differences were in the range of $\pm 3\,\%$ for all but GrAts structures, which sometimes were more anisotropic due to the orientation of graphite flakes. For them, differences up to $\pm 15\,\%$ were found. Errors were mitigated by averaging over supposedly equal C_{ij}.

Fig. 3.9 shows E as function of silica and free carbon volume fractions, as well as its dependence of average amount of C atoms in $SiO_{4-x}C_x$ tetrahedra and density. Across all samples E ranges from roughly 70 GPa to 145 GPa. The former value corresponds to that of SiO_2 glass,[391] while the latter is slightly higher than experimental values. However, the experimental data does not include compositions with similarly large amounts of C as employed here. Consequently, we assume that this relates to the lower possible amount of Si-C bonds, as discussed next. A strong correlation of E is found for the silica volume fraction and the amount of C in mixed tetrahedra. Silica glass has a low stiffness, correspondingly high fractions of silica lead to a low E. The opposite can be observed for the relation to x in $SiO_{4-x}C_x$. SiC has a very high stiffness and E increases significantly with x. As a consequence of this GrAts samples typically have a lower modulus than other samples with equal

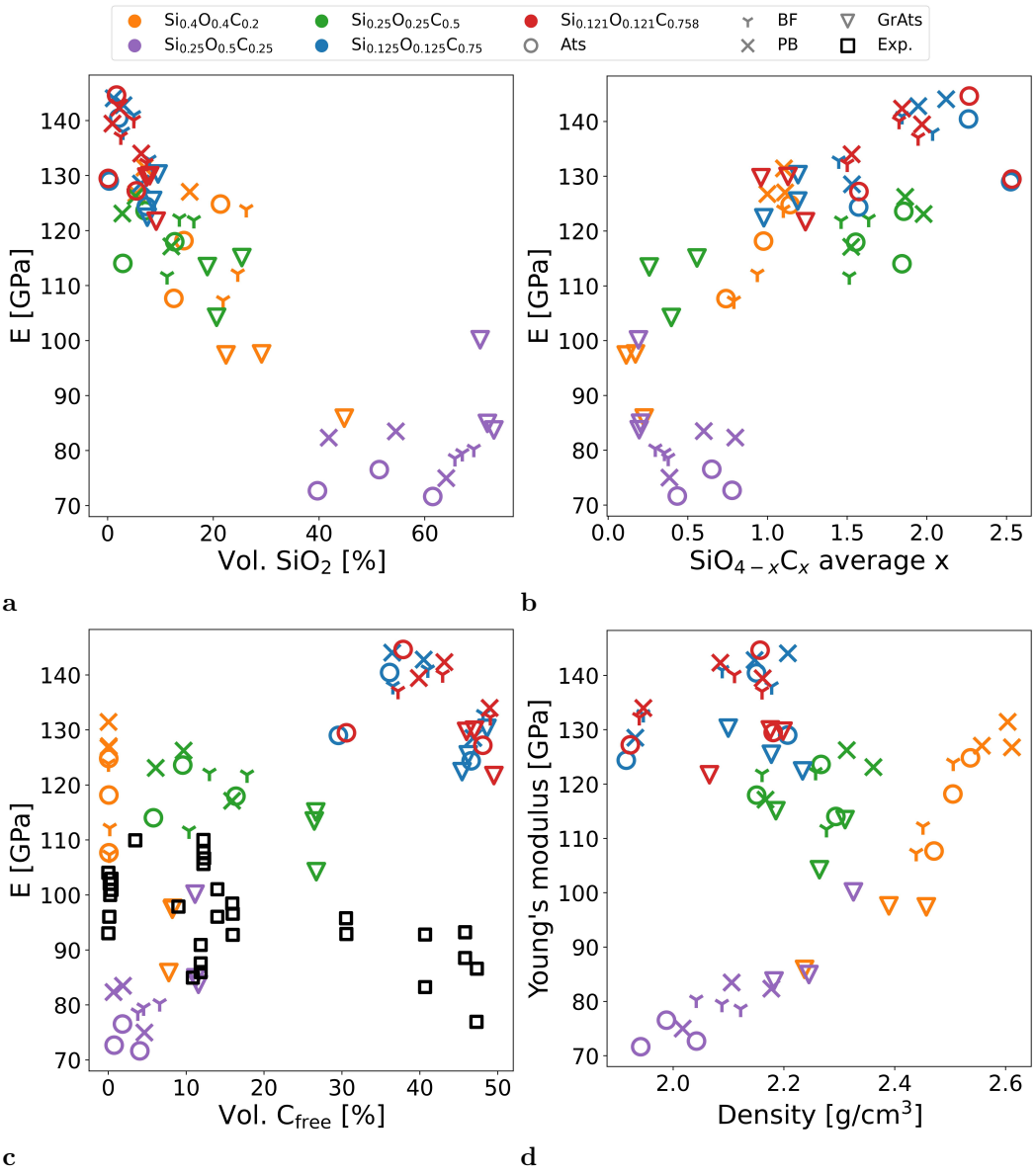

Figure 3.9: Young's moduli (E) as function of silica volume fraction (**a**), average carbon content in mixed $SiO_{4-x}C_x$ tetrahedra (**b**), free carbon volume fraction (**c**) and density (**d**) The experimental data included in (**c**) is from Refs. 133, 256, 298–301, as collected in Refs. 299 and 390.

composition, because the C atoms are trapped within graphite inclusions and not participating in SiC bonds.

Experimentally, a similar increase of the stiffness with the SiC fraction and C within mixed bonds has been observed.[298,390] These studies also found a decrease with increasing free carbon, which is not seen in the data presented here. However, Stabler et al.[299] demonstrated that the results can scatter massively based on the measurement methods and sample preparation. Furthermore, Haseen and Kroll[285] recently simulated the effect of various structural properties on E (cf. section 1.2.4.3). They observed a strong decrease of E with lower sample densities, which in turn correlates strongly with higher amounts of free carbon. Consequently, they argued that the effects are overlapping. Indeed, they found the opposite trend for samples with the same density. Overall the findings match the observation of a weak overall correlation in our data. Only when considering compositions individually the experimental downwards trend is found for all but $Si_{0.25}O_{0.5}C_{0.25}$. Here, the effect that more C atoms within the free carbon phase instead of mixed SiC tetrahedra lead to a lower stiffness can be observed again.

3.4 Conclusion

A highly diverse set of Si-O-C structures was generated employing the AL techniques implemented for MTPs and ACEP. Additional structures based on densely packed atoms or bulk fragments were fed into the process to further increase the covered configuration space. This dataset was employed to fit a highly nonlinear ACEP, which accurately predicts energies and forces of Si-O-C glass-ceramics over a wide range of compositions, temperatures and pressures. The employed nonlinear embedding term is a computationally cheap way to increase the accuracy, compared to increasing the number of basis functions.

With the potential Si-O-C samples based on different precursor configurations were synthesized in cook and quench simulations. The influence of the precursor structure and composition on the structure of the final glass-ceramic was investigated. Graphite agglomerates within the amorphous network of $SiO_{4-x}C_x$ are thermodynamically more stable than graphene like sheets when excess carbon is present in the composition. Even if not thermodynamically stable, i.e. in stoichiometric Si-O-C, the agglomerates were kinetically stabilized within MD timescales. In the case of excess carbon being present, the formation of graphite agglomerates requires significant reordering of the structure. In consequence, an interpenetrating network of silica rich domains and graphene like fragments and sheets form as an intermediate step during pyrolysis. High temperatures are required to observe the evolution towards the graphitic agglomerates on MD accessible timescales.

Finally, the Young's moduli of the samples were related to structural features of Si-O-C. We found that SiO_2 reduces the stiffness, while a high amount of C atoms in mixed $SiO_{4-x}C_x$ tetrahedra increases it. The observed correlation with the amount of free carbon phase is weak. This seems contradictory to experimental

results at the first glance, but can be explained by an overlapping effect of density and 'free' C volume, which was not accounted for in the experimental data.

4 Comparison of machine learning interatomic potentials

Previous chapters have shown the development and application of ACEPs for two complex material systems. Up to now, the ACE formalism was chosen based on published accuracy vs speed comparisons of GAPs, SNAPs, MTPs, HDNNPs and ACEPs.[51,66] The results from[51] are shown in Fig. 4.1. However, these assessments were done for single element systems. Furthermore, the field of MLIPs is rapidly evolving and recent developments such as message-passing and equivariant descriptors were not included in those tests. This chapter presents a systematic evaluation of HDNNP, MTP, ACE, NequIP, ALLEGRO and MACE IPs. They are compared in regard to their accuracy, extrapolation behavior as well as computational and data efficiency.

4.1 Fitting

4.1.1 Training data

The MLIPs were fitted to an Al-Cu-Zr dataset. It is an extended version of the Cu-Zr training data previously described and produced using the same 'manual' procedure of relaxing, then modifying glassy and crystalline structures. Crystalline

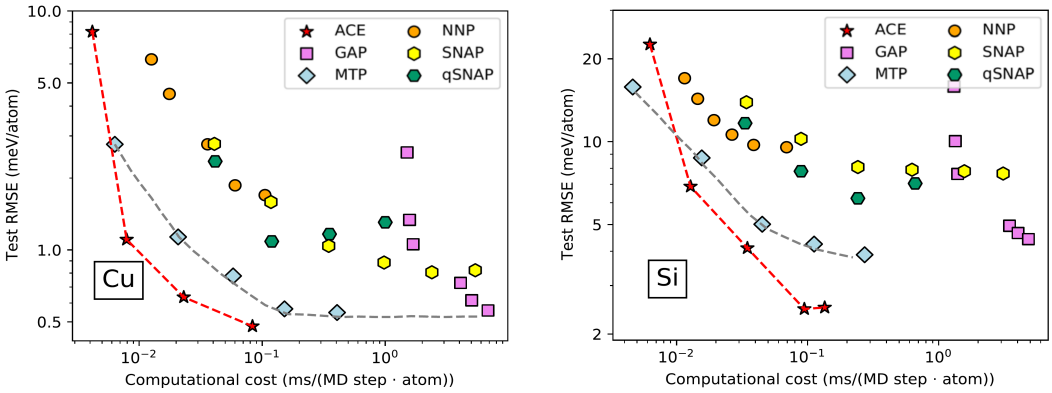

Figure 4.1: Comparison of different Cu and Si MLIPs with respect to error vs computational cost. The figure is reproduced from Ref. 51, where it is published under the Creative Commons Attribution 4.0 International License http://creativecommons.org/licenses/by/4.0/. It reuses data from Ref. 66 for the MLIPs besides ACE.

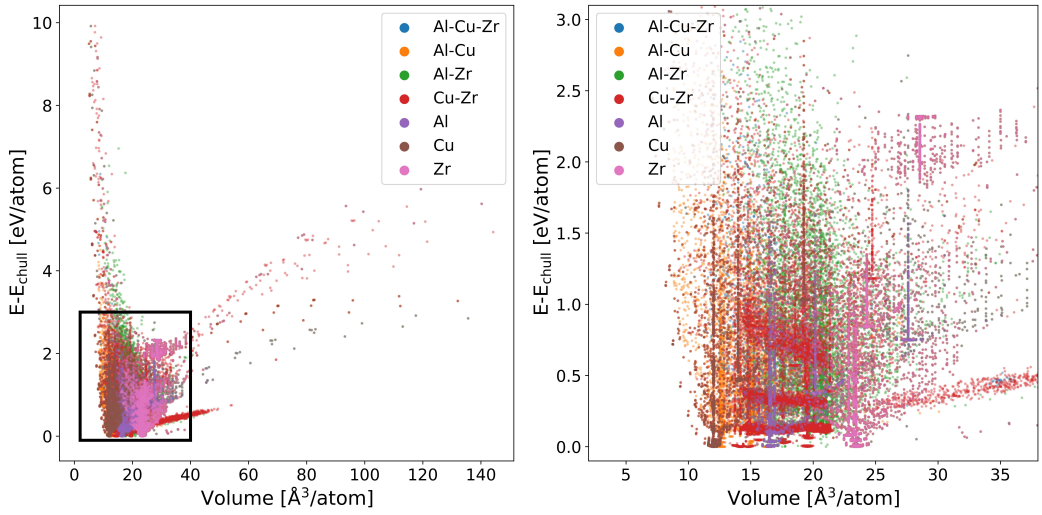

Figure 4.2: Energy-volume relation of the Al-Cu-Zr dataset employed to test MLIPs. The shown energy is the formation energy distance from the convex hull. (**b**) is a magnified version of the area indicated by the black box in (**a**)

Al-Cu, Al-Zr and Al-Cu-Zr base structures were obtained from materials project. Glasses were produced in short ab initio MD simulations. The test set was extended similarly. Both datasets were filtered using the previously described criteria for Cu-Zr. Fig. 4.2 shows the energy volume relation of the Al-Cu-Zr training data set. Compared to the Si-O-C dataset it has a narrower distribution and the amount of three element structures is rather low compared to Al-Cu, Al-Zr and Cu-Zr structures. For these subsystems many intermetallic crystalline phases exist, while only three crystalline phases containing all elements were available on Materials Project when producing the training data.

4.1.2 Splitting of training data

To probe different error measures and the data efficiency of different MLIPs (cf. section 4.2 and 4.3) the training data was split into ten parts. Data subsets containing 10 % to 100 % of structures in 10 % steps were created. The data was added in a cumulative manner, so that each subset with an increased amount of structures also contains all structures included in the previous set.

4.1.3 Parameters

The fits were done with a variety of parameters specific to the type of MLIP. Potentials like MTPs and ACEPs offer very straightforward ways to increase the accuracy, by increasing the level or amount of basis functions. Even though other settings can be changed, these are recommended and systematic, so they are modified here. On

the other hand, MLIPs like HDNNPs can be optimized by changing the descriptor functions or the architecture of the neural network. This section describes which parameters were set for each potential type employed in the following comparison.

The MTPs were fitted with levels 14, 18 and 22. Level 22 was employed for comparisons, if not otherwise noted.

ACEPs were fitted with Finnis-Sinclair like embedding of the form

$$E_i = \chi_{i,1} + \sqrt{\chi_{i,2}}, \tag{4.1}$$

also used for the Cu-Zr potential. The potentials were fitted with 200, 400, 600 and 800 basis functions per element. If not otherwise noted the version with 800 basis functions is employed in the tests.

MACE potentials were fitted with 0, 32, 64 and 128 invariant messages, where the 128 message version was employed when not otherwise noted.

In the case of HDNNPs, the descriptor functions were set to defaults recommended by Behler et al.[68,392] in the `RuNNer` fitting code. Network architectures with one and two hidden layers were tested. They contained 10, 15, 20, 5|5, 10|10 and 15|15 nodes, where n|m denotes two layers with n and m nodes in the first and second layer, respectively. The 10|10 version was found to give best testing errors and is applied if not otherwise noted.

For Allegro the parameters *env_embedded_multiplicity* (number of equivariant features used to describe the atomic envionment), *l_max* (order of spherical harmonics) and *num_layers* (layers of the neural network) were varied. Finally, they were set to 8, 2 and 1, respectively, if not noted otherwise.

NequIPs were trained with different *num_features* (multiplicity of features), and *num_layers* (message-passing layers). Data efficiency and extrapolation tests were conducted with those parameters set to 16, 2 and 2, respectively.

Finally, GAPs could not be trained with anything more than 10 % of the training data due on an HPC system with 4 TB available main memory, to their huge memory requirements. Versions with 50, 100, 500, 1000 and 2000 sparse points, i.e. environments to which structures are compared were fitted to this small database for the runtime comparison. Consequently, their accuracy is worse than that of other MLIPs, as seen in section 4.4.

4.2 Error measures

The first question that arises when comparing potentials, is which error measure to employ in the evaluation. Up to now, the RMSE of energies or forces was used. However, other error measures may give different results as discussed in the following on the example of the mean absolute error (MAE) vs RMSE.

Fig. 4.3 shows MAEs and RMSEs for series of ACEPs with 200 and 800 basis functions per element, i.e., 600 and 2400 in total. The energy training errors show a slight increase with more training data, while the force errors stay roughly equal. Such an increase points towards the accuracy limitations of the potential formalism

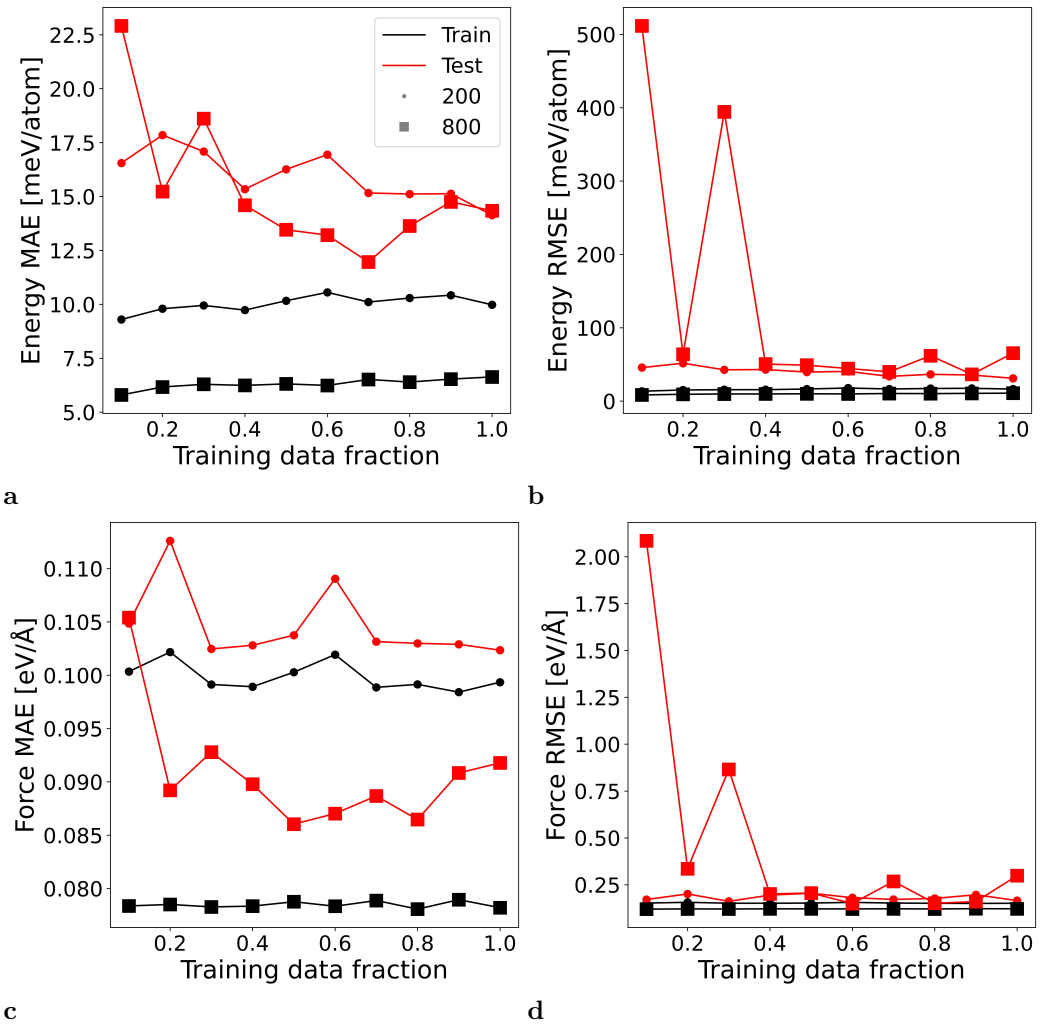

Figure 4.3: MAEs and RMSEs for ACEPs with 200 and 800 basis functions in dependence of the fraction of training data employed. The upper row shows energy, the lower row shows force errors. Training errors increase when adding data, due to the increased complexity, while testing errors go down due to a lower degree of extrapolation necessary. Due to how the RMSEs is calculated it has higher sensitivity to outliers with very high errors. Such outliers become more likely with more basis functions, because the chance that some configuration space described by the function is not covered is higher. Thus, the ACEPs with 800 basis functions have higher test RMSEs, but lower MAEs.

itself, because some configurations can not be described accurately within the same potential. The testing error decreases with more data, because a large part of configuration space is covered. Interestingly, the trends are not monotonic. Especially the testing errors for 800 basis functions oscillate rather strongly. This presumably originates in the minimization problem underlying the fitting procedure. The system of equations is massively overdetermined and has multiple local minima. Which one is found depends on the random seed employed to initialize the function coefficients. In each of these minima different structures are described with higher or lower accuracy. Due to the way the RMSE is calculated the effect of singular very high error values is higher than in the MAE leading to stronger oscillations. Single outlier structures with a high degree of extrapolation also become more likely when increasing the basis functions. This leads to the observed higher RMSEs, but lower MAEs for the potential with 800 basis functions.

Depending on the desired characteristics, the potential with 200 or with 800 basis functions may be more suitable. Correspondingly, the RMSE or the MAE may be the better error measure. If an increased reliability for potentially extrapolating structures is required, the RMSE fits better. If single outlier structures are not relevant, for example because one is interested in an average quantity over many structures, the MAE is more suitable. A plethora of other errors measure could be considered. For example, the maximum absolute error or some weighting scheme for more or less important structures could be employed. An example for such a weighting scheme is the weighting of structures based on formation energy distance from the convex hull and magnitude of forces employed for the Cu-Zr ACEP (cf. section 2.1.1). When considering such measures, however, there are infinite different ways to define it. Consequently, the choice is always somewhat arbitrary and the parametrization of an IP can not be optimal with respect to all error measures.

In the following the MAE will be employed to compare the potentials. As discussed single outlier structures have a lower weight in this measure, which also decreases the influence of factors such as the random seed, making a comparison between potentials more feasible.

4.3 Data efficiency

4.3.1 Testing errors

To compare the training data efficiency, i.e. the ability of the potential to accurately reproduce test data with a certain amount of training data, The training dataset was split into fractions as described in section 4.1.2. For each fraction the different MLIPs were fitted and their MAE for the testing data set was calculated. The results are shown in Fig. 4.4.

MACE and Allegro MLIPs have the best errors and are closely followed by NequIP, MTPs and ACEPs, while the HDNNPs errors are significantly worse. MTPs and ACEPs have very similar errors, but the MTPs seems to perform slightly better for very low amounts of training data. The HDNNPs shows the strongest

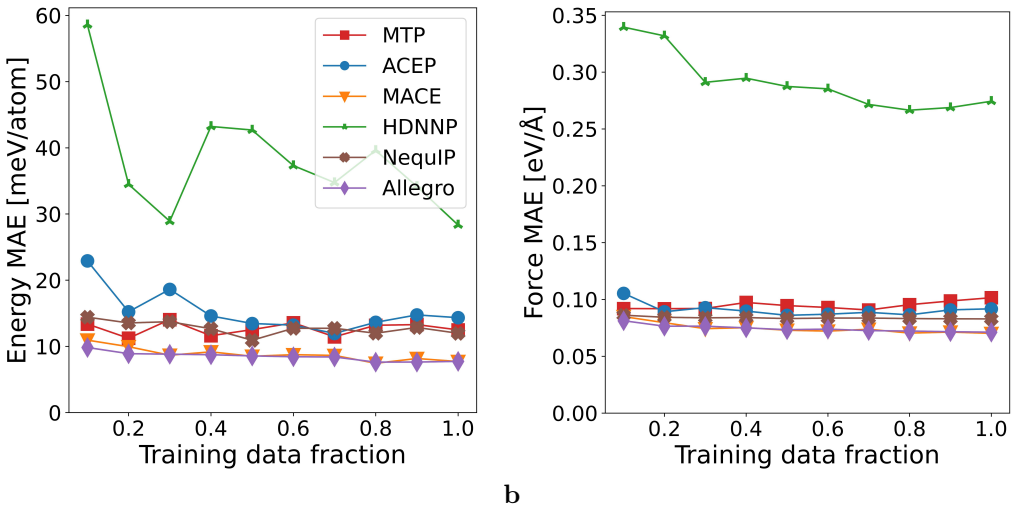

a b

Figure 4.4: Test energy (**a**) and force (**b**) MAE as function of the amount of training data used to fit potentials. The best error is found for MACE and Allegro for all amounts of data. NequIP, MTP and ACEP give very similar errors. HDNNPs show a strongly decreasing error with more data, but on an overall higher level than the other potentials, suggesting that they would benefit the most from adding even more data.

decrease in testing error, suggesting that it could benefit stronger from more data than other MLIPs. GAPs are not shown, because they could not be fitted with more than 10 % of training data (cf. section 4.1.3).

4.3.2 Relation to training errors

For comparison the training set errors are shown in Fig. 4.5. Here, MACE and Allegro still give the best results, but ACEPs are more accurate than MTPs and HDNNPs still gives the worst accuracy. However, the observed trends are different for the MLIPs. Errors of HDNNPs, MTPs and ACEPs stay approximately constant or increase. This behavior was already seen and discussed in section 4.2. It can be explained by the increased complexity within the training data, that cannot be reproduced fully by the MLIPs, so that some structures are described worse and the average error increases. The MACE, NequIP and Allegro training error, however, decreases with more data, showing that the formalisms are able to describe the increasing complexity of the full dataset. Consequently, we assume that the minimization process employed in their fitting codes benefit from the increased amount of data, allowing to find a deeper minimum of the loss function, i.e. a better result for all data points. Another point to note is the large difference between testing and training energy errors observed for the HDNNPs, especially for small amounts of data. This difference is much larger than for the other potentials and less pronounced in the case of force, hinting towards bad extrapolation capabilities.

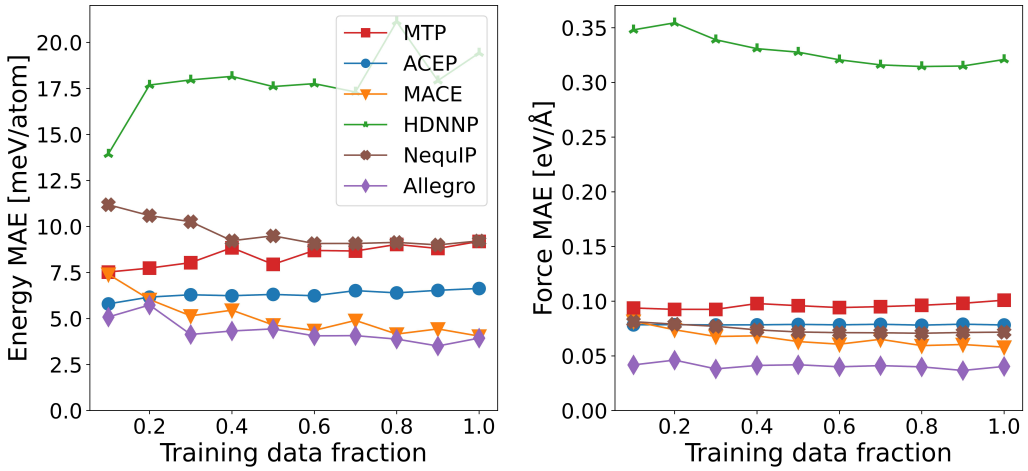

a b

Figure 4.5: Training energy (**a**) and force (**b**) MAE as function of the amount of training data used to fit potentials.

4.4 Accuracy versus computational cost

This section treats the accuracy of the MLIPs in comparison to their computation cost similarly to the analysis shown in Fig. 4.1. From the perspective of a user, i.e. someone who neither develops fitting codes nor the fits the potentials, but just wants to apply them in MD simulations, this is probably the most relevant property. Here, their performance on CPUs, which are still dominant in most supercomputers, and on GPUs, which become increasingly common, is evaluated. The latter is currently only available for ACEP, NequIP, ALLEGRO and MACE. For all potentials the runtime is evaluated using `LAMMPS`,[316] with the `KOKKOS` package for GPU acceleration. The employed hardware is a single core of an AMD Ryzen 5800X processor and an NVIDIA RTX 3060 GPU. For the test runs an FCC lattice with Al equilibrium lattice constant was randomly populated with equal amounts of Al, Cu and Zr and simulated at 300 K for 100-1000 MD steps, depending on the speed of the potential. When possible, the structure was replicated to contain 13500 atoms, however, memory intensive MLIPs required to reduce the system size to as few as 500 atoms.

4.4.1 Performance on CPUs

The accuracy and speed of the MLIPs using a CPU is shown in Fig. 4.6. MACE and Allegro offer a very high accuracy at the cost of slow evaluation times, with Allegro being slightly slower. The ACEPs are the fastest, while also achieving good accuracies comparable to those of MTPs at roughly one order of magnitude faster evaluation. As already seen in previous sections, the accuracy of the tested HDNNPs is slightly worse than that of other MLIPs. Regarding computational

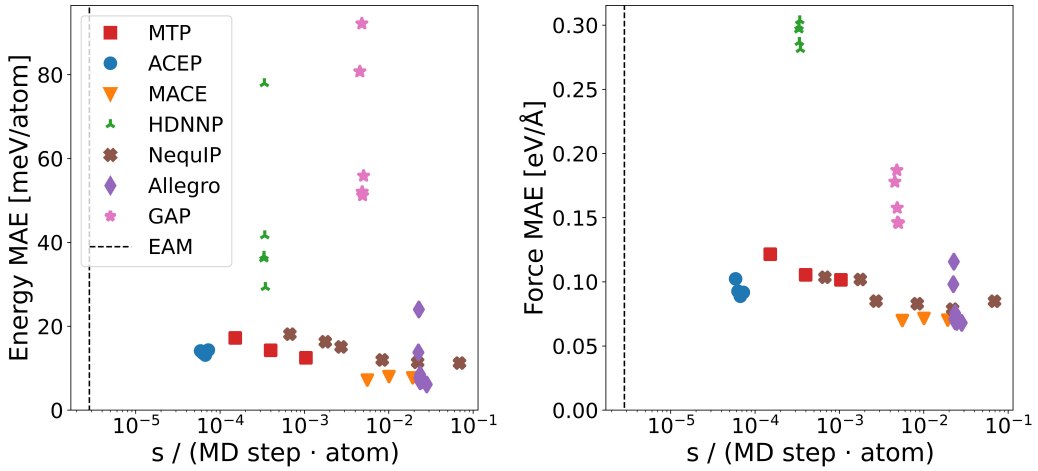

Figure 4.6: Accuracy versus speed on CPUs for different MLIPs. Further to the left means faster calculations and further down means higher accuracy. Energy (**a**) and force errors (**b**) are shown. For comparison, the dashed line shows the computational cost of an EAM potential.[206]

cost, they are comparable to MTPs. GAP evaluation times are comparable to MACE, but offer a far lower accuracy. This low accuracy, however, is probably caused by the small amount of training data that could be included in the fitting process (cf. section 4.1.3), as other studies found them on par with MTPs and ACEPs in this regard.[51,66] The accuracy and speed of NequIPs span a rather large range. Those with accuracies comparable to MTPs and ACEPs, are as expansive as MACE MLIPs.

4.4.2 Performance on GPUs

Fig. 4.7 shows the same speed comparison as before, but only for those MLIPs with an available GPU acceleration. ACEP, MACE and Allegro are implemented in `KOKKOS`, while NequIP was only accelerated by using a GPU version of `PyTorch`,[393] which is not as efficient. MACE, for example, is sped up by a factor of 12.2 with `KOKKOS`, but only a factor of 4.2 when using it with GPU enabled `PyTorch`.

On GPUs a similar relative ranking of the MLIPs is found as on CPUs, but the potentials are roughly one order of magnitude faster. The equivariant and message-passing MLIPs gain a little more and ACE a little less. Importantly, the GPU acceleration allows running ACEPs at speeds approaching that of non accelerated classical potentials, making them feasible for similar long simulations.

It should be noted that the equivariant and message-passing MLIP tests required to use smaller test structures with as few as 500 atoms to prevent memory issues. This shows that such MLIPs have significantly reduced achievable system sizes on a given computing architecture.

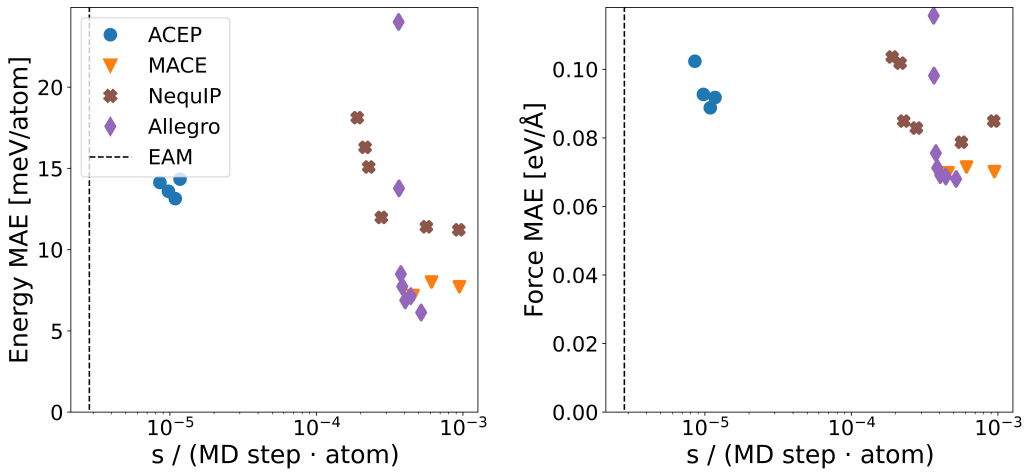

Figure 4.7: Energy (**a**) and force errors (**b**) versus speed on GPUs for different MLIPs. Compared to the CPU versions MACE is more than an order of magnitude faster. ACEPs gain a little less than an order of magnitude. The GPU accelerated version of ACEP is only around one order of magnitude slower than the non accelerated EAM, showing that fast MLIPs can be employed in similar simulations as classical IPs. The MACE fit without messages is not shown, because GPU acceleration currently works only for non-zero messages.

4.4.3 Extrapolation behavior

Finally, the extrapolation behavior of the MLIPs was tested using Al-Cu and Al-Zr C14, C15 and C36 Laves phases. An extrapolation test using Cu-Zr Laves phases was already done for the Cu-Zr potential in section 2.2.1, after which those structures were included as part of the training data. The C14 Al_2Zr phase is excluded from the extrapolation test, because it is a part of the crystalline training data coming from materials project under id mp-2772. So in total 11 intermetallic crystalline phases are used. Fig. 4.8 shows the energy MAE for the MLIPs in dependence of the amount of training data used. Additionally, the error of a potential fitted including the Laves phases is shown as dashed line.

ACEPs and Allegro extrapolate very well. NequIPs, MTPs and MACE have a slightly higher error. The HDNNPs performs significantly worse than the other MLIPs, again showing their need for large amounts of training data in the configuration space domain that is of interest.

4.5 Conclusion

Different types of MLIPs, namely HDNNP, GAP, MTP, ACEP, NequIP, Allegro and MACE were compared. HDNNPs were found to have lower accuracies than other potentials, while requiring lots of training data and not extrapolating well.

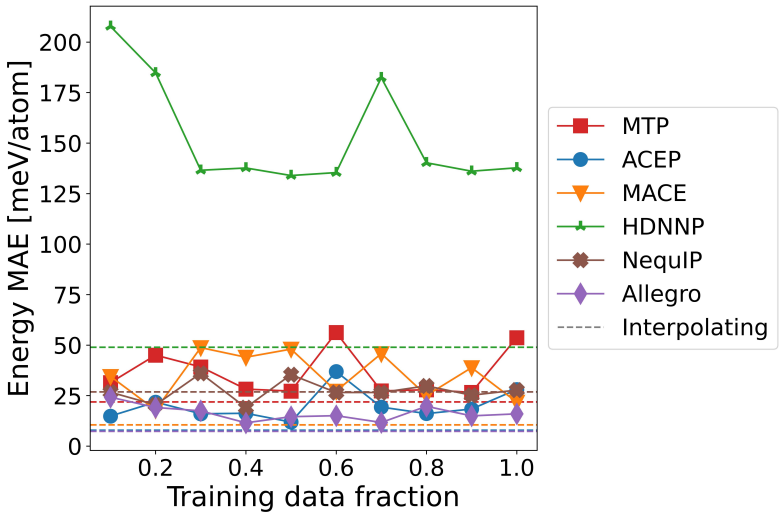

Figure 4.8: Energy MAE for extrapolating Al-Cu and Al-Zr Laves structures. The dashed lines indicate the error for potentials where the structures were included in the training set. ACEPs and Allegro show the lowest error, followed by NequIPs, MTPs and MACE potentials, which have comparable accuracy. HDNNPs have considerably higher errors than the other potentials.

However, they are rather fast to evaluate with speeds comparable to MTPs. Here, only second generation HDNNPs, i.e. without electrostatic interactions, were employed. For the treated Al-Cu-Zr system with mostly metallic bonding this should not lead to large differences. For ionic systems or molecules, however, third and fourth generation HDNNPs could offer advantages over other MLIPs.

GAPs were found to have similar speeds as MACE, i.e. much slower than the non message-passing MLIPs. Furthermore, due to their extremely high memory requirements in the training process, they could only be fitted to a tenth of the data employed for other MLIPs. Their accuracy was comparable to HDNNPs, which is probably caused by the small amount of data. MTPs offer convenient AL capabilities, systematically improvable accuracy and comparatively high speeds. The fitted ACEPs offer similar functionality. However, they are about one order of magnitude faster when using CPUs and two orders when using GPUs at similar accuracies. Furthermore, they fared better in the extrapolation tests.

The equivariant Allegro and the equivariant + message-passing MACE potentials have a superior accuracy but come at the cost of slow evaluation time and very high memory need, which puts considerable constraints on system size and simulatable time. The Allegro MLIPs extrapolated very well, while MACE was on par with MTPs and NequIPs. Despite also employing equivariant descriptors and message-passing the accuracy of NequIPs was similar to that of MTPs and ACEPs, but at much higher evaluation times.

Overall, we find ACEPs to be suitable for bulk materials with mainly metallic or

covalent bonding, a posteriori justifying their use in chapters 2 and 3. For strongly ionic systems a reevaluation with new HDNNPs would be of interest. The novel equivariant and message passing Allegro and MACE MLIPs are beneficial in cases where it is clear a priori that simulation times and sizes are small, because they offer a great accuracy at the expanse of high computational costs.

5 Conclusions

5.1 Summary

In this thesis Atomic Cluster Expansion potentials (ACEPs) for the complex multi-element systems Cu-Zr and silicon oxycarbide (Si-O-C) are developed and applied to investigate their structural, mechanical and thermodynamical properties. Furthermore, different machine learning interatomic potential (MLIP) formalisms are evaluated. This summary concisely answers the corresponding research questions raised in section 1.3. The treated material systems are representatives of two major material groups, metals and glass-ceramics. In the former undirected metallic bonding dominates, while interatomic interactions in the latter are of covalent-ionic nature. Here, MLIPs show a big advantage compared to classical interatomic potentials (IPs). Due to their flexible functional form both materials can be treated with the same formalism while still achieving very high accuracies.

The developed ACEPs for the Cu-Zr system is able to describe the system over the whole compositional range, including boundary phases, intermetallics and amorphous structures. A phase diagram calculated with the potential using thermodynamic integration shows qualitatively good agreement with experimentally determined versions, but also severely underestimated melting points. However, as shown by a comparison to melting points directly determined by density-functional theory (DFT), the underlying issue here is the quality of training data. This points out one of the largest challenges of MLIPs, they inherit all inaccuracies of underlying quantum mechanical methods. The predicted amorphous structure is made of many local motifs, while classical IPs result in a short-range order (SRO) dominated by full icosahedron (FI) ordering. Nonetheless, a similar shear localization is observed in tensile tests. In a glass-crystal composite under tensile load, a martensitic phase transformation of a B2 inclusion to the B19' phase is observed. The phase change seems to occur in order to accommodate shear strain.

Due to the flexibility of MLIPs compared to classical IPs the main task in the fitting process shifts from the choice of functional forms to the generation of representative training data. In the case of Cu-Zr this was done by handcrafting a variety of pristine and defective amorphous and crystalline structures. For Si-O-C, however, the fitted ACEP is the first one fitted to glass-ceramics, which is publicly available. Furthermore, no crystalline structures including all three elements exist making training data generation more complicated. Here, an active learning (AL) is employed to extensively sample configuration space. This sampling can even start from randomized atomic or molecular arrangements and still yield representative structural elements for the bulk phase (cf. section 3.1.1), opening the possibility to

create training data without a priori knowledge of a system. The potential predicts microstructures containing motifs similar to expected decomposition products to be energetically favorable. However, it also shows that an interpenetrating network of graphene like carbon layers and $SiO_{4-x}C_x$ tetrahedra is formed at low pyrolysis temperatures due to slow kinetics, while larger graphitic inclusions in a $SiO_{4-x}C_x$ tetrahedra matrix form at elevated temperatures. These states correspond to two microstructure models proposed in literature. The calculation of Young's moduli for multiple Si-O-C samples reveals a strong dependence on Silica volume fraction and Si-C bonds, where the former leads to a lower and the latter to a higher stiffness. The amount of graphitic or graphene like carbon, on the other hand, has a low impact.

Different MLIPs are compared for Al-Cu-Zr training data. Here, the mean absolute error (MAE) was preferred as error measure over the root mean square error (RMSE), because it puts a lower emphasis on singular high error values. High-Dimensional Neural Network Potentials (HDNNPs) and Gaussian Approximation Potential (GAP) had the worst errors, but contrary to the other MLIPs they would probably benefit from increasing the amount of training data. Here, the HDNNPs was limited by the amount of training data available, while the GAPs could not be trained to more than 10 % of the dataset due to the giant amount of required memory.

The error of MACE and Allegro, which use equivariant descriptors, and in the case of MACE message-passing, is superior compared to the other MLIPs. However, this increase in accuracy comes with around two to three orders of magnitude slower computation compared to ACEPs, which are the fastest test candidates. All potentials with a GPU accelerated variant massively profited from it, gaining around one order of magnitude speedup. In regard to extrapolation to untrained intermetallic phases the Atomic Cluster Expansion (ACE) and Allegro slightly outperform other MLIPs.

5.2 Outlook

As shown in this work, MLIPs are a very helpful tool for the modelling and simulation of complex materials. Due to the ongoing developments in the field the evaluation of different MLIPs in the last part of this thesis should be considered as snapshot of the current state. Future scientific and technological advancement are likely to result in improved accuracies and significant computational speed-ups. Exemplarily, calculation with 32- or 16-bit floats could lead to significant speedups for MLIPs with some kind of neural network architecture on GPUs. The inclusion of charge and magnetism models could further improve the applicability of MLIPs for ionic or ferromagnetic systems. Some approaches in this direction are 4th-generation[7] and spin-dependent[111] HDNNPs or extension of ACEP to general multidimensional features,[394] which has recently been demonstrated to describe magnetism in Fe.[395] Similar extensions also exist for Moment Tensor Potentials

(MTPs).[396]

New formalisms could improve upon the ACEPs developed for Cu-Zr and Si-O-C. By publicly providing not only the fitted potentials, but also the training data employed, the possibility to simply fit another MLIP is opened up for future researches. Furthermore, this enables the extension of the training data with other elements. Interesting candidates for Cu-Zr would be Al, which is already partly done for the testing of different MLIPs, and Ti due to their impact on the formation of B2-crystallites.[163] This could be further combined with Ni to investigate the formation of NiTi phases observed in Cu-Zr-Ti-Ni glasses.[397] In the case of Si-O-C an extension with H would be beneficial to attempt the simulation of pyrolysis reactions. For the usage in batteries the interaction with Li, Na and K is of interest.[267,380]

Considering the observed problems in the calculated Cu-Zr phase diagram, the current MLIPs have already reached the point where underlying DFT training data and not the formalism itself can be a limiting factor in the achievable accuracy. Here, interesting approaches are the training of MLIPs to experimental data[398,399] and 'transfer learning' with a relatively small amount of coupled cluster calculations.[400]

The unprecedented accuracy of the Cu-Zr ACEP over a wide compositional and structural range offer new possibilities for the investigation of glass-crystal matrix composites. Here, a B2-crystallite in a glassy matrix under tensile load was investigated. However, different orientations, distributions of multiple inclusions other shapes or laminates, as well as other intermetallic phases are of interest for the understanding of shear band (SB) formation and propagation in the material.[250,251,401]

Curriculum Vitae

Research experience

since	Scientific staff member (*Wissenschaftlicher Mitarbeiter*)
12/2019	Materials modeling group,
	Prof. Dr. rer. nat. Karsten Albe,
	Technische Universität Darmstadt, Germany

Education

11/2019	Master of Science in Materials Science,
	Technische Universität Darmstadt, Germany
10/2017	Bachelor of Science Materialswissenschaft,
	Technische Universität Darmstadt, Germany
06/2014	Secondary Education (*Abitur*),
	Claus-von-Stauffenberg-Schule, Rodgau, Germany

Articles

- Niklas Leimeroth, Jochen Rohrer, and Karsten Albe. "General Purpose Potential for Glassy and Crystalline Phases of Cu-Zr Alloys Based on the ACE Formalism." In: *Physical Review Materials* 8.4 (2024), p. 043602. DOI: 10.1103/PhysRevMaterials.8.043602

- Niklas Leimeroth, Jochen Rohrer, and Karsten Albe. "Structure–Property Relations of Silicon Oxycarbides Studied Using a Machine Learning Interatomic Potential." In: *Journal of the American Ceramic Society* 107.10 (2024), pp. 6896–6910. ISSN: 1551-2916. DOI: 10.1111/jace.19932

- Sarath Menon, Yury Lysogorskiy, Alexander L. M. Knoll, Niklas Leimeroth, Marvin Poul, Minaam Qamar, Jan Janssen, Matous Mrovec, Jochen Rohrer, Karsten Albe, Jörg Behler, Ralf Drautz, and Jörg Neugebauer. *From Electrons to Phase Diagrams with Classical and Machine Learning Potentials: Automated Workflows for Materials Science with Pyiron.* 2024. DOI: 10.48550/arXiv.2403.05724. arXiv: 2403.05724 [cond-mat]. URL: http://arxiv.org/abs/2403.05724. Pre-published, accepted for Publication in npj Computational Materials

Presentations and Workshops

Oral presentations and posters at international conferences. Presenting person is underlined.

- Niklas Leimeroth, Jochen Rohrer, Karsten Albe, *Towards in-depth atomistic understanding of polymer-derived silicon oxycarbides using machine-learning potentials*, DPG-Frühjahrstagung 2024, Berlin, Germany
- Niklas Leimeroth, Jochen Rohrer, Karsten Albe, *Atomistic simulation based investigation of structure-property relations in silicon oxycarbides*, NHR Conference 2023, Berlin, Germany
- Niklas Leimeroth, Jochen Rohrer, Karsten Albe, *Development and Application of an Atomic Cluster Expansion Potential for the CuZr System*, TMS 2023, San Diego, California, USA
- Marvin Poul, Niklas Leimeroth, Alexander L. M. Knoll, Marius Herbold, Jörg Neugebauer, Poster *Interatomic Potential Fitting in pyiron*, DPG-Frühjahrstagung 2022, Regensburg, Germany

Co-organization of a series of workshops and presentation of `atomicrex`[403] integration in `pyiron`:

- Construction and deconstruction of interatomic potentials, *Introduction to pyirons atomicrex interface*, 18-22.10.2022, Günzburg, Germany
- From electrons to phase diagrams, *Introduction to EAM Potentials and Hands-on tutorial*, 08-10.06.2022, online and at Ruhr University Bochum, Germany contents and recordings available at https://github.com/pyiron-workshop/potentials-workshop-2022
- Workflows for atomistic simulation, *Hands on tutorial 'Fitting an EAM potential'* 10-12.03.2021, online, contents available at https://github.com/pyiron-workshop/potentials-workshop-2021

A Appendix

A.1 Additional material for chapter 2

Name	MP ID
Cu51Zr14	1216441
CuZr2-t	193
CuZr2-c	583800
CuZr2-m	1077372
CuZr3	580287
Cu8Zr3	1195821
Cu10Zr7	1188077
CuZr-B2	2210
CuZr-B33	1080022
CuZr-B19'	1067210
Cu2Zr	1072655
Cu3Zr	1188040
Cu5Zr	30603

Table A.1: Names used in this work and corresponding Materials Project IDs for intermetallic Cu-Zr structures.

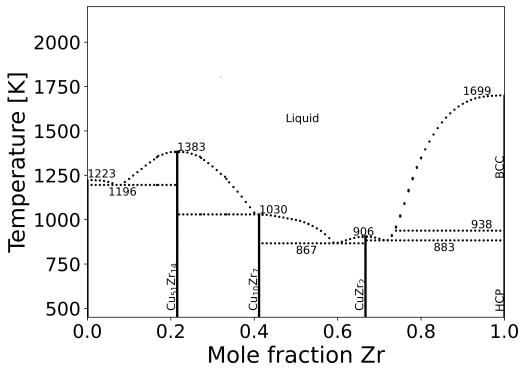

Figure A.1: Cu-Zr phase diagram calculated with the ACEP. In this version the ground state energies are not shifted.

lattice	B DFT	B ACE	C_{11} DFT	C_{11} ACE	C_{12} DFT	C_{12} ACE	C_{44} DFT	C_{44} ACE
Cu_{FCC}	139	149	180	205	119	115	76	95
Zr_{HCP}	98	114	158	209	58	100	23	59
Zr_{BCC}	89	116	65	104	100	142	32	2
Cu_5Zr	137	144	205	200	103	109	66	55
$Cu_{51}Zr_{14}$	136	140	217	215	97	103	56	52
Cu_3Zr	129	129	179	158	99	87	44	40
Cu_8Zr_3	133	144	206	207	104	116	58	44
Cu_2Zr	127	138	235	242	94	97	53	43
$Cu_{10}Zr_7$	127	147	201	200	80	94	53	46
CuZr-B2	121	133	149	178	107	126	43	43
CuZr-B33	120	128	146	138	99	106	52	39
CuZr-B19'	121	127	195	106	90	155	12	22
$CuZr_2$-t	112	135	165	233	74	99	56	63
$CuZr_2$-c	111	116	152	160	91	92	21	27
$CuZr_2$-m	110	113	179	122	75	80	31	33

Table A.2: Calculated bulk moduli and elastic constants C_{11}, C_{12}, C_{44} for Cu-Zr structures with a formation energy less than $0.1\,\mathrm{eV/atom}$ above the convex hull. All values are in GPa.

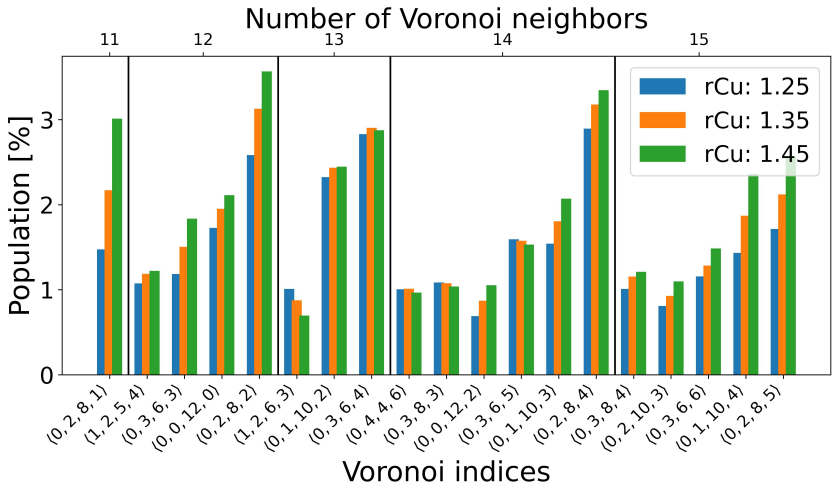

Figure A.2: The results of polydisperse Voronoi tessellation depends on the relative radii, which are adjustable parameters. In this work the atomic radii $1.35\,\text{Å}$ and $1.55\,\text{Å}$ were used for Cu and Zr, respectively. However, often the exact employed values are not given and one could also set ionic radii for example. Consequently, the sensitivity was tested. This figure shows the population of Voronoi polyhedra for the $Cu_{64}Zr_{36}$ metallic glass (MG) sample also employed in the main text, but for different Cu radii. No major changes that would influence the conclusions of this work occur even for significantly different radii.

A.2 Additional material for chapter 3

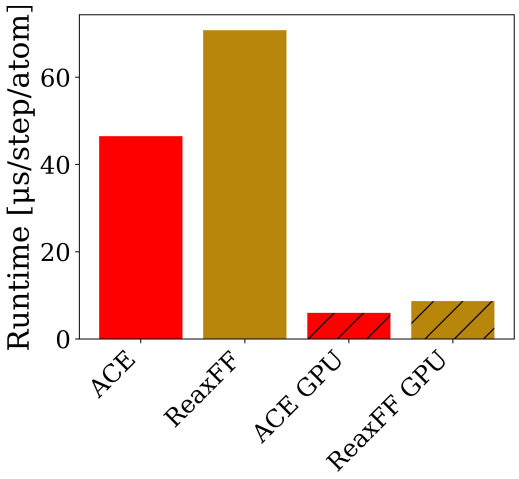

Figure A.3: ACEP and reactive force field (ReaxFF) have a similar computational cost. The speed was evaluated using LAMMPS on one core of an AMD Ryzen 5800X processor and on an NVIDIA RTX 3060 GPU. A Si-O-C structure with 80896 atoms was simulated. Here, the ACEP is slightly faster. However, the runtime of both potential types depends on several factors such as the amount of basis functions, employed cutoff or charge equilibration scheme. Consequently, other tests could show different results.

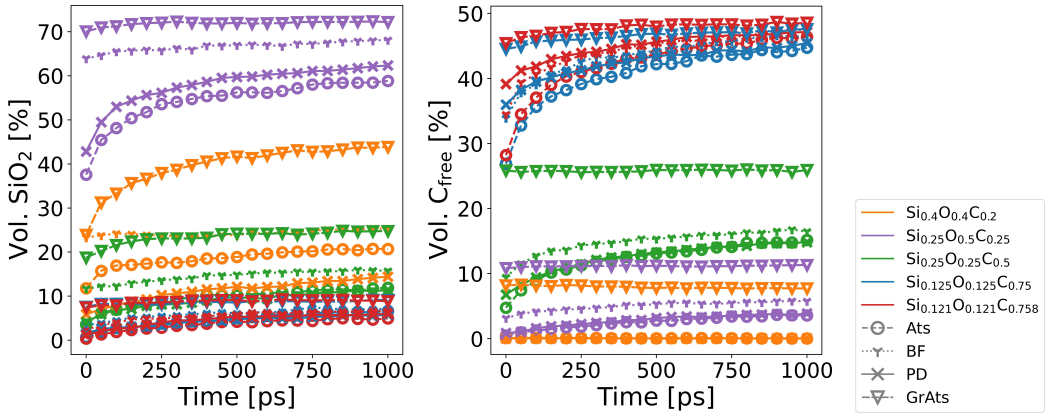

Figure A.4: After annealing for $1\,\mathrm{ns}$ silica and free carbon volume fractions are in steady state even at $2000\,\mathrm{K}$.

Bibliography

References in citation order.

[1] M. Born and R. Oppenheimer. "Zur Quantentheorie Der Molekeln." In: *Annalen der Physik* 389.20 (1927), pp. 457–484. ISSN: 1521-3889. DOI: 10.1002/andp.19273892002.

[2] Michael P. Teter, Michael C. Payne, and Douglas C. Allan. "Solution of Schrödinger's Equation for Large Systems." In: *Physical Review B* 40.18 (1989), pp. 12255–12263. DOI: 10.1103/PhysRevB.40.12255.

[3] Ruiqin Zhang and Conghao Deng. "Exact Solutions of the Schrödinger Equation for Some Quantum-Mechanical Many-Body Systems." In: *Physical Review A* 47.1 (1993), pp. 71–77. DOI: 10.1103/PhysRevA.47.71.

[4] Martin H. Müser, Sergey V. Sukhomlinov, and Lars Pastewka. "Interatomic Potentials: Achievements and Challenges." In: *Advances in Physics: X* 8.1 (2023), p. 2093129. ISSN: null. DOI: 10.1080/23746149.2022.2093129.

[5] Jörg Behler. "Perspective: Machine Learning Potentials for Atomistic Simulations." In: *The Journal of Chemical Physics* 145.17 (2016), p. 170901. ISSN: 0021-9606. DOI: 10.1063/1.4966192.

[6] Y. Mishin. "Machine-Learning Interatomic Potentials for Materials Science." 2021. arXiv: 2102.06163 [cond-mat].

[7] Jörg Behler. "Four Generations of High-Dimensional Neural Network Potentials." In: *Chemical Reviews* (2021), acs.chemrev.0c00868. ISSN: 0009-2665, 1520-6890. DOI: 10.1021/acs.chemrev.0c00868.

[8] Tsz Wai Ko and Shyue Ping Ong. "Recent Advances and Outstanding Challenges for Machine Learning Interatomic Potentials." In: *Nature Computational Science* 3.12 (2023), pp. 998–1000. ISSN: 2662-8457. DOI: 10.1038/s43588-023-00561-9.

[9] Daan Frenkel and Berend Smit. *Understanding Molecular Simulation: From Algorithms to Applications*. San Diego, UNITED STATES: Elsevier Science & Technology, 2023. ISBN: 978-0-323-91318-8.

[10] J. E. Jones and Sydney Chapman. "On the Determination of Molecular Fields.—I. From the Variation of the Viscosity of a Gas with Temperature." In: *Proceedings of the Royal Society of London. Series A, Containing Papers of a Mathematical and Physical Character* 106.738 (1997), pp. 441–462. DOI: 10.1098/rspa.1924.0081.

[11] J. E. Lennard-Jones. "Cohesion." In: *Proceedings of the Physical Society* 43.5 (1931), p. 461. ISSN: 0959-5309. DOI: 10.1088/0959-5309/43/5/301.

[12] Philip M. Morse. "Diatomic Molecules According to the Wave Mechanics. II. Vibrational Levels." In: *Physical Review* 34.1 (1929), pp. 57–64. DOI: 10.1103/PhysRev.34.57.

[13] Murray S. Daw, Stephen M. Foiles, and Michael I. Baskes. "The Embedded-Atom Method: A Review of Theory and Applications." In: *Materials Science Reports* 9.7 (1993), pp. 251–310. ISSN: 0920-2307. DOI: 10.1016/0920-2307(93)90001-U.

[14] Murray S. Daw and M. I. Baskes. "Semiempirical, Quantum Mechanical Calculation of Hydrogen Embrittlement in Metals." In: *Physical Review Letters* 50.17 (1983), pp. 1285–1288. DOI: 10.1103/PhysRevLett.50.1285.

[15] Murray S. Daw and M. I. Baskes. "Embedded-Atom Method: Derivation and Application to Impurities, Surfaces, and Other Defects in Metals." In: *Physical Review B* 29.12 (1984), pp. 6443–6453. ISSN: 0163-1829. DOI: 10.1103/PhysRevB.29.6443.

[16] M. W. Finnis and J. E. Sinclair. "A Simple Empirical N -Body Potential for Transition Metals." In: *Philosophical Magazine A* 50.1 (1984), pp. 45–55. ISSN: 0141-8610, 1460-6992. DOI: 10.1080/01418618408244210.

[17] K. W. Jacobsen, J. K. Norskov, and M. J. Puska. "Interatomic Interactions in the Effective-Medium Theory." In: *Physical Review B* 35.14 (1987), pp. 7423–7442. DOI: 10.1103/PhysRevB.35.7423.

[18] G. J. Ackland, M. W. Finnis, and V. Vitek. "Validity of the Second Moment Tight-Binding Model." In: *Journal of Physics F: Metal Physics* 18.8 (1988), p. L153. ISSN: 0305-4608. DOI: 10.1088/0305-4608/18/8/002.

[19] M. I. Baskes, J. S. Nelson, and A. F. Wright. "Semiempirical Modified Embedded-Atom Potentials for Silicon and Germanium." In: *Physical Review B* 40.9 (1989), pp. 6085–6100. DOI: 10.1103/PhysRevB.40.6085.

[20] Y. Mishin, M. J. Mehl, and D. A. Papaconstantopoulos. "Phase Stability in the Fe–Ni System: Investigation by First-Principles Calculations and Atomistic Simulations." In: *Acta Materialia* 53.15 (2005), pp. 4029–4041. ISSN: 1359-6454. DOI: 10.1016/j.actamat.2005.05.001.

[21] A. Păduraru, A. Kenoufi, N. P. Bailey, and J. Schiøtz. "An Interatomic Potential for Studying CuZr Bulk Metallic Glasses." In: *Advanced Engineering Materials* 9.6 (2007), pp. 505–508. ISSN: 1527-2648. DOI: 10.1002/adem.200700047.

[22] M. I. Mendelev and G. J. Ackland. "Development of an Interatomic Potential for the Simulation of Phase Transformations in Zirconium." In: *Philosophical Magazine Letters* 87.5 (2007), pp. 349–359. ISSN: 0950-0839. DOI: 10.1080/09500830701191393.

[23] M. I. Mendelev, M. J. Kramer, R. T. Ott, D. J. Sordelet, D. Yagodin, and P. Popel. "Development of Suitable Interatomic Potentials for Simulation of Liquid and Amorphous Cu–Zr Alloys." In: *Philosophical Magazine* 89.11 (2009), pp. 967–987. ISSN: 1478-6435. DOI: 10.1080/14786430902832773.

[24] Y. Q. Cheng, E. Ma, and H. W. Sheng. "Atomic Level Structure in Multicomponent Bulk Metallic Glass." In: *Physical Review Letters* 102.24 (2009), p. 245501. DOI: 10.1103/PhysRevLett.102.245501.

[25] D. G. Pettifor. "New Many-Body Potential for the Bond Order." In: *Physical Review Letters* 63.22 (1989), pp. 2480–2483. DOI: 10.1103/PhysRevLett.63.2480.

[26] A. P. Horsfield, A. M. Bratkovsky, M. Fearn, D. G. Pettifor, and M. Aoki. "Bond-Order Potentials: Theory and Implementation." In: *Physical Review B* 53.19 (1996), pp. 12694–12712. DOI: 10.1103/PhysRevB.53.12694.

[27] M. W. Finnis. "Bond-Order Potentials through the Ages." In: *Progress in Materials Science*. Modelling Electrons and Atoms for Materials Science 52.2 (2007), pp. 133–153. ISSN: 0079-6425. DOI: 10.1016/j.pmatsci.2006.10.003.

[28] J. Tersoff. "New Empirical Model for the Structural Properties of Silicon." In: *Physical Review Letters* 56.6 (1986), pp. 632–635. DOI: 10.1103/PhysRevLett.56.632.

[29] J. Tersoff. "Empirical Interatomic Potential for Silicon with Improved Elastic Properties." In: *Physical Review B* 38.14 (1988), pp. 9902–9905. ISSN: 0163-1829. DOI: 10.1103/PhysRevB.38.9902.

[30] Shinji Munetoh, Teruaki Motooka, Koji Moriguchi, and Akira Shintani. "Interatomic Potential for Si–O Systems Using Tersoff Parameterization." In: *Computational Materials Science* 39.2 (2007), pp. 334–339. ISSN: 0927-0256. DOI: 10.1016/j.commatsci.2006.06.010.

[31] J. Tersoff. "Modeling Solid-State Chemistry: Interatomic Potentials for Multicomponent Systems." In: *Physical Review B* 39.8 (1989), pp. 5566–5568. DOI: 10.1103/PhysRevB.39.5566.

[32] J. Tersoff. "Chemical Order in Amorphous Silicon Carbide." In: *Physical Review B* 49.23 (1994), pp. 16349–16352. DOI: 10.1103/PhysRevB.49.16349.

[33] Adri C. T. van Duin, Siddharth Dasgupta, Francois Lorant, and William A. Goddard. "ReaxFF: A Reactive Force Field for Hydrocarbons." In: *The Journal of Physical Chemistry A* 105.41 (2001), pp. 9396–9409. ISSN: 1089-5639. DOI: 10.1021/jp004368u.

[34] You Han, Dandan Jiang, Jinli Zhang, Wei Li, Zhongxue Gan, and Junjie Gu. "Development, Applications and Challenges of ReaxFF Reactive Force Field in Molecular Simulations." In: *Frontiers of Chemical Science and Engineering* 10.1 (2016), pp. 16–38. ISSN: 2095-0187. DOI: 10.1007/s11705-015-1545-z.

[35] David A. Newsome, Debasis Sengupta, Hosein Foroutan, Michael F. Russo, and Adri C. T. van Duin. "Oxidation of Silicon Carbide by O2 and H2O: A ReaxFF Reactive Molecular Dynamics Study, Part I." In: *The Journal of Physical Chemistry C* 116.30 (2012), pp. 16111–16121. ISSN: 1932-7447. DOI: 10.1021/jp306391p.

[36] Hongfei Gao, Hongjie Wang, Zihao Zhao, Min Niu, Lei Su, and Yin Wei. "Reactive Dynamics Simulation Study on the Pyrolysis of Polymer Precursors To Generate Amorphous Silicon Oxycarbide Structures." In: *The Journal of Physical Chemistry C* 122.10 (2018), pp. 5767–5773. ISSN: 1932-7447. DOI: 10.1021/acs.jpcc.7b12287.

[37] Ilia Ponomarev, Adri C. T. van Duin, and Peter Kroll. "Reactive Force Field for Simulations of the Pyrolysis of Polysiloxanes into Silicon Oxycarbide Ceramics." In: *The Journal of Physical Chemistry C* 123.27 (2019), pp. 16804–16812. ISSN: 1932-7447, 1932-7455. DOI: 10.1021/acs.jpcc.9b03810.

[38] Rustam Z. Khaliullin, Hagai Eshet, Thomas D. Kühne, Jörg Behler, and Michele Parrinello. "Graphite-Diamond Phase Coexistence Study Employing a Neural-Network Mapping of the Ab Initio Potential Energy Surface." In: *Physical Review B* 81.10 (2010), p. 100103. DOI: 10.1103/PhysRevB.81.100103.

[39] Volker L. Deringer and Gábor Csányi. "Machine Learning Based Interatomic Potential for Amorphous Carbon." In: *Physical Review B* 95.9 (2017), p. 094203. DOI: 10.1103/PhysRevB.95.094203.

[40] Mingjian Wen and Ellad B. Tadmor. "Hybrid Neural Network Potential for Multilayer Graphene." In: *Physical Review B* 100.19 (2019), p. 195419. DOI: 10.1103/PhysRevB.100.195419.

[41] Miguel A. Caro. "Optimizing Many-Body Atomic Descriptors for Enhanced Computational Performance of Machine Learning Based Interatomic Potentials." In: *Physical Review B* 100.2 (2019), p. 024112. DOI: 10.1103/PhysRevB.100.024112.

[42] Patrick Rowe, Volker L. Deringer, Piero Gasparotto, Gábor Csányi, and Angelos Michaelides. "An Accurate and Transferable Machine Learning Potential for Carbon." In: *The Journal of Chemical Physics* 153.3 (2020), p. 034702. ISSN: 0021-9606. DOI: 10.1063/5.0005084.

[43] Yusuf Shaidu, Emine Küçükbenli, Ruggero Lot, Franco Pellegrini, Efthimios Kaxiras, and Stefano de Gironcoli. "A Systematic Approach to Generating Accurate Neural Network Potentials: The Case of Carbon." In: *npj Computational Materials* 7.1 (1 2021), pp. 1–13. ISSN: 2057-3960. DOI: 10.1038/s41524-021-00508-6.

[44] Jinjin Wang, Hong Shen, Riyi Yang, Kun Xie, Chao Zhang, Liangyao Chen, Kai-Ming Ho, Cai-Zhuang Wang, and Songyou Wang. "A Deep Learning Interatomic Potential Developed for Atomistic Simulation of Carbon Materials." In: *Carbon* 186 (2022), pp. 1–8. ISSN: 0008-6223. DOI: 10.1016/j.carbon.2021.09.062.

[45] Minaam Qamar, Matous Mrovec, Yury Lysogorskiy, Anton Bochkarev, and Ralf Drautz. "Atomic Cluster Expansion for Quantum-Accurate Large-Scale Simulations of Carbon." In: *Journal of Chemical Theory and Computation* (2023). ISSN: 1549-9618. DOI: 10.1021/acs.jctc.2c01149.

[46] Albert P. Bartók, James Kermode, Noam Bernstein, and Gábor Csányi. "Machine Learning a General-Purpose Interatomic Potential for Silicon." In: *Physical Review X* 8.4 (2018), p. 041048. DOI: 10.1103/PhysRevX.8.041048.

[47] X. Qian, S. Peng, X. Li, Y. Wei, and R. Yang. "Thermal Conductivity Modeling Using Machine Learning Potentials: Application to Crystalline and Amorphous Silicon." In: *Materials Today Physics* 10 (2019), p. 100140. ISSN: 2542-5293. DOI: 10.1016/j.mtphys.2019.100140.

[48] T. Yokoi, Y. Noda, A. Nakamura, and K. Matsunaga. "Neural-Network Interatomic Potential for Grain Boundary Structures and Their Energetics in Silicon." In: *Physical Review Materials* 4.1 (2020), p. 014605. DOI: 10.1103/PhysRevMaterials.4.014605.

[49] Janine George, Geoffroy Hautier, Albert P. Bartók, Gábor Csányi, and Volker L. Deringer. "Combining Phonon Accuracy with High Transferability in Gaussian Approximation Potential Models." In: *The Journal of Chemical Physics* 153.4 (2020), p. 044104. ISSN: 0021-9606. DOI: 10.1063/5.0013826.

[50] A. Hamedani, J. Byggmästar, F. Djurabekova, G. Alahyarizadeh, R. Ghaderi, A. Minuchehr, and K. Nordlund. "Insights into the Primary Radiation Damage of Silicon by a Machine Learning Interatomic Potential." In: *Materials Research Letters* 8.10 (2020), pp. 364–372. ISSN: null. DOI: 10.1080/21663831.2020.1771451.

[51] Yury Lysogorskiy, Cas van der Oord, Anton Bochkarev, Sarath Menon, Matteo Rinaldi, Thomas Hammerschmidt, Matous Mrovec, Aidan Thompson, Gábor Csányi, Christoph Ortner, and Ralf Drautz. "Performant Implementation of the Atomic Cluster Expansion (PACE) and Application to Copper and Silicon." In: *npj Computational Materials* 7.1 (2021), p. 97. ISSN: 2057-3960. DOI: 10.1038/s41524-021-00559-9.

[52] Linus C. Erhard, Jochen Rohrer, Karsten Albe, and Volker L. Deringer. "A Machine-Learned Interatomic Potential for Silica and Its Relation to Empirical Models." In: *npj Computational Materials* 8.1 (2022), p. 90. ISSN: 2057-3960. DOI: 10.1038/s41524-022-00768-w.

[53] Linus C. Erhard, Jochen Rohrer, Karsten Albe, and Volker L. Deringer. *Modelling Atomic and Nanoscale Structure in the Silicon-Oxygen System through Active Machine Learning*. 2023. DOI: 10.48550/arXiv.2309.03587. arXiv: 2309.03587 [cond-mat]. URL: http://arxiv.org/abs/2309.03587. Pre-published.

[54] M. K. Kutzhanov, A. T. Matveev, D. G. Kvashnin, S. Corthay, A. G. Kvashnin, A. S. Konopatsky, A. V. Bondarev, N. A. Arkharova, and D. V. Shtansky. "Al/SiC Nanocomposites with Enhanced Thermomechanical Properties Obtained from Microwave Plasma-Treated Nanopowders." In: *Materials Science and Engineering: A* 824 (2021), p. 141817. ISSN: 0921-5093. DOI: 10.1016/j.msea.2021.141817.

[55] Yong Liu, Hao Wang, Linxin Guo, Zhanfeng Yan, Jian Zheng, Wei Zhou, and Jianming Xue. *Deep Learning Inter-Atomic Potential for Irradiation Damage in 3C-SiC*. 2023. DOI: 10.48550/arXiv.2305.19516. arXiv: 2305.19516 [cond-mat]. URL: http://arxiv.org/abs/2305.19516. Pre-published.

[56] Bobby G. Sumpter and Donald W. Noid. "Potential Energy Surfaces for Macromolecules. A Neural Network Technique." In: *Chemical Physics Letters* 192.5 (1992), pp. 455–462. ISSN: 0009-2614. DOI: 10.1016/0009-2614(92)85498-Y.

[57] Thomas B. Blank, Steven D. Brown, August W. Calhoun, and Douglas J. Doren. "Neural Network Models of Potential Energy Surfaces." In: *The Journal of Chemical Physics* 103.10 (1995), pp. 4129–4137. ISSN: 0021-9606. DOI: 10.1063/1.469597.

[58] Jörg Behler and Michele Parrinello. "Generalized Neural-Network Representation of High-Dimensional Potential-Energy Surfaces." In: *Physical Review Letters* 98.14 (2007), p. 146401. DOI: 10.1103/PhysRevLett.98.146401.

[59] Albert P. Bartók, Mike C. Payne, Risi Kondor, and Gábor Csányi. "Gaussian Approximation Potentials: The Accuracy of Quantum Mechanics, without the Electrons." In: *Physical Review Letters* 104.13 (2010), p. 136403. ISSN: 0031-9007, 1079-7114. DOI: 10.1103/PhysRevLett.104.136403.

[60] Alexander V. Shapeev. "Moment Tensor Potentials: A Class of Systematically Improvable Interatomic Potentials." In: *Multiscale Modeling & Simulation* 14.3 (2016), pp. 1153–1173. ISSN: 1540-3459, 1540-3467. DOI: 10.1137/15M1054183.

[61] Ralf Drautz. "Atomic Cluster Expansion for Accurate and Transferable Interatomic Potentials." In: *Physical Review B* 99.1 (2019), p. 014104. DOI: 10.1103/PhysRevB.99.014104.

[62] Simon Batzner, Albert Musaelian, Lixin Sun, Mario Geiger, Jonathan P. Mailoa, Mordechai Kornbluth, Nicola Molinari, Tess E. Smidt, and Boris Kozinsky. "E(3)-Equivariant Graph Neural Networks for Data-Efficient and Accurate Interatomic Potentials." In: *Nature Communications* 13.1 (1 2022), p. 2453. ISSN: 2041-1723. DOI: 10.1038/s41467-022-29939-5.

[63] Albert Musaelian, Simon Batzner, Anders Johansson, Lixin Sun, Cameron J. Owen, Mordechai Kornbluth, and Boris Kozinsky. *Learning Local Equivariant Representations for Large-Scale Atomistic Dynamics*. 2022. DOI: 10.48550/arXiv.2204.05249. arXiv: 2204.05249 [cond-mat, physics:physics]. URL: http://arxiv.org/abs/2204.05249. Prepublished.

[64] Ilyes Batatia, David Peter Kovacs, Gregor N. C. Simm, Christoph Ortner, and Gabor Csanyi. "MACE: Higher Order Equivariant Message Passing Neural Networks for Fast and Accurate Force Fields." In: Advances in Neural Information Processing Systems. 2022.

[65] A. P. Thompson, L. P. Swiler, C. R. Trott, S. M. Foiles, and G. J. Tucker. "Spectral Neighbor Analysis Method for Automated Generation of Quantum-Accurate Interatomic Potentials." In: *Journal of Computational Physics* 285 (2015), pp. 316–330. ISSN: 0021-9991. DOI: 10.1016/j.jcp.2014.12.018.

[66] Yunxing Zuo, Chi Chen, Xiangguo Li, Zhi Deng, Yiming Chen, Jörg Behler, Gábor Csányi, Alexander V. Shapeev, Aidan P. Thompson, Mitchell A. Wood, and Shyue Ping Ong. "Performance and Cost Assessment of Machine Learning Interatomic Potentials." In: *The Journal of Physical Chemistry A* 124.4 (2020), pp. 731–745. ISSN: 1089-5639. DOI: 10.1021/acs.jpca.9b08723.

[67] Marcel F. Langer, Alex Goeßmann, and Matthias Rupp. "Representations of Molecules and Materials for Interpolation of Quantum-Mechanical Simulations via Machine Learning." In: *npj Computational Materials* 8.1 (2022), pp. 1–14. ISSN: 2057-3960. DOI: 10.1038/s41524-022-00721-x.

[68] Jörg Behler. "Constructing High-Dimensional Neural Network Potentials: A Tutorial Review." In: *International Journal of Quantum Chemistry* 115.16 (2015), pp. 1032–1050. ISSN: 1097-461X. DOI: 10.1002/qua.24890.

[69] Nongnuch Artrith and Alexander Urban. "An Implementation of Artificial Neural-Network Potentials for Atomistic Materials Simulations: Performance for TiO2." In: *Computational Materials Science* 114 (2016), pp. 135–150. ISSN: 0927-0256. DOI: 10.1016/j.commatsci.2015.11.047.

[70] Alireza Khorshidi and Andrew A. Peterson. "Amp: A Modular Approach to Machine Learning in Atomistic Simulations." In: *Computer Physics Communications* 207 (2016), pp. 310–324. ISSN: 0010-4655. DOI: 10.1016/j.cpc.2016.05.010.

[71] J. S. Smith, O. Isayev, and A. E. Roitberg. "ANI-1: An Extensible Neural Network Potential with DFT Accuracy at Force Field Computational Cost." In: *Chemical Science* 8.4 (2017), pp. 3192–3203. DOI: 10.1039/C6SC05720A.

[72] Brian Kolb, Levi C. Lentz, and Alexie M. Kolpak. "Discovering Charge Density Functionals and Structure-Property Relationships with PROPhet: A General Framework for Coupling Machine Learning and First-Principles Methods." In: *Scientific Reports* 7.1 (1 2017), p. 1192. ISSN: 2045-2322. DOI: 10.1038/s41598-017-01251-z.

[73] Han Wang, Linfeng Zhang, Jiequn Han, and Weinan E. "DeePMD-kit: A Deep Learning Package for Many-Body Potential Energy Representation and Molecular Dynamics." In: *Computer Physics Communications* 228 (2018), pp. 178–184. ISSN: 0010-4655. DOI: 10.1016/j.cpc.2018.03.016.

[74] Andreas Singraber, Tobias Morawietz, Jörg Behler, and Christoph Dellago. "Parallel Multistream Training of High-Dimensional Neural Network Potentials." In: *Journal of Chemical Theory and Computation* 15.5 (2019), pp. 3075–3092. ISSN: 1549-9618. DOI: 10.1021/acs.jctc.8b01092.

[75] Kyuhyun Lee, Dongsun Yoo, Wonseok Jeong, and Seungwu Han. "SIMPLE-NN: An Efficient Package for Training and Executing Neural-Network Interatomic Potentials." In: *Computer Physics Communications* 242 (2019), pp. 95–103. ISSN: 0010-4655. DOI: 10.1016/j.cpc.2019.04.014.

[76] Si-Da Huang, Cheng Shang, Pei-Lin Kang, Xiao-Jie Zhang, and Zhi-Pan Liu. "LASP: Fast Global Potential Energy Surface Exploration." In: *WIREs Computational Molecular Science* 9.6 (2019), e1415. ISSN: 1759-0884. DOI: 10.1002/wcms.1415.

[77] Yunqi Shao, Matti Hellström, Pavlin D. Mitev, Lisanne Knijff, and Chao Zhang. "PiNN: A Python Library for Building Atomic Neural Networks of Molecules and Materials." In: *Journal of Chemical Information and Modeling* 60.3 (2020), pp. 1184–1193. ISSN: 1549-9596. DOI: 10.1021/acs.jcim.9b00994.

[78] Ruggero Lot, Franco Pellegrini, Yusuf Shaidu, and Emine Küçükbenli. "PANNA: Properties from Artificial Neural Network Architectures." In: *Computer Physics Communications* 256 (2020), p. 107402. ISSN: 0010-4655. DOI: 10.1016/j.cpc.2020.107402.

[79] Andreas Singraber, mpbircher, Sam Reeve, David W. H. Swenson, Jérémy Lauret, and philippedavid. *CompPhysVienna/N2p2: Version 2.1.4*. Version v2.1.4. Zenodo, 2021. DOI: 10.5281/zenodo.4750573.

[80] Andreas Singraber, Jörg Behler, and Christoph Dellago. "Library-Based LAMMPS Implementation of High-Dimensional Neural Network Potentials." In: *Journal of Chemical Theory and Computation* 15.3 (2019), pp. 1827–1840. ISSN: 1549-9618. DOI: 10.1021/acs.jctc.8b00770.

[81] Jörg Behler. "Atom-Centered Symmetry Functions for Constructing High-Dimensional Neural Network Potentials." In: *The Journal of Chemical Physics* 134.7 (2011), p. 074106. ISSN: 0021-9606. DOI: 10.1063/1.3553717.

[82] Dylan M. Anstine and Olexandr Isayev. "Machine Learning Interatomic Potentials and Long-Range Physics." In: *The Journal of Physical Chemistry A* 127.11 (2023), pp. 2417–2431. ISSN: 1089-5639. DOI: 10.1021/acs.jpca.2c06778.

[83] G Csanyi, S Winfield, J Kermode, M C Payne, A Comisso, A De Vita, and N Bernstein. "Expressive Programming for Computational Physics in Fortran 95+." In: *Newsletter of the Computational Physics Group* (2007), pp. 1–24.

[84] James R. Kermode. "F90wrap: An Automated Tool for Constructing Deep Python Interfaces to Modern Fortran Codes." In: *Journal of Physics: Condensed Matter* 32.30 (2020), p. 305901. ISSN: 0953-8984. DOI: 10.1088/1361-648X/ab82d2.

[85] David J. C. MacKay. *Information Theory, Inference and Learning Algorithms*. Cambridge University Press, 2003. 694 pp. ISBN: 978-0-521-64298-9. Google Books: AKuMj4PN_EMC.

[86] Olivier Bousquet, Ulrike von Luxburg, and Gunnar Rätsch, eds. *Advanced Lectures on Machine Learning: ML Summer Schools 2003, Canberra, Australia, February 2-14, 2003 [and] Tübingen, Germany, August 4-16, 2003: Revised Lectures*. Lecture Notes in Computer Science, Lecture Notes in Artificial Intelligence 3176. Berlin ; New York: Springer, 2004. 240 pp. ISBN: 978-3-540-23122-6.

[87] Volker L. Deringer, Albert P. Bartók, Noam Bernstein, David M. Wilkins, Michele Ceriotti, and Gábor Csányi. "Gaussian Process Regression for Materials and Molecules." In: *Chemical Reviews* 121.16 (2021), pp. 10073–10141. ISSN: 0009-2665. DOI: 10.1021/acs.chemrev.1c00022.

[88] Albert P. Bartók, Risi Kondor, and Gábor Csányi. "On Representing Chemical Environments." In: *Physical Review B* 87.18 (2013), p. 184115. DOI: 10.1103/PhysRevB.87.184115.

[89] Ivan S. Novikov, Konstantin Gubaev, Evgeny V. Podryabinkin, and Alexander V. Shapeev. "The MLIP Package: Moment Tensor Potentials with MPI and Active Learning." In: *Machine Learning: Science and Technology* 2.2 (2021), p. 025002. ISSN: 2632-2153. DOI: 10.1088/2632-2153/abc9fe.

[90] Evgeny Podryabinkin, Kamil Garifullin, Alexander Shapeev, and Ivan Novikov. *MLIP-3: Active Learning on Atomic Environments with Moment Tensor Potentials*. 2023. arXiv: 2304.13144 [physics]. URL: http://arxiv.org/abs/2304.13144. Pre-published.

[91] Anton Bochkarev, Yury Lysogorskiy, Sarath Menon, Minaam Qamar, Matous Mrovec, and Ralf Drautz. "Efficient Parametrization of the Atomic Cluster Expansion." In: *Physical Review Materials* 6.1 (2022), p. 013804. DOI: 10.1103/PhysRevMaterials.6.013804.

[92] Geneviève Dusson, Markus Bachmayr, Gábor Csányi, Ralf Drautz, Simon Etter, Cas van der Oord, and Christoph Ortner. "Atomic Cluster Expansion: Completeness, Efficiency and Stability." In: *Journal of Computational Physics* 454 (2022), p. 110946. ISSN: 0021-9991. DOI: 10.1016/j.jcp.2022.110946.

[93] Kristof T. Schütt, Farhad Arbabzadah, Stefan Chmiela, Klaus R. Müller, and Alexandre Tkatchenko. "Quantum-Chemical Insights from Deep Tensor Neural Networks." In: *Nature Communications* 8.1 (2017), p. 13890. ISSN: 2041-1723. DOI: 10.1038/ncomms13890.

[94] Kristof Schütt, Pieter-Jan Kindermans, Huziel Enoc Sauceda Felix, Stefan Chmiela, Alexandre Tkatchenko, and Klaus-Robert Müller. "SchNet: A Continuous-Filter Convolutional Neural Network for Modeling Quantum Interactions." In: *Advances in Neural Information Processing Systems*. Vol. 30. Curran Associates, Inc., 2017.

[95] Oliver T. Unke and Markus Meuwly. "PhysNet: A Neural Network for Predicting Energies, Forces, Dipole Moments, and Partial Charges." In: *Journal of Chemical Theory and Computation* 15.6 (2019), pp. 3678–3693. ISSN: 1549-9618. DOI: 10.1021/acs.jctc.9b00181.

[96] Johannes Gasteiger, Florian Becker, and Stephan Günnemann. "GemNet: Universal Directional Graph Neural Networks for Molecules." In: *Advances in Neural Information Processing Systems*. Vol. 34. Curran Associates, Inc., 2021, pp. 6790–6802.

[97] Franco Scarselli, Marco Gori, Ah Chung Tsoi, Markus Hagenbuchner, and Gabriele Monfardini. "The Graph Neural Network Model." In: *IEEE Transactions on Neural Networks* 20.1 (2009), pp. 61–80. ISSN: 1941-0093. DOI: 10.1109/TNN.2008.2005605.

[98] Zonghan Wu, Shirui Pan, Fengwen Chen, Guodong Long, Chengqi Zhang, and Philip S. Yu. "A Comprehensive Survey on Graph Neural Networks." In: *IEEE Transactions on Neural Networks and Learning Systems* 32.1 (2021), pp. 4–24. ISSN: 2162-2388. DOI: 10.1109/TNNLS.2020.2978386.

[99] Albert Musaelian, Simon Batzner, Anders Johansson, Lixin Sun, Cameron J. Owen, Mordechai Kornbluth, and Boris Kozinsky. "Learning Local Equivariant Representations for Large-Scale Atomistic Dynamics." In: *Nature Communications* 14.1 (1 2023), p. 579. ISSN: 2041-1723. DOI: 10.1038/s41467-023-36329-y.

[100] Mario Geiger and Tess Smidt. *E3nn: Euclidean Neural Networks*. arXiv, 2022. DOI: 10.48550/ARXIV.2207.09453.

[101] Mario Geiger, Tess Smidt, Alby M., Benjamin Kurt Miller, Wouter Boomsma, Bradley Dice, Kostiantyn Lapchevskyi, Maurice Weiler, Michał Tyszkiewicz, Simon Batzner, Dylan Madisetti, Martin Uhrin, Jes Frellsen, Nuri Jung, Sophia Sanborn, Mingjian Wen, Josh Rackers, Marcel Rød, and Michael Bailey. *Euclidean Neural Networks: E3nn*. Version 0.5.0. Zenodo, 2022. DOI: 10.5281/zenodo.6459381.

[102] Kaiming He, Xiangyu Zhang, Shaoqing Ren, and Jian Sun. "Deep Residual Learning for Image Recognition." In: *2016 IEEE Conference on Computer Vision and Pattern Recognition (CVPR)*. 2016 IEEE Conference on Computer Vision and Pattern Recognition (CVPR). 2016, pp. 770–778. DOI: 10.1109/CVPR.2016.90.

[103] Ilyes Batatia, Simon Batzner, Dávid Péter Kovács, Albert Musaelian, Gregor N. C. Simm, Ralf Drautz, Christoph Ortner, Boris Kozinsky, and Gábor Csányi. *The Design Space of E(3)-Equivariant Atom-Centered Interatomic Potentials*. 2022. arXiv: 2205 . 06643 [cond-mat, physics:physics, stat]. URL: http://arxiv.org/abs/2205.06643. Pre-published.

[104] Ask Hjorth Larsen, Jens Jørgen Mortensen, Jakob Blomqvist, Ivano E Castelli, Rune Christensen, Marcin Dułak, Jesper Friis, Michael N Groves, Bjørk Hammer, Cory Hargus, Eric D Hermes, Paul C Jennings, Peter Bjerre Jensen, James Kermode, John R Kitchin, Esben Leonhard Kolsbjerg, Joseph Kubal, Kristen Kaasbjerg, Steen Lysgaard, Jón Bergmann Maronsson, Tristan Maxson, Thomas Olsen, Lars Pastewka, Andrew Peterson, Carsten Rostgaard, Jakob Schiøtz, Ole Schütt, Mikkel Strange, Kristian S Thygesen, Tejs Vegge, Lasse Vilhelmsen, Michael Walter, Zhenhua Zeng, and Karsten W Jacobsen. "The Atomic Simulation Environment—a Python Library for Working with Atoms." In: *Journal of Physics: Condensed Matter* 29.27 (2017), p. 273002. ISSN: 0953-8984, 1361-648X. DOI: 10.1088/1361-648X/aa680e.

[105] Anubhav Jain, Shyue Ping Ong, Geoffroy Hautier, Wei Chen, William Davidson Richards, Stephen Dacek, Shreyas Cholia, Dan Gunter, David Skinner, Gerbrand Ceder, and Kristin A. Persson. "Commentary: The Materials Project: A Materials Genome Approach to Accelerating Materials Innovation." In: *APL Materials* 1.1 (2013), p. 011002. DOI: 10.1063/1.4812323.

[106] James E. Saal, Scott Kirklin, Muratahan Aykol, Bryce Meredig, and C. Wolverton. "Materials Design and Discovery with High-Throughput Density Functional Theory: The Open Quantum Materials Database (OQMD)." In: *JOM* 65.11 (2013), pp. 1501–1509. ISSN: 1543-1851. DOI: 10.1007/s11837-013-0755-4.

[107] Scott Kirklin, James E. Saal, Bryce Meredig, Alex Thompson, Jeff W. Doak, Muratahan Aykol, Stephan Rühl, and Chris Wolverton. "The Open Quantum Materials Database (OQMD): Assessing the Accuracy of DFT Formation Energies." In: *npj Computational Materials* 1.1 (1 2015), pp. 1–15. ISSN: 2057-3960. DOI: 10.1038/npjcompumats.2015.10.

[108] Shyue Ping Ong, William Davidson Richards, Anubhav Jain, Geoffroy Hautier, Michael Kocher, Shreyas Cholia, Dan Gunter, Vincent L. Chevrier, Kristin A. Persson, and Gerbrand Ceder. "Python Materials Genomics (Pymatgen): A Robust, Open-Source Python Library for Materials Analysis." In: *Computational Materials Science* 68 (2013), pp. 314–319. ISSN: 0927-0256. DOI: 10.1016/j.commatsci.2012.10.028.

[109] Søren L. Frederiksen, Karsten W. Jacobsen, Kevin S. Brown, and James P. Sethna. "Bayesian Ensemble Approach to Error Estimation of Interatomic Potentials." In: *Physical Review Letters* 93.16 (2004), p. 165501. DOI: 10.1103/PhysRevLett.93.165501.

[110] Marco Eckhoff and Jörg Behler. "From Molecular Fragments to the Bulk: Development of a Neural Network Potential for MOF-5." In: *Journal of Chemical Theory and Computation* 15.6 (2019), pp. 3793–3809. ISSN: 1549-9618. DOI: 10.1021/acs.jctc.8b01288.

[111] Marco Eckhoff and Jörg Behler. "High-Dimensional Neural Network Potentials for Magnetic Systems Using Spin-Dependent Atom-Centered Symmetry Functions." In: *npj Computational Materials* 7.1 (1 2021), pp. 1–11. ISSN: 2057-3960. DOI: 10.1038/s41524-021-00636-z.

[112] Ryosuke Jinnouchi, Ferenc Karsai, and Georg Kresse. "On-the-Fly Machine Learning Force Field Generation: Application to Melting Points." In: *Physical Review B* 100.1 (2019), p. 014105. DOI: 10.1103/PhysRevB.100.014105.

[113] Burr Settles. *Active Learning Literature Survey*. Technical Report. University of Wisconsin-Madison Department of Computer Sciences, 2009.

[114] Evgeny V. Podryabinkin and Alexander V. Shapeev. "Active Learning of Linearly Parametrized Interatomic Potentials." In: *Computational Materials Science* 140 (2017), pp. 171–180. ISSN: 0927-0256. DOI: 10.1016/j.commatsci.2017.08.031.

[115] Yury Lysogorskiy, Anton Bochkarev, Matous Mrovec, and Ralf Drautz. "Active Learning Strategies for Atomic Cluster Expansion Models." In: *Physical Review Materials* 7.4 (2023), p. 043801. DOI: 10.1103/PhysRevMaterials.7.043801.

[116] Zhenwei Li, James R. Kermode, and Alessandro De Vita. "Molecular Dynamics with On-the-Fly Machine Learning of Quantum-Mechanical Forces." In: *Physical Review Letters* 114.9 (2015), p. 096405. DOI: 10.1103/PhysRevLett.114.096405.

[117] Ryosuke Jinnouchi, Jonathan Lahnsteiner, Ferenc Karsai, Georg Kresse, and Menno Bokdam. "Phase Transitions of Hybrid Perovskites Simulated by Machine-Learning Force Fields Trained on the Fly with Bayesian Inference." In: *Physical Review Letters* 122.22 (2019), p. 225701. DOI: 10.1103/PhysRevLett.122.225701.

[118] Lingyu Kong, Jielan Li, Lixin Sun, Han Yang, Hongxia Hao, Chi Chen, Nongnuch Artrith, Jose Antonio Garrido Torres, Ziheng Lu, and Yichi Zhou. *Overcoming the Size Limit of First Principles Molecular Dynamics Simulations with an In-Distribution Substructure Embedding Active Learner*. 2023. DOI: 10.48550/arXiv.2311.08177. arXiv: 2311.08177 [cond-mat, physics:physics]. URL: http://arxiv.org/abs/2311.08177. Pre-published.

[119] T. Egami. "Understanding the Properties and Structure of Metallic Glasses at the Atomic Level." In: *JOM* 62.2 (2010), pp. 70–75. ISSN: 1543-1851. DOI: 10.1007/s11837-010-0036-4.

[120] Zbigniew H. Stachurski. "On Structure and Properties of Amorphous Materials." In: *Materials* 4.9 (9 2011), pp. 1564–1598. ISSN: 1996-1944. DOI: 10.3390/ma4091564.

[121] Jörg F. Löffler. "Bulk Metallic Glasses." In: *Intermetallics* 11.6 (2003), pp. 529–540. ISSN: 09669795. DOI: 10.1016/S0966-9795(03)00046-3.

[122] Christopher A. Schuh, Todd C. Hufnagel, and Upadrasta Ramamurty. "Mechanical Behavior of Amorphous Alloys." In: *Acta Materialia* 55.12 (2007), pp. 4067–4109. ISSN: 1359-6454. DOI: 10.1016/j.actamat.2007.01.052.

[123] J. Eckert, J. Das, S. Pauly, and C. Duhamel. "Mechanical Properties of Bulk Metallic Glasses and Composites." In: *Journal of Materials Research* 22.2 (2007), pp. 285–301. ISSN: 2044-5326. DOI: 10.1557/jmr.2007.0050.

[124] Ludovic Berthier and Giulio Biroli. "Theoretical Perspective on the Glass Transition and Amorphous Materials." In: *Reviews of Modern Physics* 83.2 (2011), pp. 587–645. DOI: 10.1103/RevModPhys.83.587.

[125] D. Chakravorty. "Inorganic Glasses." In: *Modern Aspects of Solid State Chemistry*. Ed. by C. N. R. Rao. Boston, MA: Springer US, 1970, pp. 391–423. ISBN: 978-1-4684-1875-0. DOI: 10.1007/978-1-4684-1875-0_16.

[126] A. Paul. "Glass Formation." In: *Chemistry of Glasses*. Ed. by A. Paul. Dordrecht: Springer Netherlands, 1982, pp. 1–15. ISBN: 978-94-009-5918-7. DOI: 10.1007/978-94-009-5918-7_1.

[127] "Early Glass in the Middle East and Europe: Innovation, Archaeology and the Contexts for Production and Use." In: *Ancient Glass: An Interdisciplinary Exploration*. Ed. by Julian Henderson. Cambridge: Cambridge University Press, 2013, pp. 127–157. ISBN: 978-1-139-02188-3. DOI: 10.1017/CBO9781139021883.006.

[128] Shigeki Sakaguchi. "Evaluation of the Critical Cooling Rate in Glass-Forming Materials Based on Viscosity." In: *Journal of Non-Crystalline Solids* 185.3 (1995), pp. 268–273. ISSN: 0022-3093. DOI: 10.1016/0022-3093(94)00682-2.

[129] W. Klement, R. H. Willens, and Pol Duwez. "Non-Crystalline Structure in Solidified Gold–Silicon Alloys." In: *Nature* 187.4740 (4740 1960), pp. 869–870. ISSN: 1476-4687. DOI: 10.1038/187869b0.

[130] H. S Chen. "Thermodynamic Considerations on the Formation and Stability of Metallic Glasses." In: *Acta Metallurgica* 22.12 (1974), pp. 1505–1511. ISSN: 0001-6160. DOI: 10.1016/0001-6160(74)90112-6.

[131] Makoto Shiojiri, Yoshio Saito, Hiroshi Okada, and Hiromi Sasaki. "Desities of Amorphous Thin Films." In: *Japanese Journal of Applied Physics* 18.10 (1979), p. 1931. ISSN: 1347-4065. DOI: 10.1143/JJAP.18.1931.

[132] M. Raible, S. G. Mayr, S. J. Linz, M. Moske, P. Hänggi, and K. Samwer. "Amorphous Thin-Film Growth: Theory Compared with Experiment." In: *Europhysics Letters* 50.1 (2000), p. 61. ISSN: 0295-5075. DOI: 10.1209/epl/i2000-00235-7.

[133] Gary M. Renlund, Svante Prochazka, and Robert H. Doremus. "Silicon Oxycarbide Glasses: Part II. Structure and Properties." In: *Journal of Materials Research* 6.12 (1991), pp. 2723–2734. ISSN: 2044-5326. DOI: 10.1557/JMR.1991.2723.

[134] Tobias Erny, Michael Seibold, Otto Jarchow, and Peter Greil. "Microstructure Development of Oxycarbide Composites during Active-Filler-Controlled Polymer Pyrolysis." In: *Journal of the American Ceramic Society* 76.1 (1993), pp. 207–213. ISSN: 1551-2916. DOI: 10.1111/j.1151-2916.1993.tb03709.x.

[135] R. S. Averback and T. DIAZ De la rubia. "Displacement Damage in Irradiated Metals and Semiconductors." In: *Solid State Physics*. Ed. by Henry Ehrenreich and Frans Spaepen. Vol. 51. Solid State Physics. Academic Press, 1998, pp. 281–402. DOI: 10.1016/S0081-1947(08)60193-9.

[136] B. Johannessen, P. Kluth, D. J. Llewellyn, G. J. Foran, D. J. Cookson, and M. C. Ridgway. "Amorphization of Embedded Cu Nanocrystals by Ion Irradiation." In: *Applied Physics Letters* 90.7 (2007), p. 073119. ISSN: 0003-6951. DOI: 10.1063/1.2644413.

[137] B. Y. Li, A. C. Li, S. Zhao, and M. A. Meyers. "Amorphization by Mechanical Deformation." In: *Materials Science and Engineering: R: Reports* 149 (2022), p. 100673. ISSN: 0927-796X. DOI: 10.1016/j.mser.2022.100673.

[138] R. Hasegawa and Ranjan Ray. "Iron-boron Metallic Glasses." In: *Journal of Applied Physics* 49.7 (2008), pp. 4174–4179. ISSN: 0021-8979. DOI: 10.1063/1.325328.

[139] R. C. Ruhl, B. C. Giessen, M. Cohen, and N. J. Grant. "New Microcrystalline Phases in the Nb-Ni and Ta-Ni Systems." In: *Acta Metallurgica* 15.11 (1967), pp. 1693–1702. ISSN: 0001-6160. DOI: 10.1016/0001-6160(67)90060-0.

[140] D. E Polk and H. S Chen. “Formation and Thermal Properties of Glassy Ni-Fe Based Alloys.” In: *Journal of Non-Crystalline Solids* 15.2 (1974), pp. 165–173. ISSN: 0022-3093. DOI: 10.1016/0022-3093(74)90045-3.

[141] Akihisa Inoue and Tsuyoshi Masumoto. “MELT-QUENCHED AMORPHOUS SUPERCONDUCTING ALLOYS.” In: *Science reports of the Research Institutes, Tohoku University. Ser. A, Physics, chemistry and metallurgy* 28.0 (1980), pp. 165–200.

[142] Mark C. Lee, James M. Kendall, and William L. Johnson. “Spheres of the Metallic Glass Au55Pb22.5Sb22.5 and Their Surface Characteristics.” In: *Applied Physics Letters* 40.5 (1982), pp. 382–384. ISSN: 0003-6951. DOI: 10.1063/1.93110.

[143] Z. Altounian, Tu Guo-hua, and J. O. Strom-Olsen. “Crystallization Characteristics of Cu-Zr Metallic Glasses from Cu70Zr30 to Cu25Zr75.” In: *Journal of Applied Physics* 53.7 (1982), pp. 4755–4760. ISSN: 0021-8979. DOI: 10.1063/1.331304.

[144] H. W. Kui, A. L. Greer, and D. Turnbull. “Formation of Bulk Metallic Glass by Fluxing.” In: *Applied Physics Letters* 45.6 (1984), pp. 615–616. ISSN: 0003-6951. DOI: 10.1063/1.95330.

[145] A. P. Tsai, A. Inoue, Y. Bizen, and T. Masumoto. “Kinetics of the Amorphous to Icosahedral Structure Transition in Al-Cu-V and Al-Mn-Si Alloys.” In: *Acta Metallurgica* 37.5 (1989), pp. 1443–1449. ISSN: 0001-6160. DOI: 10.1016/0001-6160(89)90176-4.

[146] Sung Gyoo Kim, Akihisa Inoue, and Tsuyoshi Masumoto. “High Mechanical Strengths of Mg–Ni–Y and Mg–Cu–Y Amorphous Alloys with Significant Supercooled Liquid Region.” In: *Materials Transactions, JIM* 31.11 (1990), pp. 929–934. DOI: 10.2320/matertrans1989.31.929.

[147] W. H. Wang, C. Dong, and C. H. Shek. “Bulk Metallic Glasses.” In: *Materials Science and Engineering: R: Reports* 44.2 (2004), pp. 45–89. ISSN: 0927-796X. DOI: 10.1016/j.mser.2004.03.001.

[148] Akihisa Inoue. “Stabilization of Metallic Supercooled Liquid and Bulk Amorphous Alloys.” In: *Acta Materialia* 48.1 (2000), pp. 279–306. ISSN: 1359-6454. DOI: 10.1016/S1359-6454(99)00300-6.

[149] M. F. Ashby and A. L. Greer. “Metallic Glasses as Structural Materials.” In: *Scripta Materialia*. Viewpoint Set No: 37. On Mechanical Behavior of Metallic Glasses 54.3 (2006), pp. 321–326. ISSN: 1359-6462. DOI: 10.1016/j.scriptamat.2005.09.051.

[150] Hisashi Kakiuchi, Akihisa Inoue, Masahide Onuki, Yoshishige Takano, and Tetsuo Yamaguchi. “Application of Zr-Based Bulk Glassy Alloys to Golf Clubs.” In: *Materials Transactions* 42.4 (2001), pp. 678–681. DOI: 10.2320/matertrans.42.678.

[151] William L. Johnson, David S. Lee, Marios D. Demetriou, Jong Hyun NA, and Glenn Robert GARRETT. "Golf Club Fabricated from Bulk Metallic Glasses with High Toughness and High Stiffness." Pat. WO2014120788A1 (WO). Glassimetal Technology, Inc. 2014.

[152] *Liquidmetal® - Swatch Group*. URL: https://www.swatchgroup.com/de/services/archiv/2018/liquidmetalr.

[153] Atakan Peker and Dongchun Qiao. "Zirconium Based Bulk Metallic Glasses with Hafnium." U.S. pat. 9353428B2. Washington State University WSU. 2016.

[154] Christopher D. Prest, Stephen B. Lynch, and Teodor Dabov. "Spatial Composites." U.S. pat. 11678445B2. Apple Inc. 2023.

[155] A. Makino, T. Hatanai, Y. Naitoh, T. Bitoh, A. Inoue, and T. Masumoto. "Applications of Nanocrystalline Soft Magnetic Fe-M-B (M=Zr, Nb) Alloys "NANOPERM(R)"." In: *IEEE Transactions on Magnetics* 33.5 (1997), pp. 3793–3798. ISSN: 1941-0069. DOI: 10.1109/20.619574.

[156] M. A. Willard, D. E. Laughlin, M. E. McHenry, D. Thoma, K. Sickafus, J. O. Cross, and V. G. Harris. "Structure and Magnetic Properties of $(Fe_{0.5}Co_{0.5})_{88}Zr_7B_4Cu_1$ Nanocrystalline Alloys." In: *Journal of Applied Physics* 84.12 (1998), pp. 6773–6777. ISSN: 0021-8979. DOI: 10.1063/1.369007.

[157] M. E. McHenry, F. Johnson, H. Okumura, T. Ohkubo, V. R. V. Ramanan, and D. E. Laughlin. "The Kinetics of Nanocrystallization and Microstructural Observations in FINEMET, NANOPERM and HITPERM Nanocomposite Magnetic Materials." In: *Scripta Materialia*. Nanostructured Advanced Magnetic Materials, Based on a Workshop Held at Irsee, Germany, 9-13 June, 2002 48.7 (2003), pp. 881–887. ISSN: 1359-6462. DOI: 10.1016/S1359-6462(02)00597-3.

[158] M. Kowalczyk, J. Ferenc, X. B. Liang, and T. Kulik. "Magnetic Properties of HITPERM-type Alloys at High Temperature." In: *Journal of Magnetism and Magnetic Materials*. Proceedings of the 17th International Symposium on Soft Magnetic Materials 304.2 (2006), e651–e653. ISSN: 0304-8853. DOI: 10.1016/j.jmmm.2006.02.158.

[159] F. E. Luborsky and H. H. Liebermann. "Crystallization Kinetics of Fe-B Amorphous Alloys." In: *Applied Physics Letters* 33.3 (2008), pp. 233–234. ISSN: 0003-6951. DOI: 10.1063/1.90309.

[160] K. F. Kelton. "A Perspective on Metallic Liquids and Glasses." In: *Journal of Applied Physics* 134.1 (2023), p. 010902. ISSN: 0021-8979. DOI: 10.1063/5.0144250.

[161] H. Choi-Yim and W. L. Johnson. "Bulk Metallic Glass Matrix Composites." In: *Applied Physics Letters* 71.26 (1997), pp. 3808–3810. ISSN: 0003-6951. DOI: 10.1063/1.120512.

[162] Cang Fan, R. T. Ott, and T. C. Hufnagel. “Metallic Glass Matrix Composite with Precipitated Ductile Reinforcement.” In: *Applied Physics Letters* 81.6 (2002), pp. 1020–1022. ISSN: 0003-6951. DOI: 10.1063/1.1498864.

[163] S. Pauly, J. Das, J. Bednarcik, N. Mattern, K. B. Kim, D. H. Kim, and J. Eckert. “Deformation-Induced Martensitic Transformation in Cu–Zr–(Al,Ti) Bulk Metallic Glass Composites.” In: *Scripta Materialia* 60.6 (2009), pp. 431–434. ISSN: 1359-6462. DOI: 10.1016/j.scriptamat.2008.11.015.

[164] S. Pauly, S. Gorantla, G. Wang, U. Kühn, and J. Eckert. “Transformation-Mediated Ductility in CuZr-based Bulk Metallic Glasses.” In: *Nature Materials* 9.6 (6 2010), pp. 473–477. ISSN: 1476-4660. DOI: 10.1038/nmat2767.

[165] Yuan Wu, Yuehua Xiao, Guoliang Chen, Chain T. Liu, and Zhaoping Lu. “Bulk Metallic Glass Composites with Transformation-Mediated Work-Hardening and Ductility.” In: *Advanced Materials* 22.25 (2010), pp. 2770–2773. ISSN: 1521-4095. DOI: 10.1002/adma.201000482.

[166] Y. Wu, H. Wang, H. H. Wu, Z. Y. Zhang, X. D. Hui, G. L. Chen, D. Ma, X. L. Wang, and Z. P. Lu. “Formation of Cu–Zr–Al Bulk Metallic Glass Composites with Improved Tensile Properties.” In: *Acta Materialia* 59.8 (2011), pp. 2928–2936. ISSN: 1359-6454. DOI: 10.1016/j.actamat.2011.01.029.

[167] Choongnyun Paul Kim, Yoon S. Oh, Sunghak Lee, and Nack J. Kim. “Realization of High Tensile Ductility in a Bulk Metallic Glass Composite by the Utilization of Deformation-Induced Martensitic Transformation.” In: *Scripta Materialia* 65.4 (2011), pp. 304–307. ISSN: 1359-6462. DOI: 10.1016/j.scriptamat.2011.04.037.

[168] Y. Wu, D. Ma, Q. K. Li, A. D. Stoica, W. L. Song, H. Wang, X. J. Liu, G. M. Stoica, G. Y. Wang, K. An, X. L. Wang, Mo Li, and Z. P. Lu. “Transformation-Induced Plasticity in Bulk Metallic Glass Composites Evidenced by in-Situ Neutron Diffraction.” In: *Acta Materialia* 124 (2017), pp. 478–488. ISSN: 1359-6454. DOI: 10.1016/j.actamat.2016.11.029.

[169] Yu Chen, Chunguang Tang, and Jian-Zhong Jiang. “Bulk Metallic Glass Composites Containing B2 Phase.” In: *Progress in Materials Science* 121 (2021), p. 100799. ISSN: 0079-6425. DOI: 10.1016/j.pmatsci.2021.100799.

[170] Frans Spaepen. “A Microscopic Mechanism for Steady State Inhomogeneous Flow in Metallic Glasses.” In: *Acta Metallurgica* 25.4 (1977), pp. 407–415. ISSN: 0001-6160. DOI: 10.1016/0001-6160(77)90232-2.

[171] A. S Argon. “Plastic Deformation in Metallic Glasses.” In: *Acta Metallurgica* 27.1 (1979), pp. 47–58. ISSN: 0001-6160. DOI: 10.1016/0001-6160(79)90055-5.

[172] A. S. Argon and L. T. Shi. “Development of Visco-Plastic Deformation in Metallic Glasses.” In: *Acta Metallurgica* 31.4 (1983), pp. 499–507. ISSN: 0001-6160. DOI: 10.1016/0001-6160(83)90038-X.

[173] Tobias Brink. "Heterogeneities in Metallic Glasses: Atomistic Computer Simulations on the Structure and Mechanical Properties of Copper–Zirconium Alloys and Composites." PhD thesis. Darmstadt: Technische Universität Darmstadt, 2017.

[174] Morrel H. Cohen and David Turnbull. "Molecular Transport in Liquids and Glasses." In: *The Journal of Chemical Physics* 31.5 (2004), pp. 1164–1169. ISSN: 0021-9606. DOI: 10.1063/1.1730566.

[175] David Turnbull and Morrel H. Cohen. "Free-Volume Model of the Amorphous Phase: Glass Transition." In: *The Journal of Chemical Physics* 34.1 (2004), pp. 120–125. ISSN: 0021-9606. DOI: 10.1063/1.1731549.

[176] David Turnbull and Morrel H. Cohen. "On the Free-Volume Model of the Liquid-Glass Transition." In: *The Journal of Chemical Physics* 52.6 (2003), pp. 3038–3041. ISSN: 0021-9606. DOI: 10.1063/1.1673434.

[177] D. Srolovitz, V. Vitek, and T. Egami. "An Atomistic Study of Deformation of Amorphous Metals." In: *Acta Metallurgica* 31.2 (1983), pp. 335–352. ISSN: 0001-6160. DOI: 10.1016/0001-6160(83)90110-4.

[178] M. L. Falk and J. S. Langer. "Dynamics of Viscoplastic Deformation in Amorphous Solids." In: *Physical Review E* 57.6 (1998), pp. 7192–7205. DOI: 10.1103/PhysRevE.57.7192.

[179] S. G. Mayr. "Activation Energy of Shear Transformation Zones: A Key for Understanding Rheology of Glasses and Liquids." In: *Physical Review Letters* 97.19 (2006), p. 195501. DOI: 10.1103/PhysRevLett.97.195501.

[180] Yvonne Ritter and Karsten Albe. "Thermal Annealing of Shear Bands in Deformed Metallic Glasses: Recovery Mechanisms in Cu64Zr36 Studied by Molecular Dynamics Simulations." In: *Acta Materialia* 59.18 (2011), pp. 7082–7094. ISSN: 1359-6454. DOI: 10.1016/j.actamat.2011.07.063.

[181] M. L. Falk, J. S. Langer, and L. Pechenik. "Thermal Effects in the Shear-Transformation-Zone Theory of Amorphous Plasticity: Comparisons to Metallic Glass Data." In: *Physical Review E* 70.1 (2004), p. 011507. DOI: 10.1103/PhysRevE.70.011507.

[182] J. S. Langer and L. Pechenik. "Dynamics of Shear-Transformation Zones in Amorphous Plasticity: Energetic Constraints in a Minimal Theory." In: *Physical Review E* 68.6 (2003), p. 061507. DOI: 10.1103/PhysRevE.68.061507.

[183] J. S. Langer. "Shear-Transformation-Zone Theory of Plastic Deformation near the Glass Transition." In: *Physical Review E* 77.2 (2008), p. 021502. DOI: 10.1103/PhysRevE.77.021502.

[184] Leonid Pechenik. "Dynamics of Shear-Transformation Zones in Amorphous Plasticity: Nonlinear Theory at Low Temperatures." In: *Physical Review E* 72.2 (2005), p. 021507. DOI: 10.1103/PhysRevE.72.021507.

[185] Eran Bouchbinder, J. S. Langer, and Itamar Procaccia. "Athermal Shear-Transformation-Zone Theory of Amorphous Plastic Deformation. I. Basic Principles." In: *Physical Review E* 75.3 (2007), p. 036107. DOI: 10.1103/PhysRevE.75.036107.

[186] Michael L. Falk and J.S. Langer. "Deformation and Failure of Amorphous, Solidlike Materials." In: *Annual Review of Condensed Matter Physics* 2.1 (2011), pp. 353–373. ISSN: 1947-5454, 1947-5462. DOI: 10.1146/annurev-conmatphys-062910-140452.

[187] Y. Calvayrac, J. P. Chevalier, M. Harmelin, A. Quivy, and J. Bigot. "On the Stability and Structure of Cu—Zr Based Glasses." In: *Philosophical Magazine B* 48.4 (1983), pp. 323–332. ISSN: 1364-2812. DOI: 10.1080/13642818308246485.

[188] Tang Mei-Bo, Zhao De-Qian, Pan Ming-Xiang, and Wang Wei-Hua. "Binary Cu–Zr Bulk Metallic Glasses." In: *Chinese Physics Letters* 21.5 (2004), p. 901. ISSN: 0256-307X. DOI: 10.1088/0256-307X/21/5/039.

[189] Donghua Xu, Boonrat Lohwongwatana, Gang Duan, William L. Johnson, and Carol Garland. "Bulk Metallic Glass Formation in Binary Cu-rich Alloy Series – Cu100−xZrx (X=34, 36, 38.2, 40 at.%) and Mechanical Properties of Bulk Cu64Zr36 Glass." In: *Acta Materialia* 52.9 (2004), pp. 2621–2624. ISSN: 1359-6454. DOI: 10.1016/j.actamat.2004.02.009.

[190] O. J. Kwon, Y. C. Kim, K. B. Kim, Y. K. Lee, and E. Fleury. "Formation of Amorphous Phase in the Binary Cu−Zr Alloy System." In: *Metals and Materials International* 12.3 (2006), pp. 207–212. ISSN: 1598-9623. DOI: 10.1007/BF03027532.

[191] G. Z. Ma, D. Chen, Y. Jiang, and W. Li. "Cryogenic Treatment-Induced Martensitic Transformation in Cu–Zr–Al Bulk Metallic Glass Composite." In: *Intermetallics* 18.6 (2010), pp. 1254–1257. ISSN: 0966-9795. DOI: 10.1016/j.intermet.2010.03.031.

[192] L. Yang, G. Q. Guo, L. Y. Chen, C. L. Huang, T. Ge, D. Chen, P. K. Liaw, K. Saksl, Y. Ren, Q. S. Zeng, B. LaQua, F. G. Chen, and J. Z. Jiang. "Atomic-Scale Mechanisms of the Glass-Forming Ability in Metallic Glasses." In: *Physical Review Letters* 109.10 (2012), p. 105502. DOI: 10.1103/PhysRevLett.109.105502.

[193] Peng Xue, Simon Pauly, Weimin Gan, Songshan Jiang, Hongbo Fan, Zhiliang Ning, Yongjiang Huang, and Jianfei Sun. "Enhanced Tensile Plasticity of a CuZr-based Bulk Metallic Glass Composite Induced by Ion Irradiation." In: *Journal of Materials Science & Technology* 35.10 (2019), pp. 2221–2226. ISSN: 1005-0302. DOI: 10.1016/j.jmst.2019.06.003.

[194] K. F. Gan, S. S. Jiang, Y. J. Huang, H. B. C. Yin, J. F. Sun, and A. H. W. Ngan. "Elucidating How Correlated Operation of Shear Transformation Zones Leads to Shear Localization and Fracture in Metallic Glasses: Tensile Tests on CuZr Based Metallic-Glass Microwires, Molecular Dynamics Simulations, and Modelling." In: *International Journal of Plasticity* 119 (2019), pp. 1–20. ISSN: 0749-6419. DOI: 10.1016/j.ijplas.2019.02.011.

[195] Hendrik Voigt, Aaron Rigoni, Evgeniy Boltynjuk, Mohammed Reda Chellali, Bonnie Tyler, Harald Rösner, Sergiy Divinski, Horst Hahn, and Gerhard Wilde. "Evidence for Glass–Glass Interfaces in a Columnar Cu–Zr Nanoglass." In: *Advanced Functional Materials* n/a.n/a (), p. 2302386. ISSN: 1616-3028. DOI: 10.1002/adfm.202302386.

[196] P. Zetterström, R. Delaplane, Y. D. Wang, P. K. Liaw, H. Choo, K. Saksl, H. F. Zhang, Y. Ren, and L. Zuo. "Nanoscale Defect Clusters in Metallic Glasses." In: *Journal of Physics: Condensed Matter* 19.37 (2007), p. 376217. ISSN: 0953-8984. DOI: 10.1088/0953-8984/19/37/376217.

[197] M. I. Mendelev, D. J. Sordelet, and M. J. Kramer. "Using Atomistic Computer Simulations to Analyze X-Ray Diffraction Data from Metallic Glasses." In: *Journal of Applied Physics* 102.4 (2007), p. 043501. ISSN: 0021-8979. DOI: 10.1063/1.2769157.

[198] Yvonne Ritter and Karsten Albe. "Chemical and Topological Order in Shear Bands of Cu64Zr36 and Cu36Zr64 Glasses." In: *Journal of Applied Physics* 111.10 (2012), p. 103527. ISSN: 0021-8979. DOI: 10.1063/1.4717748.

[199] Jun Ding, Yong-Qiang Cheng, and Evan Ma. "Full Icosahedra Dominate Local Order in Cu64Zr34 Metallic Glass and Supercooled Liquid." In: *Acta Materialia* 69 (2014), pp. 343–354. ISSN: 1359-6454. DOI: 10.1016/j.actamat.2014.02.005.

[200] Tobias Brink, Martin Peterlechner, Harald Rösner, Karsten Albe, and Gerhard Wilde. "Influence of Crystalline Nanoprecipitates on Shear-Band Propagation in Cu-Zr-Based Metallic Glasses." In: *Physical Review Applied* 5.5 (2016), p. 054005. ISSN: 2331-7019. DOI: 10.1103/PhysRevApplied.5.054005.

[201] C. X. Peng, D. Şopu, Y. Cheng, K. K. Song, S. H. Wang, J. Eckert, and L. Wang. "Deformation Behavior of Designed Dual-Phase CuZr Metallic Glasses." In: *Materials & Design* 168 (2019), p. 107662. ISSN: 0264-1275. DOI: 10.1016/j.matdes.2019.107662.

[202] Akash A. Deshmukh, Jatin G. Bhatt, Prashant M. Gade, and Snehanshu Pal. "Investigation of Structural Evolution in the Cu–Zr Metallic Glass at Cryogenic Temperatures by Using Molecular Dynamics Simulations." In: *Journal of Molecular Modeling* 27.10 (2021), p. 286. ISSN: 0948-5023. DOI: 10.1007/s00894-021-04886-y.

[203] Nicolás Amigo. "Role of High Pressure Treatments on the Atomic Structure of Cuzr Metallic Glasses." In: *Journal of Non-Crystalline Solids* 576 (2022), p. 121262. ISSN: 0022-3093. DOI: 10.1016/j.jnoncrysol.2021.121262.

[204] Qing Wang, Chuang Dong, Jianbing Qiang, and Yingmin Wang. "Cluster Line Criterion and Cu–Zr–Al Bulk Metallic Glass Formation." In: *Materials Science and Engineering: A*. Proceedings of the 12th International Conference on Rapidly Quenched & Metastable Materials 449–451 (2007), pp. 18–23. ISSN: 0921-5093. DOI: 10.1016/j.msea.2006.02.271.

[205] H. Men, S. J. Pang, and T. Zhang. "Glass-Forming Ability and Mechanical Properties of Cu50Zr50−xTix Alloys." In: *Materials Science and Engineering: A* 408.1 (2005), pp. 326–329. ISSN: 0921-5093. DOI: 10.1016/j.msea.2005.08.207.

[206] M. I. Mendelev, Y. Sun, F. Zhang, C. Z. Wang, and K. M. Ho. "Development of a Semi-Empirical Potential Suitable for Molecular Dynamics Simulation of Vitrification in Cu-Zr Alloys." In: *The Journal of Chemical Physics* 151.21 (2019), p. 214502. ISSN: 0021-9606. DOI: 10.1063/1.5131500.

[207] Young-Min Kim and Byeong-Joo Lee. "A Modified Embedded-Atom Method Interatomic Potential for the Cu–Zr System." In: *Journal of Materials Research* 23.4 (2008), pp. 1095–1104. ISSN: 2044-5326. DOI: 10.1557/jmr.2008.0130.

[208] Logan Ward, Anupriya Agrawal, Katharine M. Flores, and Wolfgang Windl. *Rapid Production of Accurate Embedded-Atom Method Potentials for Metal Alloys*. 2012. DOI: 10.48550/arXiv.1209.0619. arXiv: 1209.0619 [cond-mat, physics:physics]. URL: http://arxiv.org/abs/1209.0619. Prepublished.

[209] X. C. He, H. Wang, H. S. Liu, and Z. P. Jin. "Thermodynamic Description of the Cu–Ag–Zr System." In: *Calphad* 30.4 (2006), pp. 367–374. ISSN: 0364-5916. DOI: 10.1016/j.calphad.2006.09.001.

[210] Eckart Kneller, Yunus Khan, and Ursula Gorres. "The Alloy System Copper-Zirconium." In: *Z. Metallkde.* 77 (1986). DOI: 10.1515/ijmr-1986-770109.

[211] D. Arias and J. P. Abriata. "Cu-Zr (Copper-Zirconium)." In: *Journal of Phase Equilibria* 11.5 (1990), pp. 452–459. ISSN: 1054-9714. DOI: 10.1007/BF02898260.

[212] Na Wang, Changrong Li, Zhenmin Du, Fuming Wang, and Weijing Zhang. "The Thermodynamic Re-Assessment of the Cu–Zr System." In: *Calphad* 30.4 (2006), pp. 461–469. ISSN: 0364-5916. DOI: 10.1016/j.calphad.2006.06.002.

[213] H. Okamoto. "Cu-Zr (Copper-Zirconium)." In: *Journal of Phase Equilibria and Diffusion* 29.2 (2008), pp. 204–204. ISSN: 1863-7345. DOI: 10.1007/s11669-008-9267-2.

[214] Wojciech Gierlotka, Kai-Chien Zhang, and Yuan-Pei Chang. "Thermodynamic Description of the Binary Cu–Zr System." In: *Journal of Alloys and Compounds* 509.33 (2011), pp. 8313–8318. ISSN: 0925-8388. DOI: 10.1016/j.jallcom.2011.04.141.

[215] H. Okamoto. "Cu-Zr (Copper-Zirconium)." In: *Journal of Phase Equilibria and Diffusion* 33.5 (2012), pp. 417–418. ISSN: 1863-7345. DOI: 10.1007/s11669-012-0077-1.

[216] R Ray, B C Giessen, and N J Grant. "NON-CRYSTALLINE PleASES IN SPLAT COOLED TRANSITION METAL ALLOYS." In: *Scripta Metallurgica* 2.6 (1968), pp. 357–359.

[217] K. H. J. Buschow. "Short-Range Order and Thermal Stability in Amorphous Alloys." In: *Journal of Physics F: Metal Physics* 14.3 (1984), p. 593. ISSN: 0305-4608. DOI: 10.1088/0305-4608/14/3/005.

[218] Dae Hoon Kang and In-Ho Jung. "Critical Thermodynamic Evaluation and Optimization of the Ag–Zr, Cu–Zr and Ag–Cu–Zr Systems and Its Applications to Amorphous Cu–Zr–Ag Alloys." In: *Intermetallics* 18.5 (2010), pp. 815–833. ISSN: 0966-9795. DOI: 10.1016/j.intermet.2009.12.013.

[219] K. J. Zeng, M. Hämäläinen, and H. L. Lukas. "A New Thermodynamic Description of the Cu-Zr System." In: *Journal of Phase Equilibria* 15.6 (1994), pp. 577–586. ISSN: 1054-9714. DOI: 10.1007/BF02647618.

[220] S. H. Zhou and R. E. Napolitano. "Phase Stability for the Cu–Zr System: First-principles, Experiments and Solution-Based Modeling." In: *Acta Materialia* 58.6 (2010), pp. 2186–2196. ISSN: 1359-6454. DOI: 10.1016/j.actamat.2009.12.004.

[221] Yu. N. Koval, G. S. Firstov, and A. V. Kotko. "Martensitic Transformation and Shape Memory Effect in ZrCu Intermetallic Compound." In: *Scripta Metallurgica et Materialia* 27.11 (1992), pp. 1611–1616. ISSN: 0956-716X. DOI: 10.1016/0956-716X(92)90153-6.

[222] N. Mattern, A. Schöps, U. Kühn, J. Acker, O. Khvostikova, and J. Eckert. "Structural Behavior of CuxZr100−x Metallic Glass (X=35−70)." In: *Journal of Non-Crystalline Solids* 354.10 (2008), pp. 1054–1060. ISSN: 0022-3093. DOI: 10.1016/j.jnoncrysol.2007.08.035.

[223] N. Mattern, P. Jóvári, I. Kaban, S. Gruner, A. Elsner, V. Kokotin, H. Franz, B. Beuneu, and J. Eckert. "Short-Range Order of Cu–Zr Metallic Glasses." In: *Journal of Alloys and Compounds* 485.1 (2009), pp. 163–169. ISSN: 0925-8388. DOI: 10.1016/j.jallcom.2009.05.111.

[224] N. Mattern, J. Bednarčik, S. Pauly, G. Wang, J. Das, and J. Eckert. "Structural Evolution of Cu–Zr Metallic Glasses under Tension." In: *Acta Materialia* 57.14 (2009), pp. 4133–4139. ISSN: 1359-6454. DOI: 10.1016/j.actamat.2009.05.011.

[225] T. W. Barbee Jr., R. G. Walmsley, A. F. Marshall, D. L. Keith, and D. A. Stevenson. "Phase Separation in Vapor Quench Synthesized Noncrystalline Copper Zirconium Alloys." In: *Applied Physics Letters* 38.3 (1981), pp. 132–135. ISSN: 0003-6951. DOI: 10.1063/1.92275.

[226] D. Deng and A. S. Argon. "Structural Relaxation and Embrittlement of Cu59Zr41 and Fe80B20 Glasses." In: *Acta Metallurgica* 34.10 (1986), pp. 2011–2023. ISSN: 0001-6160. DOI: 10.1016/0001-6160(86)90260-9.

[227] Ch. E. Lekka, A. Ibenskas, A. R. Yavari, and G. A. Evangelakis. "Tensile Deformation Accommodation in Microscopic Metallic Glasses via Subnanocluster Reconstructions." In: *Applied Physics Letters* 91.21 (2007), p. 214103. ISSN: 0003-6951. DOI: 10.1063/1.2816912.

[228] Y. Q. Cheng, A. J. Cao, H. W. Sheng, and E. Ma. "Local Order Influences Initiation of Plastic Flow in Metallic Glass: Effects of Alloy Composition and Sample Cooling History." In: *Acta Materialia* 56.18 (2008), pp. 5263–5275. ISSN: 1359-6454. DOI: 10.1016/j.actamat.2008.07.011.

[229] A. J. Cao, Y. Q. Cheng, and E. Ma. "Structural Processes That Initiate Shear Localization in Metallic Glass." In: *Acta Materialia* 57.17 (2009), pp. 5146–5155. ISSN: 1359-6454. DOI: 10.1016/j.actamat.2009.07.016.

[230] K. A. Avchaciov, Y. Ritter, F. Djurabekova, K. Nordlund, and K. Albe. "Controlled Softening of Cu64Zr36 Metallic Glass by Ion Irradiation." In: *Applied Physics Letters* 102.18 (2013), p. 181910. ISSN: 0003-6951. DOI: 10.1063/1.4804630.

[231] J. Zemp, M. Celino, B. Schönfeld, and J. F. Löffler. "Crystal-Like Rearrangements of Icosahedra in Simulated Copper-Zirconium Metallic Glasses and Their Effect on Mechanical Properties." In: *Physical Review Letters* 115.16 (2015), p. 165501. DOI: 10.1103/PhysRevLett.115.165501.

[232] Z. D. Sha, Y. P. Feng, and Y. Li. "The Fundamental Structural Factor in Determining the Glass-Forming Ability and Mechanical Behavior in the Cu–Zr Metallic Glasses." In: *Materials Chemistry and Physics* 127.1 (2011), pp. 292–295. ISSN: 0254-0584. DOI: 10.1016/j.matchemphys.2011.02.005.

[233] J. G. Wang, Y. C. Hu, P. F. Guan, K. K. Song, L. Wang, G. Wang, Y. Pan, B. Sarac, and J. Eckert. "Hardening of Shear Band in Metallic Glass." In: *Scientific Reports* 7.1 (1 2017), p. 7076. ISSN: 2045-2322. DOI: 10.1038/s41598-017-07669-9.

[234] Christopher M. Andolina, Philip Williamson, and Wissam A. Saidi. "Optimization and Validation of a Deep Learning CuZr Atomistic Potential: Robust Applications for Crystalline and Amorphous Phases with near-DFT Accuracy." In: *The Journal of Chemical Physics* 152.15 (2020), p. 154701. ISSN: 0021-9606, 1089-7690. DOI: 10.1063/5.0005347.

[235] Yue Wang and John P. Perdew. "Spin Scaling of the Electron-Gas Correlation Energy in the High-Density Limit." In: *Physical Review B* 43.11 (1991), pp. 8911–8916. DOI: 10.1103/PhysRevB.43.8911.

[236] C. Tang and Peter Harrowell. "Predicting the Solid State Phase Diagram for Glass-Forming Alloys of Copper and Zirconium." In: *Journal of Physics: Condensed Matter* 24.24 (2012), p. 245102. ISSN: 0953-8984. DOI: 10.1088/0953-8984/24/24/245102.

[237] R. E. Ryltsev, B. A. Klumov, N. M. Chtchelkatchev, and K. Yu. Shunyaev. "Cooling Rate Dependence of Simulated Cu64.5Zr35.5 Metallic Glass Structure." In: *The Journal of Chemical Physics* 145.3 (2016), p. 034506. ISSN: 0021-9606. DOI: 10.1063/1.4958631.

[238] R. E. Ryltsev, B. A. Klumov, N. M. Chtchelkatchev, and K. Yu. Shunyaev. "Nucleation Instability in Supercooled Cu–Zr–Al Glass-Forming Liquids." In: *The Journal of Chemical Physics* 149.16 (2018), p. 164502. ISSN: 0021-9606. DOI: 10.1063/1.5054631.

[239] Tobias Brink and Karsten Albe. "From Metallic Glasses to Nanocrystals: Molecular Dynamics Simulations on the Crossover from Glass-like to Grain-Boundary-Mediated Deformation Behaviour." In: *Acta Materialia* 156 (2018), pp. 205–214. ISSN: 1359-6454. DOI: 10.1016/j.actamat.2018.06.036.

[240] Weidong Liu and Liangchi Zhang. "On the Nano/Micro-Mechanics of Metallic Glass." In: *Critical Reviews in Solid State and Materials Sciences* 40.3 (2015), pp. 137–163. ISSN: 1040-8436. DOI: 10.1080/10408436.2014.973933.

[241] Quan Dong, Jun Tan, Caiju Li, Baran Sarac, and Jürgen Eckert. "Room-Temperature Plasticity of Metallic Glass Composites: A Review." In: *Composites Part B: Engineering* 280 (2024), p. 111453. ISSN: 1359-8368. DOI: 10.1016/j.compositesb.2024.111453.

[242] A Inoue, W Zhang, T Zhang, and K Kurosaka. "High-Strength Cu-based Bulk Glassy Alloys in Cu–Zr–Ti and Cu–Hf–Ti Ternary Systems." In: *Acta Materialia* 49.14 (2001), pp. 2645–2652. ISSN: 1359-6454. DOI: 10.1016/S1359-6454(01)00181-1.

[243] Akihisa Inoue, Wei Zhang, Tao Zhang, and Kei Kurosaka. "Thermal and Mechanical Properties of Cu-Based Cu-Zr-Ti Bulk Glassy Alloys." In: *Materials Transactions* 42.6 (2001), pp. 1149–1151. DOI: 10.2320/matertrans.42.1149.

[244] L. Q. Xing, P. Ochin, and J. Bigot. "Effects of Al on the Glass-Forming Ability of Zr-Cu Based Alloys." In: *Journal of Non-Crystalline Solids* 205–207 (1996), pp. 637–640. ISSN: 0022-3093. DOI: 10.1016/S0022-3093(96)00382-1.

[245] Simon Pauly, Jozef Bednarčik, Uta Kühn, and Jürgen Eckert. "Plastically Deformable Cu–Zr Intermetallics." In: *Scripta Materialia* 63.3 (2010), pp. 336–338. ISSN: 1359-6462. DOI: 10.1016/j.scriptamat.2010.04.034.

[246] Nicholas P. Bailey, Jakob Schiøtz, and Karsten W. Jacobsen. "Atomistic Simulation Study of the Shear-Band Deformation Mechanism in Mg-Cu Metallic Glasses." In: *Physical Review B* 73.6 (2006), p. 064108. DOI: 10.1103/PhysRevB.73.064108.

[247] Yunfeng Shi and Michael L. Falk. "Atomic-Scale Simulations of Strain Localization in Three-Dimensional Model Amorphous Solids." In: *Physical Review B* 73.21 (2006), p. 214201. DOI: 10.1103/PhysRevB.73.214201.

[248] Yunfeng Shi and Michael L. Falk. "Stress-Induced Structural Transformation and Shear Banding during Simulated Nanoindentation of a Metallic Glass." In: *Acta Materialia* 55.13 (2007), pp. 4317–4324. ISSN: 1359-6454. DOI: 10.1016/j.actamat.2007.03.029.

[249] Y. Q. Cheng, A. J. Cao, and E. Ma. "Correlation between the Elastic Modulus and the Intrinsic Plastic Behavior of Metallic Glasses: The Roles of Atomic Configuration and Alloy Composition." In: *Acta Materialia* 57.11 (2009), pp. 3253–3267. ISSN: 1359-6454. DOI: 10.1016/j.actamat.2009.03.027.

[250] D. Şopu, M. Stoica, and J. Eckert. "Deformation Behavior of Metallic Glass Composites Reinforced with Shape Memory Nanowires Studied via Molecular Dynamics Simulations." In: *Applied Physics Letters* 106.21 (2015), p. 211902. ISSN: 0003-6951. DOI: 10.1063/1.4921857.

[251] D. Şopu, K. Albe, and J. Eckert. "Metallic Glass Nanolaminates with Shape Memory Alloys." In: *Acta Materialia* 159 (2018), pp. 344–351. ISSN: 1359-6454. DOI: 10.1016/j.actamat.2018.08.034.

[252] Constanze Kalcher, Tobias Brink, Jochen Rohrer, Alexander Stukowski, and Karsten Albe. "Interface-Controlled Creep in Metallic Glass Composites." In: *Acta Materialia* 141 (2017), pp. 251–260. ISSN: 1359-6454. DOI: 10.1016/j.actamat.2017.08.058.

[253] Constanze Kalcher. "Creep of Cu-Zr Metallic Glasses and Metallic Glass Composites: A Molecular Dynamics Study." PhD thesis. Darmstadt: Technische Universität Darmstadt, 2019. DOI: 10/1/thesis-kalcher.pdf.

[254] Ziyong Li, Zhangwei Chen, Jian Liu, Yuelong Fu, Changyong Liu, Pei Wang, Mingguang Jiang, and Changshi Lao. "Additive Manufacturing of Lightweight and High-Strength Polymer-Derived SiOC Ceramics." In: *Virtual and Physical Prototyping* 15.2 (2020), pp. 163–177. ISSN: 1745-2759. DOI: 10.1080/17452759.2019.1710919.

[255] Elizabeth Barrios and Lei Zhai. "A Review of the Evolution of the Nanostructure of SiCN and SiOC Polymer Derived Ceramics and the Impact on Mechanical Properties." In: *Molecular Systems Design & Engineering* 5.10 (2020), pp. 1606–1641. DOI: 10.1039/D0ME00123F.

[256] Benjamin Papendorf, Emanuel Ionescu, Hans-Joachim Kleebe, Christoph Linck, Olivier Guillon, Katharina Nonnenmacher, and Ralf Riedel. "High-Temperature Creep Behavior of Dense SiOC-Based Ceramic Nanocomposites: Microstructural and Phase Composition Effects." In: *Journal of the American Ceramic Society* 96.1 (2013), pp. 272–280. ISSN: 1551-2916. DOI: 10.1111/jace.12067.

[257] Christina Stabler, Felix Roth, Masaki Narisawa, Daniel Schliephake, Martin Heilmaier, Stefan Lauterbach, Hans-Joachim Kleebe, Ralf Riedel, and Emanuel Ionescu. "High-Temperature Creep Behavior of a SiOC Glass Ceramic Free of Segregated Carbon." In: *Journal of the European Ceramic Society*. Preparation and Application of Ultra-high Temperature Ceramic Matrix Composites 36.15 (2016), pp. 3747–3753. ISSN: 0955-2219. DOI: 10.1016/j.jeurceramsoc.2016.04.015.

[258] Ralf Riedel, Liviu Toma, Enrico Janssen, Jürgen Nuffer, Tobias Melz, and Holger Hanselka. "Piezoresistive Effect in SiOC Ceramics for Integrated Pressure Sensors." In: *Journal of the American Ceramic Society* 93.4 (2010), pp. 920–924. ISSN: 1551-2916. DOI: 10.1111/j.1551-2916.2009.03496.x.

[259] F. Roth, C. Schmerbauch, E. Ionescu, N. Nicoloso, O. Guillon, and R. Riedel. "High-Temperature Piezoresistive C / SiOC Sensors." In: *Journal of Sensors and Sensor Systems* 4.1 (2015), pp. 133–136. ISSN: 2194-8771. DOI: 10.5194/jsss-4-133-2015.

[260] Emmanuel III Ricohermoso, Susana Solano-Arana, Claudia Fasel, Ralf Riedel, and Emanuel Ionescu. "SiOC-Based Strain Gauge with Ultrahigh Piezoresistivity at High Temperatures." In: *ACS Applied Engineering Materials* 1.4 (2023), pp. 1093–1105. DOI: 10.1021/acsaenm.2c00201.

[261] V. S. Pradeep, Magdalena Graczyk-Zajac, R. Riedel, and G. D. Soraru. "New Insights in to the Lithium Storage Mechanism in Polymer Derived SiOC Anode Materials." In: *Electrochimica Acta* 119 (2014), pp. 78–85. ISSN: 0013-4686. DOI: 10.1016/j.electacta.2013.12.037.

[262] Jan Kaspar, Mathias Storch, Cristina Schitco, Ralf Riedel, and Magdalena Graczyk-Zajac. "SiOC(N)/Hard Carbon Composite Anodes for Na-Ion Batteries: Influence of Morphology on the Electrochemical Properties." In: *Journal of The Electrochemical Society* 163.2 (2015), A156. ISSN: 1945-7111. DOI: 10.1149/2.0391602jes.

[263] Pradeep Vallachira Warriam Sasikumar, Gurdial Blugan, Nicola Casati, Eirini Kakkava, Giulia Panusa, Demetri Psaltis, and Jakob Kuebler. "Polymer Derived Silicon Oxycarbide Ceramic Monoliths: Microstructure Development and Associated Materials Properties." In: *Ceramics International* 44.17 (2018), pp. 20961–20967. ISSN: 0272-8842. DOI: 10.1016/j.ceramint.2018.08.102.

[264] Christian Chandra, Handi Setiadi Cahyadi, Stevanus Alvin, Winda Devina, Jae-Ho Park, Wonyoung Chang, Kyung Yoon Chung, Sang Kyu Kwak, and Jaehoon Kim. "Revealing the Sodium Storage Mechanism in High-Temperature-Synthesized Silicon Oxycarbides." In: *Chemistry of Materials* 32.1 (2020), pp. 410–423. ISSN: 0897-4756. DOI: 10.1021/acs.chemmater.9b04018.

[265] Zhiyuan Sang, Xiao Yan, Lei Wen, Dong Su, Zhihao Zhao, Yue Liu, Huiming Ji, Ji Liang, and Shi Xue Dou. "A Graphene-Modified Flexible SiOC Ceramic Cloth for High-Performance Lithium Storage." In: *Energy Storage Materials* 25 (2020), pp. 876–884. ISSN: 2405-8297. DOI: 10.1016/j.ensm.2019.11.014.

[266] Kedong Xia, Xiao Liu, He Liu, Yun Lu, Zhenmin Liu, Yunling Li, Lingyao Duan, Zhenyu Hou, Renlong Li, and Deli Wang. "Carbon-Enriched SiOC Ceramics with Hierarchical Porous Structure as Anodes for Lithium Storage." In: *Electrochimica Acta* 372 (2021), p. 137899. ISSN: 0013-4686. DOI: 10.1016/j.electacta.2021.137899.

[267] Christian Chandra, Winda Devina, Handi Setiadi Cahyadi, Sang Kyu Kwak, and Jaehoon Kim. "Understanding Lithium, Sodium, and Potassium Storage Mechanisms in Silicon Oxycarbide." In: *Chemical Engineering Journal* 428 (2022), p. 131072. ISSN: 1385-8947. DOI: 10.1016/j.cej.2021.131072.

[268] Marco Melzi d'Eril, Andrea Zambotti, Magdalena Graczyk-Zajac, Emanuel Ionescu, Gian Domenico Sorarù, and Ralf Riedel. "Effect of Ultra-Fast Pyrolysis on Polymer-Derived SiOC Aerogels and Their Application as Anodes for Na-ion Batteries." In: *Open Ceramics* 14 (2023), p. 100354. ISSN: 2666-5395. DOI: 10.1016/j.oceram.2023.100354.

[269] Kathy Lu and Donald Erb. "Polymer Derived Silicon Oxycarbide-Based Coatings." In: *International Materials Reviews* 63.3 (2018), pp. 139–161. ISSN: 0950-6608. DOI: 10.1080/09506608.2017.1322247.

[270] Cekdar Vakifahmetoglu, Merve Buldu, Aylin Karakuscu, Andrea Ponzoni, Dawit Assefa, and Gian Domenico Soraru. "High Surface Area Carbonous Components from Emulsion Derived SiOC and Their Gas Sensing Behavior." In: *Journal of the European Ceramic Society* 35.16 (2015), pp. 4447–4452. ISSN: 0955-2219. DOI: 10.1016/j.jeurceramsoc.2015.08.030.

[271] Zhiwei Chen, Dong Su, Wenxia Zhu, Xiaoliang Sun, Xiaolei Li, and Huiming Ji. "A Superelastic SiOC@carbon Ceramic Spring for Multifunctional Pressure Sensor in Wide Temperature Range." In: *Chemical Engineering Journal* 468 (2023), p. 143635. ISSN: 1385-8947. DOI: 10.1016/j.cej.2023.143635.

[272] Qingbo Wen, Fangmu Qu, Zhaoju Yu, Magdalena Graczyk-Zajac, Xiang Xiong, and Ralf Riedel. "Si-Based Polymer-Derived Ceramics for Energy Conversion and Storage." In: *Journal of Advanced Ceramics* 11 (2022), pp. 197–246. DOI: 10.1007/s40145-021-0562-2.

[273] Marcela Arango-Ospina, Fangtong Xie, Isabel Gonzalo-Juan, Ralf Riedel, Emanuel Ionescu, and Aldo R. Boccaccini. "Review: Silicon Oxycarbide Based Materials for Biomedical Applications." In: *Applied Materials Today* 18 (2020), p. 100482. ISSN: 2352-9407. DOI: 10.1016/j.apmt.2019.100482.

[274] Richard B. Ellis. "Method of Making Electrically Conducting Glass and Articles Made Therefrom." U.S. pat. 2556616A. Corning Glass Works. 1951.

[275] A. Scarmi, G.D. Sorarù, and R. Raj. "The Role of Carbon in Unexpected Visco(an)Elastic Behavior of Amorphous Silicon Oxycarbide above 1273K." In: *Journal of Non-Crystalline Solids* 351.27-29 (2005), pp. 2238–2243. ISSN: 00223093. DOI: 10.1016/j.jnoncrysol.2005.06.008.

[276] Atanu Saha, Rishi Raj, and Don L. Williamson. "A Model for the Nanodomains in Polymer-Derived SiCO." In: *Journal of the American Ceramic Society* 89.7 (2006), pp. 2188–2195. ISSN: 1551-2916. DOI: 10.1111/j.1551-2916.2006.00920.x.

[277] S. J. Widgeon, S. Sen, G. Mera, E. Ionescu, R. Riedel, and A. Navrotsky. "29Si and 13C Solid-State NMR Spectroscopic Study of Nanometer-Scale Structure and Mass Fractal Characteristics of Amorphous Polymer Derived Silicon Oxycarbide Ceramics." In: *Chemistry of Materials* 22.23 (2010), pp. 6221–6228. ISSN: 0897-4756. DOI: 10.1021/cm1021432.

[278] Gian Domenico Sorarù, Gennaro D'Andrea, Renzo Campostrini, Florence Babonneau, and Gino Mariotto. "Structural Characterization and High-Temperature Behavior of Silicon Oxycarbide Glasses Prepared from Sol-Gel Precursors Containing Si-H Bonds." In: *Journal of the American Ceramic Society* 78.2 (1995), pp. 379–387. ISSN: 1551-2916. DOI: 10.1111/j.1151-2916.1995.tb08811.x.

[279] Felix Roth, Philipp Waleska, Christian Hess, Emanuel Ionescu, and Norbert Nicoloso. "UV Raman Spectroscopy of Segregated Carbon in Silicon Oxycarbides." In: *Journal of the Ceramic Society of Japan* 124.10 (2016), pp. 1042–1045. DOI: 10.2109/jcersj2.16100.

[280] Raquel Peña-Alonso, Gian Domenico Sorarù, and Rishi Raj. "Preparation of Ultrathin-Walled Carbon-Based Nanoporous Structures by Etching Pseudo-Amorphous Silicon Oxycarbide Ceramics." In: *Journal of the American Ceramic Society* 89.8 (2006), pp. 2473–2480. ISSN: 1551-2916. DOI: 10.1111/j.1551-2916.2006.01117.x.

[281] Christina Stabler, Emanuel Ionescu, Magdalena Graczyk-Zajac, Isabel Gonzalo-Juan, and Ralf Riedel. "Silicon Oxycarbide Glasses and Glass-Ceramics: "All-Rounder" Materials for Advanced Structural and Functional Applications." In: *Journal of the American Ceramic Society* 101.11 (2018), pp. 4817–4856. ISSN: 00027820. DOI: 10.1111/jace.15932.

[282] Federico A. Soria, Weiwei Zhang, Patricia A. Paredes-Olivera, Adri. C. T. van Duin, and Eduardo M. Patrito. "Si/C/H ReaxFF Reactive Potential for Silicon Surfaces Grafted with Organic Molecules." In: *The Journal of Physical Chemistry C* 122.41 (2018), pp. 23515–23527. ISSN: 1932-7447. DOI: 10.1021/acs.jpcc.8b07075.

[283] Vikas Tomar, Ming Gan, and Han Sung Kim. "Atomistic Analyses of the Effect of Temperature and Morphology on Mechanical Strength of Si–C–N and Si–C–O Nanocomposites." In: *Journal of the European Ceramic Society.* Special Issue: Aerospace Materials for Extreme Environments 30.11 (2010), pp. 2223–2237. ISSN: 0955-2219. DOI: 10.1016/j.jeurceramsoc.2010.03.002.

[284] Ningbo Liao, Miao Zhang, Hongming Zhou, and Wei Xue. "Modeling of Amorphous SiCxO6/5 by Classical Molecular Dynamics and First Principles Calculations." In: *Scientific Reports* 7.1 (2017), p. 42705. ISSN: 2045-2322. DOI: 10.1038/srep42705.

[285] Shariq Haseen and Peter Kroll. "Analyzing the Effect of Composition, Density, and the Morphology of the "Free" Carbon Phase on Elastic Moduli in Silicon Oxycarbide Ceramics." In: *Journal of the European Ceramic Society* 43.4 (2023), pp. 1432–1441. ISSN: 0955-2219. DOI: 10.1016/j.jeurceramsoc.2022.11.025.

[286] Gabriela Mera and Emanuel Ionescu. "Silicon-Containing Preceramic Polymers." In: *Encyclopedia of Polymer Science and Technology.* John Wiley & Sons, Ltd, 2013. ISBN: 978-0-471-44026-0. DOI: 10.1002/0471440264.pst591.

[287] Gabriela Mera, Markus Gallei, Samuel Bernard, and Emanuel Ionescu. "Ceramic Nanocomposites from Tailor-Made Preceramic Polymers." In: *Nanomaterials* 5.2 (2 2015), pp. 468–540. ISSN: 2079-4991. DOI: 10.3390/nano5020468.

[288] Y. de Hazan and D. Penner. "SiC and SiOC Ceramic Articles Produced by Stereolithography of Acrylate Modified Polycarbosilane Systems." In: *Journal of the European Ceramic Society*. Shaping of Advanced Ceramics 37.16 (2017), pp. 5205–5212. ISSN: 0955-2219. DOI: 10.1016/j.jeurceramsoc.2017.03.021.

[289] Kai Huang, Hamada Elsayed, Giorgia Franchin, and Paolo Colombo. "Additive Manufacturing of SiOC Scaffolds with Tunable Structure-Performance Relationship." In: *Journal of the European Ceramic Society* 41.15 (2021), pp. 7552–7559. ISSN: 0955-2219. DOI: 10.1016/j.jeurceramsoc.2021.08.043.

[290] Greta Merkininkaite, Darius Gailevicius, Laurynas Staisiunas, Egle Ezerskyte, Rokas Vargalis, Mangirdas Malinauskas, and Simas Sakirzanovas. "Additive Manufacturing of SiOC, SiC, and Si3N4 Ceramic 3D Microstructures." In: *Advanced Engineering Materials* 25.17 (2023), p. 2300639. ISSN: 1527-2648. DOI: 10.1002/adem.202300639.

[291] H. Bréquel, J. Parmentier, S. Walter, R. Badheka, G. Trimmel, S. Masse, J. Latournerie, P. Dempsey, C. Turquat, A. Desmartin-Chomel, L. Le Neindre-Prum, U. A. Jayasooriya, D. Hourlier, H.-J. Kleebe, G. D. Sorarù, S. Enzo, and F. Babonneau. "Systematic Structural Characterization of the High-Temperature Behavior of Nearly Stoichiometric Silicon Oxycarbide Glasses." In: *Chemistry of Materials* 16.13 (2004), pp. 2585–2598. ISSN: 0897-4756. DOI: 10.1021/cm049847a.

[292] I. Ponomarev, T. Polcar, and P. Nicolini. "New Reactive Force Field for Simulations of MoS2 Crystallization." In: *The Journal of Physical Chemistry C* 126.22 (2022), pp. 9475–9481. ISSN: 1932-7447. DOI: 10.1021/acs.jpcc.2c01075.

[293] F. Wooten, K. Winer, and D. Weaire. "Computer Generation of Structural Models of Amorphous Si and Ge." In: *Physical Review Letters* 54.13 (1985), pp. 1392–1395. DOI: 10.1103/PhysRevLett.54.1392.

[294] Peter Kroll. "Modelling and Simulation of Amorphous Silicon Oxycarbide." In: *Journal of Materials Chemistry* 13.7 (2003), pp. 1657–1668. DOI: 10.1039/B301389H.

[295] Peter Kroll. "Modeling the 'Free Carbon' Phase in Amorphous Silicon Oxycarbide." In: *Journal of Non-Crystalline Solids*. Proceedings of the International Conference on Non-Crystalline Materials (CONCIM) 351.12 (2005), pp. 1121–1126. ISSN: 0022-3093. DOI: 10.1016/j.jnoncrysol.2005.01.010.

[296] Peter Kroll. "Searching Insight into the Atomistic Structure of SiCO Ceramics." In: *Journal of Materials Chemistry* 20.46 (2010), pp. 10528–10534. DOI: 10.1039/C0JM01583K.

[297] *Ceramics Science and Technology Vol1: Structures*. 1st ed. John Wiley & Sons, Ltd, 2008. DOI: 10.1002/9783527631926.

[298] Gian Domenico Sorarù, Elisabetta Dallapiccola, and Gennaro D'Andrea. "Mechanical Characterization of Sol–Gel-Derived Silicon Oxycarbide Glasses." In: *Journal of the American Ceramic Society* 79.8 (1996), pp. 2074–2080. ISSN: 1551-2916. DOI: 10.1111/j.1151-2916.1996.tb08939.x.

[299] Christina Stabler, Fabrice Celarie, Tanguy Rouxel, René Limbach, Lothar Wondraczek, Ralf Riedel, and Emanuel Ionescu. "Effect of Composition and High-Temperature Annealing on the Local Deformation Behavior of Silicon Oxycarbides." In: *Journal of the European Ceramic Society* 39.7 (2019), pp. 2287–2296. ISSN: 09552219. DOI: 10.1016/j.jeurceramsoc.2019.02.024.

[300] S Walter, G. D Soraru, H Bréquel, and S Enzo. "Microstructural and Mechanical Characterization of Sol Gel-Derived Si–O–C Glasses." In: *Journal of the European Ceramic Society* 22.13 (2002), pp. 2389–2400. ISSN: 0955-2219. DOI: 10.1016/S0955-2219(01)00537-4.

[301] Claude Moysan, Ralf Riedel, Rahul Harshe, Tanguy Rouxel, and Franck Augereau. "Mechanical Characterization of a Polysiloxane-Derived SiOC Glass." In: *Journal of the European Ceramic Society* 27.1 (2007), pp. 397–403. ISSN: 0955-2219. DOI: 10.1016/j.jeurceramsoc.2006.01.016.

[302] Sandra Martínez-Crespiera, Emanuel Ionescu, Hans-Joachim Kleebe, and Ralf Riedel. "Pressureless Synthesis of Fully Dense and Crack-Free SiOC Bulk Ceramics via Photo-Crosslinking and Pyrolysis of a Polysiloxane." In: *Journal of the European Ceramic Society* 31.5 (2011), pp. 913–919. ISSN: 0955-2219. DOI: 10.1016/j.jeurceramsoc.2010.11.019.

[303] J. Tersoff. "New Empirical Approach for the Structure and Energy of Covalent Systems." In: *Physical Review B* 37.12 (1988), pp. 6991–7000. DOI: 10.1103/PhysRevB.37.6991.

[304] J. Tersoff. "Empirical Interatomic Potential for Carbon, with Applications to Amorphous Carbon." In: *Physical Review Letters* 61.25 (1988), pp. 2879–2882. DOI: 10.1103/PhysRevLett.61.2879.

[305] P. Hohenberg and W. Kohn. "Inhomogeneous Electron Gas." In: *Physical Review* 136 (3B 1964), B864–B871. DOI: 10.1103/PhysRev.136.B864.

[306] W. Kohn and L. J. Sham. "Self-Consistent Equations Including Exchange and Correlation Effects." In: *Physical Review* 140 (4A 1965), A1133–A1138. DOI: 10.1103/PhysRev.140.A1133.

[307] Fabien Tran, Jan Doumont, Leila Kalantari, Ahmad W. Huran, Miguel A. L. Marques, and Peter Blaha. "Semilocal Exchange-Correlation Potentials for Solid-State Calculations: Current Status and Future Directions." In: *Journal of Applied Physics* 126.11 (2019), p. 110902. ISSN: 0021-8979. DOI: 10.1063/1.5118863.

[308] Richard M. Martin. *Electronic Structure: Basic Theory and Practical Methods*. 2nd ed. Cambridge: Cambridge University Press, 2020. ISBN: 978-1-108-42990-0. DOI: 10.1017/9781108555586.

[309] G. Kresse, J. Furthmüller, and J. Hafner. "Theory of the Crystal Structures of Selenium and Tellurium: The Effect of Generalized-Gradient Corrections to the Local-Density Approximation." In: *Physical Review B* 50.18 (1994), pp. 13181–13185. DOI: 10.1103/PhysRevB.50.13181.

[310] G. Kresse and J. Furthmüller. "Efficiency of Ab-Initio Total Energy Calculations for Metals and Semiconductors Using a Plane-Wave Basis Set." In: *Computational Materials Science* 6.1 (1996), pp. 15–50. ISSN: 0927-0256. DOI: 10.1016/0927-0256(96)00008-0.

[311] G. Kresse and J. Furthmüller. "Efficient Iterative Schemes for Ab Initio Total-Energy Calculations Using a Plane-Wave Basis Set." In: *Physical Review B* 54.16 (1996), pp. 11169–11186. DOI: 10.1103/PhysRevB.54.11169.

[312] G. Kresse and D. Joubert. "From Ultrasoft Pseudopotentials to the Projector Augmented-Wave Method." In: *Physical Review B* 59.3 (1999), pp. 1758–1775. DOI: 10.1103/PhysRevB.59.1758.

[313] John P. Perdew, Kieron Burke, and Matthias Ernzerhof. "Generalized Gradient Approximation Made Simple." In: *Physical Review Letters* 77.18 (1996), pp. 3865–3868. DOI: 10.1103/PhysRevLett.77.3865.

[314] Jianwei Sun, Adrienn Ruzsinszky, and John P. Perdew. "Strongly Constrained and Appropriately Normed Semilocal Density Functional." In: *Physical Review Letters* 115.3 (2015), p. 036402. DOI: 10.1103/PhysRevLett.115.036402.

[315] Steve Plimpton. "Fast Parallel Algorithms for Short-Range Molecular Dynamics." In: *Journal of Computational Physics* 117.1 (1995), pp. 1–19. ISSN: 0021-9991. DOI: 10.1006/jcph.1995.1039.

[316] Aidan P. Thompson, H. Metin Aktulga, Richard Berger, Dan S. Bolintineanu, W. Michael Brown, Paul S. Crozier, Pieter J. in 't Veld, Axel Kohlmeyer, Stan G. Moore, Trung Dac Nguyen, Ray Shan, Mark J. Stevens, Julien Tranchida, Christian Trott, and Steven J. Plimpton. "LAMMPS - a Flexible Simulation Tool for Particle-Based Materials Modeling at the Atomic, Meso, and Continuum Scales." In: *Computer Physics Communications* 271 (2022), p. 108171. ISSN: 0010-4655. DOI: 10.1016/j.cpc.2021.108171.

[317] Wataru Shinoda, Motoyuki Shiga, and Masuhiro Mikami. "Rapid Estimation of Elastic Constants by Molecular Dynamics Simulation under Constant Stress." In: *Physical Review B* 69.13 (2004), p. 134103. DOI: 10.1103/PhysRevB.69.134103.

[318] Mark E. Tuckerman, José Alejandre, Roberto López-Rendón, Andrea L. Jochim, and Glenn J. Martyna. "A Liouville-operator Derived Measure-Preserving Integrator for Molecular Dynamics Simulations in the Isothermal–Isobaric Ensemble." In: *Journal of Physics A: Mathematical and General* 39.19 (2006), p. 5629. ISSN: 0305-4470. DOI: 10.1088/0305-4470/39/19/S18.

[319] Shuichi Nosé. "A Unified Formulation of the Constant Temperature Molecular Dynamics Methods." In: *The Journal of Chemical Physics* 81.1 (1984), pp. 511–519. ISSN: 0021-9606. DOI: 10.1063/1.447334.

[320] William G. Hoover. "Canonical Dynamics: Equilibrium Phase-Space Distributions." In: *Physical Review A* 31.3 (1985), pp. 1695–1697. DOI: 10.1103/PhysRevA.31.1695.

[321] M. Parrinello and A. Rahman. "Polymorphic Transitions in Single Crystals: A New Molecular Dynamics Method." In: *Journal of Applied Physics* 52.12 (1981), pp. 7182–7190. ISSN: 0021-8979. DOI: 10.1063/1.328693.

[322] Ellad B. Tadmor and Ronald E. Miller. *Modeling Materials: Continuum, Atomistic and Multiscale Techniques*. Cambridge: Cambridge University Press, 2011. ISBN: 978-0-521-85698-0. DOI: 10.1017/CBO9781139003582.

[323] "Chapter 3 The Method of Total Scattering and Atomic Pair Distribution Function Analysis." In: *Pergamon Materials Series*. Ed. by Takeshi Egami and Simon J. L. Billinge. Vol. 7. Underneath the Bragg Peaks, Structural Analysis of Complex Materials. Pergamon, 2003, pp. 55–99. DOI: 10.1016/S1470-1804(03)80005-6.

[324] T. E. Faber and J. M. Ziman. "A Theory of the Electrical Properties of Liquid Metals." In: *The Philosophical Magazine: A Journal of Theoretical Experimental and Applied Physics* 11.109 (1965), pp. 153–173. ISSN: 0031-8086. DOI: 10.1080/14786436508211931.

[325] Georges Voronoi. "Nouvelles applications des paramètres continus à la théorie des formes quadratiques. Deuxième mémoire. Recherches sur les parallélloèdres primitifs." In: *Journal für die reine und angewandte Mathematik (Crelles Journal)* 1908.134 (1908), pp. 198–287. ISSN: 1435-5345. DOI: 10.1515/crll.1908.134.198.

[326] Emanuel A. Lazar, Jian Han, and David J. Srolovitz. "Topological Framework for Local Structure Analysis in Condensed Matter." In: *Proceedings of the National Academy of Sciences* 112.43 (2015), E5769–E5776. DOI: 10.1073/pnas.1505788112.

[327] X. Z. Gao, M. H. Müser, L. T. Kong, and J. F. Li. "Atomic Structure and Energetics of Amorphous–Crystalline CuZr Interfaces: A Molecular Dynamics Study." In: *Modelling and Simulation in Materials Science and Engineering* 22.6 (2014), p. 065007. ISSN: 0965-0393. DOI: 10.1088/0965-0393/22/6/065007.

[328] Alexander Stukowski. "Visualization and Analysis of Atomistic Simulation Data with OVITO–the Open Visualization Tool." In: *Modelling and Simulation in Materials Science and Engineering* 18.1 (2009), p. 015012. ISSN: 0965-0393. DOI: 10.1088/0965-0393/18/1/015012.

[329] Osamu Sugino and Roberto Car. "Ab Initio Molecular Dynamics Study of First-Order Phase Transitions: Melting of Silicon." In: *Physical Review Letters* 74.10 (1995), pp. 1823–1826. DOI: 10.1103/PhysRevLett.74.1823.

[330] D. Alfè, M. J. Gillan, and G. D. Price. "Complementary Approaches to the Ab Initio Calculation of Melting Properties." In: *The Journal of Chemical Physics* 116.14 (2002), pp. 6170–6177. ISSN: 0021-9606. DOI: 10.1063/1.1460865.

[331] D. Alfè, L. Vočadlo, G. D. Price, and M. J. Gillan. "Melting Curve of Materials: Theory versus Experiments." In: *Journal of Physics: Condensed Matter* 16.14 (2004), S973. ISSN: 0953-8984. DOI: 10.1088/0953-8984/16/14/006.

[332] L. Vočadlo, D. Alfè, G. D. Price, and M. J. Gillan. "Ab Initio Melting Curve of Copper by the Phase Coexistence Approach." In: *The Journal of Chemical Physics* 120.6 (2004), pp. 2872–2878. ISSN: 0021-9606. DOI: 10.1063/1.1640344.

[333] A. B. Belonoshko, L. Burakovsky, S. P. Chen, B. Johansson, A. S. Mikhaylushkin, D. L. Preston, S. I. Simak, and D. C. Swift. "Molybdenum at High Pressure and Temperature: Melting from Another Solid Phase." In: *Physical Review Letters* 100.13 (2008), p. 135701. DOI: 10.1103/PhysRevLett.100.135701.

[334] Grégory Robert, Philippe Legrand, Philippe Arnault, Nicolas Desbiens, and Jean Clérouin. "Simple Calculation of Ab Initio Melting Curves: Application to Aluminum." In: *Physical Review E* 91.3 (2015), p. 033310. DOI: 10.1103/PhysRevE.91.033310.

[335] Li-Fang Zhu, Blazej Grabowski, and Jörg Neugebauer. "Efficient Approach to Compute Melting Properties Fully from Ab Initio with Application to Cu." In: *Physical Review B* 96.22 (2017), p. 224202. DOI: 10.1103/PhysRevB.96.224202.

[336] Maurice de Koning. "Optimizing the Driving Function for Nonequilibrium Free-Energy Calculations in the Linear Regime: A Variational Approach." In: *The Journal of Chemical Physics* 122.10 (2005), p. 104106. ISSN: 0021-9606. DOI: 10.1063/1.1860556.

[337] Daan Frenkel and Anthony J. C. Ladd. "New Monte Carlo Method to Compute the Free Energy of Arbitrary Solids. Application to the Fcc and Hcp Phases of Hard Spheres." In: *The Journal of Chemical Physics* 81.7 (1984), pp. 3188–3193. ISSN: 0021-9606. DOI: 10.1063/1.448024.

[338] Sarath Menon, Yury Lysogorskiy, Jutta Rogal, and Ralf Drautz. "Automated Free-Energy Calculation from Atomistic Simulations." In: *Physical Review Materials* 5.10 (2021), p. 103801. DOI: 10.1103/PhysRevMaterials.5.103801.

[339] Rodolfo Paula Leite, Rodrigo Freitas, Rodolfo Azevedo, and Maurice de Koning. "The Uhlenbeck-Ford Model: Exact Virial Coefficients and Application as a Reference System in Fluid-Phase Free-Energy Calculations." In: *The Journal of Chemical Physics* 145.19 (2016), p. 194101. ISSN: 0021-9606. DOI: 10.1063/1.4967775.

[340] Maurice de Koning, A. Antonelli, and Sidney Yip. "Optimized Free-Energy Evaluation Using a Single Reversible-Scaling Simulation." In: *Physical Review Letters* 83.20 (1999), pp. 3973–3977. DOI: 10.1103/PhysRevLett.83.3973.

[341] Masakatsu Watanabe and William P. Reinhardt. "Direct Dynamical Calculation of Entropy and Free Energy by Adiabatic Switching." In: *Physical Review Letters* 65.26 (1990), pp. 3301–3304. DOI: 10.1103/PhysRevLett.65.3301.

[342] Pauli Virtanen, Ralf Gommers, Travis E. Oliphant, Matt Haberland, Tyler Reddy, David Cournapeau, Evgeni Burovski, Pearu Peterson, Warren Weckesser, Jonathan Bright, Stéfan J. van der Walt, Matthew Brett, Joshua Wilson, K. Jarrod Millman, Nikolay Mayorov, Andrew R. J. Nelson, Eric Jones, Robert Kern, Eric Larson, C. J. Carey, İlhan Polat, Yu Feng, Eric W. Moore, Jake VanderPlas, Denis Laxalde, Josef Perktold, Robert Cimrman, Ian Henriksen, E. A. Quintero, Charles R. Harris, Anne M. Archibald, Antônio H. Ribeiro, Fabian Pedregosa, and Paul van Mulbregt. "SciPy 1.0: Fundamental Algorithms for Scientific Computing in Python." In: *Nature Methods* 17.3 (3 2020), pp. 261–272. ISSN: 1548-7105. DOI: 10.1038/s41592-019-0686-2.

[343] Stephan Hoyer and Joe Hamman. "Xarray: N-D Labeled Arrays and Datasets in Python." In: 5.1 (1 2017), p. 10. ISSN: 2049-9647. DOI: 10.5334/jors.148.

[344] A. Reuss. "Berechnung Der Fließgrenze von Mischkristallen Auf Grund Der Plastizitätsbedingung Für Einkristalle ." In: *ZAMM - Journal of Applied Mathematics and Mechanics / Zeitschrift für Angewandte Mathematik und Mechanik* 9.1 (1929), pp. 49–58. ISSN: 1521-4001. DOI: 10.1002/zamm.19290090104.

[345] Woldemar Voigt. *Lehrbuch der Kristallphysik*. Wiesbaden: Vieweg+Teubner Verlag, 1966. ISBN: 978-3-663-15316-0 978-3-663-15884-4. DOI: 10.1007/978-3-663-15884-4.

[346] Futoshi Shimizu, Shigenobu Ogata, and Ju Li. "Theory of Shear Banding in Metallic Glasses and Molecular Dynamics Calculations." In: *Materials Transactions* 48.11 (2007), pp. 2923–2927. DOI: 10.2320/matertrans.MJ200769.

[347] Niklas Leimeroth, Jochen Rohrer, and Karsten Albe. "General Purpose Potential for Glassy and Crystalline Phases of Cu-Zr Alloys Based on the ACE Formalism." In: *Physical Review Materials* 8.4 (2024), p. 043602. DOI: 10.1103/PhysRevMaterials.8.043602.

[348] Niklas Leimeroth, Jochen Rohrer, and Karsten Albe. *Dataset for "A General Purpose Potential for Glassy and Crystalline Phases of Cu-Zr Alloys Based on the ACE Formalism"*. Version 1. Zenodo. DOI: 10.5281/zenodo.8137854.

[349] *NIST-JANAF Thermochemical Tables - SRD 13*. Version 1.0.2. [object Object], 2013. DOI: 10.18434/T42S31.

[350] A. K. Giri and G. B. Mitra. "Extrapolated Values of Lattice Constants of Some Cubic Metals at Absolute Zero." In: *Journal of Physics D: Applied Physics* 18.7 (1985), p. L75. ISSN: 0022-3727. DOI: 10.1088/0022-3727/18/7/005.

[351] J. Goldak, L. T. Lloyd, and C. S. Barrett. "Lattice Parameters, Thermal Expansions, and Grüneisen Coefficients of Zirconium, 4.2 to 1130°K." In: *Physical Review* 144.2 (1966), pp. 478–484. DOI: 10.1103/PhysRev.144.478.

[352] A. Heiming, W. Petry, J. Trampenau, W. Miekeley, and J. Cockcroft. "The Temperature Dependence of the Lattice Parameters of Pure BCC Zr and BCC Zr-2 at.%Co." In: *Journal of Physics: Condensed Matter* 4.3 (1992), p. 727. ISSN: 0953-8984. DOI: 10.1088/0953-8984/4/3/012.

[353] J. Gegner, O. Shuleshova, R. Kobold, D. Holland-Moritz, F. Yang, W. Hornfeck, J. Bednarcik, and D. M. Herlach. "In Situ Observation of the Phase Selection from the Undercooled Melt in Cu–Zr." In: *Journal of Alloys and Compounds* 576 (2013), pp. 232–235. ISSN: 0925-8388. DOI: 10.1016/j.jallcom.2013.04.035.

[354] R. R. Bourassa and B. Lengeler. "The Formation and Migration Energies of Vacancies in Quenched Copper." In: *Journal of Physics F: Metal Physics* 6.8 (1976), p. 1405. ISSN: 0305-4608. DOI: 10.1088/0305-4608/6/8/003.

[355] R. W. Balluffi. "Vacancy Defect Mobilities and Binding Energies Obtained from Annealing Studies." In: *Journal of Nuclear Materials* 69–70 (1978), pp. 240–263. ISSN: 0022-3115. DOI: 10.1016/0022-3115(78)90247-7.

[356] G. M. Hood. "Diffusion and Vacancy Properties of α-Zr." In: *Journal of Nuclear Materials* 139.3 (1986), pp. 179–184. ISSN: 0022-3115. DOI: 10.1016/0022-3115(86)90170-4.

[357] H. M. Ledbetter. "Elastic Constants of Polycrystalline Copper at Low Temperatures. Relationship to Single-Crystal Elastic Constants." In: *physica status solidi (a)* 66.2 (1981), pp. 477–484. ISSN: 1521-396X. DOI: 10.1002/pssa.2210660209.

[358] E. S. Fisher, M. H. Manghnani, and T. J. Sokolowski. “Hydrostatic Pressure Derivatives of the Single-Crystal Elastic Moduli of Zirconium.” In: *Journal of Applied Physics* 41.7 (1970), pp. 2991–2998. ISSN: 0021-8979, 1089-7550. DOI: 10.1063/1.1659351.

[359] E. S. Fisher and C. J. Renken. “Single-Crystal Elastic Moduli and the Hcp → Bcc Transformation in Ti, Zr, and Hf.” In: *Physical Review* 135 (2A 1964), A482–A494. ISSN: 0031-899X. DOI: 10.1103/PhysRev.135.A482.

[360] Jong Hyun Jung, Axel Forslund, Prashanth Srinivasan, and Blazej Grabowski. “Dynamically Stabilized Phases with Full Ab Initio Accuracy: Thermodynamics of Ti, Zr, Hf with a Focus on the Hcp-Bcc Transition.” In: *Physical Review B* 108.18 (2023), p. 184107. DOI: 10.1103/PhysRevB.108.184107.

[361] J. Murray, A. Peruzzi, and J. P. Abriata. “The Al-Zr (Aluminum-Zirconium) System.” In: *Journal of Phase Equilibria* 13.3 (1992), pp. 277–291. ISSN: 1054-9714. DOI: 10.1007/BF02667556.

[362] Maria Helena Braga, Luis Filipe Malheiros, Fernando Castro, and Delfim Soares. “Experimental Liquidus Points and Invariant Reactions in the Cu–Zr System.” In: *International Journal of Materials Research* 89.8 (1998), pp. 541–545. ISSN: 2195-8556. DOI: 10.3139/ijmr-1998-0102.

[363] A. Glensk, B. Grabowski, T. Hickel, and J. Neugebauer. “Breakdown of the Arrhenius Law in Describing Vacancy Formation Energies: The Importance of Local Anharmonicity Revealed by Ab Initio Thermodynamics.” In: *Physical Review X* 4.1 (2014), p. 011018. DOI: 10.1103/PhysRevX.4.011018.

[364] James R. Morris and Xueyu Song. “The Melting Lines of Model Systems Calculated from Coexistence Simulations.” In: *The Journal of Chemical Physics* 116.21 (2002), pp. 9352–9358. ISSN: 0021-9606. DOI: 10.1063/1.1474581.

[365] Yong Zhang and Edward J. Maginn. “A Comparison of Methods for Melting Point Calculation Using Molecular Dynamics Simulations.” In: *The Journal of Chemical Physics* 136.14 (2012), p. 144116. ISSN: 0021-9606. DOI: 10.1063/1.3702587.

[366] Valery Borovikov, Mikhail I. Mendelev, Alexander H. King, and Richard LeSar. “Effect of Stacking Fault Energy on Mechanism of Plastic Deformation in Nanotwinned FCC Metals.” In: *Modelling and Simulation in Materials Science and Engineering* 23.5 (2015), p. 055003. ISSN: 0965-0393. DOI: 10.1088/0965-0393/23/5/055003.

[367] Armin Von Keitz and Gerhard Sauthoff. “Laves Phases for High Temperatures—Part II: Stability and Mechanical Properties.” In: *Intermetallics* 10.5 (2002), pp. 497–510. ISSN: 0966-9795. DOI: 10.1016/S0966-9795(02)00025-0.

[368] Atsushi Togo, Laurent Chaput, Terumasa Tadano, and Isao Tanaka. "Implementation Strategies in Phonopy and Phono3py." In: *Journal of Physics: Condensed Matter* 35.35 (2023), p. 353001. ISSN: 0953-8984. DOI: 10.1088/1361-648X/acd831.

[369] Atsushi Togo. "First-Principles Phonon Calculations with Phonopy and Phono3py." In: *Journal of the Physical Society of Japan* 92.1 (2023), p. 012001. ISSN: 0031-9015. DOI: 10.7566/JPSJ.92.012001.

[370] T. Tadano, Y. Gohda, and S. Tsuneyuki. "Anharmonic Force Constants Extracted from First-Principles Molecular Dynamics: Applications to Heat Transfer Simulations." In: *Journal of Physics: Condensed Matter* 26.22 (2014), p. 225402. ISSN: 0953-8984. DOI: 10.1088/0953-8984/26/22/225402.

[371] Terumasa Tadano and Shinji Tsuneyuki. "Self-Consistent Phonon Calculations of Lattice Dynamical Properties in Cubic ${\mathrm{SrTiO}}_{3}$ with First-Principles Anharmonic Force Constants." In: *Physical Review B* 92.5 (2015), p. 054301. DOI: 10.1103/PhysRevB.92.054301.

[372] N. Hatcher, O. Yu. Kontsevoi, and A. J. Freeman. "Martensitic Transformation Path of NiTi." In: *Physical Review B* 79.2 (2009), p. 020202. DOI: 10.1103/PhysRevB.79.020202.

[373] N. Hatcher, O. Yu. Kontsevoi, and A. J. Freeman. "Role of Elastic and Shear Stabilities in the Martensitic Transformation Path of NiTi." In: *Physical Review B* 80.14 (2009), p. 144203. DOI: 10.1103/PhysRevB.80.144203.

[374] Karsten Albe, Yvonne Ritter, and Daniel Şopu. "Enhancing the Plasticity of Metallic Glasses: Shear Band Formation, Nanocomposites and Nanoglasses Investigated by Molecular Dynamics Simulations." In: *Mechanics of Materials*. Nanostructured Materials 67 (2013), pp. 94–103. ISSN: 0167-6636. DOI: 10.1016/j.mechmat.2013.06.004.

[375] Li Zhang, Yong-Qiang Cheng, A-Jing Cao, Jian Xu, and Evan Ma. "Bulk Metallic Glasses with Large Plasticity: Composition Design from the Structural Perspective." In: *Acta Materialia* 57.4 (2009), pp. 1154–1164. ISSN: 1359-6454. DOI: 10.1016/j.actamat.2008.11.002.

[376] Lauri Himanen, Marc O. J. Jäger, Eiaki V. Morooka, Filippo Federici Canova, Yashasvi S. Ranawat, David Z. Gao, Patrick Rinke, and Adam S. Foster. "DScribe: Library of Descriptors for Machine Learning in Materials Science." In: *Computer Physics Communications* 247 (2020), p. 106949. ISSN: 0010-4655. DOI: 10.1016/j.cpc.2019.106949.

[377] Niklas Leimeroth, Jochen Rohrer, and Karsten Albe. "Structure–Property Relations of Silicon Oxycarbides Studied Using a Machine Learning Interatomic Potential." In: *Journal of the American Ceramic Society* 107.10 (2024), pp. 6896–6910. ISSN: 1551-2916. DOI: 10.1111/jace.19932.

[378] Niklas Leimeroth, Jochen Rohrer, and Karsten Albe. *Potential and Training Data for 'Structure-Property Relations of Silicon Oxycarbides Studied Using a Novel Machine Learning Interatomic Potential'*. DOI: 10.5281/zenodo.10131450.

[379] Jochen Rohrer, Dragoljub Vrankovic, Damian Cupid, Ralf Riedel, Hans J. Seifert, Karsten Albe, and Magdalena Graczyk-Zajac. "Si- and Sn-containing SiOCN-based Nanocomposites as Anode Materials for Lithium Ion Batteries: Synthesis, Thermodynamic Characterization and Modeling." In: *International Journal of Materials Research* 108.11 (2017), pp. 920–932. ISSN: 2195-8556. DOI: 10.3139/146.111517.

[380] Edina Šić, Jochen Rohrer, Emmanuel III Ricohermoso, Karsten Albe, Emmanuel Ionescu, Ralf Riedel, Hergen Breitzke, Torsten Gutmann, and Gerd Buntkowsky. "SiCO Ceramics as Storage Materials for Alkali Metals/Ions: Insights on Structure Moieties from Solid-State NMR and DFT Calculations." In: *ChemSusChem* n/a.n/a (), e202202241. ISSN: 1864-564X. DOI: 10.1002/cssc.202202241.

[381] L. Martínez, R. Andrade, E. G. Birgin, and J. M. Martínez. "PACKMOL: A package for building initial configurations for molecular dynamics simulations." In: *Journal of Computational Chemistry* 30.13 (2009), pp. 2157–2164. ISSN: 1096-987X. DOI: 10.1002/jcc.21224.

[382] José Mario Martínez and Leandro Martínez. "Packing Optimization for Automated Generation of Complex System's Initial Configurations for Molecular Dynamics and Docking." In: *Journal of Computational Chemistry* 24.7 (2003), pp. 819–825. ISSN: 1096-987X. DOI: 10.1002/jcc.10216.

[383] Qingbo Wen, Zhaoju Yu, and Ralf Riedel. "The Fate and Role of in Situ Formed Carbon in Polymer-Derived Ceramics." In: *Progress in Materials Science* 109 (2020), p. 100623. ISSN: 0079-6425. DOI: 10.1016/j.pmatsci.2019.100623.

[384] O. Delverdier, M. Monthioux, D. Mocaer, and R. Pailler. "Thermal Behavior of Polymer-Derived Ceramics. I. Si-C and Si-C-O Systems from Both Commercial and New Polycarbosilane (PCS) Precursors." In: *Journal of the European Ceramic Society* 12.1 (1993), pp. 27–41. ISSN: 0955-2219. DOI: 10.1016/0955-2219(93)90068-3.

[385] Carlo G. Pantano, Anant K. Singh, and Hanxi Zhang. "Silicon Oxycarbide Glasses." In: *Journal of Sol-Gel Science and Technology* 14.1 (1999), pp. 7–25. ISSN: 1573-4846. DOI: 10.1023/A:1008765829012.

[386] Alexey Bosak, Michael Krisch, Marcel Mohr, Janina Maultzsch, and Christian Thomsen. "Elasticity of Single-Crystalline Graphite: Inelastic x-Ray Scattering Study." In: *Physical Review B* 75.15 (2007), p. 153408. DOI: 10.1103/PhysRevB.75.153408.

[387] O. L. Blakslee, D. G. Proctor, E. J. Seldin, G. B. Spence, and T. Weng. "Elastic Constants of Compression-Annealed Pyrolytic Graphite." In: *Journal of Applied Physics* 41.8 (1970), pp. 3373–3382. ISSN: 0021-8979. DOI: 10.1063/1.1659428.

[388] Willi Pabst and EVA Gregorová. "Elastic Properties of Silica Polymorphs–a Review." In: *Ceramics-Silikaty* 57.3 (2013), pp. 167–184.

[389] Dinesh Varshney, S. Shriya, M. Varshney, N. Singh, and R. Khenata. "Elastic and Thermodynamical Properties of Cubic (3C) Silicon Carbide under High Pressure and High Temperature." In: *Journal of Theoretical and Applied Physics* 9.3 (2015), pp. 221–249. ISSN: 2251-7235. DOI: 10.1007/s40094-015-0183-7.

[390] Gian Domenico Sorarù, Lakshminath Kundanati, Balanand Santhosh, and Nicola Pugno. "Influence of Free Carbon on the Young's Modulus and Hardness of Polymer-Derived Silicon Oxycarbide Glasses." In: *Journal of the American Ceramic Society* 102.3 (2019), pp. 907–913. ISSN: 1551-2916. DOI: 10.1111/jace.16131.

[391] Seiji Inaba, Shigeru Fujino, and Kenji Morinaga. "Young's Modulus and Compositional Parameters of Oxide Glasses." In: *Journal of the American Ceramic Society* 82.12 (1999), pp. 3501–3507. ISSN: 1551-2916. DOI: 10.1111/j.1151-2916.1999.tb02272.x.

[392] Jörg Behler. "First Principles Neural Network Potentials for Reactive Simulations of Large Molecular and Condensed Systems." In: *Angewandte Chemie International Edition* 56.42 (2017), pp. 12828–12840. ISSN: 1521-3773. DOI: 10.1002/anie.201703114.

[393] Jason Ansel, Edward Yang, Horace He, Natalia Gimelshein, Animesh Jain, Michael Voznesensky, Bin Bao, Peter Bell, David Berard, Evgeni Burovski, Geeta Chauhan, Anjali Chourdia, Will Constable, Alban Desmaison, Zachary DeVito, Elias Ellison, Will Feng, Jiong Gong, Michael Gschwind, Brian Hirsh, Sherlock Huang, Kshiteej Kalambarkar, Laurent Kirsch, Michael Lazos, Mario Lezcano, Yanbo Liang, Jason Liang, Yinghai Lu, CK Luk, Bert Maher, Yunjie Pan, Christian Puhrsch, Matthias Reso, Mark Saroufim, Marcos Yukio Siraichi, Helen Suk, Michael Suo, Phil Tillet, Eikan Wang, Xiaodong Wang, William Wen, Shunting Zhang, Xu Zhao, Keren Zhou, Richard Zou, Ajit Mathews, Gregory Chanan, Peng Wu, and Soumith Chintala. *PyTorch 2: Faster Machine Learning Through Dynamic Python Bytecode Transformation and Graph Compilation*. ACM, 2024. DOI: 10.1145/3620665.3640366.

[394] Ralf Drautz. "Atomic Cluster Expansion of Scalar, Vectorial, and Tensorial Properties Including Magnetism and Charge Transfer." In: *Physical Review B* 102.2 (2020), p. 024104. DOI: 10.1103/PhysRevB.102.024104.

[395] Matteo Rinaldi, Matous Mrovec, Anton Bochkarev, Yury Lysogorskiy, and Ralf Drautz. "Non-Collinear Magnetic Atomic Cluster Expansion for Iron." In: *npj Computational Materials* 10.1 (1 2024), pp. 1–12. ISSN: 2057-3960. DOI: 10.1038/s41524-024-01196-8.

[396] Ivan Novikov, Blazej Grabowski, Fritz Körmann, and Alexander Shapeev. "Magnetic Moment Tensor Potentials for Collinear Spin-Polarized Materials Reproduce Different Magnetic States of Bcc Fe." In: *npj Computational Materials* 8.1 (1 2022), pp. 1–6. ISSN: 2057-3960. DOI: 10.1038/s41524-022-00696-9.

[397] Q. Li, S. S. Liu, X. H. Wang, T. Yang, C. Dong, J. T. Hu, and Y. Q. Jiang. "Mechanical and Corrosion Properties of Ti-Ni-Cu-Zr Metallic Glass Matrix Composites." In: *Journal of Alloys and Compounds* 727 (2017), pp. 1344–1350. ISSN: 0925-8388. DOI: 10.1016/j.jallcom.2017.08.120.

[398] Stephan Thaler and Julija Zavadlav. "Learning Neural Network Potentials from Experimental Data via Differentiable Trajectory Reweighting." In: *Nature Communications* 12.1 (1 2021), p. 6884. ISSN: 2041-1723. DOI: 10.1038/s41467-021-27241-4.

[399] Sakib Matin, Alice E. A. Allen, Justin Smith, Nicholas Lubbers, Ryan B. Jadrich, Richard Messerly, Benjamin Nebgen, Ying Wai Li, Sergei Tretiak, and Kipton Barros. "Machine Learning Potentials with the Iterative Boltzmann Inversion: Training to Experiment." In: *JOURNAL OF CHEMICAL THEORY AND COMPUTATION* 20.3 (2024), pp. 1274–1281. ISSN: 1549-9618, 1549-9626. DOI: 10.1021/acs.jctc.3c01051.

[400] Justin S. Smith, Benjamin T. Nebgen, Roman Zubatyuk, Nicholas Lubbers, Christian Devereux, Kipton Barros, Sergei Tretiak, Olexandr Isayev, and Adrian E. Roitberg. "Approaching Coupled Cluster Accuracy with a General-Purpose Neural Network Potential through Transfer Learning." In: *Nature Communications* 10.1 (2019), p. 2903. ISSN: 2041-1723. DOI: 10.1038/s41467-019-10827-4.

[401] X. Y. Wang, S. D. Feng, L. Qi, W. Gao, and S. L. Zhang. "Mechanical Properties of Cu50Zr50 Amorphous/B2-CuZr Crystalline Composites Studied by Molecular Dynamic Method." In: *Journal of Non-Crystalline Solids* 568 (2021), p. 120942. ISSN: 0022-3093. DOI: 10.1016/j.jnoncrysol.2021.120942.

[402] Sarath Menon, Yury Lysogorskiy, Alexander L. M. Knoll, Niklas Leimeroth, Marvin Poul, Minaam Qamar, Jan Janssen, Matous Mrovec, Jochen Rohrer, Karsten Albe, Jörg Behler, Ralf Drautz, and Jörg Neugebauer. *From Electrons to Phase Diagrams with Classical and Machine Learning Potentials: Automated Workflows for Materials Science with Pyiron*. 2024. DOI: 10.48550/arXiv.2403.05724. arXiv: 2403.05724 [cond-mat]. URL: http://arxiv.org/abs/2403.05724. Pre-published.

[403] Alexander Stukowski, Erik Fransson, Markus Mock, and Paul Erhart. "Atomicrex—a General Purpose Tool for the Construction of Atomic Interaction Models." In: *Modelling and Simulation in Materials Science and Engineering* 25.5 (2017), p. 055003. ISSN: 0965-0393. DOI: 10.1088/1361-651X/aa6ecf.